



Delft University of Technology

Document Version

Final published version

Citation (APA)

Ferrante, G. (2026). *Large eddy simulation of hydrogen combustion: Development of models and applications for sustainable power generation*. [Dissertation (TU Delft), Delft University of Technology].
<https://doi.org/10.4233/uuid:8fc599e5-d2b0-4f88-904d-84f076b463e8>

Important note

To cite this publication, please use the final published version (if applicable).
Please check the document version above.

Copyright

In case the licence states "Dutch Copyright Act (Article 25fa)", this publication was made available Green Open Access via the TU Delft Institutional Repository pursuant to Dutch Copyright Act (Article 25fa, the Taverne amendment). This provision does not affect copyright ownership.
Unless copyright is transferred by contract or statute, it remains with the copyright holder.

Sharing and reuse

Other than for strictly personal use, it is not permitted to download, forward or distribute the text or part of it, without the consent of the author(s) and/or copyright holder(s), unless the work is under an open content license such as Creative Commons.

Takedown policy

Please contact us and provide details if you believe this document breaches copyrights.
We will remove access to the work immediately and investigate your claim.

This work is downloaded from Delft University of Technology.

Large eddy simulation of hydrogen combustion

Development of models and applications
for sustainable power generation



Gioele Ferrante

LARGE EDDY SIMULATION OF HYDROGEN COMBUSTION

**DEVELOPMENT OF MODELS AND APPLICATIONS FOR
SUSTAINABLE POWER GENERATION**

Dissertation

for the purpose of obtaining the degree of doctor
at Delft University of Technology
by the authority of the Rector Magnificus, Prof.dr.ir. H. Bijl,
chair of the Board for Doctorates
to be defended publicly on Thursday 30th of April 2026 at 10:00.

by

Gioele FERRANTE

This dissertation has been approved by the promotor and the copromotor.

Composition of the doctoral committee:

Rector Magnificus,	Chairperson
Prof. Dr.-Ing. G. Eitelberg,	Delft University of Technology, <i>promotor</i>
Prof.dr. A. Gangoli Rao,	Delft University of Technology, <i>promotor</i>
Dr. I. Langella,	Delft University of Technology, <i>copromotor</i>

Independent members:

Prof.dr. D. J. E. M. Roekaerts,	Delft University of Technology
Prof.dr. F. Creta,	Sapienza University of Rome, Italy
Prof.dr. J. A. Van Oijen,	Eindhoven University of Technology, The Netherlands
Dr. D. Mira Martinez,	Barcelona Supercomputing Centre, Spain
Prof. Dr.-Ing. habil S. Hickel,	Delft University of Technology, <i>reserve member</i>

This research was performed at the Sustainable Aircraft Propulsion group within the Flight Performance and Propulsion Section, Department of Flow Physics and Technology, Faculty of Aerospace Engineering. The work is part of the research project "Advanced Power and Propulsion Unit" (APPU), supported by Safran Tech and by the Dutch Ministry of Economic Affairs and Climate under the TKI scheme (Grant number TKI HTSM/18.0170).



Keywords: Large Eddy Simulation (LES), Hydrogen combustion, Differential diffusion, Flamelet models, Lean premixed combustion, Swirl stabilized combustor

Printed by: Ridderprint BV

Front & Back: *H2 Flame No. 1*. Watercolor on paper. The painting is a reference to the TU Delft Flame of Prometheus with a hint of swirl motion. The use of watercolor recalls the main product of hydrogen combustion.

Cover design by: Gioele Ferrante

Copyright © 2026 by G. Ferrante

ISBN 978-94-6518-303-9

An electronic version of this dissertation is available at
<http://repository.tudelft.nl/>.

Alla mia famiglia

CONTENTS

Summary	ix
Samenvatting	xi
1 Introduction	1
1.1 General Prospect	1
1.2 Hydrogen premixed combustion	4
1.3 Numerical Combustion modelling	11
1.4 Scope and objectives	14
1.5 Thesis Outline	15
2 Theoretical background	17
2.1 Fundamental equations.	17
2.1.1 Instantaneous balance equations	17
2.1.2 Diffusive Transport	19
2.1.3 Chemical source term	22
2.2 Premixed combustion.	23
2.2.1 Progress Variable.	24
2.2.2 Mixture Fraction	24
2.2.3 Flame speed	26
2.2.4 Laminar flame thickness.	27
2.3 Differential diffusion	29
2.4 Stretch, Strain and curvature	33
2.5 Intrinsic instabilities	36
2.6 Turbulent premixed combustion	38
2.6.1 Regimes in turbulent premixed combustion	40
2.6.2 Turbulent hydrogen combustion.	42
2.7 Turbulent combustion modelling	44
2.8 LES Filtering	45
2.9 Favre decomposition	45
2.9.1 LES equations	46
2.10 Combustion models	47
2.10.1 Chemistry modelling.	48
2.10.2 Turbulence-chemistry interaction	49
2.11 Flamelets applicability	54
2.12 Differential diffusion modelling.	55
3 Methodology	59
3.1 Eulerian Stochastic Fields.	59
3.1.1 Turbulence-flame interaction model	59

3.2	Flamelets with presumed FDF	61
3.2.1	Baseline model.	61
3.2.2	Dynamic modelling of scalar dissipation rate	63
3.2.3	Differential diffusion modelling	66
3.2.4	Heat loss modelling	69
3.2.5	Modelling of nitrogen oxide (NO) formation	70
4	Test Cases	73
4.1	Partially premixed flame	73
4.2	Slot burner	75
4.3	Bluff body stabilized flames	75
4.3.1	Methane flame.	76
4.3.2	Hydrogen flame	77
4.4	TU Delft Swirl-stabilized combustor.	77
I	Development of flamelet models for turbulent hydrogen combustion	81
5	Analysis of a partially premixed hydrogen flame through Eulerian stochastic fields method	83
5.1	Introduction	83
5.2	Numerical details	84
5.3	Results	85
5.3.1	Flame structure and overall model performance.	85
5.3.2	Instantaneous features and burning states.	88
5.4	Summary	92
6	Dynamic Modelling of Subgrid Scalar Dissipation Rate With Differential Filter	95
6.1	Introduction	95
6.2	Test cases and numerical details	96
6.3	Results	99
6.3.1	Jet flame in hot coflow	99
6.3.2	Weakly-turbulent bluff body stabilised flame	103
6.4	Summary	105
7	Differential diffusion modelling	107
7.1	Introduction	107
7.1.1	Flamelets database.	108
7.2	Numerical details	110
7.3	Results	112
7.3.1	Slot burner.	112
7.3.2	Lifted flame in vitiated coflow	116
7.3.3	Flame burning states.	122
7.4	Summary	124

8	Differential Diffusion and Strain Coupling in flamelets/presumed FDF Large Eddy Simulations	127
8.1	Introduction	127
8.2	Set-up and methodology	128
8.3	Results and Discussion	129
8.3.1	Validation and flame structure	129
8.3.2	Average resolved stretch effects	131
8.3.3	Reacting states	133
8.4	Summary	135
II	LES study of the TU Delft swirl stabilized combustor	137
9	Investigation of mixing in a jet in swirling cross-flow configuration	139
9.1	Introduction	139
9.2	Methodology	141
9.2.1	Joint experimental and numerical methodology design	141
9.3	Results	147
9.3.1	Flow field analysis	147
9.3.2	Mixing process analysis	149
9.3.3	Suitability of He as a H ₂ surrogate	151
9.3.4	Effect of fuel composition on fuel-air mixing.	153
9.3.5	Radial species fluxes	155
9.3.6	Radial transport budget analysis	157
9.4	Conclusions.	159
9.5	Outlook & Considerations.	160
10	LES analysis of the TU Delft swirl-stabilized combustor	161
10.1	Introduction	161
10.2	Operating conditions	163
10.3	Numerical set up	164
10.4	Preliminary residence time estimation	167
10.5	75% CH ₄ -25% H ₂ case	168
10.5.1	Non-reacting case	168
10.5.2	Reacting case: flow field and flame topology	172
10.5.3	Precessing vortex core (PVC) dynamics	178
10.5.4	Reacting states and emissions	181
10.6	100% H ₂ case: near-flashback condition	188
10.7	100% H ₂ : ultra-lean condition	193
10.7.1	Flow field and flame structure: effect of AAI	194
10.7.2	Effect of differential diffusion	199
10.8	Summary	206
11	Conclusions and future work	209
11.1	Summary and conclusions	209
11.2	Final considerations, future work and recommendations	217

A	Appendix A	247
A.1	Mesh sensitivity for the lifted flame in hot coflow	247
B	Appendix B	251
B.1	Cabra flame: sensitivity to inlet turbulence	251
B.2	Cabra flame: sensitivity to kinetic mechanism	252
B.3	Sensitivity to the differential diffusion model variables	254
	Acknowledgements	259
	Curriculum Vitae	263
	List of Publications	265

SUMMARY

Combustion technology currently provides most of the global energy demand. As a consequence, it accounts for the largest share of anthropogenic carbon emissions, the main driver of the greenhouse effect and global warming. Phasing out combustion in favor of renewable energy seems like the intuitive path towards a net-zero-carbon economy. However, this transition is slow, global energy demand continues to increase rapidly, renewables can fluctuate in availability, and some sectors are hard to electrify (or “hard to abate”) due to intrinsic requirements for thermal power or high energy density, such as in heavy industry and aviation. Therefore, the development of advanced, cleaner combustion technologies is crucial to enable a non-disruptive energy transition, minimizing emissions while optimizing the use of existing energy infrastructure.

In this context, hydrogen represents a promising energy carrier due to its high energy density, carbon-free combustion, and potential for production from renewable energy. However, the complex physics of turbulent hydrogen flames pose significant challenges for the design of efficient, safe, and low-emission combustors, making accurate numerical simulations indispensable. Large Eddy Simulations (LES) are among the most powerful tools available for predicting unsteady turbulent flow features at an affordable computational cost. Among the available LES combustion models, flamelet-based approaches are particularly attractive for their robustness and computational efficiency. They are based on describing the turbulent flame as an ensemble of 1D laminar flamelets, allowing the thermochemistry to be precomputed and tabulated. While this methodology has been successfully applied to hydrocarbon combustion, its extension to hydrogen poses new challenges, mainly related to differential diffusion effects, which can significantly influence flame structure and stability in lean combustion systems.

This thesis contributes to the development and application of LES models for turbulent hydrogen combustion along two main directions. Part I focuses on the development and validation of flamelet-based LES models, with the exploration of dynamic closures for subgrid variances and the inclusion of non-unity Lewis number effects. Recently developed formulations are implemented to model differential diffusion within the flamelet-based LES framework. The predictive potential and current limitations of the proposed models are discussed based on their application to a broad range of test cases, including premixed, partially premixed, and strained hydrogen flames. In Part II, the developed models are employed to analyze the fuel-flexible, swirl-stabilized combustor developed at TU Delft within the APPU project. This combustor, designed as a low-TRL concept for a hydrogen-powered auxiliary power unit for future sustainable aircraft architectures, was studied through LES to investigate fuel–air mixing, flame stabilization, and NO_x formation across the transition from methane to hydrogen operation. The numerical analyses provided insights complementary to experimental observations, particularly focusing on the influence of axial air injection, heat losses, and the effects of differential diffusion on flame behavior and emissions.

SAMENVATTING

Verbrandingstechnologie voorziet momenteel het grootste deel van de wereldwijde energievraag. Daardoor is het verantwoordelijk voor de meerderheid van de door de mens veroorzaakte koolstofemissies. Dit is de belangrijkste oorzaak van het broeikaseffect en de opwarming van de aarde. Hoewel het geleidelijk afschaffen van verbranding, ten gunste van hernieuwbare energie, de intuïtieve weg naar een netto-nul-koolstofeconomie lijkt, is dit een langzaam proces. Daarentegen blijft de wereldwijde vraag naar energie in een rap tempo toenemen. Daarom is de ontwikkeling van geavanceerde en schonere verbrandingstechnologieën cruciaal om een energietransitie zonder verstoringen mogelijk te maken, waarbij de emissies worden geminimaliseerd en de bestaande energie-infrastructuur optimaal wordt benut.

In deze context vertegenwoordigt waterstof een veelbelovende energiedrager vanwege de hoge energiedichtheid, koolstofvrije verbranding en het potentieel voor productie uit hernieuwbare energie. De complexe fysica van turbulente waterstofvlammen vormt echter aanzienlijke uitdagingen voor het ontwerp van efficiënte, veilige en emissiearme verbrandingskamers. Hierdoor is het gebruik van nauwkeurige numerieke simulaties onmisbaar. “Large Eddy simulations” (LES) behoort tot de krachtigste tools die beschikbaar zijn voor het voorspellen van onstabiele turbulente stromingskenmerken tegen een betaalbare rekenkosten. Van de beschikbare LES-verbrandingsmodellen zijn flamelet-gebaseerde benaderingen bijzonder aantrekkelijk vanwege hun robuustheid en rekenefficiëntie. Ze zijn gebaseerd op de beschrijving van de turbulente vlam als een ensemble van eendimensionale laminaire flamelets, waardoor de thermochemie vooraf kan worden berekend en in tabellen kan worden weergegeven. Hoewel deze methodologie succesvol is toegepast op de verbranding van koolwaterstoffen, brengt de uitbreiding ervan naar waterstof nieuwe uitdagingen met zich mee. Deze uitdagingen zijn voornamelijk gerelateerd aan differentiële diffusie-effecten als gevolg van niet-eenheids Lewis-getallen, wat de vlamstructuur en stabiliteit in magere (lean) verbrandingssystemen aanzienlijk kan beïnvloeden.

Dit proefschrift draagt bij aan de ontwikkeling en toepassing van LES-modellen voor turbulente waterstofverbranding in twee hoofdrichtingen. Deel I richt zich op de ontwikkeling en validatie van op flamelet gebaseerde LES-modellen, met onderzoek naar dynamische afsluitingen voor subgridvariaties en de opname van niet-eenheids Lewis-getaleffecten. Recent ontwikkelde formuleringen worden geïmplementeerd om differentiële diffusie te modelleren binnen het op flamelet gebaseerde LES-raamwerk. Het voorspellende potentieel en de huidige beperkingen van de voorgestelde modellen worden besproken op basis van hun toepassing op een breed scala aan testgevallen, waaronder voorvermengde, gedeeltelijk voorvermengde en gespannen waterstofvlammen. In deel II worden de ontwikkelde modellen gebruikt om de brandstofflexibele, wervelgestabiliseerde verbrander te analyseren die binnen het APPU-project aan de TU Delft is ontwikkeld. Deze verbrander is ontworpen als een laag-TRL-concept voor een watersto-

faangedreven hulpaggregaat voor toekomstige duurzame vliegtuigarchitecturen. Het werd bestudeerd met behulp van LES om de brandstof-luchtmenging, vlamstabilisatie en NO_x-vorming te onderzoeken tijdens de overgang van methaan- naar waterstofverbranding. De numerieke analyses leverden aanvullende inzichten op bij de experimentele waarnemingen, met name wat betreft de invloed van axiale luchtinjectie, warmteverliezen en de effecten van differentiaalverspreiding op vlamgedrag en emissies.

1

INTRODUCTION

1.1. GENERAL PROSPECT

It has been now well established by scientific research that global warming and climate change are connected to anthropogenic action. The average global temperature has been steadily increasing since the industrial revolution and 2024 was set as the warmest year on record, with a 1.55 °C increase with respect to pre-industrial era [1]. This gradual increase in temperature is driven by the emission of greenhouse gases (GhG) released across nearly all sectors of industrial activity and daily human life in modern society. Carbon dioxide (CO₂) represents the 74.89% of total greenhouse gases in atmosphere, which makes it the primary driver of global warming, despite its lower climate forcing potential than other GhG such as methane (CH₄) and nitrous oxides (N₂O) [2]. The vast majority of CO₂ emissions stems from fossil fuel combustion in energy production, industrial processes and transportation [3]. Carbon dioxide emissions have been constantly increasing since the industrial revolution, and scientific research confirms that the natural reabsorption capacity of Earth's ecosystems has been exceeded [4].

The catastrophic consequences of global warming in the form of extreme climate events start to be alarming. For this reason, the United Nations (UN) stipulated the Paris Agreement during the Climate Change Conference COP21 in 2015 [5]. With this treaty the involved parties aim to limit global temperature rise to well below 2 ° C above pre-industrial levels, with efforts to keep it below 1.5 ° C. In alignment with these objectives, the European Commission introduced the European Green Deal [6], a set of strategic policy proposals aimed at making Europe the first carbon-neutral continent by 2050. A critical milestone within this plan is a 55% reduction in CO₂ emissions by 2030 compared to 1990 levels. This commitment became legally binding in 2021 when EU member states adopted the European Climate Law [7]. In contrast with the global trend of rising emissions, Europe successfully reduced carbon emissions by 34% since 1990. This has been achieved through energy demand reduction, a shift away from fossil fuels, and significant investments in renewable energy [1, 8].

However, on a global scale, energy demand continues to increase at an almost unchanged rate of 2% per year. Despite the rapid growth in renewable and nuclear energy, the world remains heavily dependent on fossil fuels, meaning that CO₂ emissions are still rising [3, 9]. While renewable energy and electrification are essential to decarbonization, chemical energy storage and combustion-based energy production will remain necessary for years to come [10, 11]. Even in a predominantly renewable-based energy system, power plants based on chemical energy conversion (e.g. combustion in gas turbines) may still be needed for grid stability, compensation of fluctuations in renewable energy availability and management of peak energy demand [10, 11]. Consequently, improvements in combustion efficiency, carbon emission reduction, and alternative fuels are crucial for accelerating decarbonization and achieving a non-disruptive energy transition.

Beyond energy production, transportation represents the second-largest contributor to global CO₂ emissions, accounting for approximately 21% of total emissions worldwide [3, 9]. As part of its Green Deal, the European Union aims to achieve a 90% reduction in transport-related emissions by 2050. Aviation, in particular, represents an extremely challenging field for decarbonization due to its intrinsic requirements for high power and energy density, entirely met through combustion of Jet-A fuel in gas turbine engines. Aviation emissions accounted for 3.8–4% of total EU greenhouse gas emissions in 2022, representing 13.9% of transport-related emissions. Worldwide, aviation CO₂ emissions doubled from about 0.5 billion tons in 1990 to about 1 billion tons in 2019, and they recovered to 95% of pre-COVID levels in 2023 [12, 13]. This increase is driven by a growing global demand for air travel, with passenger numbers increasing from 2 billion in 1990 to 8 billion in 2019 [13]. The International Civil Aviation Organization (ICAO) forecasts that by 2050, aviation emissions could triple compared to 2024 levels if no further measures are implemented [14].

The projected growth in aviation industry is irreconcilable with the 2050 UN and EU climate goals. Despite a decrease in carbon intensity per passenger-kilometer since 1990, thanks to improvements in fuel efficiency, air traffic management, and operations, further deep technological advancements and the adoption of alternative fuels are required to meet long-term targets [12, 13, 15, 16]. One of the strategies towards full net decarbonization is electrification. Numerous aviation technologies have been proposed, with the aim of involving battery or hydrogen fuel cells powered electric or hybrid-electric aircraft, which offer high energy efficiency and minimal direct emissions [17–19]. However, current battery technology remains insufficient for long-range flights, limiting full electrification to short-range applications. In the short-medium time horizon, aviation will continue to rely on combustion technologies while integrating alternative low-carbon fuels [12, 13, 19].

Sustainable Aviation Fuel (SAF) is recognized among the most effective and rapidly implementable solutions, as it can be used as a drop-in replacement for conventional jet-A fuel, requiring no modifications to existing aircraft or infrastructure [12, 14, 16]. Regulatory initiatives such as ReFuelEU [20] are already working towards increasing SAF adoption in commercial aviation. However, concerns about the applicability of SAF arise from the incredibly high projected demand, the environmental impact of SAF from bio-fuel origins, and issues related to production scalability and cost [13]. Together with SAF,

hydrogen (H_2) has gained significant interest as an alternative aviation fuel due to its carbon-free combustion and the possibility of producing it from water electrolysis using renewable energy. The potential of hydrogen in aviation has been recognized by policy makers [21, 22], and both academic and industrial research groups have started to direct their efforts towards hydrogen solutions [12, 18, 23, 24].

Hydrogen presents significant challenges stemming from its low volumetric energy density compared to liquid kerosene fuel, requiring larger storage volumes at high pressure or cryogenic conditions. This results in airframe redesign which poses problems in terms of efficiency, safety and certification [12]. An intermediate step between current engines and fully hydrogen powered aircraft is represented by dual-fuel combustion systems. The Advanced Power and Propulsion Unit (APPU) project [25], to which the present research contributed, aimed to introduce "energy mix" in civil aviation, by developing a fuel flexible (kerosene/ H_2) auxiliary power unit providing additional propulsive power to the aircraft (baseline model Airbus A320) and therefore reducing the fuel consumption and emissions of the main engine. Other industrial and academic projects aim directly at the redesign of the main engine to achieve dual fuel capability [24, 26, 27].

Another primary technical challenge for hydrogen based aircraft propulsion is the redesign of combustion chambers in gas turbine engines, in order to handle the flame properties of hydrogen. Aviation gas turbines operate with turbulent, often non-premixed, combustion, where liquid fuel is injected and mixed with air as it burns. On the other hand, lean premixed combustion strategies, where fuel is mixed with abundant excess air prior combustion, would open promising possibilities in terms of fuel saving and emissions reduction (CO_2 , CO, NO_x) [28, 29]. Lean premixed combustion (LPM) has been successfully implemented in stationary gas turbines for on-ground power generation, where the integration of hydrogen or hydrogen blends does not require major redesign of fuel injection strategies (as long as measures to handle the higher reactivity of hydrogen are properly implemented), as these turbines can already operate on gaseous fuels (natural gas) [11, 30, 31]. However, in aviation, the application of this technology faces challenges related to: the need of rapidly prevaporizing liquid fuel (lean premixed/prevaporized combustion, LPP), stricter safety requirements in terms of extinction resistance and relight capability, risk of flashback in the ignitable fuel/air mixture [28, 29, 32].

Various technologies for aeronautical applications have been proposed to stabilize lean flames and minimize NO_x emissions, for which an extensive review can be found in [29]. To tackle the stability issues, lean combustion can be applied in combination with rich flame fronts, for example in staged combustion, including RQL concepts [33] and rich pilot flames, often combined with swirlers, like the lean twin-annular premixing swirler (TAPS) [34, 35]. Another solution is represented by the lean direct injection concept (LDI) where fuel is directly injected and vaporized in the combustion chamber, where it quickly mixes with abundant excess air. This strategy aims to run fuel-lean most of the time avoiding a pilot and exploiting multiple (swirled) injection points. The risk of flashback is reduced by the absence of a premixing section [29, 36, 37]. When introducing hydrogen, lean premixed technology is a possible strategy to reduce its very high flame temperature, which would result in increased NO_x formation compared to kerosene (jet-A fuel) [38]. On the other hand, the high reactivity of hydrogen would ex-

acerbate the risk of flashback, increasing the design challenges [39]. Advancements in the understanding of combustion physics and in combustion modelling are necessary to reach technological goals in the use of hydrogen for gas turbines combustors.

While renewable energy remains the foundation of global decarbonization, advancements in turbulent premixed combustion are necessary to accelerate emissions reduction in the short term [10, 11, 39]. The development of a hydrogen infrastructure and hydrogen-based turbulent premixed combustion technology represents a recognized strategy to quickly reach the net-zero carbon emissions target in power production and hard to decarbonize sectors like aviation [10, 21, 40–42].

1.2. HYDROGEN PREMIXED COMBUSTION

Hydrogen is gaining significant interest as a carbon-free chemical energy carrier, particularly when produced through water electrolysis using renewable energy sources [10, 39]. The energy stored in hydrogen can then be released via electrochemical processes, such as fuel cells, or through thermochemical processes like combustion [10]. Hydrogen combustion is particularly attractive due to its high energy density per unit mass (120 MJ/kg, 2.5 times higher than methane) and a carbon-free flame. One possible application is using hydrogen as a drop-in fuel for large-scale building heating systems, facilitating the transition from natural gas with minimal infrastructure redesign. In such applications, combustion is typically laminar. However, in most industrial settings, combustion is turbulent, due to the high mass flow rates required to meet power demands and to achieve optimal fuel-oxidizer mixing [11]. Turbulent hydrogen combustion can play a crucial role in decarbonizing hard-to-abate sectors where high thermal power is required and electrification is not possible, such as heavy industry [21]. Another key application is in gas turbines, largely employed for stationary power generation and aeronautics. Land-based power plants already using natural gas can transition to hydrogen, ensuring grid stability and power supply during peak demands [10, 30]. In aviation, hydrogen is a promising fuel, but significant design modifications are required, particularly because current engines operate exclusively on liquid fuels [29, 32].

Hydrogen combustion presents unique challenges due to its high flame temperature, significantly higher than hydrocarbon fuels, which leads to increased nitrogen oxides emissions (NO, NO₂), generally referred to as NO_x [39]. These pollutants form when air is used as oxidizer, largely due to nitrogen dissociation at high temperatures, followed by reactions with oxygen [43, 44]. Strict limitations on NO_x emissions are imposed due to their toxicity, greenhouse effect and impact on the chemical properties of atmosphere [14, 37]. In non-premixed combustion, fuel and oxidizer are injected separately and mix while reacting near-stoichiometric conditions, which leads to high flame temperatures and, consequently, elevated NO_x emissions. While non-premixed flames offer stability and safety, their inherent NO_x formation necessitates mitigation strategies [29]. In ground-based applications, water or steam injection has been employed to cool the flame and reduce NO_x emissions [45], and ongoing research explores the integration of this approach with hydrogen combustion [46–48]. Lean premixed combustion, where fuel and air are mixed before ignition, offers an alternative strategy to limit flame temperature and NO_x emissions [28]. This technique, already proven in stationary gas turbines operating on natural gas, can be extended to hydrogen combustion and potentially

applied in aviation.

Lean premixed flames present challenges in terms of stability. Excessive air dilution weakens the flame and can even push the mixture beyond the lean flammability limit, where combustion extinguishes completely (lean blow-out). These concerns are particularly critical in aviation, where reliability and flame stability are a hard constraint [28, 29]. Despite its advantages, lean premixed hydrogen flames can be more difficult to stabilize than non-premixed due to the high reactivity of hydrogen. Its wider flammability range allows for stable ultra-lean combustion without the risk of blow-out, but it also increases the risk of flashback, where the flame propagates upstream into the injector [28, 39, 44, 49]. The low activation energy of hydrogen and short ignition delay time exacerbate the risk of autoignition in premixed hydrogen combustion, introducing a further source of risk for flashback.

The extremely high diffusivity of hydrogen, a result of its simple molecular structure, facilitates mixing with air but also poses challenges for storage and leakage prevention. Moreover, it leads to unique flame properties affecting stabilization in premixed conditions. In hydrogen-air mixtures, hydrogen diffuses faster than heat creating enthalpy inhomogeneities across the flame front, which gives origin to the so called differential diffusion effects [39]. This property is described by a sub-unity Lewis number, a non-dimensional parameter relating the heat diffusivity α and the hydrogen mass diffusivity D_{H_2} , $Le_{H_2} = \alpha/D_{H_2}$. Simultaneously, hydrogen diffuses faster than oxygen, altering mixture composition (preferential diffusion effects). Differential diffusion (sub-unity Lewis number) and preferential diffusion are consequences of the physicochemical properties of hydrogen and their effects cannot in general be decoupled, unless artificially isolated through numerical or analytical manipulation [39]. Differential and preferential diffusion effects, though typically subtle, couple with flame curvature, leading to reaction rate inhomogeneities and intrinsic thermo-diffusive instabilities [39, 50]. These instabilities manifest as cellular burning structures, visible as a wrinkled flame front even in laminar conditions, significantly increasing local flame surface area and propagation speed [50–52]. Depending on the operating conditions, turbulence may dominate over these effects or amplify them synergistically [53]. Together with flame front curvature, strong velocity gradients in the flow can induce strain in the flame region. It is well documented that sub-unity Lewis number can lead to reaction rate increase in strained premixed flames [54, 55]. Hydrogen flames, therefore, exhibit greater stability and resistance to strain-induced blowout compared to typical natural gas flames, which generally have a Lewis number close to unity. The complexity of these physical phenomena must be deeply understood in order to model hydrogen combustion and to design effective flame holders.

FLAME STABILIZATION AND FLASHBACK

Flame stabilization has always been a core challenge in the design of combustion devices. A stable flame requires a balance between convective time scales, related to flow velocity and fuel supply, and chemical time scales, defined by the reaction rate. If the reaction cannot keep up with the fuel supply, the flame extinguishes (blowout). In premixed combustion, the flame propagates naturally towards an ignitable mixture at a speed determined by reactant properties, including pressure, temperature and compo-

sition. Turbulence can enhance this process, by wrinkling the flame front and generating more flame surface area [50, 56].

Lean-burn technology relies on burning fuel with a large excess of oxidizer. Increasing oxidizer content reduces flame speed until it reaches the lean blowout limit. Stabilizing lean premixed flames operating in high mass flow rates and turbulent flows requires the careful design of flame holders. Favorable conditions for flame stabilization are often obtained through recirculation zones to create low-velocity regions and maintain high reactant temperatures by recirculating hot gases [57]. These are generated using bluff bodies, swirling flows or cavities [29, 58], as will be discussed next.

With hydrogen, blowout is generally not a major issue. Its simple reaction mechanism results in an exceptionally high flame speed (compared for example to hydrocarbon gases like methane), low lean flammability limit and short autoignition delay time [39, 59]. Additionally, under high mixture injection velocities, hydrogen flames may experience high strain, which increases burning rates and flame speed, facilitating flame anchoring [54]. A more critical concern is flashback, which verifies when the flame travels upstream into the injector and stabilizes in unintended locations [60]. This can lead to component failure due to excessive thermal loads. Flashback is promoted in regions with ignitable mixtures and low flow velocity. Strategies for flashback mitigation include injecting fuel as late as possible while ensuring rapid mixing to minimize ignitable regions, and increasing flow momentum in critical areas [29, 58, 60].

As thoroughly described in literature [60], flashback can occur in different modes:

- **Core flashback:** When the flame speed exceeds the flow velocity, the flame can propagate upstream into the injector core. Turbulence can worsen the problem by enhancing the flame speed through flame wrinkling. The addition of hydrogen further exacerbates this issue by increasing the flame speed and, under certain conditions, introducing coupling between turbulence-induced stretch, and flame speed [50, 61]. This kind of flashback generally does not represent an issue in regular gas turbines, as the injection velocity of the reacting mixture is commonly designed to exceed turbulent burning velocities [60]. Swirl-stabilized combustors can exhibit a low axial velocity core due to the swirling motion, making them prone to this type of flashback. In general, core flashback can be mitigated by increasing the axial momentum [49].
- **Boundary layer flashback:** The velocity gradient in the boundary layer at the injector walls creates low-velocity regions where the flame can propagate upstream. A quenching distance δ_q from the wall exists, where the flame is extinguished due to heat loss, which therefore counteracts flashback. Boundary layer flashback is generally described in terms of a critical velocity gradient value: above this value, the boundary layer region where the flame propagation speed would theoretically exceed the flow velocity, and be susceptible to flashback, is entirely contained within the distance affected by heat loss and flashback cannot occur. The complex dynamics of wall flashback are extensively discussed in [60, 62], and depend on the interplay between boundary layer velocity gradients, mixture composition, wall temperature, and strain. Turbulence has been observed to increase the critical velocity gradient [60]. When hydrogen is introduced, its high reactivity results

in reduced quenching distances (as small as one tenth that of methane) and higher critical velocity gradients. For very lean hydrogen/air mixtures, strain can enhance hydrogen flame speed, further increasing the risk of boundary layer flashback [54]. This type of flashback can be mitigated by increasing the flow velocity (thus exceeding the critical velocity gradient) or by injecting air to energize the boundary layer, which also locally reduces the flame speed by making the mixture leaner. High wall temperature of the injector components can heat the incoming mixture and increase flame speed; strategies to prevent this include wall cooling or the use of high heat capacity materials.

- **Autoignition driven flashback:** In practical combustion systems, metallic injection components are heated by the combustion process, and in gas turbines, the incoming air is preheated by the compressor. This can raise the temperature of the combustible mixture to its autoignition value, above which it may spontaneously ignite after an autoignition delay time, τ_{ig} , typically ranging from 10^{-6} to 10^0 seconds, depending on the thermodynamic state of the mixture (equivalence ratio, pressure, and temperature). If the local residence time (dictated by convection time) is shorter than the ignition delay time, ignition kernels may form at undesired locations, upstream of the flame stabilization zone. Once an ignition kernel forms within the injector (e.g., in the mixing section), the resulting heat release alters the surrounding flow, pressure, and temperature fields. This may lead to low or even reversed velocities that promote flame propagation upstream. Additionally, ignition kernels generate pressure waves travelling in all directions; this can lead to compression heating of the upstream mixture within the injector that increases the local temperature, further shortening the ignition delay time and creating other upstream autoignition kernels. This feedback cycle can lead to upstream-propagating flashback at velocities approaching the speed of sound (strong ignition [63]). When operating with hydrogen, this type of flashback becomes particularly critical. Although hydrogen has a higher autoignition temperature than methane, its autoignition delay time is significantly shorter, especially at elevated temperatures [60, 63]. Therefore, strict control of inlet temperature and injection velocity is required. Some studies have investigated water injection as a strategy to prevent autoignition-induced flashback [48].

- **Combustion-induced vortex breakdown-driven flashback (CIVB):**

In swirl-stabilized combustors, flames are aerodynamically stabilized by a central recirculation zone (CRZ) formed through vortex breakdown (VB). Along the burner axis, the mean axial velocity decreases to zero at the tip of the CRZ, where a stagnation point forms, and becomes negative further downstream within the CRZ. The flame anchors in the low-velocity region just upstream of the stagnation point. These combustors typically feature a mixing section where fuel and air blend in the swirling flow. A stably anchored flame may accelerate upstream due to instantaneous fluctuations, shifting the flame tip into the mixing section. Previous studies highlight the destabilizing effect of the baroclinic torque [64, 65], by which the coupling between the radial pressure gradient (necessary for radial equilibrium in swirling flows) and the axial negative density gradient (caused by

thermal expansion) generates azimuthal vorticity, inducing strong axial backflow along the injector axis. As the flame advances upstream, the stagnation point also shifts upstream. The trailing region of the CRZ closes forming a recirculation bubble with strong backflow velocity that propagates into the mixing tube, as sketched in Fig. 1.1. The combined effect of thermal expansion, vorticity generation, and induced backflow drags the flame further upstream. The flame may then anchor at the swirler (permanent flashback) or extinguish in the mixing section, leading to a periodic CIVB driven flashback cycle (intermittent flashback) [60, 64, 66]. The presence of a precessing vortex core (PVC) and its interaction with the CRZ, particularly its breakdown induced by thermal expansion, has been identified as a potential cause for the initial upstream flame acceleration initiating CIVB flashback [65]. Preventing this type of flashback requires careful tailoring of axial and radial components of the swirling flow. Design strategies include avoiding a mixing tube and ensuring rapid mixing near the combustor [36, 37], or operating in a partially premixed mode [67]. Another approach, explored in this work, involves increasing core axial momentum through air injection [49, 68]. Although solid central bodies or central air or fuel lances may reduce the CIVB flashback propensity, similar mechanisms may still occur [60, 66].

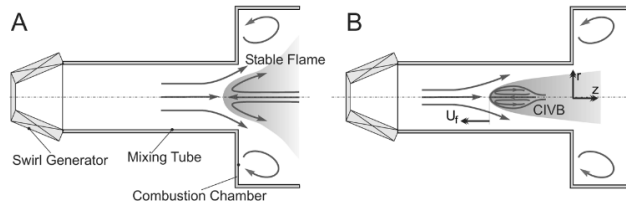


Figure 1.1: Sketch of a swirl-stabilized combustor and representation of combustion-induced vortex breakdown flashback, reproduced from Kröner et al. [69].

- **Thermoacoustically induced flashback:**

Flashback can be initiated by fluctuations in the velocity field produced by intrinsic thermoacoustic instabilities of premixed combustion systems [57, 60]. Thermoacoustic instabilities occur when acoustic waves (pressure fluctuations) couple with fluctuations of heat release in a feedback cycle, which closes when pressure and HRR fluctuations are in phase (with phase difference less than 90°). The feedback cycle is typically sustained through a coupling mechanism between pressure and HRR fluctuations, which can be based either on velocity fluctuations or on equivalence ratio fluctuations. In the first case, pressure fluctuations downstream of the injector cause variations in the mass flow rate of the reactant mixture supplied to the flame, thereby inducing HRR fluctuations. In the second case, pressure fluctuations affect fuel delivery in the premixing section, altering the local equivalence ratio of the mixture entering the flame and consequently modifying the HRR [57]. Intrinsic hydrodynamic instabilities of the combustor geometry, such as vortex shedding in wakes, Kelvin–Helmholtz instabilities in shear flows (e.g., at injector rims), and precessing vortex cores (in swirl stabilized combustors), have been

identified either as initiation mechanisms for the thermoacoustic feedback cycle or as processes that couple with and amplify the cycle [57].

Although in a combustor the mean axial velocity exceeds the flame propagation speed, by design, periodic fluctuations induced by thermoacoustic instabilities, initiated or reinforced by hydrodynamic instabilities, can cause axial velocity drops or even flow reversal. Under such conditions, the flame propagation speed exceeds the axial flow velocity, allowing the flame to propagate upstream into the injector section. This phenomenon has been observed experimentally for a backward-facing step, where Kelvin–Helmholtz instability initiates the flashback process [70]. Swirl-stabilized combustors are also highly prone to this type of flashback initiated by self-excited pressure oscillations, as shown in [71] and in [72], where acoustic oscillations were also externally forced to investigate flashback across different forcing frequencies. Thermoacoustically induced flashback may result either in permanent flashback, with the flame stabilizing in an undesired location, or in intermittent flashback, where the flame temporarily propagates upstream but subsequently returns to its intended stabilization position [71, 72].

STABILIZATION CONCEPTS

Flame stabilization is obtained through the design of dedicated flame holders. Their functioning principle is mainly based on generating low velocity regions (wakes, recirculation zones, shear layers) to prevent blow out, and heating the reactants through hot product gases recirculation or the use of pilot flames [57]. These elements must be finely tuned to avoid conditions favorable to flashback and NO_x formation especially when adapted to hydrogen. Examples of typical flame holders are:

- **Bluff body:** An obstruction is placed in the flow path at the injector exit creating a wake region of low velocity and hot products recirculation for flame anchoring [73–75]. They are typically used for premixed mixtures, additional fuel/air can be injected in the wake along the centerline for enhanced stabilization [76]. The bluff body geometry is designed to create a converging nozzle cross-section, increasing local velocity to prevent flashback. It often presents sharp angles which prevent upstream flame propagation and fix the separation point, stabilizing the wake position. In this configuration most turbulence is generated at the bluff body base. The high flow acceleration at the bluff body base leads to intense positive strain rate tangential to the flame, which affects reaction rates and in particular enhances flame stability in lean hydrogen combustion [74]. A drawback is represented by the flame stabilization close to the metallic bluff body, necessitating careful thermal load management. This configuration is commonly studied at laboratory scale under various power conditions, both confined and unconfined, for hydrocarbon and hydrogen fuels.
- **Piloted flames:** The main flame is stabilized by a smaller flame providing continuous heat for ignition. This configuration allows to achieve high-power operation with high mass flow rates resulting in more turbulent flames. It is commonly used in gas turbines, combining a pilot flame with a main flame [11, 29]. Laboratory

studies investigate these flames using turbulent jet flames in hot coflows, allowing a broad range of configurations [77, 78]. Depending on parameters such as main jet composition, flow rate, and coflow temperature, the flame can attach to the nozzle or lift off. Lifted flames allow additional jet/coflow mixing before ignition, forming partially premixed multimode flames (premixed, non-premixed, autoigniting) [77, 79]. In other cases, the main jet reacts with both the pilot flame and external air. This configurations have been extensively studied for both hydrocarbon gas and hydrogen and are often considered in the context of mild combustion [80].

- **Cavity/trapped vortex:** A recessed wall cavity creates a recirculating trapped vortex, generally additionally driven by injection of fuel or fuel/air mixture in the cavity, that stabilizes the flame and retains hot gases [81]. This configuration offers a multitude of design degrees of freedom, supporting both lean premixed combustion and rich-quick quench- lean combustion (RQL concept) via additional fuel injection into the cavity. The main drawback of this design consists in the flame stabilizing at the wall, resulting in high thermal loads and heat loss effects. This configuration attracted interest for hydrogen combustion due to its versatility and flashback resistance.

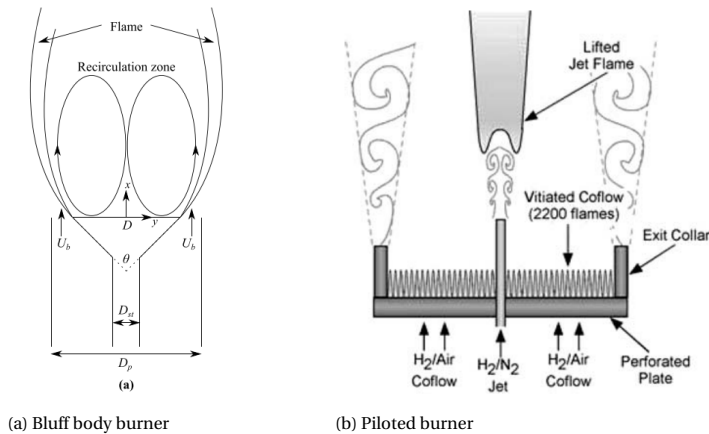


Figure 1.2: Schematic representations of (a) the bluff-body stabilized flame analysed numerically by Massey *et al.* (adapted from [82]) and (b) the partially premixed hydrogen flame in hot coflow experimentally investigated by Cabra *et al.* (adapted from [77]).

- **Micromix concept:** The micromix combustion concept, introduced several years ago, has attracted significant interest for hydrogen combustion applications [38, 83]. It consists in splitting the total fuel supply into numerous smaller hydrogen jets reacting in non-premixed mode, but with significant excess air, leveraging the wide flammability range of hydrogen. This strategy is inherently flashback free, allows significant mass flow rates with low flame temperature and residence time, minimizing NO_x formation. It allows high power and is already employed for gas

turbines and under study for aeronautic applications. Challenges arise from its susceptibility to thermoacoustic instabilities and small scale ducts design.

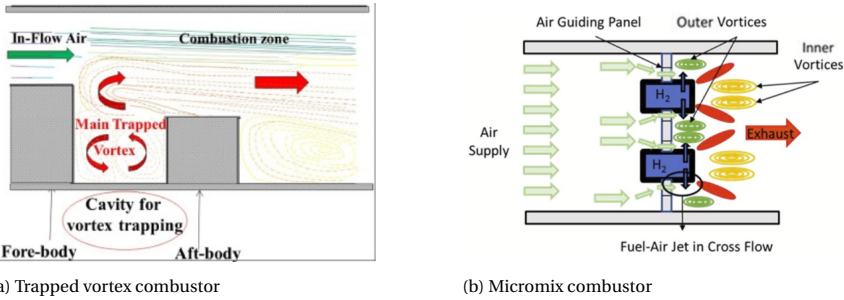


Figure 1.3: Schematic representations of (a) trapped vortex flame stabilization (adapted from Zhao et al. [81]) and (b) the micromix concept (adapted from Berger et al. [84]).

- Swirl stabilized combustor:** The vortex breakdown of a swirling flow forms an inner recirculation zone where the flame is aerodynamically stabilized [85]. This configuration supports high power and is widely used in stationary gas turbines and aviation, with both gaseous and liquid sprayed fuels. It can be applied for lean premixed combustion, featuring a mixing section [86] or for lean direct injection concepts LDI [29, 37, 65]. Many laboratory-scale swirled combustors have been developed for natural gas and are now being explored for hydrogen [31, 87]. While natural gas combustors can relatively easily be operated in fully premixed conditions [88, 89], hydrogen premixing increases flashback risk, requiring precise mixing strategies [31, 67]. The goal is to achieve fast, late mixing to mitigate flashback risks. If a mixing tube is used, the system is vulnerable to combustion CIVB flashback (as described in the previous section), core, and boundary layer flashback. Strategies such as axial air injection (as investigated in this thesis) and boundary layer air injection can help by increasing the axial momentum of the mixture and reducing fuel concentration [49, 68]. Swirled combustors can also exhibit oscillating dynamics, such as precessing vortex core (PVC) effects [65]. The flame may stabilize not only in the central recirculation zone but also in the outer shear layer at the injector exit, introducing issues related to thermal loads and heat loss effects [44, 87]. The recently developed Hylon burner operating with hydrogen [67], does not feature a mixing tube, and mixing occurs within the combustion chamber, ultimately operating under partially premixed conditions. This reduces flashback risks and can prevent near-walls flame stabilization, reducing thermal loads.

1.3. NUMERICAL COMBUSTION MODELLING

The development of accurate numerical predictive tools is of high interest for the understanding of the complex physics of turbulent reacting flows and the design of combustor devices, as outlined above. With the advancement of parallel and high performance computing since the 1990s, computational fluid dynamics (CFD) has reached the capability of simulating extremely complex turbulent flows of engineering signifi-

cance, quickly becoming an essential design tool for industrial applications [90]. Today's computational resources enable direct numerical simulations (DNS) over increasingly large domains that were once considered infeasible [91]. However, DNS remains impractical for industrial applications and is primarily used to investigate microscale fluid physics and develop closures for lower-resolution models, namely (Unsteady) Reynolds-Averaged Navier-Stokes ((U)RANS) and Large Eddy Simulations (LES) [56, 91]. Industrial development has heavily relied on RANS simulation due to its efficiency in predicting average flow features at competitive computational costs. This allows for multiple simulations under different conditions, facilitating sensitivity analyses and iterative design processes. Unsteady RANS simulations further enable the study of transient features in the average flow field, such as low-frequency oscillations. Despite their applicability and overall effectiveness for reacting flows, RANS approaches often fail to capture the inherently unsteady and multiscale nature of turbulent combustion. Examples include local extinctions, flame wrinkling, flame/turbulence interactions, and transient phenomena like ignition, flashback, and thermoacoustics [92].

In this context, LES is highly attractive due to its capability to predict unsteady flow features at a nowadays affordable computational cost [56, 92, 93]. In a LES, a filtered version of the Navier-Stokes equations is solved to directly compute the time evolution of the largest turbulent flow structures up to a spatial resolution imposed by the filter width. The filtering operation is commonly applied implicitly by spatially discretizing the domain through a computational grid. The actual filter shape and width is generally not explicitly selected *a-priori*, but results from the imposed grid spacing Δ and the chosen discretization method for the terms in the filtered Navier-Stokes equations. The unresolved turbulent scales falling below the LES filter size are called sub-grid scales (SGS) and their effects on the resolved flow are modelled. This modelling is generally implemented by relating SGS scales to resolved quantities [93, 94], solving additional equations for subgrid turbulent kinetic energy [95], or employing similarity assumptions between subgrid and resolved scales, which is the foundation of many dynamic models [96]. The possibility of employing dynamic models is considered among the advantages offered by LES strategy [92]. These last approaches allow for a local space and time varying modelling of the subgrid quantities, based on the local flow conditions and grid properties. The choice of the SGS modelling strategy affects the effective shape and width of the LES filter applied implicitly within the simulation.

The large-scale motion of the turbulent flow contains most of the turbulent kinetic energy (TKE) and, as a best practice, the filter size should allow at least 80 % of the TKE to be resolved [97], minimizing the influence of the subgrid model. In non-reacting flows, the grid resolution, and implicitly the cutoff between resolved and unresolved scales, is mainly determined to balance turbulence resolution and computational cost. However, in combustion simulations, the flame thickness is often smaller than the smallest resolved turbulent scale [92]. An accurate flame resolution would require an extremely fine filter size, resulting in DNS level resolution, impractical for design applications. As a result, reactions in the flame front must be treated as a subgrid phenomenon requiring dedicated modelling. The intrinsic anisotropy of subgrid turbulence/flame interaction makes these models more complex than for non-reacting flows, as additional physics beyond turbulence must be considered. The absence of a resolved part of the reaction

terms makes the application of dynamic models not straightforward [92]. Some dynamic models extending the similarity assumption between subgrid and resolved scales to reacting cases have been proven to be applicable to the modelling of turbulent subgrid transport, flame wrinkling, scalar dissipation rate and scalar subgrid variances [98–100]. A dynamic strategy for the closure of combustion variables subgrid variance is explored in the present thesis [101, 102].

Many LES combustion models have been developed to describe the complex chemical reaction process in a computationally affordable way and to account for subgrid turbulence-chemistry interactions, with extensive reviews available in the literature, e.g. [103, 104]. The research presented in this dissertation focuses primarily on flamelets-based approaches, which have been widely used due to their relatively low computational cost, robustness, and versatility [105–107]. Flamelet models rely on the assumption that a turbulent flame can be represented as an ensemble of locally one-dimensional laminar flamelets, which allows to separate turbulence from thermochemistry. The possible thermochemical states assumed by the reacting mixture are computed *a priori* using 1D laminar flame (flamelets) solutions, parametrized on a small number of controlling variables (e.g. a mixture fraction, progress variable, enthalpy) and tabulated. A filtered transport equation for the controlling variables is solved within the LES and their local value is used to access the tabulated information. This largely reduce the computational cost with respect to models based on detailed chemistry, where a transport equation for each chemical species involved in the reaction is solved, together with the computation of reacting rates, based on local thermodynamical state and composition of the mixture.

One of the methods to account for the effect of turbulence on flame wrinkling at a subgrid level relies on a statistical approach, where a filtered density function (FDF) describes the subgrid probability distribution of the thermochemical states of the mixture. The shape of the FDF can be presumed *a-priori*, presumed FDF (PFDF) or resulting from a transported FDF (TFDF) approach [103, 104, 108, 109]. In the latter the solution of the FDF transport equation is reconstructed from the transport equation of stochastic samples which can be lagrangian particles representing a local instantaneous mixture thermochemical state or eulerian stocastic fields (ESF) representing the instantaneous thermochemical state of the mixture over the whole domain [110, 111]. On the other hand, in PFDF approaches typically used in conjunction with flamelets-based models, the definition of the local shape of the presumed FDF requires information about the subgrid instantaneous statistical moments (e.g. subgrid variance) of the controlling variables.

Flamelets-based LES methods with presumed FDF have been extensively applied to the prediction of hydrocarbon flames, yielding highly satisfactory results across various conditions (e.g., see [109, 112]). However, they often rely on the assumption of equi-diffusivity of species and heat, which does not hold for non-unity Lewis number fuels, such as hydrogen [39]. The inclusion of non-unity Lewis number effects in flamelet LES and their relevance for turbulent hydrogen combustion are thoroughly investigated in this study. This represents a crucial step towards achieving reliable LES models for the practical design of next-generation hydrogen combustors.

1.4. SCOPE AND OBJECTIVES

This research focuses on the numerical modelling of hydrogen combustion using Large Eddy Simulation (LES). The study is divided into two parts: 1) model development and validation, and 2) model application for the analysis of a swirl-stabilized combustor.

PART I: DEVELOPMENT AND VALIDATION OF FLAMELET MODELS FOR TURBULENT HYDROGEN COMBUSTION

The study builds upon well-established flamelet models commonly used for hydrocarbon combustion in LES. The primary objective is to extend and validate these models for hydrogen combustion, ensuring accuracy, robustness and computational efficiency.

The specific objectives include:

- **Hybrid modelling for partially premixed flames:** Analyze a partially premixed turbulent hydrogen flame using detailed chemistry and the Eulerian Stochastic Fields (ESF) method as a baseline, where modelling assumptions are minimized. Develop and test a hybrid model with flamelet based chemistry reduction and Eulerian stochastic fields (ESF) turbulence-chemistry interaction model on the same case, investigating the capabilities of flamelets-based LES for the prediction of turbulent partially premixed hydrogen flames.
- **Dynamic model for subgrid progress variable variance closure:** Investigate the accuracy of a dynamic model for the closure of transport equation of the progress variable subgrid variance in LES with flamelet based tabulation and FDF closure. The dynamic model is tested on premixed highly turbulent hydrogen flame and a lower turbulent methane bluff-body stabilized flame.
- **Differential diffusion modelling in flamelets-based models for LES :** Implement, validate, and compare different methods to include differential diffusion effects in flamelets-based LES. Evaluate model performance across various test cases, including premixed, partially premixed, and strained premixed turbulent hydrogen flames.

PART II: LES STUDY OF THE TU DELFT SWIRL-STABILIZED COMBUSTOR

The APPU project [25], carried out at TU Delft, aimed to demonstrate a novel aircraft architecture, starting from an A320 baseline, in which part of the propulsive and auxiliary power demand is shifted from kerosene-fuelled main engines to a fuel-flexible, hydrogen-powered auxiliary power unit driving an aft-mounted boundary layer ingestion (BLI) propulsor. A rendering of this design concept is shown in Fig. 1.4. Emissions are reduced not only through the use of hydrogen, but also by the aerodynamic benefits of the BLI configuration, which reduces drag by wake filling. The concept offers a pragmatic response to the challenges of introducing hydrogen into aviation by proposing an energy-mix solution. It avoids the need for radical redesign, can be implemented more rapidly on future generation of A320 aircraft, and retains system reliability since most components are already certified. The aircraft remains capable of operating on kerosene when hydrogen is not available, while the hydrogen storage requirements are relatively modest compared to a fully hydrogen-powered aircraft, limiting the extent of structural

redesign. Research within the project was organised in three main directions: overall system design and integration; aerodynamic optimisation of the BLI propulsor and empennage; and the preliminary design of a hydrogen-fuelled combustor with emission analysis, including the prospect of future kerosene dual-fuel capability. The present research contributed to this last aspect.



Figure 1.4: Rendering of the conceptual design of the next generation A320 aircraft with integration of the APPU system, showing the modified empennage and aft-mounted auxiliary propulsor in boundary layer ingestion configuration.

The work reported in Part II of the present thesis consists of a numerical study, carried out alongside with experimental investigations conducted in parallel by coworkers at TU Delft, analysing a laboratory-scale swirl-stabilised lean premixed combustor, a low-technology readiness level (TRL) representation of the APPU combustion chamber. The setup was initially developed and experimentally investigated for natural gas (methane) [113–115], a convenient intermediate step towards operation with full hydrogen, due to the gaseous nature of the fuel and simplicity of flame stabilization, with respect to hydrogen. The present study is limited to the preliminary analysis of fuel blends, ranging from full natural gas to full hydrogen operation, while the investigation of dual-fuel capability with kerosene combustion is addressed in subsequent ongoing projects, i.e. HOPE [26]. The key objectives are:

- **Non-reacting flow analysis:** Investigate the mixing characteristics of the experimental setup in the absence of combustion using non-reacting LES with detailed transport of each species composing the fuel and air stream is resolved.
- **Hydrogen combustion simulation through flamelet/FDF LES approach:** Apply the flamelet/ FDF model developed in Part I to investigate cases with 25% and 100% hydrogen content. Explore the role of mixing, axial air injection (AAI), differential diffusion, and heat losses in flame stabilization and NO_x emissions performance.

1.5. THESIS OUTLINE

The remainder of the thesis is organized as follows. Chapter 2 provides the theoretical background, introducing governing equations, hydrogen combustion features, turbu-

lent combustion modelling and differential diffusion modelling. Chapter 3 describes the numerical details for the large eddy simulations of the test cases introduced in Chapter 4.

The results section is divided in two parts. In Part I the development of a robust flamelet based LES model for the analysis of turbulent hydrogen combustion is presented. Specifically, Chapter 5 focuses on the analysis of a partially premixed turbulent hydrogen flame through Eulerian stochastic fields method, both with detailed chemistry and flamelets chemistry tabulation. Chapter 6 focuses on the presumed FDF turbulence-chemistry interaction approach, and the comparison of strategies for the dynamic closure of the subgrid progress variable scalar dissipation rate, for the correct prediction of the subgrid progress variable variance. In Chapters 7 and 8 two strategies for the inclusion of differential diffusion effects are implemented and tested for the LES analysis of: a premixed turbulent hydrogen flame, a partially premixed lifted flame and a bluff body stabilized hydrogen flame. Part II focuses on hydrogen combustion applications, where a practical laboratory scale swirl-stabilized combustor is studied. Chapter 9 presents non-reacting studies to characterize the fuel-air mixing features within the set up. Finally, the operating conditions with 75% CH₄ -25% H₂ fuel blend (in volume) and full H₂ fuel are investigated through the in-house developed flamelet/presumed FDF model and the results are described in Chapter 10, with focus on differential diffusion, heat loss and axial air injection effects. Chapter 11 concludes the work, summarizing the main findings and suggesting perspectives for future research.

2

THEORETICAL BACKGROUND

2.1. FUNDAMENTAL EQUATIONS

2.1.1. INSTANTANEOUS BALANCE EQUATIONS

With respect to classical non-reacting fluid dynamics, combustion introduces several additional modelling complexities [56]. The considered fluid is a reacting non-isothermal gas, composed by a multitude of chemical species. The composition of the fluid varies due to inter-species mixing, for example between air and fuel in mixing layers, and due to chemical reactions, generally taking place rapidly compared to the flow time scales and across a very thin region. All of the thermochemical properties of the considered mixture, i.e. : specific heat, enthalpy, molecular weight and species diffusion coefficients, vary depending on the instantaneous local composition and temperature. Even when modelling low-Mach cases, therefore without compressibility effects associated to high flow velocity, the density ρ is not constant as it rapidly decreases of a factor between 4 and 8 from the reactants to the products, due to the strong heat release and thermal expansion. On the other hand, this study focuses on deflagration where the flame propagates slower than the speed of sound, and the pressure can be considered constant across the flame front.

The constitutive equations for reacting flows are based on the Navier-Stokes set. Defining u_i as the velocity components in the spatial direction x_i and p as the pressure, the fundamental equation of mass and momentum conservation in Einstein's notation read, respectively:

- Mass conservation

$$\frac{\partial \rho}{\partial t} + \frac{\partial(\rho u_i)}{\partial x_i} = 0, \quad (2.1)$$

- Momentum conservation

$$\frac{\partial(\rho u_j)}{\partial t} + \frac{\partial(\rho u_i u_j)}{\partial x_i} = -\frac{\partial p}{\partial x_j} + \frac{\partial \tau_{ij}}{\partial x_i}, \quad (2.2)$$

where τ_{ij} denotes the viscous stress tensor, related to the dynamic viscosity μ and the strain rate tensor, as described in Sec. 2.1.2. In the present studies the buoyancy term is neglected.

To track the varying mixture composition due to mixing and reaction, a transport equation for the mass fraction Y_k of each of the N_s chemical species is defined:

- Species transport

$$\frac{\partial(\rho Y_k)}{\partial t} + \frac{\partial(\rho u_i Y_k)}{\partial x_i} = -\frac{\partial J_{k,i}}{\partial x_i} + \dot{\omega}_k, \quad k = 1, \dots, N_s, \quad (2.3)$$

where $\dot{\omega}_k$ is the net chemical source/sink term of species k (in $[\text{kg}/\text{m}^3/\text{s}]$), resulting from the total production or destruction through each reaction involving the species k . It is generally related to local species concentration and temperature, through Arrhenius law as described next. The term $J_{k,i}$ is the molecular diffusion flux of species k in the direction x_i which needs modelling.

An energy conservation equation is necessary to close the Navier Stokes set, due to non-constant density and temperature T . The conservation equation for total enthalpy h , sum of sensible enthalpy h_s and enthalpy of formation Δh_f^0 at a reference temperature $T_0 = 298.15$ K, reads:

- Absolute enthalpy conservation

$$\frac{\partial(\rho h)}{\partial t} + \frac{\partial(\rho u_i h)}{\partial x_i} = \frac{\partial p}{\partial t} - \frac{\partial q_i}{\partial x_i} + \frac{\partial \tau_{ij} u_i}{\partial x_j}, \quad (2.4)$$

The present research focuses on deflagrations, where the flame speed (which will be defined in details in Sec. 2.2.3) is about 2 to 3 times lower than the speed of sound in the mixture of cold reactants and the combustion process is about isobaric[56]. The flow velocity is typically of the order of the flame speed, therefore the Mach number is small. Under the low mach number assumption the terms related to pressure variations (first term on the right hand side of Eq. 2.4) and enthalpy loss due to viscous stress (last term on the right hand side) can be neglected [56, 104]. The term q_j denotes the enthalpy flux component in direction x_j , which needs modelling. In the absence of external heat sources or sinks, deflagration is an adiabatic process, where part of the enthalpy of formation of the reactants is converted to higher sensible enthalpy in the products. For this reason, it can be noted that there is no source term associated to the absolute enthalpy equation. Temperature is related to enthalpy through the caloric equation of state:

$$h = \Delta h_f^0 + h_s = \Delta h_f^0 + \int_{T_0}^T C_p(T') dT' \quad (2.5)$$

where C_p is the specific heat of the mixture at constant pressure computed from the specific heat of the single species k composing the mixture $C_p = \sum_{k=1}^N Y_k C_{p_k}(T)$. The dependence of the species c_{p_k} on temperature is typically expressed as polynomial functions (JANAF) [116].

The system of equations is closed through the ideal gas equation of state

$$\frac{p}{\rho} = \frac{R_0}{W} T, \quad (2.6)$$

where R_0 is the universal gas constant and W is the molecular weight of the mixture. When the combustion process is isobaric (deflagration and low Mach number) the pressure in the ideal gas equation of state is constant and can be set to a reference value p_0 . Density variations across the flame are directly associated to variations in temperature [56].

2.1.2. DIFFUSIVE TRANSPORT

Diffusive transport describes the redistribution of quantities due to the chaotic motion of molecules associated to their thermal agitation. In gases that are at non-equilibrium state, this transport is governed by gradients in temperature, concentration, or velocity, which drive diffusion through specific diffusion coefficients. Diffusion acts to smooth out these gradients, allowing the gas to reach a new equilibrium state. The coefficients that characterize diffusive processes, measured in $[m^2/s]$, include the thermal diffusivity α , the species mass diffusivity D_k and the kinematic viscosity $\nu = \mu/\rho$. To compare the relative significance of these transport mechanisms, a set of non-dimensional numbers is introduced.

The **Prandtl number** compares the diffusive transport of momentum (kinematic viscosity) with thermal diffusivity:

$$\text{Pr} = \frac{\nu}{\alpha} = \frac{\mu C_p}{\lambda}. \quad (2.7)$$

The **Schmidt number** of a species k compares the diffusive transport of momentum with the mass diffusion of the species:

$$\text{Sc}_k = \frac{\nu}{D_k} = \frac{\mu}{\rho D_k} \quad (2.8)$$

The **Lewis number** of a species k relates the thermal diffusivity to the mass diffusivity of that species:

$$\text{Le}_k = \frac{\alpha}{D_k} = \frac{\text{Sc}_k}{\text{Pr}} \quad (2.9)$$

VISCOUS STRESS

Under the assumption of newtonian fluid, the viscous stress tensor is linearly related to the strain rate tensor S_{ij} and the dynamic viscosity is constant with the stress state:

$$\tau_{ij} = \mu \left(\frac{\partial u_i}{\partial x_j} + \frac{\partial u_j}{\partial x_i} \right) - \frac{2}{3} \mu \frac{\partial u_k}{\partial x_k} \delta_{ij}, \quad (2.10)$$

where δ_{ij} is the Kronecker delta. The dynamic viscosity μ depends on the local temperature and mixture composition. In combustion problems, the viscosity increase due to temperature variations dominates over variations related to mixture compositions.

Therefore, in lean conditions the mixture viscosity can be approximated with Sutherland's law [117] referring to air properties:

$$\mu_{air}(T) = A_s \frac{\sqrt{T}}{1 + \frac{T_s}{T}}, \quad A_s = 1.67e-6 \frac{\text{kg}}{\text{m s K}^{0.5}}, \quad T_s = 170.672 \text{ K}. \quad (2.11)$$

However, in partially premixed combustion and with large differences between fuel and air viscosity (for example with hydrogen), the viscosity of the mixture may be more significantly affected by composition. The local value of the viscosity of each species μ_k can be computed from temperature through Sutherland's law or as a logarithmic polynomial fitting function. Different mixing laws can be used to retrieve the viscosity of the mixture from the viscosity values of each individual species, for example Wilke's law [118] or its simplified version proposed by Herning and Zipperer [119]. Alternatively, mass-weighted averaging [120] is often implemented for its simplicity, though it can be inaccurate for mixtures with large molecular weight differences.

DIFFUSIVE SPECIES MASS FLUX

The diffusion flux in the direction x_i of a species k is expressed in terms of a diffusion velocity $v_{k,i}$ relative to the mixture as:

$$J_{k,i} = \rho Y_k v_{k,i} \quad (2.12)$$

The most accurate calculation for the local diffusion velocity components of each species consists in the solution of the computationally expensive Stefan-Maxwell system of equations [56]. An approximation of the solution of the system is represented by Fick's law:

$$J_{k,i} = -\rho D_k \frac{\partial Y_k}{\partial x_i}. \quad (2.13)$$

Fick's law is strictly valid only for bi-component mixtures or for multi component mixtures where each species is equally diffusive. However it is often used for simplicity, for example assuming D_k as the diffusion coefficient of a species k with respect to the most abundant species in the mixture [104]. In the present work, Fick's approximation is adopted for its simplicity of implementation when the assumption of unity Lewis number is made for every species. In most cases, when considering lean combustion, the diffusion coefficient can be computed considering air properties as $D_k = \mu / \text{Sc}_{\text{air}}$ where $\text{Sc}_{\text{air}} = 0.7$ [121], as the mixture is mainly composed by air, in mass. When more complex diffusive processes take place, for example in hydrogen combustion, a more detailed description is necessary. A better approximation of the Stefan-Maxwell solution was proposed by Hirschfelder and Curtiss [122]:

$$v_{k,i} = -\frac{D_k^M}{X_k} \frac{\partial X_i}{\partial x_i}, \quad (2.14)$$

where X_k is the mole fraction of species k , related to the mass fraction Y_k through the molecular weights of species and mixture $W_k X_k = Y_k W$. The diffusion coefficient of species k with respect to the mixture (mixture-averaged approach) is then computed as:

$$D_k^M = \frac{1 - Y_k}{\sum_{j \neq k} X_j / D_{jk}}, \quad (2.15)$$

where the binary diffusion coefficients D_{jk} between species j and k depend on temperature. The mass diffusion coefficient can therefore be rewritten in terms of mass fraction gradient:

$$J_{k,i} = \rho Y_k v_{k,i} = -\rho D_k^M \frac{\partial Y_k}{\partial x_i} - \rho D_k^M \frac{Y_k}{W} \frac{\partial W}{\partial x_i}. \quad (2.16)$$

Eq. 2.16 resembles Fick's law, presenting an additional term related to spatial gradients of molecular weight. This second term is typically neglected for hydrocarbon-air mixtures, where molecular weight differences between fuel and oxidizer are small. However, in hydrogen combustion, significant molecular weight gradients can arise and the term should ideally be retained. Nonetheless, the error deriving from neglecting this term was observed to be minor in lean hydrogen-air flames [123, 124].

When an approximated solution of the Stefan–Maxwell equation set is employed to model diffusion, the mass conservation of species is not automatically guaranteed. In particular, total mass conservation requires the sum of species diffusive fluxes to be zero, $\sum_k Y_k v_{k,i} = 0$. To account for this issue, two approaches are generally adopted [56]. One approach is to solve a transport equation only for $N_s - 1$ species and compute the mass fraction of the most abundant species as $Y_{N_s} = 1 - \sum_{k=1}^{N_s-1} Y_k$. In this way, the inconsistencies in diffusion velocities are incorporated into the most abundant species and mass conservation is ensured. This assumption is adopted in the present work for the calculation of 1D laminar flames, for the species transport equation in Chap. 9 and for the derivation of differential diffusion model M2 [125] in Sec. 3.2.3. This choice is justified by the fact that, under the conditions considered in the present thesis, N_2 is always the most abundant component. In a more accurate approach, a correction velocity \mathbf{v}_c is introduced so that $J_{k,i} = \rho Y_k (v_{k,i} + v_{c,i})$. The correction velocity is derived by locally enforcing mass conservation. Its value is the same for every species but varies in space and time according to the local mixture composition and the gradients of species mole fractions:

$$v_{c,i} = \sum_{k=1}^{N_s} D_k^M \frac{W_k}{W} \frac{\partial X_k}{\partial x_i} \quad (2.17)$$

This second approach is employed in the derivation of the differential diffusion model M1 [124] in Sec. 3.2.3.

An additional contribution to the mass diffusion flux is represented by thermal diffusion or Soret effect:

$$J_{k,i}^{\text{Soret}} = -\rho D_k^T \frac{\partial T}{\partial x_i} \frac{W_k X_k}{T}, \quad (2.18)$$

where D_k^T is the thermal diffusion coefficient. Due to thermal diffusion, gradients in temperature induce an additional mass diffusive flux of the species [126]. This term is generally negligible for unity Lewis number fuels, but its relevance was confirmed in the case of (lean) hydrogen combustion [39, 123, 127, 128]. In fact, thermal diffusion tends

to exacerbate the effects associated with the high diffusivity of hydrogen compared to the other species and heat, referred to as preferential and differential diffusion effects, respectively, as introduced later in Sec. 2.3. One of the objectives of the present thesis is the inclusion of differential and preferential diffusion in Large Eddy Simulation models for hydrogen combustion. Therefore, only these effects will be included in the modelling in order to isolate their sensitivity, and the analysis of thermal diffusion is therefore left outside the scope of the present investigation.

ENTHALPY DIFFUSION FLUX

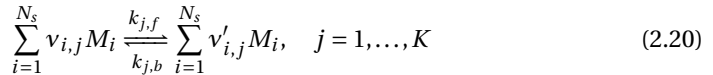
The diffusive enthalpy flux in direction x_i is modelled as:

$$q_i = -\lambda \frac{\partial T}{\partial x_i} + \rho \sum_{k=1}^{N_s} h_k v_{k,i} Y_k \quad (2.19)$$

where λ is the thermal conductivity. The first term describes the heat flux due to temperature gradient according to Fourier's law while the second term represents the enthalpy variation associated to species inter-diffusion, where $v_{k,i}$ should be modelled consistently with mass diffusive transport. This term goes to zero when species equi-diffusivity is assumed. The second term is responsible for enthalpy variations across the flame front in reacting mixtures containing highly diffusive species, like hydrogen. The thermal conductivity is related to the thermal diffusivity $\alpha = \lambda / (\rho C_p)$. As for the kinetic viscosity, the thermal diffusivity of each species, α_k , can be determined through a logarithmic polynomial function of temperature. A mixing rule, such as Mathur's law [129] or Wilke's [118], can then be applied to compute the overall thermal diffusivity of the mixture.

2.1.3. CHEMICAL SOURCE TERM

The reactants to products conversion is not a single step phenomenon, but it is composed by a chain of intermediate reversible reactions causing the formation and destruction of intermediate species. Considering a system where N_s chemical species (indices i) participate in K distinct reactions (indices j), the general representation of these reactions can be expressed as [50]:



where M_i denotes the chemical species i , and $v_{i,j}$ and $v'_{i,j}$ are the molar stoichiometric coefficients corresponding to species i in reaction j , in the reactants and in the products, respectively. The symbols $k_{j,f}$ and $k_{j,b}$ denote the forward and backward reaction rates of reaction j respectively, generally expressed as a function of temperature through Arrhenius law. The net variation in molar concentration of a species $\hat{\omega}_i$ (in [mol/m³/s]), and consequently its mass reaction rate $\dot{\omega}_i$ (in [kg/m³/s]), is computed through the generalized law of mass action:

$$\dot{\omega}_i = W_i \hat{\omega}_i = W_i \sum_{j=1}^M (v'_{i,j} - v_{i,j}) \omega_j. \quad (2.21)$$

In the previous, the net reaction rate $\hat{\omega}_i$ of a species i is expressed through the contribution of the reaction rates of each reaction ω_j , which depend on species molar concentration and specific reaction rate constants.

The volumetric heat release rate (HRR) \dot{q} due to combustion (in $\text{J}/\text{m}^3/\text{s}$) can be expressed as a variation in enthalpy of formation Δh_f^0 of the reacting mixture and represent the source term of sensible enthalpy h_s . It is expressed in terms of the contribution of the reaction rate of each species as:

$$\dot{q} = - \sum_{i=1}^{N_s} \hat{\omega}_i \Delta h_f^0. \quad (2.22)$$

2.2. PREMIXED COMBUSTION

In premixed flames, the reactants are mixed at molecular level before combustion occurs. Assuming an irreversible combustion reaction, the mixture is at stoichiometric conditions when all reactants (fuel F and oxygen O_2) are completely converted into products (P):



where ν_F and ν_{O_2} are the stoichiometric coefficients for fuel and oxygen, respectively. Under these conditions, the mass stoichiometric ratio is given by:

$$s = \frac{\nu_{\text{O}_2} W_{\text{O}_2}}{\nu_F W_F} = \left(\frac{Y_{\text{O}_2}}{Y_F} \right)_s \quad (2.24)$$

A fuel-oxidizer mixture may contain an excess of either fuel or oxidizer, leading to rich or lean conditions, respectively. The equivalence ratio ϕ quantifies the mixture composition relative to the stoichiometric condition, where $\phi = 1$:

$$\phi = \frac{n_F / n_{\text{O}_2}}{\nu_F / \nu_{\text{O}_2}} = \frac{X_F / X_{\text{O}_2}}{(X_F / X_{\text{O}_2})_s} = \frac{Y_F / Y_{\text{O}_2}}{s} \quad (2.25)$$

where n_F and n_{O_2} denote respectively the number of moles of fuel and oxygen in the mixture. Premixed flames propagate naturally towards the unburnt reactant mixture due to heat diffusion from the flame front, which preheats and ignites the fresh gases. The laminar flame speed, S_L , represents the velocity at which the flame front advances relative to the unburned mixture. Premixed flames stabilize in regions where reactants have a local velocity component normal to the flame that equals S_L .

In many real-world applications, combustion is not strictly defined by either premixed or non-premixed regime. Partially premixed flames exhibit characteristics of both, as the fuel and oxidizer are not completely mixed before reaction, and mixing continues through the combustion process. The flame could then exhibit both premixed and non-premixed mode, as in triple flames, often occurring in lifted flame [130, 131], or burn in premixed mode along gradients of equivalence ratio (stratified flames) [132–134].

Premixed flames are characterized by a set of key parameters that help describe their behavior and structure, as described next.

2.2.1. PROGRESS VARIABLE

In premixed flames, variations in species mass fractions, temperature, and other thermophysical properties across the flame front are strongly correlated. These variations can be effectively described using the progress variable c , a single scalar parameter that represents the degree of completion of the reaction.

A scaled definition of c is commonly adopted such that $c = 0$ in the reactants and $c = 1$ in the products. It can be based on reduced temperature θ :

$$\theta = \frac{T - T_u}{T_b - T_u} \quad (2.26)$$

or on a combination of the mass fraction of suitable major product or reactants species Y_k , like CO_2 or H_2O :

$$c = \frac{\sum_k (Y_k - Y_{k,u})}{\sum_k (Y_{k,b} - Y_{k,u})} \quad (2.27)$$

where the subscripts u and b denotes the unburnt (reactants) and burnt (products) conditions. The two definitions are equivalent if each species has unity Lewis number [56].

In some modelling approaches, unscaled definitions of the progress variable are preferred to optimize the dependency of thermophysical properties on c , ensuring monotonicity and avoiding steep gradients [135, 136]. They are generally defined as linear combinations of species:

$$c = \sum_i^{N_s} \mathcal{C}_i Y_i \quad (2.28)$$

where N_s represents the number of species and \mathcal{C}_i are weighting coefficients. For an unscaled progress variable definition a transport equation can be expressed as:

$$\frac{\partial(\rho c)}{\partial t} + \frac{\partial(\rho u_i c)}{\partial x_i} = \frac{\partial}{\partial x_i} \left(\rho D_c \frac{\partial c}{\partial x_i} \right) + \dot{\omega}_c. \quad (2.29)$$

where D_c is the mass diffusion coefficient for the progress variable and the chemical source term is related to the net reaction rates of the species used for the progress variable definition. With scaled progress variable definitions, for example $\dot{\omega}_c = \dot{\omega}_k / (Y_{k,b} - Y_{k,u})$, the scaling term is not constant and depends on the local mixture composition, which introduces additional terms in the equations [136, 137], as described in Sec. 3.2. Furthermore, the equation is mathematically exact only under the assumption of species equi-diffusivity and unity Lewis number $Le_k = 1$ for each species, in which case the diffusion coefficient of c simplifies to the thermal diffusivity, i.e., $D_c = \alpha$. However, for highly diffusive fuels like hydrogen, this assumption requires careful treatment, as introduced in Sec. 3.2.3.

2.2.2. MIXTURE FRACTION

The mixture fraction is a parameter describing the mixing of fuel and oxidizer, varying linearly from $z = 1$ in pure fuel to $z = 0$ in pure oxidizer. Defined as a conserved scalar, it was originally introduced to describe non-premixed flames, where combustion is governed by molecular mixing between oxidizer and fuel, with the flame stabilizing where

stoichiometric conditions are achieved. For a one-step irreversible reaction, it can be defined as in [124, 138]:

$$z = \frac{sY_F - Y_{O_2} + Y_{O_2,2}}{sY_{F,1} + Y_{O_2,2}} \quad (2.30)$$

where the subscripts $_1$ and $_2$ refer to the fuel and oxidizer streams, respectively. In a non-diluted fuel stream $Y_{F,1} = 1$, while in air $Y_{O_2,2} = 0.23$. A direct relation exists between the equivalence ratio and the mixture fraction:

$$\phi = \frac{Y_{F,1}}{Y_{O_2,2}} \frac{sz}{1-z}. \quad (2.31)$$

The mixture fraction value corresponding to stoichiometric conditions $\phi = 1$ can be obtained as:

$$z_{st} = \frac{Y_{O_2,2}}{sY_{F,1} + Y_{O_2,2}}. \quad (2.32)$$

A more general formulation for the mixture fraction is given by Bilger's definition, which is based on the conservation of elemental mass fractions [139, 140]. For example for hydrogen-air (oxygen) combustion:

$$z_{\text{Bilg}} = \frac{0.5W_H(z_H - z_{H,2}) - W_O^{-1}(z_O - z_{O,2})}{0.5W_H(z_{H,1} - z_{H,2}) - W_O^{-1}(z_{O,1} - z_{O,2})}, \quad (2.33)$$

z_H and z_O refers to the elemental mass fractions of hydrogen and oxygen, respectively.

In real combustion systems, flames are often partially premixed, meaning their composition varies across different flame regions. The mixture fraction is therefore useful in these cases because it provides a description of fuel-oxidizer mixing both prior to and during combustion. The mixture fraction transport is governed by a convection-diffusion equation:

$$\frac{\partial(\rho z)}{\partial t} + \frac{\partial(\rho u_i z)}{\partial x_i} = \frac{\partial}{\partial x_i} \left(\rho D_z \frac{\partial z}{\partial x_i} \right). \quad (2.34)$$

As for the progress variable, the mass diffusion coefficient of the mixture fraction D_z is taken to be equal to the thermal diffusivity, under the assumption of species equi-diffusivity and unity Lewis number $Le_k = 1$ for each species. In these conditions, the mixture fraction remains constant throughout a premixed flame at a given equivalence ratio. This implies that it is independent of c , allowing a partially premixed (adiabatic) systems to be fully described by two parameters: z , representing mixing, and c , representing reaction progress. However, when species diffuse at different rates, the mixture fraction is no longer constant along the flame. Instead, it becomes correlated with the progress variable due to the different diffusive transport between fuel and oxygen, as discussed in Sec. 2.3.

2.2.3. FLAME SPEED

In premixed flames the laminar flame speed S_L describes the velocity at which the flame front propagates towards the unburnt reactants, and three definitions can be considered. The **displacement speed** is defined as:

$$s_d = \frac{1}{|\nabla c|} \left(\frac{\partial c}{\partial t} + u \cdot \nabla c \right), \quad (2.35)$$

which describes the speed of the flame front with respect to the reactant mixture. The term $(\partial c / \partial t) / |\nabla c|$ is the **absolute flame speed**, which represents the speed of the flame front with respect to a fixed reference framework. When the displacement speed matches the velocity of the incoming reactants in the direction normal to the flame front, $\hat{\mathbf{n}}$, the absolute flame speed is zero.

The global consumption speed S_c can be defined as the integral of the fuel consumption rate across the flame front [56]:

$$S_c = - \frac{1}{\rho_u (Y_{F,u} - Y_{F,b})} \int_{-\infty}^{\infty} \dot{\omega}_F dn, \quad (2.36)$$

where Y_F indicates the mass fraction of fuel, $\dot{\omega}_F$ is the fuel consumption rate and the subscripts $_u$ and $_b$ denotes the unburnt and burnt mixtures. The differential dn indicates a linear integral along the direction normal to the flame front $\hat{\mathbf{n}} = -\nabla c / |\nabla c|$. This consumption speed ultimately depends on the intensity of the reaction, which is governed by the reactant composition, temperature, and operating pressure. As an example, Fig. 2.1 shows the computed flame speed (left) and peak fuel consumption rate (right) for methane-air and hydrogen-air mixtures at various equivalence ratios, obtained using 1D unstretched freely propagating premixed flame simulations with the solver Chem1D [141]. In these computations the unstretched laminar flame speed is an eigenvalue of the problem, as it must balance the velocity of the incoming reactants, and it can be computed as $S_L^0 = \dot{m}_u / \rho_u$, where \dot{m}_u is the mixture mass flow rate. In a freely propagating unstretched 1D premixed flame, the global consumption speed and laminar flame speed have about the same value. Figure 2.1 highlights the significantly higher flame speed of hydrogen, up to six times that of methane, associated with higher peak consumption rate. Furthermore, it can be seen how methane exhibits a peak around stoichiometry, while for hydrogen the maximum consumption rate peaks more towards $\phi = 1.5$. As will be discussed in details in Sec. 2.3, this occurs due to the fast diffusion of H_2 and atomic H radical (differential diffusion effects), which causes local redistributions of equivalence ratio and enthalpy.

To explain the underlying reasons behind the higher laminar burning velocity of hydrogen, Pitsch [39] refers to the analytical expression for the unstretched laminar burning velocity proposed in [55] from asymptotic analysis:

$$(\rho_u s_L^0)^2 \sim \frac{Le}{Ze^2} \frac{\lambda}{c_p} \exp\left(-\frac{E_a}{R_0 T_b}\right), \quad (2.37)$$

where T_b refers to the products temperature (adiabatic flame temperature) and Le is an effective Lewis number derived from the individual Lewis number of hydrogen and oxygen [144], and Ze is the Zeldovich number, defined as $Ze = \frac{E_a(T_b - T_u)}{R_0 T_b^2}$. Here, E_a is

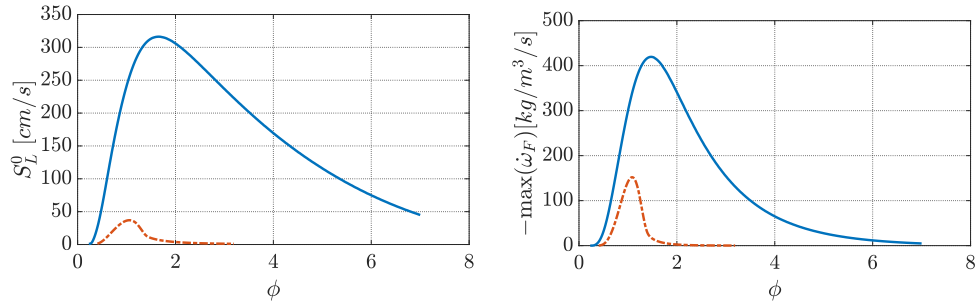


Figure 2.1: Unstretched laminar flame speed S_L^0 (left) and maximum fuel consumption rate (right) versus equivalence ratio ϕ for H₂-air (—) and CH₄-air (---) flames at $p = 1$ atm and reactants temperature $T_u = 300$ K. Results obtained from 1D laminar flames computations using CHEMID [141] with GRI3.0 [142] and San Diego [143] kinetic mechanism for methane and hydrogen fuels, respectively.

the activation energy of the one step global reaction and R_0 is the universal gas constant. As shown in Eq. (2.37), three primary factors contribute to hydrogen's exceptionally high laminar flame speed: high adiabatic flame temperature, high diffusivity, and low activation energy. While flame temperature is a contributing factor, numerical studies have demonstrated that even when the adiabatic flame temperature is reduced via nitrogen dilution, hydrogen still exhibits remarkably high flame speeds [39]. Similarly, hydrogen's high diffusivity enhances flame propagation in stoichiometric and rich mixtures, but it alone cannot account for the increase in flame speed with respect to methane. Moreover, on the lean side, high diffusivity actually reduces the flame speed compared to cases where diffusive transport is artificially reduced, as shown in Sec. 2.3. The dominant factor, as identified in [39], is hydrogen's low activation energy. Unlike methane, where the branching reaction primarily consumes radicals, hydrogen's chain-branching mechanism actively generates high abundance of atomic H radicals. They diffuse upstream into the reactants, transporting a non-negligible enthalpy flux into the preheat zone [145]. This upstream diffusion initiates low-temperature exothermic oxidation reactions, which further preheat the mixture, effectively enhancing reaction rates and flame propagation.

Flame speed is a fundamental parameter for characterizing combustion and comparing chemical and flow time scales in turbulent flames, as discussed in Sec. 2.6. It has been emphasized that the flame speed of an unstretched premixed flame depends on the mixture's composition, thermodynamic and transport properties, and reaction kinetics. In practical configurations, flame fronts are often subjected to stretch due to velocity gradients and curvature, and in such cases, both the flame speed and the reaction rate become sensitive to the mixture's diffusive properties, as discussed in Sec. 2.4. These effects are particularly important in premixed flames under turbulence-induced stretch, which will be further discussed in Sec. 2.6.

2.2.4. LAMINAR FLAME THICKNESS

In premixed flames, the laminar flame thickness δ_L defines the spatial region where heat and species diffusion, along with chemical reactions, lead to significant changes in the

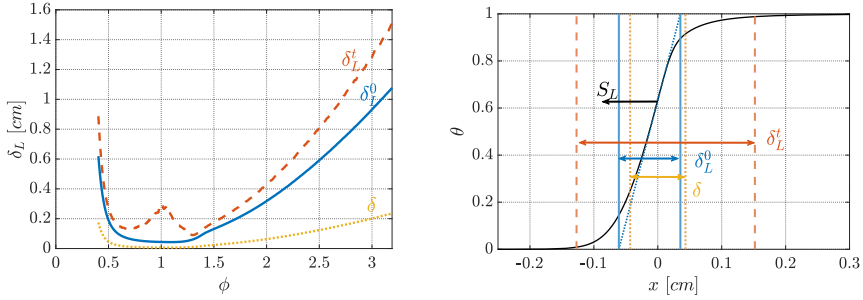


Figure 2.2: Left: comparison of the three laminar flame thickness definitions for methane-air flames at different equivalence ratios. Right: visualization of the three definitions for a methane-air flame front at $\phi = 0.6$. Results obtained from 1D laminar flame computations at $p = 1$ atm and reactants temperature $T_u = 300$ K, as in Fig. 2.1.

mixture. It provides a characteristic length scale for chemical processes, particularly useful in turbulent combustion to compare chemical scales and turbulent flow scales, as described in Sec. 2.6. It also serves as a reference value for the choice of the computational grid resolution in numerical simulations [56].

Different laminar flame thickness definitions can be adopted [50, 56]. Considering the reduced temperature profile θ of a 1D premixed laminar flame in Fig. 2.2 (right) a **total flame thickness** δ_L^t can be identified as the distance over which the temperature increases from 1% to 99% of the total temperature change. Another definition is the Zel'dovich **diffusive thickness** [146] which is based on scaling laws and local convection/diffusion balance: $\delta = \lambda_u / (\rho_u C_{p,u} S_L)$, where the subscript u refers to the unburnt mixture properties. Alternatively, a definition based on temperature gradients, the **thermal thickness**, can be given: $\delta_L^0 = |\max(\nabla\theta)|^{-1}$.

Fig. 2.2 (right) gives a visual representation of the various definitions for methane-air 1D premixed freely propagating flames. The x axis is offset so that $x = 0$ corresponds to the maximum temperature gradient. It can be seen that δ_L^t tends to overestimate the flame thickness by including both the preheat zone and the oxidation layer, where most of the fuel consuming reactions are completed, but minor species still recombine via slower reactions [56]. The other two definitions identify more localized high-temperature gradient regions and δ gives the smallest estimation. In the present work, the flame thickness definition based on temperature gradients is preferred and is computed from 1D simulations as needed.

For freely propagating premixed flames, the flame thickness depends on the equivalence ratio, reactant temperature, and operating pressure. It is generally inversely proportional to the reaction rate: higher reaction rates lead to thinner flames due to faster reactant consumption. Figure 2.2 (left) shows the computed thickness values for methane flames, revealing a minimum around stoichiometry, where the reaction rate and flame speed are highest (as seen in Fig. 2.1). The overestimation of δ_L^t is most prominent around stoichiometry, where slow recombination reactions extend the oxidation layer.

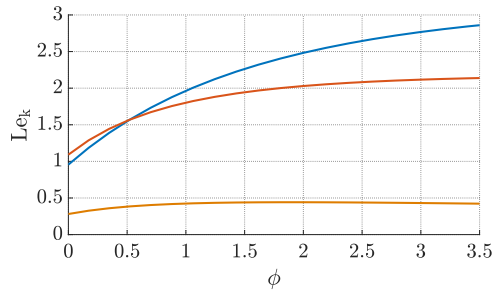


Figure 2.3: Lewis number of nitrogen Le_{N_2} (—), oxygen Le_{O_2} (—) and hydrogen Le_{H_2} (—) versus equivalence ratio ϕ in a H_2 -air mixture at 300 K.

2.3. DIFFERENTIAL DIFFUSION

The assumption of equi-diffusivity between species and heat significantly simplifies combustion modelling and it has been widely employed for hydrocarbons fuels with Lewis number reasonably close to unity. [56, 104]. However, this does not hold true for fuels with Lewis numbers significantly different from unity, such as hydrogen (where $Le_{H_2} < 1$) or propane (with $Le_{C_3H_8} > 1$) in mixtures with air. This introduces differences between species mass diffusive transport and heat diffusion. The effect related to the difference between the mixture thermal diffusivity and mass diffusivity of a species is named differential diffusion [132], or non-unity Lewis number effect, by some authors [55]. Moreover, preferential diffusion refers to the differences in mass diffusivities between two reactants (for example between hydrogen and oxygen) [55, 146]. In hydrogen combustion both effects are present as a result of its high diffusivity and they can only be artificially distinguished in numerical or analytical studies [39, 127, 147]. The two terms are often used as synonyms, even though it is conceptually more accurate to distinguish them [55, 92, 132].

Figure 2.3 shows the Lewis number of hydrogen, oxygen, and nitrogen in hydrogen-air mixtures at different equivalence ratios, computed from a mixture-averaged mass diffusion coefficient D_k^m and thermal diffusivity α , calculated as polynomial function of temperature logarithm as described in Sec. 2.1.2. For lean mixtures, $\phi < 1$, the Lewis number of hydrogen is around 0.3–0.4, while those of nitrogen and oxygen are above unity. This difference persists at richer equivalence ratios. In the study of differential and preferential diffusion effects, an effective Lewis number is defined as a weighted average of the Lewis numbers of the deficient and excess reactants (e.g., Le_{O_2} and Le_{H_2}), where the weighting favors the deficient reactant at off-stoichiometric conditions, and it converges to the exact average as the equivalence ratio approaches $\phi \rightarrow 1$ [132].

Differential and preferential diffusion significantly influence the structure of hydrogen premixed flames. This is illustrated here through one dimensional computations of unstretched premixed H_2 -air flames, comparing cases where unity Lewis number is imposed for all species ($Le_k = 1$) versus cases incorporating differential diffusion by modelling the mixture-averaged diffusion coefficients, as detailed in Section 2.1.2. Hydrogen diffuses towards the reaction zone at a higher rate than oxygen and nitrogen, due to its

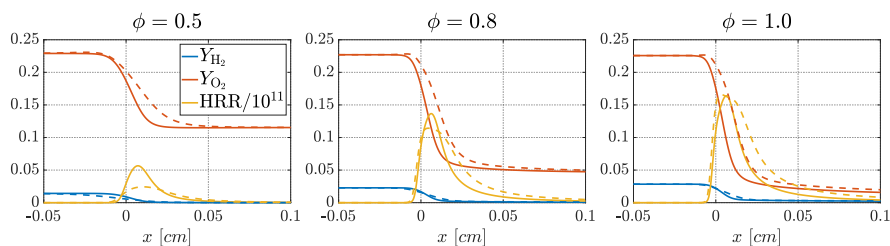


Figure 2.4: Major species mass fractions and heat release rate distribution from 1D simulations of hydrogen-air freely propagating laminar premixed flames at different equivalence ratios, reactants temperature $T_u = 300$ K and pressure $p = 1$ atm. Solid lines: unity Lewis number imposed to every species. Dashed lines: mixture-averaged diffusion model. Results obtained using CHEM1D [141] with San Diego [143] kinetic mechanism. The volumetric heat release rate (HRR) is expressed in $[J/m^3/s]$.

higher diffusivity. This behavior is evident in Fig. 2.4, where hydrogen begins diffusing towards the flame ahead of the preheat zone, leading to an overshoot in the oxygen mass fraction as compared to the equi-diffusive case. It can be seen that increased diffusion length scales result in a broadening of the flame transport zone and reaction zone, as the area interested by non-zero heat release rate (see Eq. 2.22) is broader. At low equivalence ratio the peak of HRR decreases with respect to unity Lewis number case, but a tail with higher values is observed towards the reactants. At higher equivalence ratio the region where heat release takes place broadens both towards the reactants and towards the products (Fig. 2.4 center) and at stoichiometry the peak significantly moves towards the preheat zone and its value reaches the one corresponding to the equi-diffusive case (Fig. 2.4 right).

The faster diffusion of hydrogen directly affects the mixture fraction, which exhibits variations across the flame thickness. Under the equi-diffusivity assumption, the mixture fraction remains constant throughout a 1D flame, but with differential diffusion included, it decreases through the flame thickness, resulting in locally leaner mixtures. Fig. 2.5 (left) illustrates this effect at different equivalence ratios as a function of a progress variable based on water. Hydrogen continues to diffuse towards the flame front until it reacts, generating products with diffusivities closer to those of the other major species, causing the mixture fraction to return to its initial value. Figure 2.7 (left) quantifies the relative mixture fraction reduction along the spatial coordinate x at various equivalence ratios. At lean conditions, this relative decrease is more pronounced. At lean equivalence ratios, the region affected by mixture fraction reduction extends further due to the larger laminar flame thickness. In this regime, diffusive transport scales are comparable to convective and reactive scales.

As a direct consequence in local equivalence ratio reduction along the flame, differential diffusion reduces the peak reaction rate (for a progress variable based on H_2O) on the lean side while increasing it on the rich side, Fig. 2.5 (right). The peak reaction rate shifts from $\phi = 1$ to $\phi = 1.5$ when differential diffusion is accounted for. A similar trend is observed in the laminar flame speed, reported in Fig. 2.6 (left), where differential diffusion reduces the laminar flame speed S_L on the lean side (up to $\phi = 0.6$) while enhancing it at richer equivalence ratios. This suggests that between $\phi = 0.6$ and 1, differential dif-

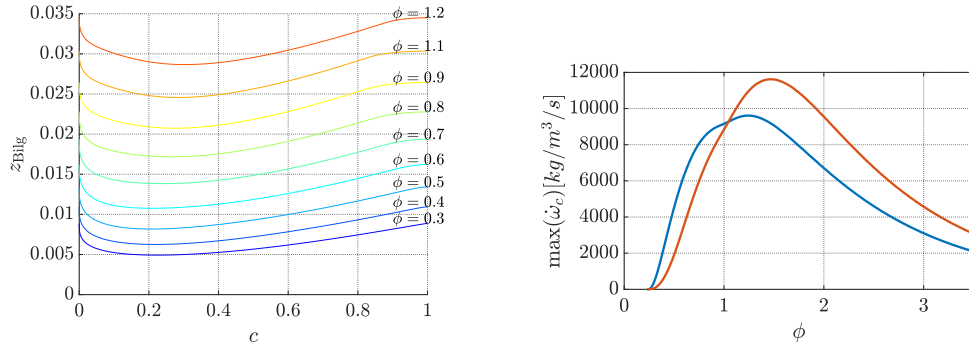


Figure 2.5: Effects of differential diffusion on 1D freely propagating H_2 -air flames at different equivalence ratios, reactants temperature $T_u = 300$ K and pressure $p = 1$ atm. Results obtained as for Fig. 2.4. Left: mixture fraction distribution z_{BiIlg} , in progress variable space c , when differential diffusion is included with mixture-averaged diffusion model. Right: peak reaction rate of progress variable versus equivalence ratio when unity Lewis number imposed to each species (—) and with mixture-averaged diffusion model (—).

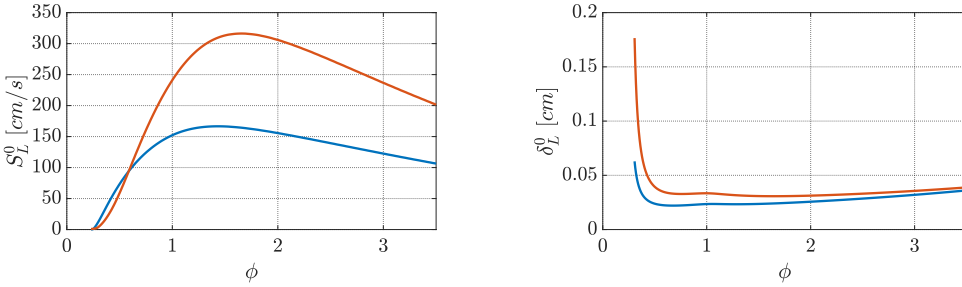


Figure 2.6: Effects of differential diffusion on 1D freely propagating H_2 -air flames at different equivalence ratios, reactants temperature $T_u = 300$ K and pressure $p = 1$ atm. Results obtained as for Fig. 2.4. Laminar flame speed S_L^0 (left) and laminar flame thickness δ_L^0 (right) versus equivalence ratio when unity Lewis number imposed to each species (—) and with mixture-averaged diffusion model (—). Results obtained as in Fig. 2.5.

fusion leads to a decrease in the peak reaction rate but an increase in its integral along x , indicating a broader flame structure, as can be observed by looking at the heat release rate in Fig. 2.4. Indeed, Fig. 2.6 shows that including differential diffusion increases the laminar flame thickness across all equivalence ratios. The enhanced diffusive transport of H_2 and H leads to a redistribution of the reaction rate, thickening the preheat region, modifying temperature gradients, and ultimately widening the flame [39]. The increased thickness is especially significant in lean mixtures, where differential diffusion reduces the reaction rate values. Indeed, the role of diffusive transport at lean conditions is quite significant compared to convection and reaction (as the flame speed and incoming mixture velocity are relatively low, compared for example to near-stoichiometry conditions), and changes in diffusivity values highly affect the flame thickness.

By looking at Eq. (2.19), it can be seen that enthalpy diffusion is driven by temperature gradients and heat diffusivity but also through mass diffusion of individual species. Under the equi-diffusive unity Lewis number assumption, total enthalpy transport re-

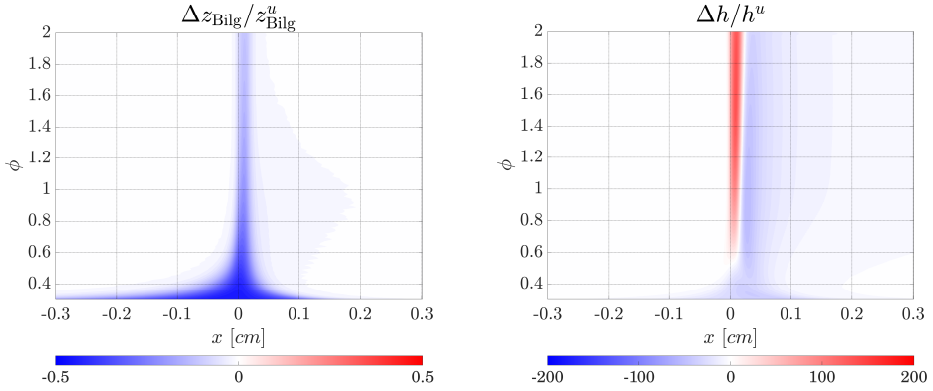


Figure 2.7: Relative variations (in physical space x [cm]) of mixture fraction Δz_{Bilg} (left) and total enthalpy Δh (right) with respect to unburnt conditions (denoted by the superscript u) for 1D freely propagating H_2 -air flames at different equivalence ratios, reactants temperature of $T_{\text{U}} = 300$ K and pressure $p = 1$ atm when differential diffusion is included with mixture-averaged diffusion model. Results obtained as for Fig. 2.5.

mains balanced. Absolute enthalpy is constant through the flame and its value depends solely on reactant composition and temperature. However, when differential diffusion is considered, enthalpy redistributes across the flame front due to the imbalance between hydrogen diffusion toward the flame and heat diffusion from the flame to the reactants. In [125, 148] it is highlighted how the diffusivity of hydrogen affects enthalpy flux with two contributions: by directly carrying enthalpy through mass diffusion, but also affecting the local mixture composition, therefore λ and C_p and affecting the Fourier term Eq. 2.19.

Figure 2.7 (right) shows the relative enthalpy variation compared to the reactant enthalpy in physical space. At very lean conditions, enthalpy decreases up to 50 times relative to its nominal value, following the trend observed for the mixture fraction. Since hydrogen is characterized by a high specific heat capacity (C_p) and thus higher sensible enthalpy than oxygen, its preferential diffusion toward the flame results in enthalpy reduction. This trend continues for richer equivalence ratios up to approximately $\phi \approx 0.6$. However, for increasing equivalence ratio, enthalpy reduction in the preheat zone becomes less pronounced, and for $\phi > 0.6$, an overshoot in enthalpy precedes the reaction zone, followed by a decrease relative to the nominal reactants enthalpy. Notably, the overshoot can reach values up to 150 times higher than the enthalpy level in the reactants, whereas the undershoot is limited to around 50 times. In physical space, the overshoot is confined to a narrower region than the undershoot. Interestingly, $\phi \approx 0.6$ represents a crossover point for the flame speed when comparing unity Lewis number and differential diffusion cases (Fig. 2.6). The enthalpy overshoot reaches a maximum at $\phi \approx 1.5$, coinciding with the peak reaction rate location in Fig. 2.5. This behavior can be attributed to the dynamics described in [39], which involve atomic H radicals. Differential diffusion affects not only H_2 but also atomic H, which forms abundantly due to hydrogen branching reactions and subsequently diffuses toward the reactants, with

effects on mixture fraction and enthalpy [145, 148]. This process leads to the transport of high-enthalpy radicals into the preheat zone, shifting the heat release rate peak upstream, thickening the preheat region, and counteracting the enthalpy depletion due to H_2 diffusion. The availability of H radicals increases with the equivalence ratio due to the higher hydrogen content and reaction intensity.

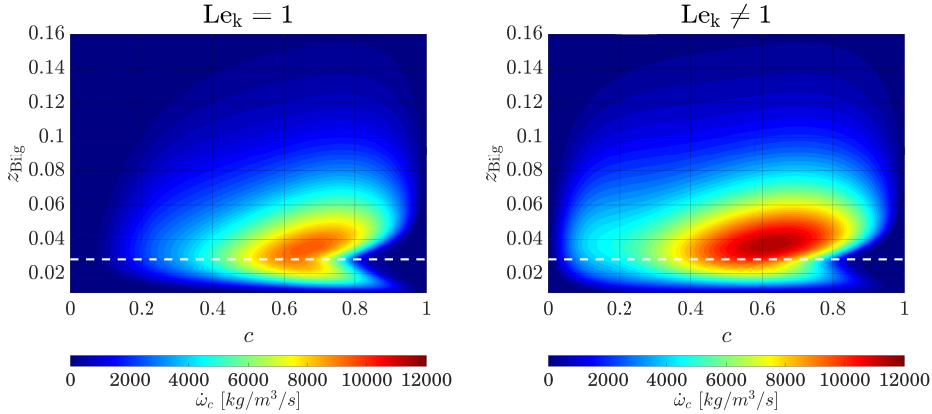


Figure 2.8: Contour plots of progress variable reaction rate for 1D freely propagating hydrogen-air flames ($T_u = 300\text{K}$, $p_0 = 1\text{atm}$) in mixture fraction and progress variable space $z_{\text{Bilg}} - c$. Left: equidiffusive case. Right: inclusion of differential diffusion through mixture-averaged model. The white dashed line indicates the stoichiometric condition $z_{\text{Bilg}} = z_{st} = 0.028$.

Figure 2.8 illustrates the progress variable reaction rate in the progress variable and mixture fraction spaces under unity (left) and non-unity (right) Lewis number assumptions. Consistently with previous observations, differential diffusion shifts the reaction rate peak to richer conditions while increasing its magnitude on the rich side, whereas the peak value is reduced on the lean side. Furthermore, differential diffusion redistributes the reaction rate profile along the progress variable, broadening the range over which the reaction rate remains significant, a direct consequence of the increased flame thickness.

The complex interplay between reaction kinetics, differential diffusion, radicals formation and transport governs the unique characteristics of hydrogen flames across different equivalence ratios, which must be carefully considered for an accurate modelling. Among these, the flame sensitivity to stretch, strongly influenced by differential and preferential diffusion, is particularly relevant and is addressed in the following section.

2.4. STRETCH, STRAIN AND CURVATURE

Premixed flames are aerodynamically stretched when they stabilize in regions where external velocity gradients are present or if the flame front propagates with curvature [50]. Stretch is formally defined as the rate of change of flame surface area as [149]:

$$K = \frac{1}{A} \frac{dA}{dt}, \quad (2.38)$$

It can be expressed as the sum of the contribution due to flame curvature k_f and tangential strain rate S_t as [54, 147]:

$$K = S_t + k_f s_d, \quad (2.39)$$

where the displacement speed s_d is defined as in Eq. 2.35. Flame curvature is defined as the divergence of the flame normal unit vector \hat{n} pointing towards the reactants:

$$\hat{n} = -\frac{\nabla c}{|\nabla c|}, \quad k_f = \nabla \cdot \hat{n}. \quad (2.40)$$

The strain rate tangential to the flame front is computed as:

$$S_t = \nabla \cdot u - \hat{n} \cdot \nabla u \cdot \hat{n} \quad (2.41)$$

In laminar flames, positive tangential strain is observed in stagnation-point flames, such as in wall-stabilized or counterflow configurations, while negative curvature is characteristic of flame tips in Bunsen-type burners. Another example of stretched flames are expanding spherical flames, often used in experiments to measure flame speed.

Flame stretch modifies the local velocity field, inducing tangential velocity gradients along the flame surface. This generates a misalignment between convective transport, which can be visualized by the streamlines, and diffusive flux normal to the flame front. Due to this, non-equidiffusive transport, either non-unity Lewis number effects or preferential diffusion between deficient and excess reactant, results in local variations in enthalpy and equivalence ratio upstream of the reaction zone, respectively. These variations, in turn, influence the flame temperature and burning rate [50, 55, 147].

Figure 2.9 (left) illustrates the response of flame temperature to positive stretch under equidiffusive conditions and non-unity Lewis number of the deficient reactant. For fuels with Lewis number close to unity, flame temperature and burning rate remains unaltered under moderate stretch levels. However, when stretch approaches a certain limit, the tangential convective timescale may become too short for the chemical kinetics to keep pace, ultimately leading to incomplete combustion and extinction. For sub-unity Lewis number of the deficient reactant, positive stretch causes an enthalpy and equivalence ratio increase in the preheat zone, resulting in higher (superadiabatic) temperature with respect to the unstretched case. This effect strengthens the flame's resistance to stretch-induced extinction, raising the critical stretch rate at which extinction occurs. On the contrary, for Lewis numbers greater than unity, the opposite trend is observed, leading to increased susceptibility to extinction.

The response of laminar flame speed to stretch is quantified by the Markstein length \mathcal{L} , which is defined as:

$$S_L = S_L^0 - \mathcal{L}K. \quad (2.42)$$

The Markstein length was originally defined to describe the effects of curvature on flame speed and successively to describe the overall effect of stretch, including both strain and curvature. However it was remarked in [150], following the work in [151], that two different Markstein lengths can be defined based on the individual contributions of strain and curvature. The two lengths coincide for steady flames, while they differ for expanding

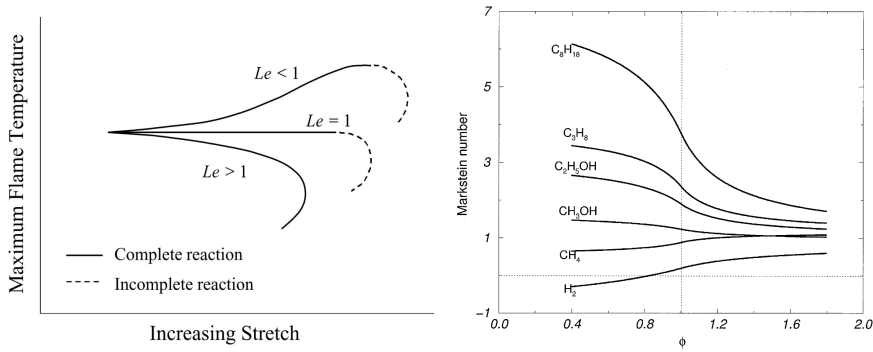


Figure 2.9: Left: effects of stretch, non equidiffusion and completeness of reaction on flame temperature and extinction turning point behaviour (adapted from Law [50]). Right: Markstein number value at varying equivalence ratio for different fuels (adapted from Bechtold *et al.* [146]).

or imploding flame fronts [150]. An analytical formulation for \mathcal{L} has been proposed in [147], revealing its dependence on key parameters such as the reactants to products density ratio σ , the Zel'dovich number (linked to activation energy), and the Lewis number of the deficient reactant. Experimental and analytical studies [146] showed that the Markstein number (obtained non-dimensionalizing the Markstein length by the flame thickness) varies significantly with fuel type and equivalence ratio, as shown in Fig. 2.9 (right). For hydrogen-air mixtures, a critical effective Lewis number exists at about $\phi \sim 0.8$, below which the Markstein length becomes negative and positive stretch causes the flame speed to increase [152]. At very lean conditions hydrogen is more resistant to extinction by stretch, as positive stretch induces mixture fraction and enthalpy increase with respect to the unstretched flames. On the other hand negative curvature (for example Bunsen burner flame tip) can experience cooling and local extinction.

Numerical 1D simulations in [153] revealed that strong tangential strain increases the mixture fraction values throughout the flame, counteracting the natural effect of mixture fraction decrease caused by differential diffusion in unstretched flame. As a result of the increased dominance of convection over diffusion effects, thermochemical properties tend to those of equidiffusive flames.

In [145] the redistribution of enthalpy in strained and curved flames is assessed. It is highlighted that H_2 and H_2O transport enthalpy into the reaction zone while atomic H extracts it and transports it towards low temperature regions. Flame strain enhances diffusive fluxes, increasing H radical production and altering enthalpy distribution until a certain limit value, after which the reaction rate decreases. The authors identify that at high pressures an increase in the H radicals consumption rate increases the strain level at which the flame reactivity starts to decrease, suggesting that high pressure increases the resistance of hydrogen flames to extinction by strain, with implication on turbulence combustion modelling.

The response of reaction rate and flame speed to flame stretch is strongly influenced by the diffusive properties of the mixture and is described by the Markstein length. In particular, the coupling between flame front curvature and local reaction rates can amplify perturbations, leading to intrinsic flame instabilities known as thermodiffusive in-

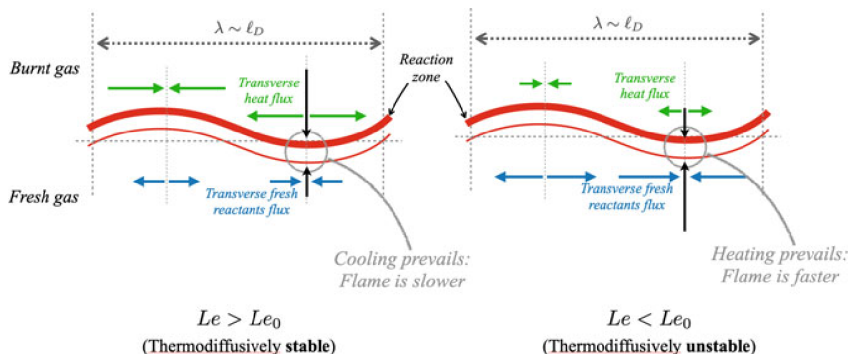


Figure 2.10: Schematic visualization of the imbalance between transverse diffusive flux of heat and mass in thermodynamically stable (left) and unstable (right) mixtures, image reproduced from [154].

stabilities. These phenomena, which are highly relevant in hydrogen combustion, are examined in more detail in the following section.

2.5. INTRINSIC INSTABILITIES

Laminar premixed flames can be subject to intrinsic instabilities, which can amplify initial perturbations in the flame front, leading to self-induced flame wrinkling and/or local inhomogeneities in consumption speed and temperature.

Hydrodynamic instabilities, known as Darrieus-Landau (DL) instabilities, arise due to the large density variation across the flame front [132]. This density decrease induces an acceleration in the velocity component normal to the flame surface in the burnt gases to satisfy continuity. Any curvature in the flame front perturbs the velocity field, so that positively curved flame sections (convex towards the reactants) decelerate the incoming mixture. If the laminar flame speed remains constant, the flame propagates faster in the reactants, reinforcing the perturbation indefinitely. The opposite occurs for negative curvature.

Thermo-diffusive (TD) instabilities, are caused by the non-unity Lewis number of the deficient reactant, and, differently from DL instabilities, their occurrence depends on the mixture composition [39, 132]. These instabilities are particularly significant in very lean hydrogen-air mixtures, where the effective Lewis number falls below a critical threshold Le_0 , resulting in a negative Markstein length [39]. In the presence of a curvature disturbance, local variations in the flame speed amplify the perturbation. With reference to Eq. (2.42), positive curvature (resulting in positive stretch) increases the flame speed, propagating the flame front further into the reactants, while negative curvature has the opposite effect.

From the point of view of diffusive transport, the coupling between flame front curvature and flame speed is attributed to a focusing effect of the curved flame front segments, which is explained in [54, 154] through the presence of transversal diffusion flux components, tangential to the flame front, as sketched in Fig. 2.10. Positive curvature has an effect of focusing hydrogen diffusion towards the reaction zone. Heat diffuses

from the reaction zone to the reactants (de-focusing), but due to lower thermal diffusivity (sub-unity Lewis number), a positive net enthalpy gain occurs, Fig. 2.10. Moreover, the highest diffusivity of hydrogen compared to oxygen (preferential diffusion), causes the focusing effect to increase hydrogen diffusive flux more than that of oxygen, resulting in a net equivalence ratio increase. The highest enthalpy and equivalence ratio cause the increase of reaction rate and flame speed on convex sections, sustaining the TD instability and leading to superadiabatic temperatures. Conversely, negative curvature, in the form of flame cusps, results in reduced temperature and equivalence ratio, often leading to local extinction.

In [39], it was demonstrated that TD instabilities are primarily governed by the faster diffusion of hydrogen as compared to heat (sub-unity Lewis number) rather than preferential diffusion, by means of 2D direct numerical simulations (DNS) of laminar hydrogen-air flames at an equivalence ratio of $\phi = 0.4$. By artificially assigning the same sub-unity Lewis number to each species, therefore suppressing preferential diffusion effects, TD instabilities still developed, exhibiting superadiabatic temperatures but without variations on the local equivalence ratio. On the contrary, rescaling the Lewis number of each species as $Le_k^* = Le_k / Le_{H_2}$, which only allows preferential diffusion while setting the Lewis number of hydrogen to unity, did not generate TD instabilities. Nevertheless, the equivalence ratio variations caused by preferential diffusion in thermo-diffusive instabilities have been shown to influence NO formation in hydrogen flames [155].

The growth of intrinsic instabilities is studied using dispersion relations, which describe the linear early-stage amplification of small curvature perturbations, described by a growth rate, as a function of their wavelength $\bar{\omega}(k)$ [132, 154]. Darrieus-Landau mechanism is destabilizing across all wavenumbers, the growth rate varies linearly with the disturbance wave number and depends on the unburnt-to-burnt gas density ratio σ . On the other hand, TD instabilities amplify long-wavelength disturbances, with a peak value of the growth rate for wavelengths of the order of laminar flame thickness, while short-wavelength perturbations are stabilised [154]. The main factors governing TD instability growth rate have been identified in the Zeldovich number, the effective Lewis number, and σ , which are the same parameters determining the Markstein length [147].

In the long term these instabilities evolve non-linearly causing the cellular burning structures that characterize lean hydrogen flames, as observed numerically and experimentally [50, 51]. Numerical simulations revealed that TD instabilities develop from small scales structures, in the order of the laminar flame thickness, and evolve with the formation and destruction of larger scale structures referred to as "finger-like" structures [156]. This is illustrated in Fig. 2.11, where the flame front exhibits numerous small-scale, high-curvature cusps alongside the development of larger "finger-like" structures, shown in close-up in the right panel. Consistent with the previously discussed diffusive transport dynamics, positively curved segments of the flame front are followed by superadiabatic temperatures on the product side, while cusps (regions of negative curvature) are associated with reduced heat release and lower local temperatures, sometimes even resulting in a local opening of the flame front.

Intrinsic instabilities lead to an increase in consumption speed per unit cross-sectional area, described by the ratio:

$$\frac{s_c}{S_L^0} = \frac{A}{A^0} I^0. \quad (2.43)$$

In this equation, two contributions are identified. The wrinkling factor A/A^0 is the ratio between the actual flame surface area A and the unperturbed planar flame surface area A_0 , and it quantifies the increase in flame surface area due to DL and TD instabilities. The stretch factor I_0 represents the local variation in flame propagation speed due to stretch effects. In [157], a correlation was proposed between the flame speed enhancement $\frac{s_c}{S_L^0}$ and the Zeldovich number, the effective Lewis number, and $\sigma = \rho_u/\rho_b$, which are also the key parameters controlling the Markstein length [39, 147]. Alternatively, this correlation can be expressed in terms of the thermodynamic conditions of the reactants: unburnt temperature T_u , pressure p , and equivalence ratio ϕ . In [158], Rieth identifies the influence of radical recombination kinetics on I^0 at elevated operating pressures, proposing a scaling for the stretch factor based on the Zeldovich number and, additionally, the Peclet number Pe , which compares the maximum convection to diffusion transport rates in 1-D unstrained premixed flames at nominal conditions [39].

These instabilities pose significant challenges in practical combustor design. Lean hydrogen flames are prone to enhanced propagation speeds and increased flashback susceptibility, both of which are exacerbated by flame front curvature and stretch. In addition, thermodiffusive instabilities influence NO formation through their impact on local temperature and strain fields [155]. Their interaction with turbulence can either dampen or intensify these effects, underscoring the need for accurate modelling. Understanding these mechanisms and their implications is crucial for developing robust lean hydrogen combustion systems, particularly under turbulent conditions explored in the following section.

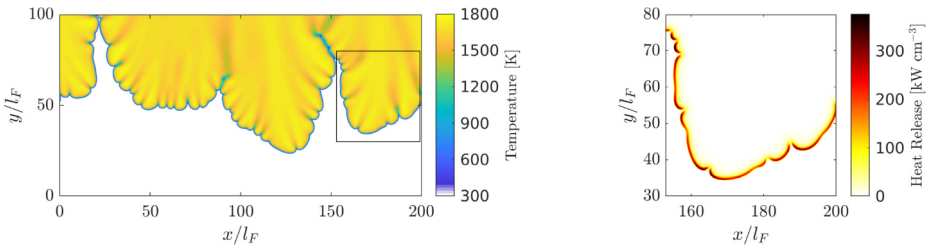


Figure 2.11: Snapshot of the temperature field showing small-scale cellular structures and large-scale finger-like structures along the flame front (left panel), flame propagating from top to bottom. Hydrogen-air at $\phi = 0.4$. Local temperatures strongly exceed the adiabatic temperature of $T_b = 1643$ K. The right panel shows a closeup of a flame finger colored with the heat release. The location of the closeup is indicated in the left panel by a rectangle. Image reproduced from Berger *et al.* [156].

2.6. TURBULENT PREMIXED COMBUSTION

Most combustion processes of engineering interest involve turbulence due to high mass flow rates and its role in maximizing mixing. In turbulent conditions, a complex interplay arises between the flame front and the eddies composing the turbulent motion,

significantly influencing flame dynamics.

Turbulent combustion is characterized by a wide spectrum of time and length scales associated with both turbulent flow motion and chemical reactions. The relative importance of chemical and flow scales, along with their competing interactions, gives rise to distinct combustion phenomenology. Its inherently multiscale nature makes turbulent combustion highly computationally challenging for the high number of variables, resolution constraints and problem stiffness.

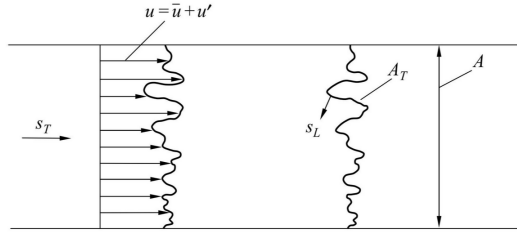


Figure 2.12: Schematic representation of a turbulent flame front, image reproduced from [54]

In turbulent premixed combustion, as in the laminar case, fuel and oxidizer mix at the molecular level before ignition. However, here, the flow entering the flame zone is turbulent, characterized by a high Reynolds number. The turbulent structures perturb the flame front through wrinkling [54, 56, 159], increasing the flame surface area and thereby enhancing the global consumption rate. In a statistically steady 1D flow, the flame region can be described as a turbulent planar flame brush, with a thickness enveloping all locations reached by the wrinkled flame over time. The turbulent flame displacement speed S_T can be defined over a control volume \mathcal{V} analogously to the laminar consumption speed:

$$A\rho_u Y_{F,u} S_T = - \int_{\mathcal{V}} \dot{\omega}_F d\mathcal{V} \quad (2.44)$$

where A represents the cross-sectional area of \mathcal{V} , as shown in Fig. 2.12. Experiments have shown that increasing turbulence intensity and Reynolds number initially leads to a quasi-linear increase in turbulent flame speed. Assuming the flame locally retains its laminar propagation speed S_L^0 (unstretched), Dahmköhler [159] explained this increase as a direct consequence of enhanced available flame surface area A_T due to wrinkling:

$$\frac{S_T}{S_L^0} = \frac{A_T}{A} \quad (2.45)$$

Empirical correlations with the velocity root mean square u' have been proposed $S_T \sim S_L(1 + u'/S_L^0)$. However, at sufficiently high turbulence levels, a bending effect occurs where the S_T increase with u' is no longer linear and tends to a plateau, marking the onset of local quenching. This occurs when turbulent convective fluctuations become comparable to chemical time scales, leading to local extinction due to excessive stretch.

Wrinkling and flame surface area enhancement due to turbulence are often described in terms of stretch, which is studied by decomposing its effects into flame surface gen-

eration (caused by tangential strain and positive curvature) and flame surface destruction (due to negative curvature) [39]. At very high stretch levels, the reaction rate and laminar flame speed decrease, leading to quenching and explaining the bending effect in turbulent flame speed. To account for these effects, a stretch factor must be introduced, similarly to what discussed in Sec. 2.5 for laminar thermo-diffusive response: $S_T/S_L^0 = I_0 A_T/A$. For flames with unity Lewis number, the stretch factor remains nearly constant with wrinkling, as the reaction rate and flame speed do not strongly respond to stretch, except at very high levels where quenching occurs. However, flames with sub-unity Lewis numbers such as lean hydrogen flames, exhibit a non negligible response to stretch. Therefore, turbulence-flame interactions become more intricate, and classical theoretical descriptions may not suffice.

Together with the effects of turbulence on reaction, combustion also influences the turbulent flow field. The intense heat release and resulting temperature rise increase the viscosity of the mixture, reducing the local Reynolds number and potentially inducing relaminarization or damping of turbulent fluctuations. Simultaneously, thermal expansion accelerates the mixture as it converts to products over a thin reaction zone, generating vorticity and potentially enhancing turbulence intensity [104].

2.6.1. REGIMES IN TURBULENT PREMIXED COMBUSTION

Historically, the phenomenology of turbulent premixed combustion has been described and classified through the comparison of the turbulent time scales τ_t and the chemical time scales τ_c by means of non-dimensional numbers. To this scope, the Damköhler number is defined as:

$$Da(l_t) = \frac{\tau_t}{\tau_c} = \frac{l_t S_L}{u' \delta_L^0}, \quad (2.46)$$

where the chemical time scale is estimated by means of the laminar flame speed S_L and laminar flame thickness δ_L^0 , while the turbulent time scale is defined through the turbulent integral length scale l_t and the velocity rms u' . For high Da the reaction is fast as compared to the turbulent flow scales. Combustion therefore generally occurs in a thin region which is convected, wrinkled and stretched by turbulence. The internal flame structure is not largely affected by turbulence and the flame can be described locally by a laminar flame element called flamelet. In the limit of very low Damköhler number the reaction is very slow in comparison to turbulence time scales. Turbulent transport becomes dominant over diffusion and reaction scales, leading to possible reactants products mixing and approaching the perfectly stirred reactor regime.

In addition to the Damköhler, the Karlovitz number Ka compares the chemical length scales (either flame thickness or reaction region thickness $\delta_r \sim 0.1\delta_L^0$) to the smallest turbulent scales, namely the Kolmogorov time scale τ_k and length scale η_k :

$$Ka = \frac{\tau_c}{\tau_k} = \frac{u'_k \delta_L^0}{\eta_k S_L^0} = \left(\frac{\delta_L^0}{\eta_k} \right)^2, \quad Ka_R = \left(\frac{\delta_r}{\eta_k} \right)^2 \sim \frac{Ka}{100}, \quad (2.47)$$

where u'_k is the Kolmogorov velocity scale, and Ka_r is the Karlovitz number based on the reaction region thickness. By means of these non-dimensional numbers, premixed combustion is categorized in regimes, represented in the Borghi-Peters diagram [138], reported in Fig. 2.13 (left).

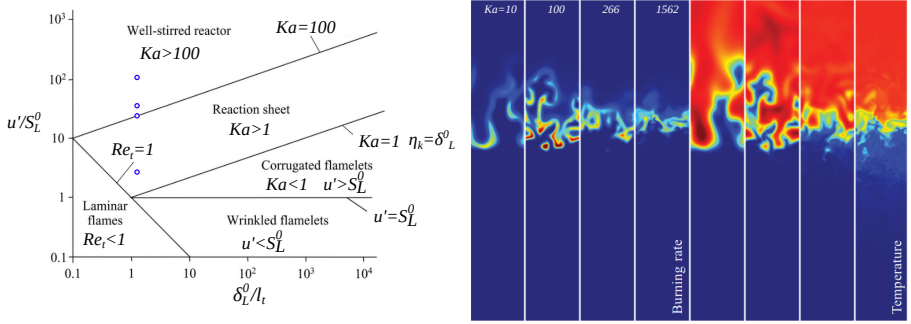


Figure 2.13: Left: Regime diagram for turbulent premixed combustion [138]. Right: direct numerical simulations of turbulent hydrogen-air flames at different Karlovitz numbers performed by Aspden *et al.*[61]. The corresponding operating points are reported on the left diagram, marked by circles.

Based on the Borghi diagram (Fig. 2.13), premixed combustion regimes include:

- **Flamelet regime** ($Ka < 1$, $Da > 1$): The flame thickness is much smaller than every turbulent scale. Turbulent eddies are therefore not able to affect the flame structure that locally retains its laminar-like structure. This regime can be further divided into:
 - *Wrinkled flamelets* ($u' < S_L^0$): the turnover velocity of eddies is small compared to the flame speed. The flame propagating is therefore just mildly corrugated by the turbulent structures
 - *Corrugated flamelets* ($u' > S_L^0$): a stronger flame-eddy interaction is present due to the high turbulent velocity fluctuations u' and the flame front is highly wrinkled by the eddies, possibly leading to the creation of pockets of unburnt and burnt mixture
- **Thickened wrinkled flame regime or thin reaction zone** ($1 < Ka \leq 100$): The kolmogorov scales are small enough to enter the flame and affect its structure. However they are not small enough to affect the reaction zone, which remains thin, but they can thicken the preheat zone.
- **Distributed reactions regime or well-stirred reactor** ($Ka > 100$): Both preheat and reaction zones are affected by turbulence and the laminar flame structure is disrupted. Turbulent transport dominates over reaction and diffusion. Reaction takes place in a distributed manner and the presence of eddies in the reaction zone leads to higher heat diffusivity, temperature reduction and quenching.

Fig. 2.13 (right) illustrates results from direct numerical simulations of hydrogen-air turbulent premixed flames at different Karlovitz numbers, helping to visualize the transition between regimes as turbulent scales become finer. However, the results reveal critical issues in this categorization, as a recognizable flame structure persists even at high Ka .

These distinctions represent early attempts at classification, based solely on scale comparisons under frozen turbulence conditions, neglecting any influence of the flame over the turbulent structures. In reality, the flame induces anisotropy and reduces the local Reynolds number, potentially leading to relaminarization and altering the interactions between flame and turbulence. The flame can adapt to the incoming turbulent flow, modifying it and becoming more resistant to wrinkling and thickening than initially estimated. While it is often assumed that the smallest eddies have the strongest effect on the flame, they are also the least energetic in isotropic turbulence and may be dissipated by the flame itself [160]. Recent studies, reviewed in [160], propose revised regime boundaries based on updated measurements and simulations, showing that flame structures can persist at significantly higher Karlovitz numbers. Furthermore, the effects of turbulence on laminar flame properties are often overlooked. This is particularly relevant for non-unity Lewis number fuels like hydrogen, where heat and mass diffusivities differ, leading to unique turbulence interactions. As discussed in Sec. 2.4, positive stretch enhances reaction rates, shortening chemical time scales and altering the local Karlovitz number. Simultaneously, thermo-diffusive (TD) instabilities can persist in turbulent conditions, modifying the expected flame regime boundaries. In [61, 161] it is remarked that the boundary of distributed regime cannot be universally assumed as $Ka = 100$, but it is instead fuel-dependent, influenced by factors such as density jump and Lewis number, since for low Le increasing strain and Karlovitz number results in increasing reaction rate and a simultaneous decrease in chemical time scales. These aspects are explored further in the next section.

2.6.2. TURBULENT HYDROGEN COMBUSTION

In turbulent combustion, molecular diffusivity generally plays a secondary role compared to convective turbulent transport. However, hydrogen presents a unique case due to its exceptionally high diffusivity. The interplay between turbulence and intrinsic thermodiffusive (TD) instabilities and hydrogen flames response to stretch have been the focus of intensive research [39]. Experimental and numerical studies indicate that thermodiffusive instabilities and cellular burning structures persist in turbulent hydrogen flames [52], even at relatively high Reynolds [162] and Karlovitz numbers [61, 163]. The influence of reactant diffusivity on turbulent flame speed has been highlighted in [164].

Numerical studies further indicate that not only do TD instabilities remain in the presence of turbulence, but they interact synergistically with turbulence and their relevance intensifies with increasing Karlovitz number [53]. Turbulent structures introduce additional curvature to the self-induced wrinkling of the flame front, leading to an overall increase in flame surface area. Moreover, as observed in laminar TD-unstable flames, positively curved flame segments dominate over negatively curved cusps, enhancing the consumption speed and increasing the effective equivalence ratio. Additionally, the predominantly positive tangential strain induced by turbulence further amplifies this effect. The combined influence of increased curvature and strain results in a higher stretch factor I_0 compared to laminar thermodiffusively unstable flames [52, 53]. Rieth *et al.* [158, 165] identified the coupling between hydrogen differential diffusion and flame front curvature as a dominant process on the consumption rate distribution even at significantly higher Karlovitz number, which was observed to be even amplified at high pressure con-

ditions. High pressure conditions were also investigated in [145] focusing on the interplay between radical atomic H availability and diffusive flux with enthalpy redistribution and reacting zone thickening at high strain and curvature conditions, suggesting that high pressure promotes the hydrogen flame resilience to strain and preserve the synergistic diffusion-stretch interactions up to high turbulence levels, hindering the transition to the distributed regime.

Given the strong coupling between turbulence and thermodiffusive instabilities, it was suggested that the Karlovitz number (Ka) and the boundaries of the distributed reaction zone in the Borghi-Peters diagram may require redefinition. In [166, 167] it was shown that at the same Da and Ka , the presence of TD instabilities fundamentally alters turbulence-chemistry interactions, thereby modifying the morphology of turbulent flames. In [161, 167], the need for a rescaling of Ka based on local effective chemical timescales, including stretch effects, is emphasized. Nevertheless, the Karlovitz number is still identified as the main parameter to characterize turbulence-flame interaction. A critical Karlovitz number is identified beyond which turbulent transport dominates over diffusion and thermal dilatation, disrupting the flame front structure. Above this value flame features collapse to universal behavior, invariant of further turbulence intensity increase. This critical Ka is clearly not universally $Ka = 100$ and depends on density gradients, as thermal expansion can affect turbulence, and Lewis number [61]. At lower Lewis number the critical Ka increases, due to the enhancing effect of strain on the reaction rate. The transition to the distributed regime for hydrogen flames occurs well beyond $Ka = 100$, closer to $Ka \sim 1000$ [161]. This can be visualized in Fig. 2.13 (right), where a flame front structure is retained well beyond $Ka = 100$ for hydrogen.

Although TD instabilities persist beyond $Ka = 100$, they become progressively suppressed as Ka increases. This mitigates variations in local equivalence ratio and reduces the formation of superadiabatic temperatures [61, 168]. In [168] it was observed that the inhibition of cellular and finger-like structures, leading to a net reduction in flame surface generation, eventually overcomes the effect of an increasing stretch factor, causing the overall consumption rate to plateau with increasing Ka . High pressure conditions were investigated in [145] focusing on the interplay between radical atomic H availability and diffusive flux with enthalpy redistribution and reacting zone thickening at high strain and curvature conditions, suggesting that high pressure promotes the hydrogen flame resilience to strain and preserve the synergistic diffusion-stretch interactions up to high turbulence levels, obstructing the transition to the distributed regime.

The insights provided in the discussion above have important implications for the modelling and design of lean hydrogen turbulent flames in practical combustion applications. Being aware of the range of relevance of differential diffusion and TD instabilities is crucial, as these effects can significantly impact turbulent flame speed, potentially leading to unexpected flashback risks and altered emissions characteristics. In partially premixed hydrogen flames, TD instabilities may not always be present, as they primarily occur at relatively low equivalence ratios. In such cases, macroscopic mixing-induced equivalence ratio variations may become the dominant factor. Nevertheless, accurate modelling of differential diffusion remains essential for predictive simulations and practical design considerations.

2.7. TURBULENT COMBUSTION MODELLING

Through computational fluid dynamics (CFD), the equations presented earlier are solved to simulate turbulent flame characteristics and predict temperature distribution, flame stabilization, and mixing behavior. Modelling must be able to capture all the phenomenology described so far in order to serve as a meaningful tool for combustor technology design.

The highest level of accuracy and complexity is offered by Direct Numerical Simulation (DNS), where Eqs. (2.1–2.4) are resolved directly. DNS is extremely costly due to the large number of species and the complexity of chemistry modelling. For hydrogen, it is relatively more feasible due to the simplicity of the reaction mechanism and the limited number of species involved, especially when compared to more complex hydrocarbon fuels. In non-reacting turbulent flows, the computational cost is already significant due to the resolution required to capture the turbulent structures. As noted earlier, combustion scales can be smaller than Kolmogorov scales or comparable and chemistry can become the resolution limiting factor. DNS remains unfeasible for large-scale combustors and is primarily used for fundamental physics investigations on turbulence-flame interaction [61, 90, 91] or the study of simple combustor geometries, like single channels in micromix configurations [169], slot burners [53] or simplified domains of swirled combustors [170].

Reynolds-Averaged Navier–Stokes (RANS) simulations apply ensemble averaging to the governing equations and solve for the mean flow [104]. Turbulent stresses and transport effects on the mean flow are modeled. Unsteady RANS (URANS) can capture unsteady dynamics in the mean field. These approaches have been widely used for design due to their low computational cost and their ability to capture key flow features when well-calibrated. However, they require significant parameter tuning and fail to capture many important physical phenomena [92, 171].

In Large Eddy Simulation (LES) a low-pass filtered version of the governing equations is resolved. This strategy inherently captures more physics than RANS as the most energetic turbulence motion is resolved directly, while the smallest turbulent scales falling below the filter size are modelled [92]. Its computational cost lies between DNS and RANS, making it a practical tool for practical combustor design, while offering a significantly higher level of detail than RANS. In particular, LES can resolve turbulent mixing, flame front wrinkling, and unsteady phenomena such as flashback or periodic unsteady dynamics, for example vortex shedding, Kelvin-Helmholtz instabilities, precessing vortex core (PVC). For these reasons, LES represents one of the highest levels of detail and accuracy currently achievable for realistic combustor simulations.

This research focuses on turbulent hydrogen combustion, with the ultimate objective of studying its application for gas turbine combustors. The aim is to develop a simulation tool that provides enough physical detail while remaining computationally affordable for capturing the complex reacting flows involved. The study of phenomenon like flashback, coupling between differential diffusion and stretch in turbulent hydrogen flames and periodic combustion features requires detailed, time and space resolved simulations. For these reasons, LES is chosen as the most appropriate numerical tool in the present research.

2.8. LES FILTERING

To derive the LES equations, a filtering operator is introduced, defined by the spatial convolution of a quantity $Q(\mathbf{x}, t)$ with a filter kernel $G(\mathbf{x})$:

$$\overline{Q(\mathbf{x})} = \int Q(\mathbf{x}^*) G(\mathbf{x}^* - \mathbf{x}) d\mathbf{x}^* \quad (2.48)$$

The filter function G is characterized by a cutoff width Δ , and the filtering operation removes components of Q associated with wavelengths smaller than Δ . The filtering operator can be viewed with a spatial weighted average and the weight distribution is determined by the shape of the filter kernel in space. Typical filters in physical space include the box filter, which assumes a uniform value within a box of size Δ and drops sharply to zero for $|\mathbf{x}^* - \mathbf{x}| > \Delta/2$, and the Gaussian filter, which peaks at $\mathbf{x}^* = \mathbf{x}$ and decays rapidly with increasing $|\mathbf{x}^* - \mathbf{x}|$ [93, 104]. Alternatively, filtering can be performed in spectral space. For example, a sharp cutoff filter sets to zero all wavenumbers above π/Δ in the Fourier representation of Q , which corresponds to a spatial resolution cutoff of 2Δ [93, 104].

The quantity Q can be decomposed into a filtered (resolved) part and a sub-filter part, "fluctuating" around the filtered value: $Q(\mathbf{x}) = \overline{Q} + Q'$. Unlike Reynolds averaging used in RANS [104], filtering does not guarantee that filtering the fluctuating part makes it vanish: $\overline{Q'} \neq 0$, and $\overline{\overline{Q'}} \neq \overline{Q}$, unless a sharp spectral cutoff is applied [104].

In practice, the LES filtering operation is applied implicitly through the spatial discretization of the computational domain using a numerical grid and the chosen numerical scheme to discretize the governing equations (e.g., finite volume, finite difference, or spectral methods [172]). The filtered governing equations are solved directly, and the influence of the sub-filter scales on the resolved flow is modeled using subgrid-scale (SGS) models. In some dynamic modelling approaches, the resolved quantities are explicitly filtered by a test filter whose width is larger than the LES filter size, in order to enforce scale similarity between the smallest resolved scales and the subgrid scales [96, 173].

To derive the filtered governing equations, the filtering operation must ideally commute with differential operators. This condition is generally satisfied only if the filter is homogeneous in space. When a non-uniform grid is used, the filter becomes non-homogeneous, leading to commutation errors [174]. These numerical errors are generally assumed to be accounted for within the SGS modelling [104], and some additional compensation can be achieved through the use of dynamic modelling approaches [172].

2.9. FAVRE DECOMPOSITION

The decomposition of a quantity Q into a filtered and a sub-filter part is widely used to derive LES formulations for constant density flows [93]. However, when dealing with problems such as reacting flows with thermal expansion, high Mach number flows with compressibility effects, or mixing between streams of different temperature and composition, the variable density introduces complications in deriving the filtered governing equations.

As an example, referring to Eq. (2.1), the LES filtering of the term ρu_i yields:

$$\overline{\rho u_i} = \overline{(\bar{\rho} + \rho')(\bar{u}_i + u'_i)} = \bar{\rho} \bar{u}_i + \bar{\rho} \overline{u'_i} + \overline{\rho' \bar{u}_i} + \overline{\rho' u'_i}, \quad (2.49)$$

which reveals the presence of several correlation terms between filtered and sub-filtered components of density and velocity. A similar issue arises in the other governing equations, which include even more complex triadic terms such as $\rho u_i u_j$ in the momentum equation.

To address this problem, Favre [175] proposed a density-weighted filtering operation defined as $\tilde{Q} = \overline{\rho Q / \bar{\rho}}$, such that, for example, $\overline{\rho u_i} = \bar{\rho} \tilde{u}_i$. A Favre decomposition can then be introduced as $Q = \tilde{Q} + Q''$, with properties analogous to those described in the previous section.

2.9.1. LES EQUATIONS

The LES equations are derived by Favre-filtering the fundamental equations set for reacting flows presented in Sec. 2.1.1, resulting in:

$$\frac{\partial \bar{\rho}}{\partial t} + \frac{\partial \bar{\rho} \tilde{u}_j}{\partial x_j} = 0, \quad (2.50)$$

$$\frac{\partial \bar{\rho} \tilde{u}_i}{\partial t} + \frac{\partial \bar{\rho} \tilde{u}_i \tilde{u}_j}{\partial x_j} = -\frac{\partial \bar{p}}{\partial x_i} + \frac{\partial \bar{\tau}_{ij}}{\partial x_j} - \frac{\partial}{\partial x_j} [\bar{\rho} (\widetilde{u_i u_j} - \tilde{u}_i \tilde{u}_j)], \quad (2.51)$$

$$\frac{\partial \bar{\rho} \tilde{Y}_k}{\partial t} + \frac{\partial \bar{\rho} \tilde{u}_j \tilde{Y}_k}{\partial x_j} = \frac{\partial}{\partial x_j} \left(\bar{\rho} \tilde{D}_k \frac{\partial \tilde{Y}_k}{\partial x_j} \right) - \frac{\partial}{\partial x_j} [\bar{\rho} (\widetilde{u_j Y_k} - \tilde{u}_j \tilde{Y}_k)] + \bar{\omega}_k, \quad (2.52)$$

$$\frac{\partial \bar{\rho} \tilde{h}}{\partial t} + \frac{\partial \bar{\rho} \tilde{u}_j \tilde{h}}{\partial x_j} = \frac{\partial}{\partial x_j} \left(\bar{\rho} \frac{\tilde{\nu}}{Pr} \frac{\partial \tilde{h}}{\partial x_j} \right) - \frac{\partial}{\partial x_j} [\bar{\rho} (\widetilde{u_j h} - \tilde{u}_j \tilde{h})] \quad (2.53)$$

$$\bar{p} = \frac{\bar{\rho} R_0 \tilde{T}}{\bar{W}}, \quad (2.54)$$

Filtered diffusion fluxes of species and enthalpy have been approximated as:

$$\overline{\rho D_\Psi \frac{\partial \Psi}{\partial x_j}} \approx \bar{\rho} \tilde{D}_\Psi \frac{\partial \tilde{\Psi}}{\partial x_j} \quad (2.55)$$

Similarly, referring to Eq. (2.10), the resolved viscous stress tensor is modelled as:

$$\overline{\tau_{ij}} = 2\bar{\rho} \tilde{\nu} (\tilde{S}_{ij} - \tilde{S}_{kk} \delta_{ij}/3), \quad (2.56)$$

where $\tilde{S}_{ij} = \frac{1}{2} \left(\frac{\partial \tilde{u}_j}{\partial x_i} + \frac{\partial \tilde{u}_i}{\partial x_j} \right)$ is the Favre-filtered strain rate tensor. The residual stress tensor τ_{ij}^r is modelled using eddy diffusivity concept by means of the subgrid kinematic viscosity ν_{SGS} as:

$$\tau_{ij}^r = -\bar{\rho} (\widetilde{u_i u_j} - \tilde{u}_i \tilde{u}_j) = 2\bar{\rho} \nu_{SGS} (\tilde{S}_{ij} - \tilde{S}_{kk} \delta_{ij}/3) \quad (2.57)$$

The isotropic part of the residual stress tensor, represented by the last term on the right-hand side, is typically incorporated into the pressure term and handled via a pressure

correction algorithm, following the same treatment applied to the resolved viscous stress tensor $\overline{\tau_{ij}}$ [172].

Various subgrid turbulence models can be employed to define the subgrid scale viscosity. In the present research, this term is closed using a one-equation model as $\nu_{SGS} = C_k k^{1/2} \Delta$, where Δ is the LES filter width (estimated as the cubic root of the local cell volume in the computation), $C_k \approx 0.1$ is a model constant, and k is the SGS kinetic energy for which an additional transport equation is solved [95, 176, 177]:

$$\frac{\partial \overline{\rho} k}{\partial t} + \frac{\partial \overline{\rho} \tilde{u}_j k}{\partial x_j} \approx \frac{\partial}{\partial x_j} \left(\tilde{\mu} \frac{\partial k}{\partial x_j} \right) + \tilde{u}_i \frac{\partial (\tau_{ij}^r + 2k\delta_{ij}/3)}{\partial x_j} - \frac{\partial f_j}{\partial x_j} - \varepsilon_k. \quad (2.58)$$

In the above equation, $f_j = \overline{\rho}(\overline{u_j u_i u_i} - \tilde{u}_j \overline{u_i u_i})/2 \approx \overline{\rho} \nu_{SGS} (\partial k / \partial x_j)$ is the turbulent residual flux of k and $\varepsilon_k \approx C_\varepsilon \overline{\rho} k^{3/2} / \Delta$ is the dissipation rate of SGS turbulent kinetic energy where the model constant is set to $C_\varepsilon = 1.048$.

The subgrid turbulent fluxes of a generic quantity ψ are modeled by means of a standard gradient hypothesis:

$$\overline{\rho}(\overline{u_j \psi} - \tilde{u}_j \tilde{\psi}) = -\overline{\rho} \frac{\nu_{SGS}}{Sc_t} \frac{\partial \tilde{\psi}}{\partial x_j}, \quad (2.59)$$

where Sc_t is the SGS Schmidt number relating the subgrid kinematic eddy viscosity and subgrid eddy diffusivity $Sc_t = \nu_{SGS} / D_{SGS}$. Under the Reynolds analogy the two subgrid quantities are equal and the SGS Schmidt number is close to unity. In the present research the value is taken equal to $Sc_t = Sc = 0.7$, following previous studies [89, 178, 179]. In a similar fashion, a SGS Prandtl number is employed for the subgrid turbulent enthalpy flux and $Pr_t = \nu_{SGS} / \alpha_{SGS} = Pr = 0.7$. However, in [179] it was highlighted that the SGS Schmidt number value may differ depending on the local turbulence conditions.

The filtered reaction rate cannot be directly evaluated using the Arrhenius equation due to the nonlinearity of its terms. As a result, $\overline{\omega}_k \neq \omega_k(\overline{Y}_1, \dots, \overline{Y}_N, \overline{T})$. Approaches based on Taylor series expansions have been proven to be not viable, as filtering introduces numerous unclosed terms, and truncating higher-order terms leads to significant errors due to the strong nonlinearity of the reaction kinetics [104]. Therefore, closing the filtered reaction rate remains one of the most challenging aspects of turbulent combustion modelling. The next section explores this in details, presenting common strategies for modelling the filtered reaction rate in LES of turbulent reacting flows.

2.10. COMBUSTION MODELS

The complexity of combustion Large Eddy Simulation (LES) arises from the high dimensionality of chemical kinetics modelling and resolution considerations, particularly in the interaction between turbulent and chemical scales. The modelling effort has been therefore mainly directed towards chemistry reduction and subgrid turbulence-chemistry interaction models. Extensive reviews can be found in [56, 92, 104] and a brief summary is given next.

2.10.1. CHEMISTRY MODELLING

modelling chemical kinetics in turbulent combustion is challenging due to the large number of species and reactions, spanning a wide range of timescales. Each species requires a dedicated transport equation, and reaction rates are computed using Arrhenius-type expressions that depend on local temperature and composition. These reaction source terms introduce significant stiffness, as fast radical reactions and slow fuel oxidation processes coexist, imposing strict constraints on spatial and temporal discretization.

One-step infinitely fast reaction models offer a highly simplified representation of combustion chemistry. While they can capture global features, they cannot resolve the detailed flame structure, formation of intermediate species and pollutants and they cannot describe finite-rate chemistry interaction with turbulence [56].

To include finite-rate chemistry, reduced kinetic mechanisms have been developed from detailed chemistry. Early approaches involved manually selecting dominant reactions and applying quasi-steady-state or partial equilibrium assumptions [56, 180], resulting in overall limited computational savings. More recent developments introduced automated methods for skeletal mechanisms [181], which are particularly useful for LES with detailed chemistry [44]. While hydrogen chemistry is relatively simple, these methods are useful when studying blends (e.g., with methane or ammonia) or reducing nitrogen mechanisms for accurate NO prediction [44].

For LES, the most significant cost reductions come from tabulated chemistry approaches [56]. One early application is the Intrinsic Low Dimensional Manifold (ILDM), where fast chemistry is represented by a lower-dimensional space of species (or progress variable) and pre-tabulated [182]. This concept was then extended to the widely used flamelet-based tabulated chemistry models [105, 183, 184]. In flamelet models, all thermochemical quantities are precomputed from canonical 1D laminar flame (flamelets) simulations, typically laminar premixed or non-premixed flames, and stored in a lookup table. The tables are accessed through a small number of controlling variables, commonly progress variables, mixture fraction, and enthalpy, for which a transport equation is solved. During LES, these quantities are retrieved via interpolation, reducing the online computational cost compared to solving detailed kinetics. In more recent approaches neural networks are trained on flamelets database to substitute the tabulation and interpolation process, leading to significant computational cost reduction [185–187]. A wide range of flamelet models exists, varying by flame prototype configuration, manifold dimensionality, and choice of control variables. A recent comprehensive review can be found in [188]. Initial flamelet models were developed for non-premixed flames, parametrized by mixture fraction and scalar dissipation rate [189]. Successive extensions incorporate complex effects like heat loss [134], unsteady strain and transient phenomena [190], extinction and ignition [106], slow NO chemistry [135], radiation [191], autoignition [192], and multi-regime combustion [193].

An alternative to precomputed tables is In-Situ Adaptive Tabulation (ISAT), where the table is constructed dynamically during the simulation. New chemical states are either retrieved from memory or computed and added to the table. ISAT enables local refinement of the thermochemical space and can be competitive with high-dimensional pre-tabulations [194].

For pure hydrogen, the limited number of species and reactions makes detailed chemistry relatively affordable. However, reduction and tabulation strategies remain essential when dealing with fuel blends (e.g., H_2/CH_4 or H_2/NH_3) or for accurate modelling of minor species like NO [39, 44, 148].

In LES the application of reduced or tabulated chemistry requires a subgrid-scale (SGS) model to account for turbulence-chemistry interactions [56]. In fact, Turbulent wrinkling alters the subgrid-scale distribution of control variables, influencing the filtered thermochemical state, as described next.

2.10.2. TURBULENCE-CHEMISTRY INTERACTION

In Large Eddy Simulation (LES), only the largest turbulent structures, typically around 80% of the turbulent kinetic energy, are resolved [97]. The filter width is therefore larger than the Kolmogorov length scale. In cases with moderate Karlovitz numbers, the flame thickness is comparable to or smaller than the Kolmogorov scale, meaning that the flame front lies entirely within the sub-grid scales, which implies the necessity of dedicated sub-grid modelling. In many practical applications, such as gas turbines with highly turbulent flames, the flame thickness may exceed the Kolmogorov scale. Nevertheless, a significant portion of the turbulence effects on combustion, such as flame wrinkling and broadening, still occurs at sub-grid scales. Therefore, while part of the turbulent wrinkling can be resolved, most of the turbulence-chemistry interaction requires sub-grid modelling [104].

To address the challenges of modelling turbulence–chemistry interaction, a variety of strategies have been developed, as extensively reviewed in [56, 92, 104, 171, 195]. While many of these models were initially formulated in the context of Reynolds-Averaged Navier–Stokes (RANS) simulations, they have since been adapted for use in Large Eddy Simulation (LES). Broadly, these modelling strategies can be categorized into geometrical and statistical approaches. Depending on the application, some can incorporate detailed chemical kinetics or tabulated chemistry, such as flamelet-based tabulations, to manage computational cost, as described in details next.

GEOMETRICAL APPROACHES

Geometrical methods are implicitly linked to a flamelet assumption, where the flame remains thin with respect to the turbulent structures. These methods aim to geometrically reconstruct the flame location and morphology, often treating it as a propagating surface [104, 195].

- **Eddy Break up model**

Eddy break up model can be considered among the geometrical approaches if the progress variable is assumed to be bimodal $\tilde{c} = 1$, $\tilde{c} = 0$, implying a topological representation of the flame front as a thin surface separating reactants and products. Originally developed for RANS and later adapted to LES, it assumes high Damköhler and Reynolds number, with a description of the flame similar to the distributed regime [196]. The reaction rate is assumed to be controlled by turbulent mixing between fresh and burnt gases, and a characteristic turbulent mixing timescale is estimated from turbulent kinetic energy k and its dissipation rate ϵ $\tau_t = k/\epsilon$. The progress variable filtered reaction rate is therefore:

$$\bar{\omega}_c = -C_{EBU} \bar{\rho} \frac{\sqrt{\sigma_c^2}}{\tau_t}, \quad (2.60)$$

where σ_c^2 is the subgrid variance of the progress variable and C_{EBU} is a model constant close to unity. Assuming infinitely fast chemistry the subgrid distribution of the progress variable becomes bi-modal and the SGS variance is simplified to: $\sigma_c^2 = \bar{c}(1 - \bar{c})$. This formulation is attractive for its simplicity and facility of implementation. However, it relies on isotropic turbulence, with no effect of combustion on turbulence, and it tends to overestimate the reaction rate in high strain rate regions [104]. Moreover, the reaction rate is fully controlled by turbulence conditions and does not depend on any chemical properties of the fuel. Extensions to account for reaction kinetics description were proposed in [197].

- **G-field equation or level set**

In this approach the flame front is viewed as a very thin interface separating unburnt and burnt gases. The flame front is identified either as an isosurface of a progress variable or via a level-set function $G(\mathbf{x})$, which denotes the signed distance of a generic domain point from the flame front [198, 199]. An equation (G-equation) in propagative form is solved to describe the evolution of this material surface. It was pointed out in [200] that the G-equation has physical meaning only along the instantaneous flame front and the extension to a filtered G-equation in the LES context requires careful mathematical consideration. The concept was therefore extended to the description of a turbulent flame brush in [200], through the equation:

$$\frac{\partial \tilde{G}}{\partial t} + \tilde{u} \cdot \nabla \tilde{G} = \frac{\rho_u}{\bar{\rho}} S_T |\nabla \tilde{G}| \quad (2.61)$$

Accurate modelling of the turbulent flame speed S_T , and inclusion of heat release on the surrounding mixture is necessary [104]. This model provides a kinematic description of flame propagation but does not resolve the internal flame structure. To account for this, Moureau *et al.* [201] proposed an approach based on the coupled resolution of the filtered G-equation and the filtered transport equation of a progress variable, which allows to describe the resolved turbulent transport in the preheat region and retrieve the turbulent flame structure. While it is effective for smooth, continuous flame fronts, this model cannot inherently capture extinction or reignition events.

- **Flame surface density**

Similarly to the level-set approach this model describes the flame as an interface which is convected, diffused, curved and strained by the turbulent velocity field [202]. The flame surface density Σ describes the available flame surface area per unit volume, which allows to define the reaction rate of a species k as $\bar{\omega}_k = \bar{\Omega}_k \Sigma$, where $\bar{\Omega}_k$ is the mean local burning rate per unit of flame area. This framework decouples the turbulence-induced wrinkling (captured by Σ) from the chemical

kinetics (embedded in $\hat{\Omega}_k$), which may include the effects of curvature, strain, and heat loss. Transport equations for both the progress variable and Σ are typically solved, and the latter is often modeled in terms of flame wrinkling factor. This methodology has been successfully employed with dynamic models in LES [203–205].

- **Thickened flame model (TFM)**

In this approach, the flame is artificially thickened with respect to its actual size while retaining the same laminar flame speed, which allows to solve for the flame front structure on a coarser grid. This is achieved by multiplying the thermal and species molecular diffusivities by a factor F , and by dividing the reaction rate of each species by the same factor [206]. Species transport equations, can thus be directly resolved across the thickened flame front [206] as:

$$\frac{\partial \rho Y_k}{\partial t} + \frac{\partial \rho Y_k u_i}{\partial x_i} = \frac{\partial}{\partial x_i} \left(\rho E F D_k \frac{\partial Y_k}{\partial x_i} \right) + \frac{E}{F} \dot{\omega}_k \quad (2.62)$$

Differential diffusion effects can be taken into account at a resolved level, by assigning a specific diffusion coefficient D_k to each species [44]. Recent studies [207] proposed subgrid scale models for thermo-diffusive instabilities in the TFM context. The diffusion coefficients and reaction rates are multiplied by an efficiency function E , deriving from subgrid scale model to ensure that the flame propagation speed is unaffected by the flame thickening and to account for sub-grid turbulence chemistry interaction, e.g. subgrid flame wrinkling [206]. The efficiency function E measures the reduction in the sub-grid flame surface due to the thickening process and is defined as the ratio between the wrinkling parameter for unthickened and thickened flames, $E = \Xi|_{\delta=\delta_i} / \Xi|_{\delta=F\delta_i}$. Dynamic variants [208, 209] adapt the thickening based on local flow conditions. TFM can be used with either fully detailed chemical mechanisms or flamelet based tabulated chemistry. Further details on this model can be found in [98, 206, 208, 210].

- **Filtered tabulated chemistry (FTACLES)**

In this approach the flame front is locally described using a database of 1D laminar premixed flamelets computed *a priori* and tabulated. The effects of under-resolution of the flame front due to the typical LES computational grid spacing are accounted for by filtering *a priori* the 1D flamelets with a Gaussian kernel of width comparable to the LES filter size [107]. The objective is to preserve the correct flame propagation speed, even when subgrid-scale turbulence is absent, ensuring that the LES model converges toward the DNS limit as the LES filter width tends to zero. Extension to turbulent regimes is achieved by introducing a model for sub-grid flame wrinkling, based on a flame surface density (FSD) correction, linking the filtered reaction rate to the resolved flame surface area.

STATISTICAL APPROACHES

Unlike geometrical models, statistical methods describe the flame structure in terms of probabilistic distributions of intermediate thermochemical states. These approaches

quantify subgrid turbulence–chemistry interactions (wrinkling and broadening) by means of a subgrid filtered density function FDF of the thermochemical quantities or by considering the conditional statistics moments of species and temperature.

2

- **Filtered density function (FDF) models**

In these models the subgrid fluctuations of thermochemical quantities induced by turbulent mixing and wrinkling are described by means of a subgrid probability distribution [56, 104]. Defining $\mathbf{Y} = (Y_1, \dots, Y_N, T)$ as the local vector of the thermochemical variables describing the composition and temperature state of the mixture at a certain time, the joint filtered density function $\bar{P}(\mathbf{Y}^*; \mathbf{x}, t)$ represents the probability of finding a specific composition and temperature at a given location.

This way, the filtered reaction rate of a species k can be expressed as:

$$\bar{\omega}_k(\mathbf{x}, t) = \int_{\mathbf{Y}} \dot{\omega}_k(\mathbf{Y}^*) \bar{P}(\mathbf{Y}^*; \mathbf{x}, t) d\mathbf{Y}^*, \quad (2.63)$$

where $\dot{\omega}_k(\mathbf{Y}^*)$ is the unfiltered reaction rate corresponding to a specific composition and temperature state, as computed from detailed chemistry.

The local value of the subgrid FDF can follow a presumed shape (presumed FDF models) or computed through a transport equation (transported FDF models).

- **Presumed filtered density function (PFDf)**

Presumed FDF models are generally employed in combination with chemistry tabulation, whereby a reduced set of controlling variables, such as c and z , is used to represent the full thermochemical state space. The shape of the subgrid FDF is described in terms of the statistical moments of these control variables. In practice, only the first two moments are retained: the filtered control variable value \tilde{c} and its subgrid variance σ_c^2 .

For two normalized controlling variables defined over the interval $[0, 1]$, the closure for a generic filtered quantity \bar{Q} (e.g., a reaction rate) takes the form:

$$\bar{Q}(\tilde{c}, \tilde{z}, \sigma_c^2, \sigma_z^2) = \int_0^1 \int_0^1 Q(c, z) \bar{P}(c, z; \tilde{c}, \tilde{z}, \sigma_c^2, \sigma_z^2) dc dz. \quad (2.64)$$

The filtered joint FDF is typically assumed to be the product of the distributions of the individual controlling variables, implying statistical independence [104, 106, 136, 211]. In this formulation, the filtered quantity depends only on the local values of the control variables and their associated subgrid variances. A transport equation is solved for the filtered control variables, while the subgrid variances can either be computed algebraically or obtained by solving additional transport equations.

One of the earliest implementations of this approach is the Bray-Moss-Libby (BML) model [212, 213], originally developed within the RANS framework. In this model, the FDF is analytically represented by a combination of three probability density functions, corresponding to fully reacted, unreacted, and

partially reacted states. This leads to a very simple and computationally cheap model, where the pre-integration can be computed analytically.

A more refined variant adopts a presumed β -function shape for the FDF [107, 109]. This function is particularly advantageous, as it can be fully defined using only the first two statistical moments. Moreover, the β distribution has useful mathematical properties: depending on the moment values, its shape can range from symmetric bell shape, to strongly skewed or even nearly bimodal [56]. This flexibility makes it especially suitable for capturing the physical features of turbulent premixed and partially premixed flames. This modelling approach is adopted in the present work, and further details are provided in the following chapter.

– **Transported filtered density function (TFDF)**

In a more general alternative to presumed FDF, a transport equation for the local FDF can be solved, in the so called transported PDF (TPDF) approach. In these methods the FDF is represented by a set of samples evolving according to modelled stochastic differential equations [110]. The samples can either represent a local instantaneous condition (Lagrangian stochastic particle method (LSPM)) or an instantaneous condition in the whole domain (Eulerian stochastic field (ESF) method). For both approaches appropriate models are needed for convection and micromixing, but the chemical source term is closed. Also, to keep the stochastic error low, the number of samples must be sufficiently high (typically up to 100 particles per cell in the LSPM and up to 10 fields in ESF approaches respectively) [111]. In ESF method the continuous fields, spanning the entire domain, are spatially differentiable and temporally continuous, but not time-differentiable. This implies that there are no spatially varying sampling errors, and only a relatively small number of fields, 4 to 8 typically [214], is needed to accurately capture the statistical moments.

The ESF method can be combined with a fully detailed chemical mechanism (FC-ESF), solving the stochastic fields for the species mass fractions and the enthalpy, or with a tabulated chemistry technique such as the FGM (FGM-ESF), where the Eulerian fields are solved for the controlling variables (e.g. progress variable and mixture fraction), as introduced in Chap. 3.

• **Conditional momentum closure (CMC)**

This model was originally derived in [215] and extended to LES [216]. It describes the intermediate thermochemical states within the flame structure by considering conditional statistics. The conditional mean $\overline{\rho Y_i | c = c^*}$ is defined as the average value of a thermochemical quantity when a control variable (e.g. a progress variable) assumes a specific value c^* . A transport equation can be solved for the conditional quantities assuming that fluctuations of the conditional mean can be neglected. However, these equations present unclosed terms whose modelling is not straightforward [104]

A central objective of the present research is the development and assessment of a

flamelet-based presumed FDF model for hydrogen combustion, including the formulation of differential diffusion models. These models have been proven to be robust, computationally efficient and accurate and they represent a promising tool for the design of practical hydrogen combustion devices. Prior to the development of presumed FDF models, transported FDF approaches are employed in the present research to investigate a partially premixed hydrogen flame test case, and a hybrid strategy combining transported FDF and flamelet tabulations is proposed. The thickened flame model is employed to perform preliminary simulations of a practical laboratory-scale hydrogen combustor prior to applying the in-house flamelet/presumed FDF framework tailored for hydrogen.

2.11. FLAMELETS APPLICABILITY

When chemical timescales are short compared to turbulent time scales, the flame structure, controlled by heat and mass diffusion, remains unaffected by turbulent structures, which can only wrinkle and strain the flame front, or thicken the preheat region. A turbulent flame therefore retains a locally laminar structure, which thermochemical states can be precomputed from laminar 1D flamelets simulations and parameterized.

As described in Sec. 2.6.1, the flamelet regime was originally defined for low Karlovitz numbers ($1 < Ka < 100$), where turbulence does not disrupt the inner flame structure. This classification, based on scale comparison, did not stem from direct observations and neglected important factors such as the damping effect of chemistry on turbulence and stretch effects on reaction rates. As reviewed by Driscoll *et al.* [112], both experimental and numerical studies have shown that turbulence primarily thickens the preheat zone, while the reaction zone remains thin. In some cases, even at increasing Ka , quenching occurs before eddies can influence the reaction zone. Driscoll *et al.* further proposed revising the boundaries of the thickened preheat zone and the distributed reaction regime, noting that the flamelet regime remains applicable at higher Karlovitz and Reynolds numbers than previously assumed, with the transition to a well-stirred reactor regime occurring well beyond the classical Borghi limits.

Practical combustion systems typically operate at high Reynolds numbers and Karlovitz numbers on the order of $Ka \approx 10^2$. Laboratory-scale experiments tend to involve slightly lower Reynolds numbers but similar Ka , and can still be effectively described by flamelet models. Various studies [217–219] have confirmed that the flamelet structure, along with the ability to numerically represent thermochemical states using flamelets [161, 193, 220–222], remains valid across a broader range of turbulent conditions than previously expected.

In the case of hydrogen flames, the inherently high flame speed results in lower effective Karlovitz numbers under equivalent turbulence intensities, supporting the applicability of flamelet models. Due to its negative Markstein length, stretch actually increases flame speed in lean hydrogen-air mixtures, so that a flamelet structure can resist at higher turbulence levels. These properties were verified by Aspden *et al.* [161], who investigated hydrogen flames at high Karlovitz numbers and observed that they retain a flamelet-like structure well beyond $Ka = 100$. Signs of distributed reaction and turbulence-dominated mixing begin to appear near $Ka \sim 1000$, but even at $Ka \sim 8700$, the flame behavior is not yet fully invariant to turbulence. Furthermore, they argue that

the conditions leading to distributed combustion are practically unrealizable in real systems.

In summary, flamelet-based models offer a robust and computationally efficient framework for modelling turbulent combustion. Their domain of applicability has proven to be broader than initially assumed, supporting their use in LES for a wide range of combustion regimes. These findings are particularly encouraging for the modelling of practical turbulent hydrogen combustors, where flamelet approaches can remain valid and effective.

2.12. DIFFERENTIAL DIFFUSION MODELLING

The relevance of differential diffusion effects in hydrogen combustion is thoroughly discussed in Sec. 2.3-2.5, and it is highlighted in Sec. 2.6.2 that thermodiffusive instabilities remain important even in turbulent combustion. Although diffusive processes are often considered to be of second-order with respect to turbulent transport [39], neglecting them in turbulent hydrogen combustion modelling can lead to inaccurate predictions in flame propagation speed and therefore flame stabilization dynamics, flashback and NO emissions. In order to be used for design purposes, numerical models should therefore be able to capture differential diffusion and thermodiffusive instabilities. To date, models for the prediction of differential diffusion and thermodiffusive instabilities are not yet fully available for LES [39], and one of the main objectives of the present research is to contribute to fill this gap.

The highest level of fidelity in resolving differential diffusion is achieved through Direct Numerical Simulation (DNS) coupled with detailed chemistry. These simulations provide resolution and quantitative details beyond what can be achieved experimentally. In such frameworks, a diffusion coefficient can be assigned to each species based on local composition and temperature. While solving the full Stefan–Maxwell system is possible, it has been shown that mixture-averaged models [167, 223] offer reasonable approximations for detailed analysis of differential diffusion phenomena.

In the context of tabulated chemistry, two major challenges emerge: 1) defining appropriate diffusion coefficients for the controlling variables. 2) Determining the dimensions of the tabulated manifolds and controlling parameters [39]. Tabulated approaches do not directly solve for species mass fractions, and the definition of diffusion coefficients for the controlling variables is not trivial. In equidiffusive cases, these are often approximated using the thermal diffusivity. However, to account for differential diffusion, various models have been proposed for DNS studies of laminar flames to correct the transport equations of the controlling variables.

Regele et al. [124] proposed a correction to the mixture fraction transport equation, which in their study was the only controlling variable based on the hydrogen mass fraction, thus strongly influenced by differential diffusion. They introduced a source term, $\dot{\omega}_z$, and a corrected diffusion coefficient that can be tabulated. Successively, the approach was extended for its application with a mixture-averaged diffusive transport model by relaxing the constant (non-unity) Lewis number assumption and including Soret effect [123].

Another approach is proposed in [125, 134], where three controlling variables are employed (progress variable, mixture fraction and absolute enthalpy) and defined as linear

combinations of species mass fractions. In a 1D flamelet, the higher diffusivity of hydrogen introduces differences in the mass fraction distribution of every other species, when compared to an equidiffusive case, as previously shown in Fig. 2.4. Therefore, the diffusive transport of the controlling variables is highly affected by differential diffusion, especially if their definition contains the H_2 mass fraction. Consequently, a correct diffusive flux for a controlling variable can be obtained as a linear combination of the individual species fluxes. Schepers *et al.* [148] applied this method for the simulation of a planar thermo-diffusively unstable hydrogen air flame with flamelet generated manifolds (FGM). They quantifying the contribution of each species to the controlling variable and enthalpy flux and selected the highest contributing species for the construction of the progress variable. Good results with respect to detailed chemistry were obtained parametrizing the FGM on mixture fraction and a progress variable built on water and hydrogen mass fraction. They underlined the relevance of atomic H in the enthalpy transport and stressed the importance to include this species in the progress variable definition if enthalpy is used as a controlling variable.

Generally, two controlling variables are sufficient to capture the essential physics of mixing and reaction, while enthalpy can be included to represent heat losses [134, 135]. However, differential diffusion introduces additional physical phenomena. Its coupling with flame curvature and strain may lead to the occurrence of new thermochemical states due to the redistribution of mixture fraction and enthalpy. These states may not be captured in manifolds built solely on 1D freely propagating premixed flames with varying equivalence ratios and enthalpy. Thus, a larger set of controlling variables may be required. Recent studies questioned whether a good description of mixture fraction and progress variable transport alone can suffice under curved flame conditions, whether enthalpy must also be included, or even if 1D flamelets incorporating curvature and strain via additional source/sink terms may be necessary. A priori analyses on this topic are discussed in [53, 224, 225]. In [145], the redistribution of mixture fraction and enthalpy due to curvature and strain is examined in details to assess whether a corrected mixture fraction alone is adequate for describing the resulting thermochemical states.

The correction models described earlier are now being extended to Large Eddy Simulation (LES). For instance, Kai *et al.* [226] introduce correction terms tied to mixture fraction and progress variable interdependence. In a recent study, the model from Regele *et al.* [124] is extended to LES, including Soret effects, and is applied to the simulation of a slot burner configuration [225]. The model in [134] was successfully employed in [133] for LES analysis of a hydrogen/methane/air stratified flame adopting a thickened flame model with flamelet tabulated chemistry. These models were observed to successfully capture thermodiffusive instabilities, superadiabatic temperatures, and species/enthalpy redistributions at resolved scales [225–227].

In LES, the cell sizes are typically on the order of the laminar flame thickness. Since curvature length scales relevant to thermodiffusive instabilities are also of this order, part of the flame front self-wrinkling can be resolved. Still, phenomena like focusing effects, surface generation, and stretch response may occur at subgrid scales. In [39] the challenges associated to the non linear growth of TD instabilities from subgrid scales to resolved scales, through a reverse cascade process, are remarked. As such, ongoing research focuses on modelling the effect of sub-filter flame surface generation, stretch,

and TD instability growth for the LES framework [228].

Models employing detailed chemistry can address the effects of differential diffusion [44, 229, 230], since diffusion coefficients can be computed locally based on local temperature and composition, like in DNS. In thickened flame models with detailed chemistry the mixture fraction and enthalpy redistribution due to coupling of differential diffusion and curvature can be captured at the resolved level [44]. However, the dynamics of thermodiffusive instabilities are strongly influenced by the thickening factor, which can alter the local balance between convective and diffusive transport (i.e. stretch effect in sub-unity Lewis number conditions) [227, 231].

The discussion presented so far indicates that accounting for differential diffusion and thermodiffusive instabilities is crucial for the development of accurate models for turbulent hydrogen combustion. The correction strategies developed in [124] and [125] represent a promising approach for the inclusion of differential diffusion within flamelet models. In the present research, these two approaches are extended within flamelet based LES with presumed FDF framework, incorporating prefiltering of the correction terms. Their performance is evaluated on two reference cases: a thermodiffusively unstable premixed hydrogen flame [53], and a partially premixed lifted flame. Furthermore, the model proposed in [125] is applied to more complex configurations, including a bluff-body stabilized flame, characterized by high strain, and a swirl-stabilized combustor developed at TU Delft.

3

METHODOLOGY

In this chapter the details of the combustion models and subgrid closures employed for the LES presented in the thesis are discussed. The specific numerical details about solver, discretization schemes and chemistry modelling are given separately for each simulation presented in Parts I and II.

3.1. EULERIAN STOCHASTIC FIELDS

In Chapter 5 two combustion models, both based on the transported FDF with Eulerian stochastic fields (ESF) approach, are employed for the simulation of the partially premixed lifted hydrogen flame studied in [77], see Chap. 4. The first consists in the standard formulation with fully detailed chemistry, where a transport equation is solved for each species [110, 111]. In the second approach, similar to the one adopted in [232], a flamelet generated manifold (FGM) is instead used to represent the thermochemical states [105]. The FGM is parametrized in terms of the Bilger's mixture fraction z [139, 140] and a normalised progress variable c , defined as $c = (Y_{\text{H}_2\text{O}} - Y_{\text{H}_2\text{O},\text{b}})/(Y_{\text{H}_2\text{O},\text{b}} - Y_{\text{H}_2\text{O},\text{u}})$, for which transport equations are solved.

3.1.1. TURBULENCE-FLAME INTERACTION MODEL

The effect of turbulence on chemistry at the sub-grid level is described using a transported filtered density function (TFDF). Here, Φ denotes the composition vector of the N_α thermochemical variables ϕ_α (or controlling variables in the FGM case) and Ψ is the sample space of the values it can assume. From the fine grained (or marginal) probability density function PDF $P(\Psi; \mathbf{x}, t)$, representing the probability of finding composition vector within a certain state in one realization of the flow [233], the Favre-filtered sub-grid joint density function at a certain location \mathbf{x} and time t is defined by the convolution of a given LES filter G as in [232, 234]:

$$\tilde{P}(\Psi; \mathbf{x}, t) = \int_{\mathcal{V}} \frac{\rho(\mathbf{x} - \mathbf{x}')}{\bar{\rho}} P(\Psi; \mathbf{x}', t) G(\mathbf{x} - \mathbf{x}') d\mathbf{x}'. \quad (3.1)$$

This equation describes the probability of the composition vector Φ to be found in the sample $\Psi + d\Psi$ of its possible realizations within the LES filter volume \mathcal{V} . A transport equation for the FDF can be written as in [104, 235]:

$$\begin{aligned} \frac{\partial \bar{\rho} \tilde{P}}{\partial t} + \frac{\partial \bar{\rho} \tilde{u}_j \tilde{P}}{\partial x_j} + \sum_{\alpha=1}^{N_\alpha} \frac{\partial}{\partial \psi_\alpha} (\dot{\omega}_\alpha \tilde{P}) &= \\ = \frac{\partial}{\partial x_j} \left[\left(\frac{\bar{\rho}}{\rho D} + \frac{\mu_t}{Sc_t} \right) \frac{\partial \tilde{P}}{\partial x_j} \right] - \sum_{\alpha=1}^{N_\alpha} \sum_{\beta=1}^{N_\beta} \frac{\partial^2}{\partial \psi_\alpha \partial \psi_\beta} \left(\frac{\bar{\rho}}{\rho D} \frac{\partial \phi_\alpha}{\partial x_i} \frac{\partial \phi_\beta}{\partial x_i} \Big|_{\phi=\Psi} \tilde{P} \right), \end{aligned} \quad (3.2)$$

where sub-grid turbulent transport has been modelled by standard gradient hypothesis, analogously to Eq. 2.59, with the SGS Schmidt number Sc_t taken equal to 0.7 in the presented analysis, and being $\mu_t = \bar{\rho} \nu_{SGS}$ the SGS dynamic viscosity. The reaction rates $\dot{\omega}_\alpha$ of species or progress variable do not need closure and can be directly computed from chemical kinetics or retrieved from the flamelets database. The last term in the equation is the micro-mixing term, which needs closure [111, 232].

However, the high dimensionality of the FDF makes the deterministic solution of the transport equation not viable. Instead, a Monte Carlo simulation approach is used to recover the statistical moments of the thermochemical quantities or controlling variables following the ESF approach [110, 111, 234, 236], as described next. A series of $n = 1, 2, \dots, N$ Eulerian stochastic fields ζ_α^n is defined to represent possible values of each of the N_α thermochemical variables. A transport equation for each stochastic field is solved to reconstruct the pointwise time evolution of the subgrid moments by defining a stochastic system with statistics congruent to the ones described by Eq. (3.2). Applying Itô integration formalism, as described in [110, 236], the stochastic partial differential equations governing the stochastic fields take the form:

$$\begin{aligned} \bar{\rho} d\zeta_\alpha^n + \frac{\partial (\bar{\rho} \tilde{u}_j \zeta_\alpha^n)}{\partial x_j} dt &= \\ \frac{\partial}{\partial x_j} \left(\left(\frac{\bar{\rho}}{\rho D} + \frac{\mu_t}{Sc_t} \right) \frac{\partial \zeta_\alpha^n}{\partial x_j} \right) dt + \bar{\rho} \left(\frac{2\mu_t}{\bar{\rho} Sc_t} \right)^{1/2} \frac{\partial \zeta_\alpha^n}{\partial x_j} dW_j^n - \frac{\bar{\rho}}{2\tau_{SGS}} (\zeta_\alpha^n - \tilde{\phi}_\alpha) dt + \dot{\omega}_\alpha^n (\zeta_\alpha^n) dt. \end{aligned} \quad (3.3)$$

In the previous equation, the second-last term on the right hand side is the micro-mixing term modelled by Interaction by Exchange with the Mean (IEM) approach. Here, the subgrid mixing time scale is modelled as $\tau_{SGS} = \Delta^2 / (C_d \nu_{SGS})$ being Δ the LES filter size and $C_d \approx 2$ a model constant [111]. The second term on the right hand side of Eq. 3.3 is the stochastic term, which makes the fields non-differentiable in time, while they are differentiable in space. It contains increments of a Wiener process vector representing brownian motion, approximated as $dW_j^n = \gamma_j \sqrt{dt}$, where $\gamma_j = \{-1, 1\}$ is a random dichotomic vector. The Wiener process vector is homogeneous in space but different for each field. Each component $j = 1, 2, 3$ of the random vector follows a normal distribution in time with zero mean and variance equal to the time increment Δt . The stochastic term is also proportional to the subgrid turbulent viscosity and the local resolved spatial gradient of the considered stochastic field. Following the discussion in [110, 111] the stochastic term only contains a contribution of subgrid viscosity, and not molecular viscosity, in order to avoid the action of stochastic fluctuations in regions of laminar flow or

of high grid resolution. Adopting the Itô formulation, the stochastic term is evaluated at the beginning of each time step.

Finally, the filtered value of each thermochemical quantity ϕ_α , also necessary for the IEM model, can thus be reconstructed from the stochastic fields as $\tilde{\phi}_\alpha = \frac{1}{N} \sum_{n=1}^N \zeta_\alpha^n$. Similarly, its subgrid variance is computed as $\phi_{\alpha,SGS} = \frac{1}{N} \sum_{n=1}^N (\zeta_\alpha^n - \tilde{\phi}_\alpha)^2$

It can be noted that the unity Lewis number assumption is adopted in the derivation of the equation so that a diffusion coefficient equal to the thermal diffusivity $D = \alpha$ is employed for every species. Alternative closures for the inclusion of non-unity Lewis number effect in the TPDF have been proposed and applied for example in [229, 237, 238] where the mixing model is modified and a specific diffusion coefficient D_α is used for each thermochemical variable. However, differential diffusion modelling in the ESF context is beyond the scope of the present thesis, where models for non-unity Lewis number effects are investigated only within the flamelet/presumed FDF approach, as detailed in the next subsection.

3.2. FLAMELETS WITH PRESUMED FDF

The majority of LES are carried out in the present work through the flamelet model with presumed FDF developed in [89, 121, 239–241] and tested on hydrocarbon turbulent flames at different conditions. In the present study, the model is employed for the first time in the analysis of turbulent hydrogen flames. Two differential diffusion models are implemented in the baseline code and tested, as introduced later. The baseline model is further extended with strategies for the prediction of NO formation and transport and the inclusion of heat loss effect on the reaction rate.

3.2.1. BASELINE MODEL

Flamelet based models rely on the assumption that the smallest turbulent eddies can stretch and wrinkle the flame front but are not able to affect the inner flame structure. All the thermochemical states in the reacting mixture can thus be described by a series of 1D laminar flamelets, whose structure is computed *a priori*, using a reduced number of controlling variables, significantly decreasing the number of scalars transported in LES [135]. It was shown in many past works [112, 220] that in the context of LES the flamelet assumption holds for a wide range of combustion regimes, including relatively high Karlovitz numbers. This is because at high Karlovitz numbers the turbulent flame can still be seen as an ensemble of locally thin laminar flames distributed in space, where the wrinkling effect and broadening of the flame brush due to turbulence is modelled statistically.

In the present study the chemical database is built on a set of unstrained 1D premixed flamelets parametrised on a progress variable c and spanning the flammability range for different values of mixture fraction z [139]. The mixture fraction is defined according to Bilger's definition [139]. The reaction progress is estimated using a scaled progress variable. Following previous works [89, 184, 220, 242], the sum of CO₂ and CO is used in the present study when the fuel is a hydrocarbon, and the mass fraction of water vapour is used when the fuel is hydrogen. This choice guarantees a monotonic behaviour of the progress variable as the reaction progresses, at least for the cases under

investigation, which is essential for the correct behaviour of the flamelet modelling

When differential diffusion is not taken into account and unity Lewis number is assumed for every species, the Favre-filtered mixture fraction \tilde{z} is a passive scalar describing the fuel and oxidiser streams mixing and its Favre-filtered transport equation is:

$$\bar{\rho} \frac{D\tilde{z}}{Dt} = \nabla \cdot \left[\left(\overline{\rho D} + \frac{\mu_t}{Sc_t} \right) \nabla \tilde{z} \right]. \quad (3.4)$$

The filtered molecular mass diffusion coefficient is defined as $\overline{\rho D} = \tilde{\mu}/Sc$, where Sc is the laminar Schmidt number. The subgrid flux of z is modelled through standard gradient hypothesis where the SGS viscosity, μ_t , is defined by the turbulence model, and $Sc_t = Sc = 0.7$ is the SGS Schmidt number. Similarly, the transport equation for the filtered progress variable \tilde{c} yields:

$$\bar{\rho} \frac{D\tilde{c}}{Dt} = \nabla \cdot \left[\left(\overline{\rho D} + \frac{\mu_t}{Sc_t} \right) \nabla \tilde{c} \right] + \bar{\omega}_c. \quad (3.5)$$

The filtered reaction rate $\bar{\omega}_c$ in the above equation is expressed by means of the joint subgrid filtered density function FDF $P(c, z)$ as [92, 104, 137, 241]

$$\bar{\omega}_c(\tilde{c}, \tilde{z}, \sigma_c^2, \sigma_z^2) = \bar{\rho} \int_0^1 \int_0^1 \frac{\dot{\omega}_c(c, z)}{\rho(c, z)} P(c, z; \tilde{c}, \tilde{z}, \sigma_c^2, \sigma_z^2) dc dz + \bar{\omega}_{np}. \quad (3.6)$$

where the progress variable reaction rate $\dot{\omega}_c(c, z)$ within the integral is taken from 1D laminar flamelets computation. A Beta distribution is chosen to describe the joint FDF $P(c, z)$ following previous studies [107, 109] and given the good performance observed in regimes similar to those investigated in the present study [241, 243]. Under the assumption of statistical independence at the SGS level between the controlling variables, the joint FDF is then expressed as the product of two distinct FDFs [104, 106, 136, 211], $P(c, z; \tilde{c}, \tilde{z}, \sigma_c^2, \sigma_z^2) \approx P(c; \tilde{c}, \sigma_c^2) P(z; \tilde{z}, \sigma_z^2)$, which was shown to be reasonable for well resolved LES [92, 104, 211]. The integral in Eq. 3.6 is computed a priori and tabulated for values of $\tilde{c} \in [0, 1]$, filtered mixture fraction within the flammability range $\tilde{z} \in [z_{lean}, z_{rich}]$, and $\sigma_c^2 \in [0, \tilde{c}(1 - \tilde{c})]$, $\sigma_z^2 \in [0, \tilde{z}(1 - \tilde{z})]$, where the second term represent the limit where the controlling variable subgrid distribution becomes bi-modal.

The term $\bar{\omega}_{np}$ results from the use of a scaled progress variable and the dependence of the scaling factor $\psi_{max}(z)$ on the mixture fraction. It represents a correction due to non-premixed mode and is defined as [89, 240]:

$$\bar{\omega}_{np}(\tilde{z}, \sigma_z^2) = \bar{\rho} \tilde{c} \tilde{\chi}_z \int_0^1 \frac{1}{\psi_{max}(z)} \frac{d^2 \psi_{max}(z)}{dz^2} P(z; \tilde{z}, \sigma_z^2) dz. \quad (3.7)$$

where $\tilde{\chi}_z = \tilde{D} \nabla \tilde{z} \cdot \nabla \tilde{z} + \tilde{\epsilon}_z$ is the sum of resolved and SGS scalar dissipation rate (SDR) of mixture fraction, and the subgrid part is modelled using linear relaxation as $\tilde{\epsilon}_z = c_z (v_t / \Delta^2) \sigma_z^2$, with $c_z \approx 2$ [103] and $\Delta = \mathcal{V}^{1/3}$, \mathcal{V} being the volume of the local cell in the computational mesh. The integral on the RHS is precomputed and tabulated.

The shape of the Beta distribution depends on filtered value of the controlling variables (\tilde{c} or \tilde{z}) and their subgrid variance (σ_c^2 or σ_z^2), which are computed by solving their

transport equations. For the subgrid variance of the mixture fraction the transport equation reads:

$$\bar{\rho} \frac{D\sigma_z^2}{Dt} = \nabla \cdot \left[\left(\bar{\rho} \bar{D} + \frac{\mu_t}{Sc_t} \right) \nabla \sigma_z^2 \right] - 2\bar{\rho} \tilde{\varepsilon}_z + 2 \frac{\mu_t}{Sc_t} (\nabla \tilde{z} \cdot \nabla \tilde{z}), \quad (3.8)$$

where on the LHS is the material derivative. On the RHS the first term includes molecular diffusive transport and subgrid flux closed through standard gradient hypothesis. The second term represent the destruction mixture fraction subgrid variance, containing the mixture fraction subgrid scalar dissipation rate $\tilde{\varepsilon}_z$, modelled as previously described. The last term represent the subgrid variance generation by interaction between subgrid turbulent flux and resolved mixture fraction z gradient.

The transport equation of the progress variable subgrid variance yields:

$$\bar{\rho} \frac{D\sigma_c^2}{Dt} = \nabla \cdot \left[\left(\bar{\rho} \bar{D} + \frac{\mu_t}{Sc_t} \right) \nabla \sigma_c^2 \right] - 2\bar{\rho} \tilde{\varepsilon}_c + 2 \frac{\mu_t}{Sc_t} (\nabla \tilde{c} \cdot \nabla \tilde{c}) + 2(\overline{c\dot{\omega}_c} - \tilde{c}\dot{\omega}_c), \quad (3.9)$$

containing the same terms as in Eq. 3.8 with the extra term (last term on RHS) describing a source/sink of subgrid variance due to chemical processes. The source term $c\dot{\omega}_c$ is computed consistently to Eq. (3.6) and tabulated. The progress variable SGS scalar dissipation rate $\tilde{\varepsilon}_c$ cannot be modelled through linear relaxation as for the mixture fraction, and its treatment is discussed in details in the next section.

Enthalpy \tilde{h} is not used as additional controlling variable, as often done in problems including minor heat losses [134], but its filtered transport equation Eq. 2.53 is still resolved to capture multi stream mixing. Moreover, the absolute enthalpy is employed to compute the filtered temperature, using the theorem of the integral mean as done in previous works (e.g. see [89]): $\tilde{T} = T_0 + (\tilde{h} - \Delta \tilde{h}_f^0) / \widehat{C}_p^{eff}$, where $T_0 = 298.15$ K is the reference temperature. The enthalpy of formation Δh_f^0 and the effective specific heat at constant pressure of the mixture $\widehat{C}_p^{eff} = \int_{T_0}^T C_p(T') dT' / (T - T_0)$ are computed from the 1D laminar flamelets. The filtered values of these quantities are obtained through pre-integration consistently with Eq. (3.6) and tabulated. The mixture density is then calculated enforcing the ideal gas equation of state $\bar{\rho} = p_o \widehat{W} / R_0 \tilde{T}$, where the filtered mixture molecular weight \widehat{W} is also computed from the 1D flamelets, pre-integrated and tabulated, and p_o is the operative pressure.

3.2.2. DYNAMIC MODELLING OF SCALAR DISSIPATION RATE

The progress variable SGS scalar dissipation rate (SDR), $\tilde{\varepsilon}_c$, was shown to be a critical parameter for the correct estimation of σ_c^2 . This term represents the unresolved part of the filtered SDR, \tilde{N}_c , defined as:

$$\bar{\rho} \tilde{N}_c = \bar{\rho} \widetilde{D}_c (\nabla \tilde{c} \cdot \nabla \tilde{c}) + \bar{\rho} \tilde{\varepsilon}_c, \quad (3.10)$$

where ρ is the mixture density and \widetilde{D}_c is the filtered diffusion coefficient of \tilde{c} . Overbar and tilde symbols refer respectively to simple and Favre filtered operations. Models for $\tilde{\varepsilon}_c$ are commonly proportional to the SGS variance and can be written in general form as:

$$\tilde{\varepsilon}_c = f_1 \sigma_c^2 / \beta_c, \quad (3.11)$$

where β_c is a modelling constant and f_1 is a function that depends on turbulence and combustion parameters. Past works have shown that this function needs to account for the dissipation of both SGS turbulent and reactive processes and therefore simple approaches such as the linear-relaxation model are not suitable for this quantity [239]. In the present study the model originally proposed in [244] and then adapted for LES in [89, 102, 239]. The model constant β_c depends on flame curvature, diffusion and reaction processes, and is generally scale-dependent. Its choice is of crucial importance to obtain the correct estimation of SGS variance. Thus, while the use of a static value of the combustion constant may lead to good results, it requires an accurate preliminary tuning. Furthermore, the value might need to change in space and time for cases where the aforementioned processes or the numerical mesh (thus the LES filter) is not homogeneously distributed, and for such cases a single constant value might not be suitable.

The subgrid SDR of c in Eq. (3.9) is modelled with Eq. (3.11), where f_1 is computed as in [89, 244–246]

$$f_1 = \left[1 - \exp\left(\frac{-0.75\Delta}{\delta_L^0}\right) \right] \left[(2K_c - \tau C_4) \frac{S_L^0}{\delta_L^0} + C_3' \frac{\varepsilon_k}{k} \right]. \quad (3.12)$$

In the above equation S_L^0 , δ_L^0 are respectively laminar flame speed and thermal thickness, while $\tau = (T_b - Y_u)/T_u$ is the heat release factor. These quantities depend on mixture fraction and are obtained from flamelets calculations and tabulated. The term Δ is the local filter width, k and ε_{SGS} are the local SGS turbulent kinetic energy and its dissipation rate, computed according to the SGS turbulence model. The other parameters, i.e. K_c , C_4 and C_3' , are not tunable and they are functions of the local laminar flame properties, grid refinement and turbulence properties; more information can be found in [89, 102, 121].

The value of the model constant β_c in Eq. (6.1) might vary in space depending on the local flow conditions. In such cases dynamic approaches can be used to avoid the fine-tuning of the modelling constant. Dynamic approaches have been employed in LES as an effective method to model subgrid quantities and are based on the scale similarity assumption [93]. These methods have been largely used for non reacting flows to model the subgrid stress tensor through the knowledge of the neighbouring smallest resolved scales (Germano's identity) [96]. The concept of similarity between the smallest resolved scale and the unresolved scales comes in this case from the argument of the turbulence cascade within the inertial range of the turbulent kinetic energy (TKE) spectrum, and is enforced in the LES by the use of a test filter width about twice that of the smallest resolved scale. In case of reacting flows the application of such procedures is less trivial due to the energy release by the flame at the small scales. Nevertheless, the applicability of scale-similarity was shown to still hold for a number of different modelling approaches including flame wrinkling, flame surface density, and scalar dissipation rate [98, 102, 177, 203–205, 247].

A dynamic procedure for the modelling of the subgrid scalar dissipation rate is employed here, following previous works e.g. [102]. By indicating the filtered scalar dissipation rate of c with $\tilde{N}_c \equiv \bar{D}_c \nabla c \cdot \nabla c = \bar{D}_c \nabla \tilde{c} \cdot \nabla \tilde{c} + \tilde{\varepsilon}_c$, the application of scale similarity to

the next (test-filter) scale reads

$$\widehat{\rho} \widehat{N}_c - \widehat{\rho} \widehat{D}_c \nabla \widehat{c} \cdot \nabla \widehat{c} = \widehat{\rho} f_1(\mathbf{q}) \frac{\widehat{\sigma}_c^2}{\widehat{\beta}_c}, \quad (3.13)$$

where $f_1(\mathbf{q})\sigma_c^2/\beta_c$ is the functional form used for $\tilde{\varepsilon}_c$, the the symbol $\widehat{\cdot}$ indicates the (Favre) test-filter operation and $\mathbf{q} \equiv (k, \varepsilon_k, \Delta, \dots)$ is the entire set of spatially-varying parameters to which f_1 depends on. By using Germano's identity, the left-hand side of above equation can be rewritten as:

$$\begin{aligned} & \left(\overline{\widehat{\rho} \widehat{D}_c \nabla \widehat{c} \cdot \nabla \widehat{c}} + \overline{\widehat{\rho} f_1(\mathbf{q}) \frac{\widehat{\sigma}_c^2}{\widehat{\beta}_c}} - \overline{\widehat{\rho} \widehat{D}_c \nabla \widehat{c} \cdot \nabla \widehat{c}} \right) + \left(\overline{\widehat{\rho} \widehat{D}_c \nabla \widehat{c} \cdot \nabla \widehat{c}} - \widehat{\rho} \widehat{D}_c \nabla \widehat{c} \cdot \nabla \widehat{c} \right) \\ & = \overline{\widehat{\rho} f_1(\mathbf{q}) \frac{\widehat{\sigma}_c^2}{\widehat{\beta}_c}} + \left(\overline{\widehat{\rho} \widehat{D}_c \nabla \widehat{c} \cdot \nabla \widehat{c}} - \widehat{\rho} \widehat{D}_c \nabla \widehat{c} \cdot \nabla \widehat{c} \right). \end{aligned} \quad (3.14)$$

At this point β_c can be found in two ways. In the first case, one assumes that it is scale-invariant, i.e. $\widehat{\beta}_c = \beta_c$, and the equation can be solved explicitly as

$$\beta_c = \frac{b - a}{L} = \frac{\overline{\widehat{\rho} f_1 \sigma_c^2} - \widehat{\rho} \widehat{f}_1 \widehat{\sigma}_c^2}{\widehat{\rho} \widehat{D} \nabla \widehat{c} \cdot \nabla \widehat{c} - \overline{\widehat{\rho} \widehat{D} \nabla \widehat{c} \cdot \nabla \widehat{c}}}, \quad (3.15)$$

where the parameters $b = \overline{\widehat{\rho} f_1 \sigma_c^2}$, $a = \widehat{\rho} \widehat{f}_1 \widehat{\sigma}_c^2$ and $L = \widehat{\rho} \widehat{D} \nabla \widehat{c} \cdot \nabla \widehat{c} - \overline{\widehat{\rho} \widehat{D} \nabla \widehat{c} \cdot \nabla \widehat{c}}$ have been introduced for simplicity. On the other hand, the assumption of scale-invariance might be too restrictive as β_c was found in previous studies to actually depend on the filter size, as discussed earlier. As an alternative, one can relax this assumption by rewriting Eq. (3.13) as:

$$\widehat{\beta}_c = - \frac{a}{L - b/\beta_c} = - \frac{\widehat{\rho} \widehat{f}_1 \widehat{\sigma}_c^2}{\left(\widehat{\rho} \widehat{D} \nabla \widehat{c} \cdot \nabla \widehat{c} - \overline{\widehat{\rho} \widehat{D} \nabla \widehat{c} \cdot \nabla \widehat{c}} \right) - \overline{\widehat{\rho} f_1(\mathbf{q}) \frac{\widehat{\sigma}_c^2}{\widehat{\beta}_c}}}. \quad (3.16)$$

The above equation needs an estimation for β_c on the right-hand side of the equation, which is usually taken in LES solvers from the previous time step or the previous iteration (if more than one per time step). On the other hand, a minimum number of iterations is required for the iterative process to converge, which limits the application of this method.

TEST FILTER DEFINITION

Another issue related to the applications of Eqs. (3.15) and (3.16) is that a test filter has to be chosen. In the context of non-reactive simulations with eddy-viscosity type closures it was shown that the LES filter is similar to a Gaussian filter when the LES is well resolved (minimal influence of mesh), and approaches a box filter as the mesh coarsens [93]. The choice of the test filter has of course impact on the calculation of the β_c parameter. In the present study an algebraic and a differential filter are compared. The test-filtering

operation on the general, spatially-varying quantity ϕ is described by the following convolution operation

$$\hat{\phi}(x) = \int_{\mathcal{V}} \phi(x') \mathcal{F}(x - x') dx', \quad (3.17)$$

where \mathcal{V} is the integration volume and \mathcal{F} is the test filter function. In the algebraic case, the test filter is obtained by imposing a shape function (usually a Gaussian shape) of a certain width, taken to be twice the LES filter width in the present work. After discretisation the above integral assumes the general form:

$$\hat{\phi} = \frac{\sum_k A_k^f \phi_k^f}{\sum_k A_k^f}, \quad (3.18)$$

where A_k^f are weight coefficients evaluated on the numerical cell and its surrounding cells. The issue with this formulation is that the evaluation of both coefficients A_k^f and function values ϕ_k^f is subject to interpolation errors, which may become particularly relevant on unstructured meshes [209].

Following [209, 248] the convolution within the filtering operation can be expanded in series of Taylor around the value at point x . Without loss of generalities, for the one-dimensional case and assuming a symmetric filter, this would read as

$$\hat{\phi}(x, t) = \phi(x, t) + \frac{\hat{\Delta}^2}{24} \frac{\partial^2}{\partial x^2} \phi(x, t) + \mathcal{O}(\Delta^4). \quad (3.19)$$

Similarities with the Fourier diffusion differential equation can be noted, and this filtering approach is therefore termed as differential filter. Solving this equation directly can however lead to numerical instabilities (Pseudo Fourier conditions). In the present work, it is proposed to solve this equation implicitly in the finite volumes framework within the time marching integration. In order to do so, the quantity $\hat{\phi}(x, t)$ can be seen as the solution of the following differential equation:

$$\frac{d\hat{\phi}(\mathbf{x}, t)}{dt} = \frac{\hat{\Delta}_x^2}{6\Delta_t} \nabla^2 \hat{\phi}(\mathbf{x}, t). \quad (3.20)$$

where Δ_t is the LES time step, and $\hat{\Delta} = 2\Delta_x$ has been used, with $\Delta_x = \mathcal{V}^{1/3}$ being the LES filter width estimated as the cubic root of the local cell volume \mathcal{V} . Equations (3.19) and (3.20) are equivalent to the third order if the latter is solved with an implicit Euler time marching scheme. The advantage of solving the differential equation is that it can be embedded within the finite volume framework therefore minimizing the noise produced by interpolation errors, at the cost of additional computational effort. In Chap. 6, results obtained from the algebraic test filter and differential test filtering approaches are discussed and compared.

3.2.3. DIFFERENTIAL DIFFUSION MODELLING

In the LES framework, a correction of the controlling variables diffusive transport is necessary to account for differential diffusion effects, as local equivalence ratio redistribu-

tion and flame curvature are coupled at the resolved scales. Two models originally developed for DNS of laminar flames are extended here for a turbulent LES case in the context of presumed FDF closure.

DIFFERENTIAL DIFFUSION MODEL M1

The first differential diffusion model, proposed in [124], consists in deriving a correction for the mixture fraction transport equation only. This model assumes equal mass diffusivity for all species and heat $D_k = D = \alpha$, except for hydrogen, whose Lewis number is taken to be $Le_{H_2} = 0.3$. Starting from the exact definition of hydrogen and oxygen diffusive fluxes, including the diffusion correction velocity as in Sec. 2.1.2, a corrected diffusion flux for the mixture fraction is derived and included in the transport equation as follows:

$$\rho \frac{Dz}{Dt} = \nabla \cdot (\rho D_z \nabla z) + \dot{\omega}_z, \quad (3.21)$$

where a modified diffusion coefficient D_z and a source term $\dot{\omega}_z$ appear. With respect to the definition in [124], the correction terms are here reformulated to be compatible with the use of a scaled progress variable:

$$\dot{\omega}_z = -\nabla \cdot \left[\rho D \left(\frac{1}{s+1} \right) \left(\frac{1}{Le_{H_2}} - 1 \right) (1-z) \nabla (c\psi_{\max}) \right]. \quad (3.22)$$

where s is the oxygen to fuel stoichiometric mass ratio. It can be seen how this additional term acts as a source or sink across the flame front through its dependence on the gradient of c and it was observed to yield the correct local equivalence ratio redistribution across the resolved flame front [124]. The term D_z is defined as:

$$D_z = D \left[1 + \left(\frac{1}{Le_{H_2}} - 1 \right) (1-z) \right]. \quad (3.23)$$

This expression ensures a correction in the diffusion coefficient also in non-reacting regions, thus accounting for the higher diffusivity of H_2 in mixing processes. Equation (3.21) must be Favre-filtered to be solved in the LES context, which is done in the present work as follows. The ‘uncorrected’ mass diffusivity D , taken equal to the heat diffusivity, is pre-integrated and tabulated in a manner similar to Eq. (3.6). Additional terms arise due to subgrid correlations, for example between the mixture fraction and the gradient of progress variable. Therefore two implementation strategies are here proposed and compared. In one case an approach similar to [249] is adopted, where the value of $\dot{\omega}_z(c, z)$ is obtained within the laminar flamelets, by computing the differential operators appearing in Eq. 3.22 as one dimensional derivatives along the flamelet in physical space. The term $\dot{\omega}_z(c, z)$ is thus pre-integrated consistently with Eq. (3.6) to obtain the filtered mixture fraction source term $\tilde{\omega}_z$, and tabulated. This implementation is termed as M1_{TAB} in the present work. The other approach, referred to as M1_{RES}, consists in implementing Equation (3.22) directly in the LES transport equation. This implies neglecting the subgrid correlations and only considering resolved filtered quantities (e.g. \tilde{z} , $\nabla \tilde{c}$) for the calculation of $\tilde{\omega}_z$. As remarked in [39] this assumption is weaker in lean cases where the term $(1-z)$ is close to unity.

DIFFERENTIAL DIFFUSION MODEL M2

The second differential diffusion model considered in this work was proposed in [250] and more recently reformulated in [125]. This approach is based on the expression of the controlling variables as a linear combination of the species:

$$\begin{aligned} c &= \sum_i^{N_s} \mathcal{C}_i Y_i, \\ z &= \sum_i^{N_s} z_i Y_i, \end{aligned} \quad (3.24)$$

where N_s is the total number of species, and \mathcal{C}_i and z_i are constant coefficients for every species. For each species i , Le_i is assumed to be non-unity, but constant along the flamelet. The molecular diffusion fluxes of the controlling variables are therefore expressed as:

$$\begin{aligned} \mathbf{j}_c &= -\frac{\lambda}{C_p} \nabla \left(\sum_{i=1}^{N_s-1} \frac{\mathcal{C}_i - \mathcal{C}_{N_s}}{Le_i} Y_i \right) = -\frac{\lambda}{C_p} \nabla \beta_c, \\ \mathbf{j}_z &= -\frac{\lambda}{C_p} \nabla \left(\sum_{i=1}^{N_s-1} \frac{z_i - z_{N_s}}{Le_i} Y_i \right) = -\frac{\lambda}{C_p} \nabla \beta_z, \end{aligned} \quad (3.25)$$

where \mathcal{C}_{N_s} is the coefficient of the most abundant species, N_2 for the present study. With reference to Sec. 2.1.2, this approach guarantees mass conservation in the computation of the diffusive fluxes, The above equations take thus the form of diffusive transport terms depending on the gradient of the β_c and β_z parameters. The diffusive behaviour of all species in the LES can now be taken into account by tabulating the additional parameters β_c , β_z and the λ/C_p ratio. In the definition employed here, the progress variable only depends on water and it is scaled, so that $\mathcal{C}_{\text{H}_2\text{O}} = 1/\psi_{\text{max}}(z)$ and $\mathcal{C}_i = 0$ for every other species. For the jet-in-coflow partially premixed case, water is also present in the reactants. Therefore, considering the definition in Eq. 2.27, the expression for β_c becomes:

$$\beta_c = \frac{Y_{\text{H}_2\text{O}} - Y_{\text{H}_2\text{O}}^{\text{reac}}}{Le_{\text{H}_2\text{O}} \psi_{\text{max}}(z)} \quad (3.26)$$

A similar procedure is followed for the enthalpy equation, where the heat flux \mathbf{q} can be written as:

$$\mathbf{q} = -\lambda \nabla T - \left(\sum_{i=1}^{N_s-1} (h_i - h_{N_s}) \frac{1}{Le_i} \frac{\lambda}{C_p} \nabla Y_i \right) \quad (3.27)$$

where h_i is the enthalpy of species i . In the above equation, the first term on the right-hand side is the conductive flux, while the second term describes the redistribution of enthalpy associated with the different diffusion of species. Following the derivation in [125] the above equation can be rewritten as:

$$\begin{aligned} \mathbf{q} &= -\frac{\lambda}{C_p} \left(C_p - \sum_{i=1}^{N_s-1} \frac{C_{p_i} - C_{p_{N_s}}}{Le_i} Y_i \right) \nabla T - \frac{\lambda}{C_p} \nabla \left(\sum_{i=1}^{N_s-1} \frac{h_i - h_{N_s}}{Le_i} Y_i \right) = \\ &= -\frac{\lambda}{C_p} \beta_{h_1} \nabla T - \frac{\lambda}{C_p} \nabla \beta_{h_2}, \end{aligned} \quad (3.28)$$

where C_{p_i} refers to the specific heat capacity at constant pressure of species i . The two terms on the right-hand side in the above equation represent differential diffusion effects on the heat flux due respectively to local redistribution of specific heat and enthalpy, and to the diffusion of species within the mixture. The final set of modified equations for control variables and enthalpy solved in the LES with model M2 is:

$$\begin{aligned}\frac{\bar{\rho}}{\rho} \frac{D\tilde{c}}{Dt} &= \nabla \cdot \frac{\mu_t}{Sc_t} \nabla \tilde{c} + \nabla \cdot \bar{\rho} \tilde{D} \nabla \tilde{\beta}_{c\phi} + \bar{\omega}_c, \\ \frac{\bar{\rho}}{\rho} \frac{D\tilde{z}}{Dt} &= \nabla \cdot \frac{\mu_t}{Sc_t} \nabla \tilde{z} + \nabla \cdot \bar{\rho} \tilde{D} \nabla \tilde{\beta}_z, \\ \frac{\bar{\rho}}{\rho} \frac{D\tilde{h}}{Dt} &= \nabla \cdot \left(\frac{\mu_t}{Pr_t} \right) \nabla \tilde{h} + \nabla \cdot (\bar{\rho} \tilde{D} \tilde{\beta}_{h_1} \nabla \tilde{T} + \bar{\rho} \tilde{D} \nabla \tilde{\beta}_{h_2}).\end{aligned}\quad (3.29)$$

The filtered coefficients $\tilde{\beta}_i$ and the filtered diffusivity \tilde{D} in the equations above are obtained from the flamelets computations, pre-integrated according to Eq. (3.6) and tabulated.

The model derived in [124] (from which M1 is adapted) was subsequently extended in [123] to incorporate mixture-averaged diffusion modelling [56], allowing for non-constant Lewis numbers for each species and including the Soret effect. Similarly, Mukundakumar *et al.* [125] demonstrated how their original model (from which model M2 was derived) can be extended to account for non-constant Lewis numbers, a diffusion correction velocity, and the Soret effect. In the present work, the primary focus is on the initial implementation of differential diffusion effects within a flamelet-based LES framework with presumed FDF, together with comparisons against the baseline model. Therefore, the original formulations of these models are retained in order to assess the sensitivity of the LES model to the differential diffusion (DD) modelling, isolating its effect from thermal diffusion. Extending the LES flamelet framework to relax the constant Lewis number assumption and to include Soret effects will be addressed in future work.

3.2.4. HEAT LOSS MODELLING

In flamelet models, the most common way to incorporate heat loss effects is by including enthalpy as a controlling variable [134, 135]. Laminar 1D flamelet manifolds can be built upon freely propagating flames at lower enthalpy, extinguishing flames, or burner-stabilized flames, where an enthalpy sink is imposed across the flame thickness [141]. Implementing this strategy would require the use of a total of five control variables (two filtered control parameters, their subgrid variances, and enthalpy). Since this approach is computationally demanding given the hyperdimensional flamelet database, and given that only an assessment of the impact of heat losses for a specific case (to be presented in Chap. 10.1) is needed for the scope of the present thesis, a different approach is proposed and followed here to account for heat losses in the reactive flow. This simplified model is developed to qualitatively analyse the sensitivity of flame topology to heat loss and estimate the combustor regions most affected by enthalpy reduction. Starting from flamelet manifolds at $T_u = 300$ K across different equivalence ratios, 1D simulations are

extended by varying the reactant temperature between $T_u = 200$ K–400 K, corresponding to approximately $\pm 50\%$ variations in flame enthalpy.

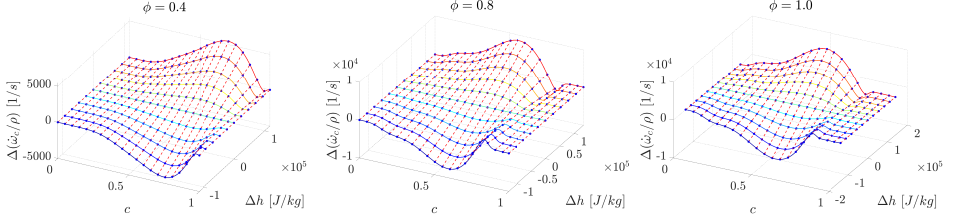


Figure 3.1: Third order polynomial fit of reaction rate variations $\Delta\dot{\omega}_c$ versus enthalpy variations Δh with respect to the reference case at $T_u = 300$ K, for different progress variable values c and reactants mixture z (equivalence ratio ϕ).

At each mixture fraction and progress variable value, the change in reaction rate relative to the $T_u = 300$ K reference case, $\Delta\dot{\omega}_c$, is evaluated. This variation is then expressed as a polynomial function of the enthalpy difference with respect to the reference manifold at $T_u = 300$ K using least-squares fitting of a third-order polynomial. An example of the fitting process is shown in Fig. 3.1 at three equivalence ratios (mixture fractions) for a fuel blend of CH_4 with 25% H_2 by volume. The reaction rate, evaluated from 1D flames, can be expressed as:

$$\dot{\omega}_c(c, z, h) = \dot{\omega}_c^{Ad}(c, z) + \Delta\dot{\omega}_c(c, z, \Delta h) \quad (3.30)$$

Here, the superscript Ad refers to the baseline manifold with reactants at 300K, and $\Delta h(z)$ is the enthalpy difference relative to the 300K case. In the absence of differential diffusion, this is only a function of the mixture fraction. The enthalpy-dependent variation in the reaction rate is approximated by:

$$\Delta\dot{\omega}_c(c, z, \Delta h) \approx A_h \Delta h^3 + B_h \Delta h^2 + C_h \Delta h \quad (3.31)$$

The polynomial coefficients are precomputed and integrated using the presumed FDF approach, consistently with Eq. 3.6. In the LES, the filtered enthalpy variation $\Delta\tilde{h}$ is calculated from the local filtered enthalpy \tilde{h} , obtained from a solved transport equation, and the reference enthalpy $\tilde{h}_{Ad}(\tilde{z})$, which is preintegrated and tabulated. The model is used with constant temperature boundary conditions at the wall, generating an enthalpy flux and a thermal boundary layer where $\Delta\tilde{h} < 0$.

This model shares similarities with the one proposed in [251], where the dependence of a certain variable (e.g. the reaction rate) on the enthalpy variations with respect to the adiabatic value is expressed as a Taylor expansion, whose coefficients are tabulated, without introducing additional control variables. It provides a rough estimate of heat loss impact on the reaction rate and is used here solely to evaluate flame anchoring sensitivity (or flashback) to non-adiabatic wall boundary conditions.

3.2.5. MODELLING OF NITROGEN OXIDE (NO) FORMATION

Modelling NO formation is particularly challenging due to its slow chemical timescale, orders of magnitude longer than fuel oxidation, and in practical perfectly premixed com-

bustors its emission levels are typically below the equilibrium value corresponding to the operating equivalence ratio, because of the short residence times compared to the NO chemical timescales. NO formation is highly sensitive to temperature (via the thermal NO_x mechanism) and local equivalence ratio, making it strongly affected by temperature fluctuations and composition inhomogeneities induced by turbulence as it forms. Since NO concentrations are much lower than major species, even small errors in temperature or composition can lead to significant prediction inaccuracies.

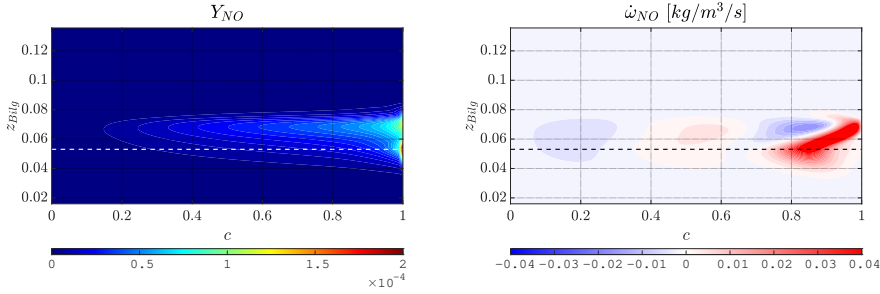


Figure 3.2: Left: NO mass fraction Y_{NO} in the mixture fraction and progress variable space $z_{Bilg} - c$ as computed from laminar unstretched 1D premixed flames with fuel blend 75%CH₄ - 25% H₂ in volume. Right: NO net reaction rate at the same conditions. Dashed line marks the stoichiometric condition

The difference in chemical time scales is a critical source of error when modelling NO in the flamelet framework. In fact, using the tabulated value at $c = 1$ (i.e., complete combustion) would correspond to NO at chemical equilibrium, leading to overprediction [135, 190]. However, NO formation via flamelet-based methods has been successfully modelled [252], with strategies such as unsteady flamelets proposed in [190]. Another key challenge lies in the selection of the kinetic mechanism, as validation often shows discrepancies from experimental data [44].

A common approach in the literature is to solve a transport equation for NO [135, 191], which enables decoupling from the main reaction progress and captures the impact of turbulence-induced fluctuations in temperature and composition on the slow NO formation process. To further decouple NO from the main flame structure, one could define a dedicated progress variable based on NO, or include NO in the definition of the existing progress variable [135]. This would enhance resolution in manifold regions where the main reaction has reached equilibrium ($c = 1$), but NO continues to form, i.e., $\dot{w}_{NO} \neq 0$.

In the present study, NO formation in the TUDelft swirl-stabilized combustor is investigated in Chapter 10. Preliminary simulations are performed using a thickened flame model as previously described, combined with the detailed GRI3.0 chemical mechanism [142], which allows to directly solve for the NO formation in details. In subsequent simulations using the in-house flamelet based LES model, an approach similar to that proposed in [191] is adopted. A filtered transport equation for \bar{Y}_{NO} is solved. As shown in Fig. 3.2, the NO reaction rate can exhibit both positive and negative values for a fuel blend of CH₄ with 25% H₂ by volume. This is due to its formation in different flame regions depending on the dominant pathway and its subsequent diffusion and oxidation

to NO_2 , which can result in negative net reaction rates [135, 253]. Therefore, following [191], the filtered NO reaction rate is expressed as:

$$\bar{\dot{\omega}}_{\text{NO}} = \bar{\dot{\omega}}_{\text{NO}}^+ + \frac{\bar{\dot{\omega}}_{\text{NO}}^-}{\bar{Y}_{\text{NO}}} \quad (3.32)$$

The terms $\bar{\dot{\omega}}_{\text{NO}}^+$ and $\bar{\dot{\omega}}_{\text{NO}}^-$ are precomputed from laminar flamelets using Eq. 3.6 and tabulated. Since the combustor operates under lean conditions, parametrizing NO production in terms of a progress variable defined on the major product species of the main combustion reaction, i.e. c based on H_2O or CO_2 , is acceptable, since, as shown in Fig. 3.2, NO formation ceases at high c values on the lean side and $\dot{\omega}_{\text{NO}} \rightarrow 0$ for $c \rightarrow 1$.

4

TEST CASES

Four laboratory-scale combustors are used as test cases for the validation and benchmarking of the numerical models. Each case is selected for its specific features to explore a range of combustion modes and turbulence conditions. Three turbulent hydrogen flames are considered: (1) a highly turbulent, partially premixed hydrogen flame; (2) a moderately turbulent, perfectly premixed hydrogen flame; and (3) a perfectly premixed, bluff-body-stabilized hydrogen flame. In addition, one bluff-body-stabilized methane flame is analyzed. Following validation on these canonical flames, the numerical models are applied to the laboratory-scale swirl-stabilized combustor at TU Delft, which is more representative of practical combustion chambers.

4.1. PARTIALLY PREMIXED FLAME

The first case study investigated is the partially premixed lifted hydrogen flame in hot coflow, studied experimentally by Cabra *et al.* [77]. The setup, sketched in Fig. 4.1 (a), consists of a central nozzle with an inner diameter D of 4.57 mm and an outer diameter of 6.35 mm, issuing a fuel mixture composed of 25% H_2 and 75% N_2 in volume. The bulk velocity of the fuel stream is 107 m/s, resulting in a Reynolds number of approximately $Re \sim 23'600$. A significant amount of turbulence develops in the shear region downstream the nozzle exit. The hot coflow is at a temperature of 1045 K and is composed by the products (H_2O , O_2 and N_2) of a lean H_2 /air flame at equivalence ratio $\phi = 0.25$. In [77] the mixture fraction z is defined according to Bilger's formulation [139], considering the main jet as fuel stream and the coflow as oxidizer stream, resulting in a value at stoichiometry of $z_{st} = 0.4741$. The flames producing the hot coflow are stabilized on a perforated plate with a diameter of 210 mm located 70 mm upstream of the central nozzle exit. The plate is confined by a collar, in order to prevent the entrainment of external air to interfere with the flame region. This way, the central jet is surrounded by a homogeneous coflow of known temperature and composition.

The fuel from the main jet mixes with the oxidizer provided by the lean hot coflow, resulting in a lifted flame, whose base stabilizes by turbulent premixed flame propagation

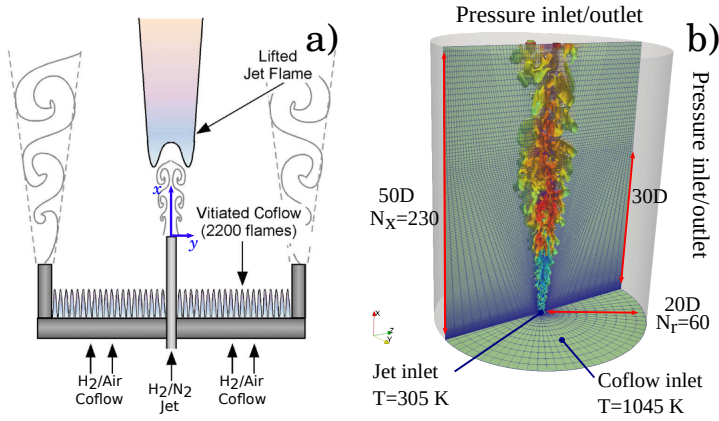


Figure 4.1: Sketch of the lifted flame burner [77] (left), lifted flame computational domain (center), slotted burner computational domain (right).

enhanced by possible autoignition events [77]. The total flame length is observed to be $L = 30D$, and the lift-off height is approximately $H = 10D$. Measurements using Raman-Rayleigh scattering and laser induced fluorescence were taken on the centreline from 0 to 26 nozzle diameters downstream. Radial profiles were measured at streamwise locations from $8D$ to $26D$. Wu *et al.* [131] further characterised the turbulent flow field under different operating conditions for both reacting and non reacting cases. Laser doppler velocimetry (LDV) was used to provide measurements of average axial velocity, axial and radial velocity rms and Reynolds shear stress.

The present test case has been selected due to its complex partially premixed combustion mode and stabilization mechanism of the hydrogen flame, making it highly suitable for evaluating the capabilities of the combustion models discussed in this work. It is characterized by a broad turbulent kinetic energy spectrum, with a relatively high Reynolds number and high Damköhler number, which makes this test case a good benchmark for testing dynamic modeling strategies under highly turbulent conditions. Furthermore, the availability of extensive experimental data allows for a precise assessment and validation of the simulation approaches.

Table 4.1: Operating conditions of the lifted partially premixed hydrogen flame case.

	D [mm]	U_{bulk} [m/s]	Re	T [K]	X_{H_2}	X_{O_2}	X_{N_2}	$X_{\text{H}_2\text{O}}$
Jet	4.57	107	23'600	305	0.25	-	0.7427	-
Coflow	210	3.5	-	1045	-	0.1474	0.7534	0.0989

The test case is analysed through LES at the operating conditions summarized in Tab. 4.1. In Chapter 5, the case is studied using the transported FDF model (ESF) in combination with detailed chemistry, aiming to investigate the flame topology with minimal modeling assumptions. Subsequently, the setup serves as a validation case for a hybrid FGM-ESF approach. In Chapter 6, it is employed to assess the performance of

dynamic subgrid-scale model closures on both structured and unstructured grids. Finally, in Chapter 7, this test case is used to evaluate implemented differential diffusion model within a flamelet-based presumed FDF LES framework, specifically targeting a partially premixed hydrogen flame, which shares features with realistic practical combustor applications, e.g. the TUDelft swirl-stabilized technically premixed combustor in chapter 10. Details of the mesh, boundary conditions, and numerical setup for each LES analysis of this test case are presented in the corresponding chapters, specifically in Sections 5.2, 6.2, and 7.2.

4.2. SLOT BURNER

The turbulent lean premixed hydrogen-air flame in slot burner configuration studied in [53] by means of DNS is simulated in Chapter 7 to gain insight into the capabilities of the flamelet/presumed FDF LES model to capture relevant effects of differential diffusion on the flame topology. A hydrogen/air mixture at an equivalence ratio of $\phi = 0.4$ and temperature $T_{\text{reac}} = 300$ K is issued at a bulk velocity $U_{\text{bulk}} = 24$ m/s into a secondary stream composed by the combustion products at temperature $T_{\text{prod}} = 1425$ K and velocity $U_{\text{prod}} = 3.5$ m/s, see Fig. 4.2. The jet Reynolds number based on the nozzle width $H = 8$ mm is $\text{Re} = 11000$. Berger *et al.* [53] observed that when an equidiffusive assumption was used, the flame speed was only affected by turbulence, while flame self wrinkling and local variations of flame temperature and reaction rate were observed with differential diffusion. This second case resulted in an increased turbulent flame speed and an overall shorter flame. Therefore, this test case represents a good benchmark for the assessment of the effectiveness of the differential diffusion models in the LES. Only the thermo-diffusively unstable case is simulated in the present study. Table 4.2 reports the operating conditions of the case, including reactants and products compositions in terms of species mole fractions X_i . Details of the mesh, boundary conditions, and numerical setup used in the LES of this test case are provided in Chap. 7, Sec. 7.2.

Table 4.2: Operating conditions for the premixed hydrogen slot burner case.

	U_{bulk} [m/s]	Re	T [K]	X_{H_2}	X_{O_2}	X_{N_2}	$X_{\text{H}_2\text{O}}$
Reactants stream	24.0	11'000	300	0.0116	0.2296	0.7588	0.0
Products stream	3.5	-	1425	-	0.1376	0.7588	0.1036

4.3. BLUFF BODY STABILIZED FLAMES

As described in Sec. 1.2, in bluff body stabilized flames, an obstruction is placed at the nozzle exit creating a low velocity wake region. The flame can anchor on the shear layer between the main flow and the wake. This flame holder is generally characterized by mild turbulence levels and relatively high strain at the bluff body base. In the present study, the methane bluff-body stabilized flame in confined conditions studied in [75] is analysed, together with a more recently developed full hydrogen unconfined flame [254].

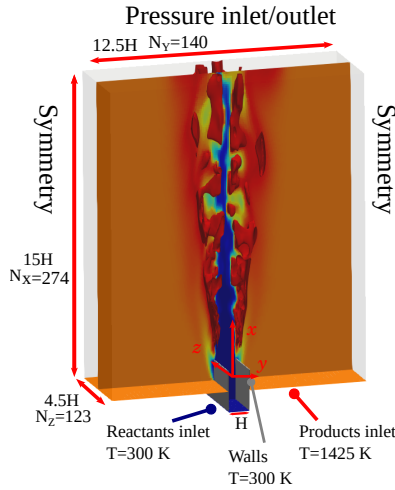


Figure 4.2: Sketch of the computational domain adopted in the present work for the simulation of the case studied in [53]

4.3.1. METHANE FLAME

The lean premixed, bluff-body stabilized flame studied in [75] (Figure 4.3) is considered in Chapter 6 to study dynamic closures. In this set-up, a low bulk velocity stream of 5 m/s of methane/air mixture at equivalence ratio $\phi = 0.75$ and inlet temperature $T_{in} = 300$ K is issued into a cylindrical duct with confinement ratio $R_{out}/R_{in} = 2$, as sketched in Fig. 4.3. The Reynolds number based on the bluff body diameter $D = 25$ mm is $Re = 7950$. This configuration leads to moderate levels of turbulence in the bluff body wake, where a recirculation zone is formed, which is *ad hoc* to compare the ability of the dynamic models for relatively narrow energy spectrum. The considered operating conditions are summarized in Tab. 4.3. Details of the mesh, boundary conditions, and numerical setup used in the LES of this test case are provided in Chap. 6, Sec. 6.2.

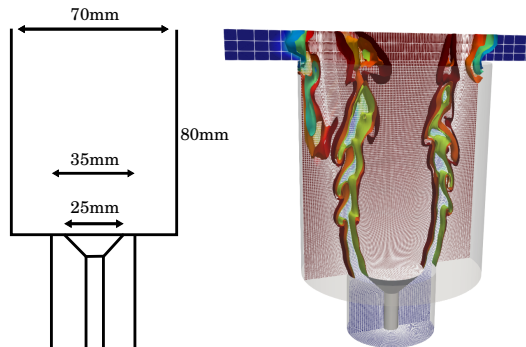


Figure 4.3: Sketch of the computational domain adopted in the present work for the simulation of the low-turbulence bluff-body flame of Dawson *et al.* [75]

4.3.2. HYDROGEN FLAME

A second premixed bluff body stabilized flame is investigated in Chapter 8. This flame holder, developed at the Norwegian University of Science and Technology (NTNU), was specifically designed for premixed hydrogen combustion therefore, featuring smaller size when compared to the previous methane flame holder. This configuration is schematically illustrated in Fig. 4.4. The geometry is the same as investigated by [254], although the flame analyzed in the present work is unconfined. Details on geometry and experimental data can be found on the TNF Workshop archive [255]. The conical bluff body has a diameter $d_b = 13$ mm and half-cone angle $\alpha = 45^\circ$. The hydrogen-air mixture is introduced with a temperature $T = 300$ K through an annular duct with an external diameter $d_b = 19$ mm and a bluff-body holder diameter of 5 mm. The burner operates without confinement, allowing the flame to develop freely in an environment at atmospheric pressure and temperature. The operating conditions are summarized in Tab. 4.3. Experimental dataset consists of OH* chemiluminescence and RMS and time-averaged velocity, measured at different streamwise locations from the bluff body base. Details of the mesh, boundary conditions, and numerical setup used in the LES of this test case are provided in Chap. 8, Sec. 8.2.

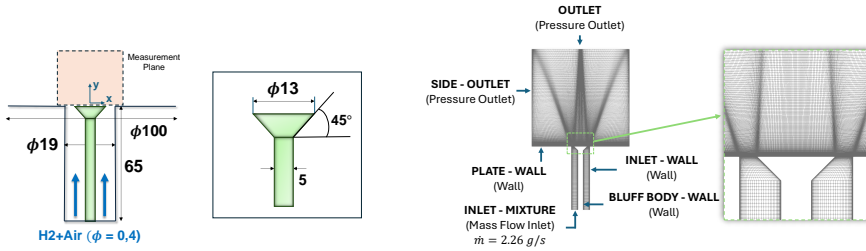


Figure 4.4: Schematic of the NTNU premixed hydrogen burner (left), and corresponding numerical mesh and boundary conditions (right). All dimensions are reported in mm.

Table 4.3: Operating conditions for the premixed bluff-body stabilized flames.

	U_{bulk} [m/s]	Re	T [K]	ϕ	X_{CH_4}	X_{H_2}	X_{O_2}	X_{N_2}
CH ₄ case [75]	5.0	7'950	300	0.75	0.073	-	0.194	0.733
H ₂ case [254]	8.75	6'648	300	0.4	-	0.1246	0.183	0.692

4.4. TUDELFT SWIRL-STABILIZED COMBUSTOR

The TU Delft swirl-stabilized combustor was developed within the APPU project as a laboratory-scale setup for advancing fuel-flexible combustion chamber technologies. The original design emerged from a series of research efforts [113–115], and the combustor is capable of operating at atmospheric pressure using gaseous fuel blends of CH₄ and H₂. Current developments aim to extend its capabilities through the integration of liquid kerosene injection systems [27].

A schematic of the setup investigated in this study is shown in Fig. 4.5. Air enters the base of the injector through four radial ports, with a diameter of $D_{air} = 5.5\text{mm}$. It is then guided into an axial swirler composed by eight vanes, featuring an outer diameter of 24 mm and an inner diameter of 10 mm. The swirler imposes a tangential component to the air velocity field, and the swirling flow is discharged into a mixing tube of diameter $D_{MT} = 24\text{mm}$ and length $l_{MT} = 60\text{mm}$. Two different swirler configurations have been studied experimentally [68], each characterized by an analytical geometric swirl number of $Sw_{geom}=0.7$ and $Sw_{geom}=1.1$, respectively, as defined by [256]. In the present work, the focus is on the $Sw_{geom}=1.1$ configuration only. The combustor features an axial air injection (AAI) system, allowing additional control over the axial momentum of the airflow, as a flashback prevention strategy. The total air mass flow rate is divided such that a portion \dot{m}_{AAI} bypasses the swirler and enters the mixing tube directly through a dedicated axial duct with a diameter of $d_{AAI} = 8\text{mm}$. The AAI fraction is defined as:

$$AAI = \frac{\dot{m}_{AAI}}{\dot{m}_{AAI} + \dot{m}_{sw}}, \quad (4.1)$$

where \dot{m}_{sw} is the mass flow rate of air entering the swirler. Gaseous fuel, composed of CH_4 and H_2 , is injected into the mixing tube just downstream of the swirler through four radial ports ($d_{fuel} = 3.175\text{mm}$), creating a jet-in-swirling-crossflow configuration. The mixing process occurs along the length of the mixing tube, after which the mixture enters an optically accessible combustion chamber with a diameter $D_{CC}=150\text{mm}$ and a length of $l_{CC} = 400\text{mm}$. The coordinate system is defined with its origin at the centerline of the mixing tube, positioned at the combustion chamber inlet, with the y-axis aligned with the streamwise direction of the flow.

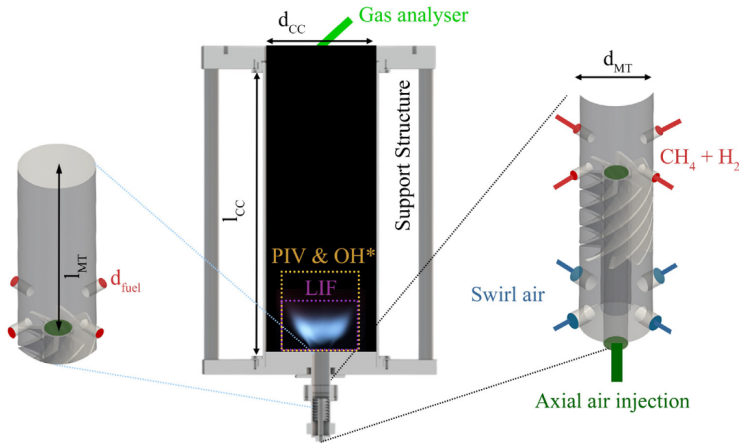


Figure 4.5: Schematic representation of the TU Delft swirl-stabilized burner with a detailed view of the injector and the acquisition locations of experimental measurements. Courtesy of Sarah Link [68].

For the simulations in the present work, a reference power setting of $P = 12\text{kW}$ is considered, with a corresponding air mass flow rate of $\dot{m}_{air} = 0.00538\text{kg/s}$. Depending on the selected fuel blend, the nominal equivalence ratio ϕ_{nom} varies according to the

effective lower heating value of the fuel LHV_{fuel} . Specific operating conditions for each case are detailed in the respective chapters. Experimental studies have shown that, at this power setting, an AAI of 20% was necessary to stabilize a flame fueled by 100

Several experimental diagnostics are available to support numerical simulations [68]. Velocity fields in the axial plane were measured using Particle Image Velocimetry (PIV). OH^* chemiluminescence provides line-of-sight information about flame shape and anchoring, and the signal can be Abel-deconvoluted to retrieve visual description of high heat release rate regions within the chamber axial plane. Additionally, PLIF (pulsed laser induced fluorescence) technique offer a qualitative spatially resolved visualization of the concentration of OH and NO species within the combustion chamber the flame front and anchoring behavior. Quantitative measurements of emissions were obtained using a gas analyzer placed along the central axis at the combustor exit, providing mole fractions of NO and CO [68].

Details of the mesh, boundary conditions, and numerical setup for each LES analysis of this test case are presented in the corresponding Chapters 9,10, specifically in Sections 9.2.1 and 10.3, respectively.

I

DEVELOPMENT OF FLAMELET MODELS FOR TURBULENT HYDROGEN COMBUSTION

5

ANALYSIS OF A PARTIALLY PREMIXED HYDROGEN FLAME THROUGH EULERIAN STOCHASTIC FIELDS METHOD

5.1. INTRODUCTION

One of the critical aspects in developing LES models for turbulent hydrogen combustion is the accurate treatment of subgrid-scale turbulence–chemistry interaction. In LES, the grid resolution is typically of the order of the laminar flame thickness, making the flame front and its interaction with turbulence largely a subgrid phenomenon.

As discussed in chapter 2, statistical approaches, such as filtered density function (FDF) methods, represent a very effective and robust approach for subgrid combustion modelling. In these methods the local thermochemical state of the mixture is described through a statistical distribution, which can either be presumed or transported. While presumed FDF methods (PFDF) involve stronger modelling assumptions about the shape and statistical independence of scalars, transported FDF approaches (TFDF) minimize such assumptions and allow for a description of the chemical reaction source terms in a closed form. In these methods the FDF is represented by a set of samples evolving according to modelled stochastic differential equations. The samples can either represent a local instantaneous condition (Lagrangian stochastic particle method (LSPM)) or an instantaneous condition in the whole domain (Eulerian stochastic field (ESF) method). Transported FDF methods are typically combined with detailed chemistry.

In this chapter, a combination of the ESF method with a tabulated chemistry approach based on the Flamelet Generated Manifold (FGM) is proposed, similarly to the

Parts of this chapter have been presented at the Mediterranean Combustion Symposium 2025

work in [232], and applied for the LES of a hydrogen flame. This hybrid FGM-ESF model introduces modelling assumptions on chemistry, but significantly improves computational efficiency by solving for a reduced set of control variables (mixture fraction and progress variable) instead of solving equations for every single species. The goal is to retain the strengths of ESF in representing subgrid turbulence–chemistry interaction, while reducing the computational cost associated with fully detailed chemistry.

Both fully detailed chemistry (FC-ESF) and the FGM-ESF model are applied to simulate the partially premixed lifted hydrogen flame, described in chapter 4. This configuration is selected for its broad range of physical features, including turbulent fuel-oxidiser mixing at various temperatures, aerodynamic flame stabilization through hot products, and multi mode combustion, characteristics typically found in combustors for practical applications. The case is first analysed using the FC-ESF method to gain insights into flame structure and dynamics, which serves as a reference. The FGM-ESF model is then applied to the same configuration to assess the predictive capability of flamelet tabulation on the various flame features in comparison to detailed chemistry. These preliminary investigations are propaedeutic for successive developments of flamelet-based LES models and presumed FDF approaches for hydrogen combustion addressed in subsequent chapters.

5.2. NUMERICAL DETAILS

LES are run using the open-source software OpenFOAM-v6, which uses the finite volume approach to discretise the reactive Navier-Stokes equations. Second order spatial discretization schemes are adopted for every transported quantity, including the stochastic fields, with limiters towards first order for regions characterized by strong gradients. First order Euler scheme is adopted for temporal integration and a fixed timestep is imposed to guarantee a CFL number below 0.5 in the regions of interest. The equations for continuity, momentum, sensible enthalpy, described in Sec.2.9.1 and the stochastic fields of species (replaced by progress variable and mixture fraction in the case of the FGM-ESF model), according to Sec. 3.1, are solved using a low-Mach, density varying formulation where the pressure-implicit with splitting operator (PISO) loop [257] is used to couple pressure and velocity field. An outer loop with at least 5 iterations is used to improve convergence of the thermochemical quantities. The WALE model [258] is used to close the SGS stress in the momentum equation. The turbulent transport terms in all scalar equations are closed using a gradient hypothesis, and the molecular viscosity is computed via Sutherland's law, Eq. 2.11. Diffusion constants are computed in the assumption of unity Lewis number and using a Schmidt (Prandtl for the energy equation) number of 0.7. Although the assumption of unity Lewis number is arguable for a case with hydrogen fuel, the relatively high turbulence level of the studied case and the dilution of the hydrogen stream with nitrogen makes the assumption reasonable, as discussed in [101] and Chapter 7 and as further verified by the good comparison with statistics from experiments to be shown next. The inclusion of differential diffusion modelling within the transported FDF LES context was explored in [229], where mild effects on the flame lift off height were observed, with improvements of the predictions in comparison to experimental data. However, the investigation of differential diffusion implementation in the ESF framework is beyond the scope of the present thesis, where differential

diffusion modelling is instead investigated in the flamelet-based LES approach with presumed FDF, see Chap. 3.2.3. Density is computed using the equation of state, in which the molecular weight is reconstructed from the transported species in the case of the FC-ESF model, and from the pre-computed table in the case of the FGM-ESF model.

With reference to Fig. 4.1, the numerical domain consists of a cylinder spanning about $40D$ and $50D$ respectively in the radial and axial directions, being D the diameter of the central fuel nozzle. The domain is discretized using a structured mesh of $230 \times 60 \times 80$ cells respectively in axial, radial and azimuthal directions, amounting to 897'000 cells in total. The cells are non-uniformly distributed so that they cluster in the region of the shear layer and up to about $30D$ from the nozzle exit. The typical cell size in this region is of the order of the laminar flame thickness, $\delta_l \approx 0.66$ -1 mm. The same mesh is shown to be accurate enough and to satisfy Pope's 80% turbulent kinetic energy criterion [97], as analysed in details in the next chapter [101]. Boundary conditions are assigned as follows. A turbulent inlet velocity profile with synthetic turbulence is imposed at the nozzle exit using the approach in [259], where the turbulent velocity profile and rms of axial and radial components are taken from experimental measurements in [162, 260]. The integral length scale at the inlet is $l_0 = 0.07D$ and was chosen after preliminary analysis by targeting the correct jet spreading rate and its mixing with the coflow (quantified by measurements of mixture fraction). Particular sensitivity of the jet evolution and flame lift off high to the inlet turbulence was observed, as later described in Chapter 7. Atmospheric pressure is imposed at the outlet, and zero-gradient conditions are imposed to outlet and lateral boundary for all scalars. Temperature at the inlets is assigned according to the experiment, as reported in Tab. 4.1. For the FGM-ESF case, the progress variable is zero at the inlets, and ignition is artificially imposed by creating a cylindrical sub region with $\tilde{c} = 1$. The mixture fraction is 1 at the jet inlet and 0 in the coflow. The LES are run for 4 flow-through times, defined as the time needed by an element of fluid on the centreline to travel $40D$. Of these, the last three are used to collect statistics. The flamelet database in the case of the FGM-ESF model consists of 300 unstretched freely-propagating one-dimensional flamelets spanning the flammability limits, computed using the solver CHEM1D [141] with the San Diego chemical kinetics mechanism [143]. The temperature and species mass fractions in the reactants of each flamelet vary linearly with the mixture fraction from their value in the oxidiser (the hot coflow), $z = 0$, to the fuel stream, $z = 1$, as reported in Tab. 4.1. Each flamelet is discretised in the progress variable space using 100 points. Outside the flammability limits values needed for the LES are interpolated between the closest flamelet value and the value in the fuel and coflow streams respectively, except for the reaction rate of progress variable which is set to zero.

5.3. RESULTS

5.3.1. FLAME STRUCTURE AND OVERALL MODEL PERFORMANCE

Results obtained using the ESF-FC and ESF-FGM models are first compared to experimental data to assess the respective capabilities of the two models in predicting the correct flame structure. Radial profiles of mean and rms axial velocity are compared to experimental data from [77] in Fig. 5.1 (left).

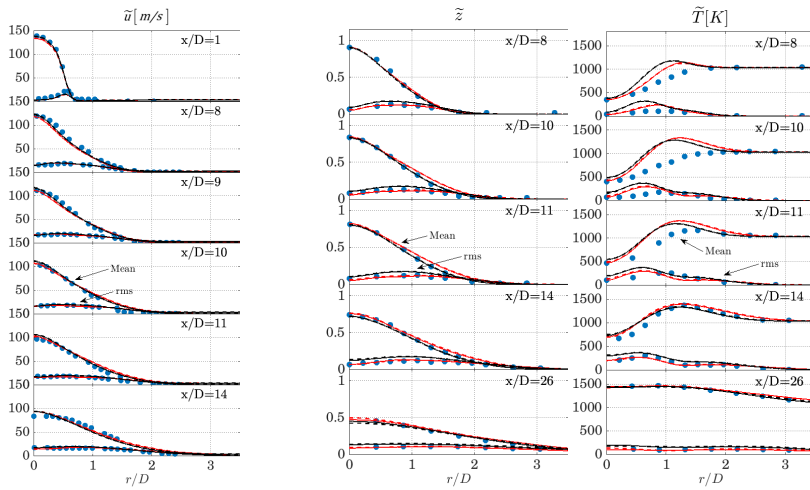


Figure 5.1: Radial profiles at different axial locations of mean and rms axial velocity (left), mixture fraction (center) and temperature (right) from experiments [77] (●) and LES with FC-ESF model (2 fields —, 8 fields - -) and ESF-FGM model (2 fields —, 8 fields - -).

5

Results from LES are shown for two Eulerian stochastic fields (2F) and eight Eulerian stochastic fields (8F). Both FC-ESF and FGM-ESF approaches are observed to predict the velocity and rms fields with very good accuracy as compared to experiments, indicating that turbulent shear layer characteristics and jet spreading rate are well captured in both cases. Radial profiles of mean and rms temperature and mixture fraction are further shown in Fig. 5.1 (right). Also for these quantities, the FC-ESF and FGM-ESF approaches give similar predictions. Some higher temperature is observed at $x/D = 8$ for $r \approx D$ in the case of the FGM-ESF, which is due to the fact that the flame lift-off height is predicted more upstream as compared to the FC-ESF approach. Both approaches, however, underestimate the flame lift-off height of about three nozzle diameters, which explains the local temperature peak found at $x/D \leq 10$ in Fig. 5.1, which is not present in the experimental measurements. At these locations, in fact, the mixture temperature increases only due to the mixing between the cold fuel stream and the hot coflow from the pilot. The mis-prediction of lift-off height is in line with previous studies [234, 260] and the further analysis carried out in the present thesis, in Chaps. 6 and 7 [101, 261], and was expected due to the strong sensitivity of this parameter to the inlet turbulence conditions as mentioned in Sec. 5.2 and investigated in Appendix B. The FC-ESF and FGM-ESF models predict the rms values of mixture fraction, \tilde{z}_{rms} with very good accuracy, with the FGM-ESF model giving some slightly higher predictions as compared to experimental values. The rms of temperature is also predicted with relatively good accuracy by both models, and some over-prediction observed for $x \leq 10D$ is associated to the over-prediction of temperature observed due to the underestimation of the lift-off height.

For each considered variable, the sensitivity to the number of Eulerian stochastic fields is found to be minimal for the studied configuration. In particular, the profiles at

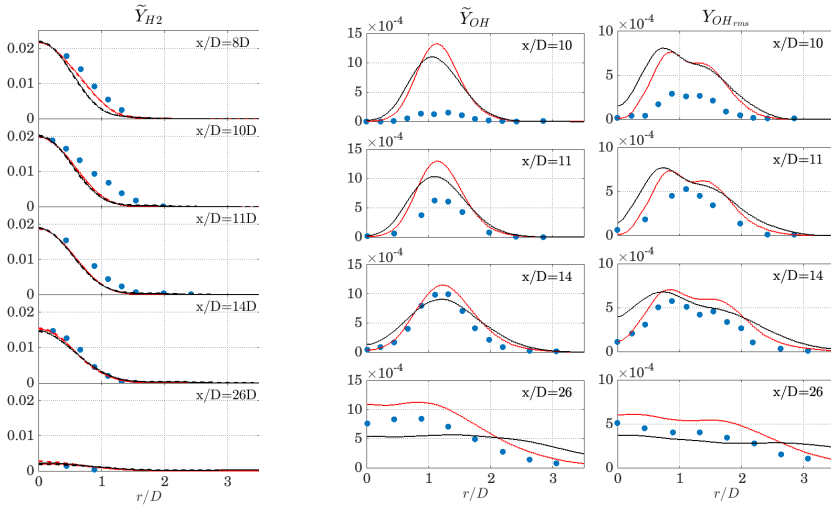


Figure 5.2: Radial profiles of mean H_2 mass fraction (left), mean OH mass fraction (centre) and its rms (right), obtained from experiments [77] (●) and LES with FC-ESF model (2 fields —, 8 fields - -) and ESF-FGM model (2 fields —, 8 fields - -).

$N = 2$ and $N = 8$ predicted by the FGM-ESF approach appear almost identical, suggesting that this approach can be employed at relatively low cost. Due to the above sensitivity, only results obtained for the $N = 2$ cases will be discussed in the remainder of the paper.

Time averaged radial profiles of chemical species as predicted by the two approaches are compared against experiments in Fig. 5.2, which shows a good agreement between the hydrogen mass fraction Y_{H_2} profiles predicted by the two numerical models and experimental measurements. Some under-prediction of hydrogen mass fraction is observed at axial locations $x < 14D$, consistently with the under-prediction of the flame lift-off height in the LES. In fact, the two models predict lower hydrogen mass fractions in the shear layer region, where the flame stabilizes at $r/D \approx 1$ and hydrogen consumption starts to take place more upstream than what observed experimentally. As observed from the temperature radial profiles, the FGM-ESF model predicts a more upstream flame stabilization point as compared to FC-ESF, and consequently lower hydrogen mass fraction in the flame region at $x = 8D$. Nevertheless, no significant further differences are observed in the predictions from the two models, confirming that the FGM-ESF approach is able to mimic the behaviour of the main species with good accuracy.

Profiles of mean and rms OH mass fraction Y_{OH} are compared with experimental measurements in Fig. 5.2 (right) to assess the capability of the two LES models to describe the formation and reaction of intermediate species. OH data is shown for simplicity only for axial locations $x \geq 10$, where a flame is present in both simulations and experiments. Results show that the prediction of Y_{OH} is more sensitive to the computed flame stabilization height and chemistry modelling, compared to the major species. Indeed, the slightly more upstream flame position in the LES, as compared to experiments,

leads to non-negligible overestimation of OH mass fraction at axial locations $x \leq 11D$ with both models. The FC-ESF approach provides accurate predictions of average and rms \tilde{Y}_{OH} at $x \geq 14D$. An over-prediction as compared to the measured values is observed at $x/D = 10$, due to the fact that this location is around the flame anchoring position, which is slightly under-predicted by the numerical simulations. The ESF-FGM approach yields relatively good predictions as compared to the FC-ESF approach. Interestingly, the FGM-ESF approach results in lower OH values than FC-ESF despite predicting a more upstream flame, which may be a direct result of the assumptions underlying the FGM approach. In the FGM-ESF case the level of OH is tabulated as function of the progress variable based on H_2O , assuming presence of a flamelet structure. This does not take into account possible deviations of the thermochemical states from the tabulated manifold, associated for example to the response of OH-chemistry to rapid strain rate variations. Despite this, the predictions of OH from the FGM-ESF method remain relatively similar to those of the more detailed FC-ESF method, suggesting that the correct flame structure is still predicted in the former case.

In the next section further characteristics of the reacting flow field as predicted by the two approaches are compared to evaluate potential capabilities and limitations of the FGM-ESF in predicting the correct burning states.

5

5.3.2. INSTANTANEOUS FEATURES AND BURNING STATES

Due to the partially premixed nature of the lifted flame, the FGM-ESF model might be limited in predicting the correct burning modes, and consequently the correct reaction rates, as a dataset of premixed flamelets is used to represent the thermochemistry. By general inspection, the reacting flow field predicted by the two approaches presents similar features, as can be observed by the reaction rate countours and the isolines of progress variable in Fig. 5.3a. In particular, one can notice that the anchoring point, or lift-off height, of the flame is predicted at about the same location (mildly more upstream in the case of the FGM-ESF model). An inspection at the progress variable reaction rate (normalized water mass fraction) near this anchoring point in the same figure shows that this quantity is predicted similarly by the two combustion models, which explains the overall similar statistics observed in the previous section.

Additionally, the Takeno flame index [262] is computed to identify the flow regions where the mixture burns in premixed or non-premixed mode. The flame index is defined here as:

$$\text{F.I.} = \frac{\nabla Y_{H_2} \cdot \nabla Y_{O_2}}{|\nabla Y_{H_2} \cdot \nabla Y_{O_2}|} \quad (5.1)$$

and assumes value 1 if the combustion is premixed and -1 if it is non-premixed. Although the accuracy of this definition has been argued in a number of past studies, it is acceptable in the context in the present work where only a qualitative assessment of the relative capabilities of the two combustion approaches is needed.

Midplane contours of the flame index are shown for a generic time step in Fig. 5.3b as predicted by FC-ESF and FGM-ESF approaches. Isolines of stoichiometric mixture fraction and progress variable $\tilde{c} = 0.5$ are also shown to indicate fuel-oxydiser mixing line and flame location. The flame index as predicted by the FC-ESF model approach is -1 in the region of inert fuel-oxidiser mixing upstream of the flame as the gradients

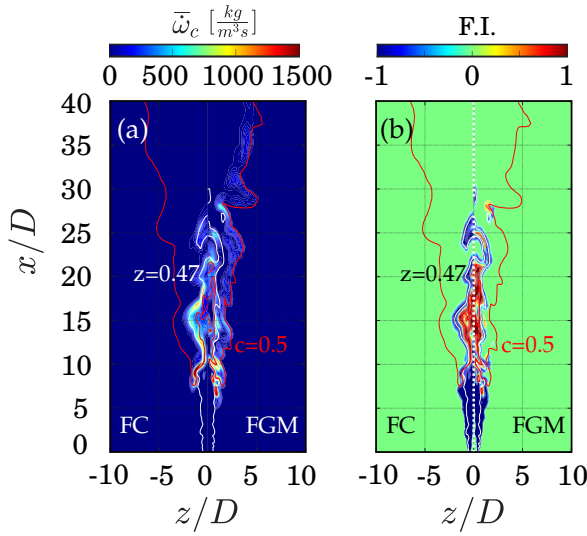


Figure 5.3: Midplane contours of instantaneous normalised water reaction rate (left) and flame index (right). Stoichiometric mixture fraction $\bar{z} = 0.47$ and progress variable $\bar{c} = 0.5$ are marked as white and red solid lines, respectively.

of H_2 and O_2 are aligned and pointing in opposite direction. Near the flame ignition point, ($x/D \approx 8$), a spot burning in premixed mode is found on the lean side (radially outwards in respect to the stoichiometric line), while non-premixed mode is observed in correspondence of stoichiometric condition. Further downstream in the flame region ($10 \leq x/D \leq 20$), the core of the jet appears dominated by premixed mode at rich conditions (see region near the isoline of \bar{c}), and this region is surrounded by residual unburnt fuel that reacts with oxygen in the external coflow in non-premixed mode (see values of $\text{F.I.} = -1$) along the stoichiometric line. The FGM-ESF approach also predicts a similar index distribution, despite the mass fractions of oxygen and fuel are retrieved from the flamelets database and thus depend on the controlling variables.

To better investigate the instantaneous burning features predicted by the two modelling approaches, scatter plots of instantaneous temperature, OH mass fraction, water mass fraction, and its normalised reaction rate, are shown versus mixture fraction in Fig. 5.4. Reaction rate and OH values are collected only in the flame region, identified here with the locations where $\bar{\omega}_c$ is above 2% of its maximum value from flamelets calculation. Values for T and $Y_{\text{H}_2\text{O}}$ are instead only collected in the region where $\bar{c} > 0.1$ in order to exclude the unburnt reactants while retaining the burnt condition. The FGM-ESF model predicts peak temperatures which encompass all burning states found in the flamelets database, for which the adiabatic flame temperature against mixture fraction is reported as a blue line. Conversely, equilibrium values are not fully reached in the case of the FC-ESF model, suggesting that detailed chemistry and species transport leads to the prediction of an overall slower combustion time scale, compared to turbulent mixing time scale, with respect to what predicted by the flamelet approach. Nevertheless, the conditional average of temperature from the two models remains very similar, ex-

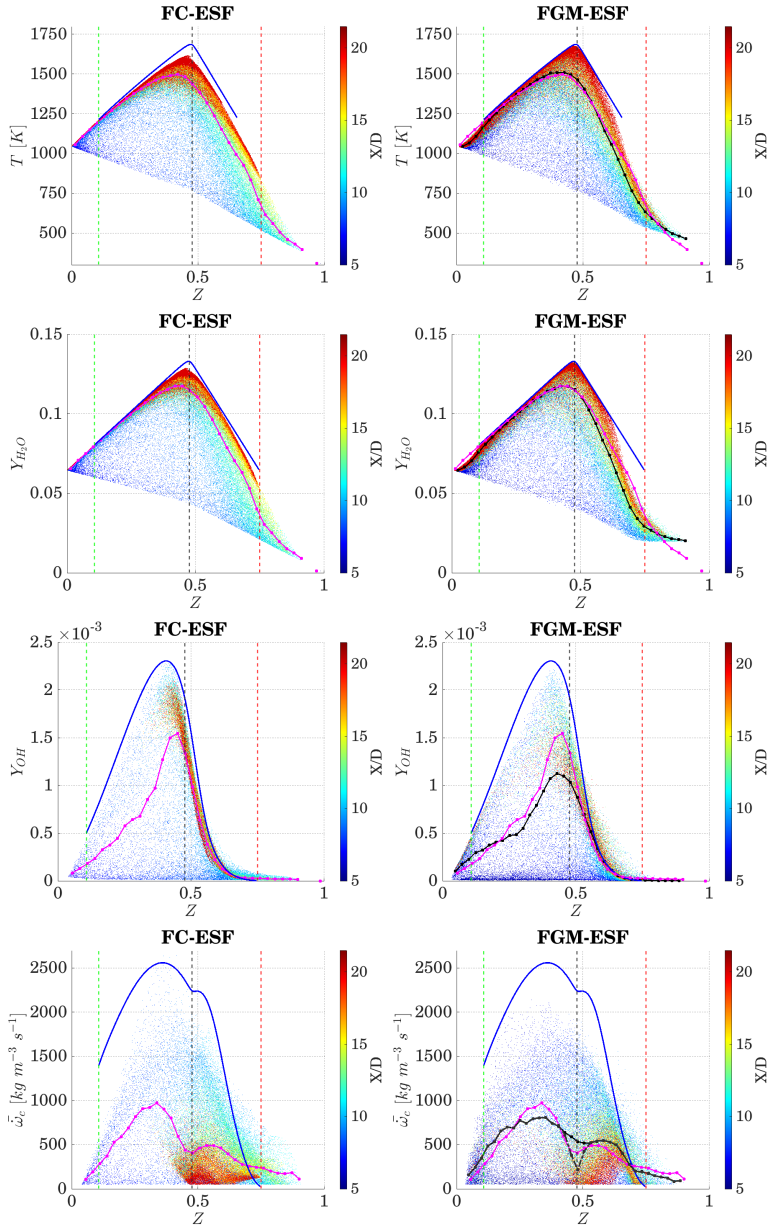


Figure 5.4: Scatter plots of temperature T , water mass fraction Y_{H_2O} , OH mass fraction and normalised water reaction rate $\bar{\omega}_c$ versus mixture fraction in the flame region, coloured by the distance form nozzle exit x/D and obtained using FC-ESF and FGM-ESF models. Equilibrium conditions and maximum reaction rate computed from the flamelet database are shown with blue lines (—). Vertical dashed lines indicate lean (--) and rich (--) flammability limits, and stoichiometric condition (-). Conditional averages are also shown for the FC-ESF case (—) and the FGM-ESF case (—). For the reaction rate plot, the conditional mean in the case of the FGM-ESF model is shown with (- -) and without (—) the correction term $\bar{\omega}_{np}$.

cept for very rich conditions where the conditional mean is observed to be higher in the case of the FC-ESF model (to be discussed later). The scatter plots of water mass fraction shows that slightly more water is produced in the case of the FGM-ESF model near stoichiometry, which could further support the argument of a slower reaction time scale. However, the conditional mean in the mixture fraction space remains similar between the two modelling approaches.

In addition to different reaction time scales, these observations could suggest that detailed chemistry modelling better represents secondary dissociation reactions of water into OH, particularly present at high temperatures close to stoichiometry, which are instead not captured by tabulated chemistry. These reactions cause reductions in water mass fraction and temperature around stoichiometry while increasing OH mass fraction, in line with the observations in Fig. 5.2 and the scatter plots in Fig. 5.4. Consistently, a lower peak value of the Y_{OH} conditional mean is observed from the scatter plots for the FGM-ESF model as compared to the FC-ESF case in Fig. 5.4. The two models show similar distribution of OH values within the whole range of the flamelets database. Consistently with flamelets computation, peak values are observed around stoichiometric conditions towards the lean side, $\tilde{z} \approx 0.45$, and these states are reached at axial locations $x \approx 13D$ in the LES. At lean conditions, the maximum OH values are observed in correspondence of the flame base, $x \approx 8 - 10D$ (blue coloured points in the scatter plot), while further downstream (red coloured points) the maximum values are only reached at rich conditions, corresponding to inner jet regions towards the core (see contours in Fig. 5.3 and radial mixture fraction profiles in Fig. 5.1). The predicted OH distribution is directly linked to the flame structure and correlates with the distribution of reaction rate, as described next.

By looking at the scatter plots of normalised water reaction rate versus mixture fraction (Fig. 5.4, bottom row), the two models give overall similar predictions, with two peaks markedly visible in the conditional means respectively on lean and rich sides. While the lean peak is found at about the same mixture fraction value by the two approaches, the rich peak is slightly shifted towards the rich side in the case of the FGM-ESF approach as compared to the FC-ESF approach, indicating that the mixture is found on average at richer conditions before being burnt. Note that in both approaches the burning states near the rich flammability limit are predicted with a reaction rate which is higher than the maximum obtained from a premixed flamelet computation at the same mixture fraction. This is due to the simultaneous mixture fraction redistribution by turbulence affecting the reaction process in the inner rich branch of the flame. Overall, these results suggest that the FGM-ESF approach is capable to predict these states, at least from a qualitative standpoint. From a quantitative point of view, reaction rates are higher in the case of the FGM-ESF model for values of \tilde{z} near stoichiometry and up until $\tilde{z} \approx 0.7$, confirming the argument of the faster combustion time scale compared to turbulent mixing time scale predicted by the FGM-ESF approach, at least for this range of \tilde{z} . On the other hand, values of reaction rates in the lean range $0.2 \leq \tilde{z} \leq 0.4$ and close to the rich flammability limit are higher in the case of the FC-ESF model.

By cross correlating the flame index contour in Fig. 5.3 with the reaction rate scatter plots in Fig. 5.4, one can infer that the reaction rate peak located on the lean side is associated to lean premixed combustion occurring mostly near the flame base $x/D \approx$

5, while rich premixed combustion occurs mostly downstream (see rightmost peak of conditional reaction rate in Fig. 5.4). Near stoichiometric conditions the flame burns in non-premixed mode and reactions are observed to be stronger near the flame base, as observed from Fig. 5.4 where high reaction rate values at stoichiometric conditions (black dashed line) are found at upstream locations (blue colour) while lower reaction rate values are found at more downstream locations (red colour).

These non-premixed burning states could be responsible for the higher conditional reaction rate observed around stoichiometric conditions for the FGM-ESF model, which on the other hand fully relies on a manifold of premixed flamelets. To assess this, the correction term $\bar{\omega}_{np}$ defined in Eq. 3.7 is computed *a posteriori* from filtered quantities and its effect on the reaction rate conditional mean $\bar{\omega}_c + \bar{\omega}_{np}$ is shown in Fig. 5.4 for the FGM-ESF model. This term accounts for the dependency of the progress variable scaling factor on the mixture fraction $\psi_{\max}(z)$, and therefore for the effects of partial premixing. The figure indicates that the conditional mean of "corrected" reaction rate from the FGM-ESF model recovers the values predicted by FC-ESF model near stoichiometric conditions, while the correction is less relevant at lean and rich conditions. Note that $\bar{\omega}_{np}$ is of leading order and prevalently negative in the non-premixed regions found at stoichiometric conditions [136], implying that the uncorrected reaction rates are higher in the non-premixed regions. In turn, this is in line with the higher temperature and water mass fraction values predicted around stoichiometric conditions by the FGM-ESF model, as seen from the scatter plots in Fig. 5.4, and the more upstream flame stabilization as compared to the FC-ESF predictions, see Figs. 5.3 and 5.1.

5.4. SUMMARY

A partially premixed hydrogen lifted flame was investigated by means of large eddy simulations with eulerian stochastic (ESF) fields subgrid closure. A recently-developed hybrid model based on flamelet generated manifold (FGM) tabulation of the thermochemical states was assessed in comparison to experimental data and results obtained using the classical ESF method with fully detailed chemistry (FC-ESF).

An excellent agreement with experimental measurements is observed in terms of mean and rms velocity and mixture fraction predicted by the ESF model with both fully detailed chemistry and FGM tabulation. Temperature and major species fields are also accurately predicted by the two LES models, despite some under-prediction of the flame lift-off height. In general, the FGM model based on premixed flamelets appears to mimic well the results of the fully detailed chemistry approach. The main reaction process is well described by the FGM model with slightly higher reaction rates at the lean premixed flame base and a more upstream flame stabilization as compared to the fully detailed chemistry, but without considerable differences in the prediction of the major species fields. On the other hand, some differences are observed in the prediction of the intermediate species OH, which is more sensitive to chemistry modelling and flame location. The FGM predicts overall lower mass fractions of this species as its value is retrieved from the thermochemical states collected in the premixed flamelets database. Despite the OH chemical kinetics described by the FC-ESF approach may deviate from the tabulated states, the FGM approach is able to give satisfactory quantitative predictions.

An investigation of the instantaneous realizations of the burning states reveals that higher reaction rate values are obtained from the FGM-ESF model, except for a lean region at relatively upstream locations and for very rich conditions, which is in line with the prediction of a more upstream flame stabilization point. Near the stoichiometric conditions these differences may be caused by combustion in non-premixed mode. Nevertheless, the use of a correction factor non-premixed combustion effects is shown *a-posteriori* to suffice in restoring the burning state predicted by detailed chemistry, despite the thermochemical database in the FGM is based on premixed flamelets only. In lean and very rich regions, where premixed mode is dominant, only mild difference is observed in the local realizations of reaction rate predicted by the two models. Overall, the FGM-ESF model predicts qualitatively similar distribution of reacting states compared to FC-ESF including predictions of reaction rate values about the maximum flamelet value on the rich side and the double-peak shape of conditional reaction rate distribution in mixture fraction space. Quantitative differences only seem to mildly affect the prediction of statistics.

The presented analysis provides a starting point for modelling partially premixed hydrogen combustion with a flamelet-based chemistry tabulation, offering insights into the advantages and limitations of this approach in such combustion systems. Building upon these results, presumed FDF subgrid modelling is introduced in the next chapter, where a dynamic closure for the transport equation of the subgrid-scale variance of the progress variable is tested. Part of the next investigation is carried out using the same test case explored in the present chapter.

6

DYNAMIC MODELLING OF SUBGRID SCALAR DISSIPATION RATE WITH DIFFERENTIAL FILTER

6.1. INTRODUCTION

Among the number of combustion models available in the LES framework, flamelet-based approaches coupled with presumed filtered density function (FDF), described in details in Sec.3.2, offer a very robust and computationally efficient strategy for the accurate description of turbulence–chemistry interactions. They have been tested on a broad range of combustion systems, providing highly satisfactory results in premixed and partially premixed regimes [108, 135, 263–265]. Therefore, they represent a promising tool for the present research, aiming at developing numerical models for computationally efficient analysis and design of hydrogen turbulent combustion systems.

Accurate modelling for the subgrid-scale (SGS) variance of the progress variable is critical in flamelet-based LES models with presumed FDF. This quantity directly influences the filtered reaction rate $\overline{\dot{\omega}_c}$ and the overall fidelity of turbulence–chemistry interaction modelling. As described in Sec.3.2, the transport equation for the SGS variance of the progress variable includes a sink term based on the unresolved (SGS) scalar dissipation rate of the progress variable $\tilde{\epsilon}_c$ needs closure. Models for $\tilde{\epsilon}_c$ are commonly proportional to the SGS variance and can be written in general form as:

$$\tilde{\epsilon}_c = f_1 \sigma_c^2 / \beta_c, \quad (6.1)$$

where β_c is a modelling constant and f_1 is a function, defined in Eq. 3.12 [89, 102], depending on local parameters describing turbulence, combustion and LES filter. The model constant β_c depends on flame curvature, diffusion and reaction processes, and is generally scale-dependent. Its choice is of crucial importance to obtain the correct estimation of SGS variance. Thus, while the use of a static value of the combustion constant may lead to good results, it requires an accurate preliminary tuning. Furthermore,

the value might need to vary in space and time for cases where the aforementioned processes or the numerical mesh (thus the LES filter) is not homogeneously distributed, and for such cases a single constant value might not be suitable.

For these reasons, the application of a dynamic approach for the adaptive calculation of the model constant may represent a very suitable strategy. Relatively recently, scale similarity assumptions for modelling parameters such as flame wrinkling and flame surface density have been proposed and investigated, e.g. see [98, 103, 247, 266]. Dynamic models based on the scalar dissipation rate have been also investigated [102, 245]. Although these models were observed to work on different regimes, the assumption of scale similarity is arguable for reacting quantities, and it is unclear whether the application of dynamic modelling leads to correct estimation of the modelling constant. An example was provided in [209], where it was discussed that on unstructured meshes the classical test-filter approaches based on Gaussian shapes lead to excessive noise and incorrect results due to the pseudo-Fourier condition [201]. Nevertheless, to the best of the authors' knowledge, a thorough investigation of the influence of the test filter in dynamic modelling for combustion LES still does not exist.

In the present chapter the aim is to fill this knowledge gap by investigating different test filtering techniques, and evaluating the outcomes on two different combustion systems in order to evaluate the performance under different turbulent and computational mesh conditions. In particular, the study employs the so-called differential filters, presented in details in Sec. 3.2.2, where the general test filtered quantity $\hat{\phi}$ is obtained through the resolution of a differential equation rather than the direct application of a Gaussian filter. This class of filters has been commonly used for non-reacting flows (e.g. see [267]), but not for reacting cases. The advantages and limitations of these are compared to classic algebraic approaches, see Sec. 3.2.2, from both modelling and computational cost perspectives, for the dynamic computation of the model constant β_c in the context of flamelet-based LES with presumed FDF. The analysis is performed by simulating the highly turbulent partially premixed lifted hydrogen flame already investigated in Chap. 5 with the ESF approach, firstly on the same block structured mesh employed for previous study, and successively on an unstructured mesh with similar refinement level. The study is then extended to the lean premixed, bluff-body stabilized methane flame studied in [75], introduced in Chap. 4, which presents lower turbulence intensity.

6.2. TEST CASES AND NUMERICAL DETAILS

For the analysis in the present work, two test cases are selected. The first, Case A (Fig. 4.1), is the lifted jet flame in hot vitiated coflow developed by Cabra *et al.* [77]. This case is characterized by relatively high Reynolds number and a relatively wide turbulent kinetic energy spectrum. The second case, Case B (Figure 4.3), is the lean premixed, bluff-body stabilized flame studied in [75]. This configuration leads to moderate levels of turbulence in the bluff body wake, where a recirculation zone is formed, which is *ad hoc* to compare the ability of the dynamic models for relatively narrow energy spectrum.

The two cases, at operating conditions summarized in Tables 4.1-4.3, are simulated using an *in house* solver implemented in OpenFOAM v9, which uses the finite volume approach and a low-Mach approximation to solve the reacting Navier-Stokes equations along with the four transport equations for the controlling variables discussed in Sec. 3.2.

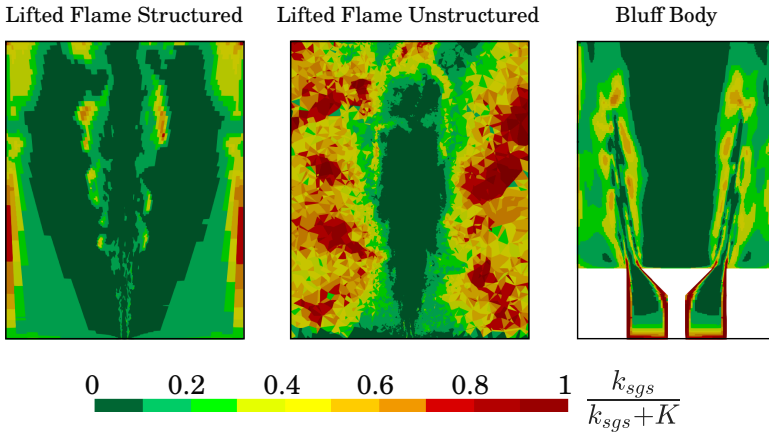


Figure 6.1: Pope criterion: ratio of the subgrid kinetic energy k_{SGS} (from turbulence model) and total turbulence kinetic energy (K resolved + modelled).

The Pressure-Implicit with Splitting Operator (PISO) loop [257] is used for the pressure-velocity coupling, with a minimum of 5 additional outer iterations per time step for the other equations. An implicit Euler scheme is used for time marching along with a time step ensuring that the CFL number is below 0.3 everywhere in the domain. Second order schemes are used for the spatial gradients, with Gamma limiters [172] to improve stability in the region of the flame where strong gradients are present.

Two block-structured meshes of 0.9 and 2.6 million hexahedral cells are generated using Ansys ICEM CFD software and used for cases A and B, respectively. Additionally, case A is also simulated on a computational grid of 3.3 million tetrahedral cells to investigate the effects of the test filters also when an unstructured mesh is in use. Each grid is refined within the flame region to have a ratio between cell size and laminar flame thickness of about 1.

The Pope criterion [97] is employed to assess that at least 80% of the total turbulent kinetic energy falls within the resolved scales and ensure a suitable grid resolution. For this purpose midplane contours of the ratio $k_{SGS}/(K + k_{SGS})$ are shown in Fig. 6.1, where k_{SGS} is the subgrid kinetic energy taken from its transport equation (Eq. 2.58 and K is the resolved turbulent kinetic energy. The contour plots show that the modelled k_{SGS} falls below the 20% of the total turbulent kinetic energy in the regions of interest of the domain, i.e around the flame. It has to be noted that high values of this ratio are encountered at the walls, where most of the kinetic energy in the boundary layer is modelled through wall functions, and in low turbulence regions of the domain, where both k_{SGS} and K approach zero, which also explains the relatively larger values observed for case B (bluff body).

For case A, constant ambient pressure is imposed at the outlet and at the lateral cylindrical surface, while zero normal gradient condition is imposed to the other quantities. Constant temperature conditions are imposed at the jet and coflow inlet according to Tab. 4.1, and a constant axial velocity of 3.5 m/s is imposed at the coflow inlet. A synthetic eddies generator [259] is used to impose a time-varying turbulent velocity profile

at the jet inlet. A target mean velocity profile and rms velocity profile are imposed according to the measurements reported in [131, 260, 268]. The flame lift-off height was observed to be very sensitive to the turbulent inlet condition [260] and a value for the integral turbulent length scale l_0 must be accurately chosen. As no experimental characterization is available for this quantity, a sensitivity analysis was performed and a value of $l_0 = 0.07D$ was selected for the block-structured mesh, as it was observed to provide a good representation of jet spreading, and good agreement with measured averaged and rms mixture fraction and velocity profiles. A mesh sensitivity analysis (reported in the Appendix Section) and the Pope's criterion for turbulent kinetic energy reported in Fig. 6.1 show that the block-structured and the unstructured meshes have similar level of refinement and are able to resolve most of the turbulent kinetic energy. However, the instantaneous velocity conditions produced by the synthetic eddies generator can be dependent on the selected mesh, also for same values of the integral length scale. For this reason, to obtain similar turbulent velocity field (mean and rms velocity) near the nozzle exit $x = 1D$, where experimental measurements are available, a value of $l_0 = 0.05D$ was imposed for the unstructured mesh. On the two meshes, the comparisons between the two test filter strategies, which represent the objective of the present work, are conducted at the same integral length scale value.

For case B, a plenum is located downstream of the flame region to prevent influence of the outlet boundary conditions on the flame and constant ambient pressure is imposed at its outlet, see Fig. 4.3. Adiabatic boundary conditions are used for temperature and enthalpy at the wall and no-slip conditions for the velocity. Spalding wall functions are used for the SGS viscosity at the wall [269].

The precomputed and tabulated thermochemistry is built on premixed freely propagating laminar 1D flamelets at given reactants conditions. The calculation is performed using the CHEM1D solver [141] together with GRI3.0 mechanism [142] for the methane-air flame (case B) and San Diego mechanism [270] for the hydrogen flame (case A). A unity Lewis number is considered for every species when modelling the diffusive transport in both test cases. Under this assumption, the mixture fraction value is constant along a single flamelet and equal to its value in the reactants. A total of 100 and 50 points are used to discretize respectively the progress variable space (varying between 0 and 1) and its SGS variance (varying between 0 and $c(1 - c)$). For case B, a single methane-air flamelet at an equivalence ratio of $\phi = 0.75$ and reactants temperature of $T_{react} = 300$ K is considered. For Case A (lifted hydrogen jet flame in hot coflow), also the mixture fraction and its SGS variance are included as control variables, therefore a database of 300 freely propagating premixed flamelets is built, with reactants equivalence ratios spanning the flammability range, corresponding to a mixture fraction range $z = [0.1, 0.75]$ and stoichiometric conditions at $z_{st} = 0.474$. In this case, the mixture fraction represents the mixing between jet and coflow streams. Therefore, the reactants temperature and species mass fractions vary linearly with the mixture fraction, between their value in the coflow (oxydiser stream $z = 0$), to their value in the jet (fuel stream $z = 1$), as reported in Tab. 4.1. When tabulated, the mixture fraction z range is discretised with 160 linearly spaced points within the flammability limits, and its subgrid variance σ_z^2 is discretised using 15 exponentially-spaced points between 0 and $z(1 - z)$. Thermodynamic states outside the flammability limits are linearly interpolated between the values at the lean

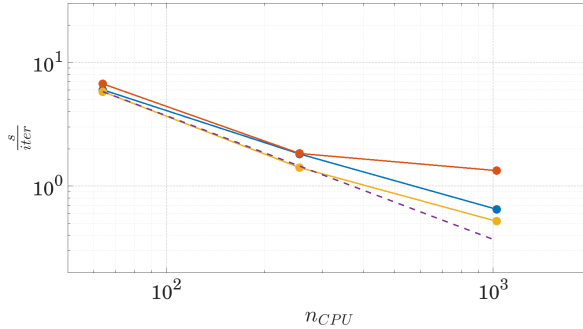


Figure 6.2: Time required, in seconds per iteration, to compute the modelling parameter β_c using differential (—) and algebraic (—) test filters, for different number of CPU-cores, n_{CPU} used in parallel. The scaling obtained using a static (fixed) value of β_c (---) and the ideal scaling (---) are also reported for reference.

(rich) flammability limit and air (fuel) conditions.

A typical computation of a characteristic flow through time for cases A and B takes about 4k and 12.5k CPU-hours (on block-structured meshes), respectively, using 256 cores in parallel on a 2.6 GHz Intel Xeon processor architecture. The CPU time for the different strategies for the definition of the model parameter are compared in Fig. 6.2. The two dynamic strategies show a similar computational cost, which is up to 26% higher than for the static case at 256 cores used in parallel. For larger number of cores the computation time using the differential filter is up to two times higher than for the algebraic filter due to non-optimised scalability within the algorithm currently implemented.

6.3. RESULTS

The objective in this section is to understand the capabilities of the differential test-filter of Eq. 3.20 in predicting the correct flow field as compared to the algebraic approach of Eq. 3.18. In order to have a detailed comparison and drive quantitative insights on the accuracy of the proposed filter, case A (lifted flame in hot coflow) is investigated first. In fact, a wide amount of data is available for this case from the experimental campaigns [77, 271], which includes radial profiles of velocity, temperature and mixture fraction, allowing to validate the proposed models. This case is thus analysed next before the bluff-body case. Note that the modelling constant β_c in Eq. 6.1 is evaluated for both test-filter approaches by the use of Eq. 3.15.

6.3.1. JET FLAME IN HOT COFLOW

This case is firstly analysed using the block-structured mesh in order to minimize possible interpolation errors in the computation of the coefficients in Eq. 3.18. An overview of the flow field as predicted by using the two test filters is presented in Fig. 6.3, showing midplane contours of temperature, modelling constant β_c , and SGS variance of c , σ_c^2 . As can be seen from the figure, the β_c field as predicted by the differential test filter appears to be very similar to that predicted by the explicit algebraic formulation. This similarity is attributed to the aforementioned minimization of interpolation errors by the use of

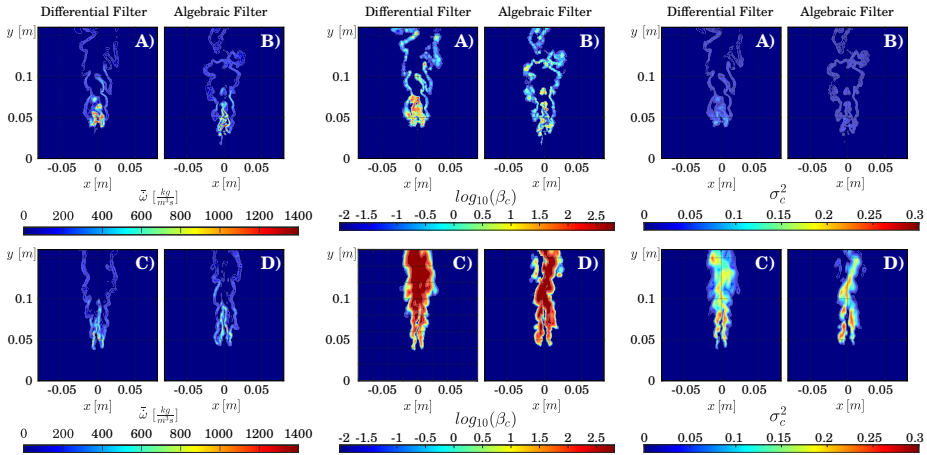


Figure 6.3: Comparison between instantaneous fields of filtered reaction rate of progress variable (left), β_c parameter (centre) and SGS variance of progress variable σ_c^2 (right), as predicted using the algebraic and differential filters, for Case A (jet in hot coflow). Results are shown for the unstructured (top) and block-structured meshes (bottom).

6

a block-structured mesh, and to the relatively high level of turbulence associated with the high bulk velocity of the fuel jet, leading to a relatively wide spectrum of scalar dissipation rate (SDR). Consequently, the instantaneous features of the subgrid variance of progress variable, whose value depends on the SDR, are also similar. The temperature contour in the same figure further reveals that the lift-off height is predicted similarly when either the algebraic or the differential filter are used. Radial profiles of mean mixture fraction, temperature, velocity, and their variances in time, shown in Fig. 6.4, further indicate that both filter methods perform very well when comparing LES predictions to the experimental data.

The results above lead to the two important following observations:

1. An algebraic test filter holds well for reacting cases with a relatively high level of turbulence and block-structured meshes;
2. The model proposed in Eq. 3.20 mimics well the same flow field, indicating that this equation is consistent and accurate despite the truncation to the third order.

Now that the two test-filter approaches have been validated against experimental results, further investigations can be conducted by replacing the block-structured mesh with an unstructured one in order to assess whether there is any difference in the results obtained by the use of the two test filters. It is worth to note that the unstructured mesh is constructed to maintain the LES filter size in the region of the flame equal or very similar to that of the block-structured mesh, which is in turn of the order of the laminar flame thickness. This way the two test filters can be directly compared for the same filter width. Instantaneous flow features in terms of progress variable reaction rate, β_c and σ_c^2 are shown in Fig. 6.3 (top row). When the differential filter is used, the lift-off height on the unstructured mesh is predicted at about the same position estimated when the

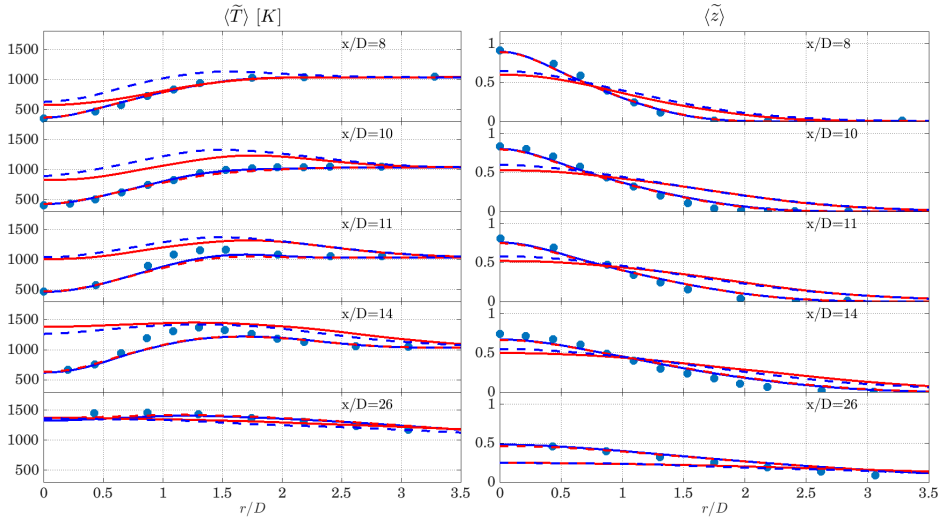


Figure 6.4: Radial profiles of time averaged temperature and mixture fraction at different axial locations from experimental measurements (symbols) and LES: unstructured mesh with differential (—) and algebraic (---) test filters; block-structured mesh with differential (—) and algebraic (---) test filters.

block-structured mesh was used (about 50 mm from the nozzle exit). Vice versa, when the algebraic filter is used, the lift-off height is predicted about 15 mm upstream. This is a consequence of somewhat lower values of β_c predicted in the latter case, resulting in lower values of SGS variance σ_c^2 (see Fig. 6.3, top-right), which in turn imply higher values of reaction rate in the flamelet model used and thus a more upstream flame stabilization. This shift is of course reflected in the statistics presented in Fig. 6.4. It is worth noting that overall better results are obtained by using the block-structured mesh, when compared to the experimental data. Nevertheless, this result is biased by selection of the inlet turbulence length scale value imposed to the synthetic eddies generator. A fine tuning of this parameter for the unstructured mesh, however, goes beyond the scope of this work, where the objective is to mimic the main effect of the modelling constant on the SDR (and consequently the SGS variance), which for this configuration is immediately reflected on the flame liftoff height discussed above. It is also worth noting that unstructured meshes are known to introduce more numerical diffusion (for the same filter size) than block-structured meshes [103, 272], which implies that the turbulence imposed at the nozzle exit may develop differently than for the block-structured mesh. The reader can find a mesh sensitivity analysis (for both BS and US meshes) and additional comments on this point in the Appendix Section.

Further insights on the behaviour of the model constant when algebraic and differential test filters are used is provided by looking at the distribution of β_c within the flame region in Fig. 6.5. Values are collected using several time snapshots only for the regions within the flammability limits and with the further condition $0.05 \leq \tilde{c} \leq 0.95$ in order to exclude points outside the flame front. Note that, being β_c scale-dependent in principle, its distribution is expected to be different when different meshes are used, which is evi-

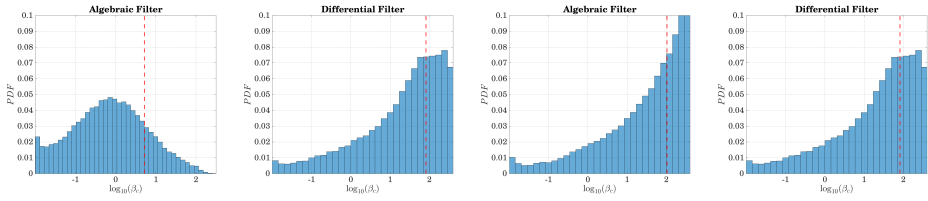


Figure 6.5: Distribution of β_c in the lifted flame for the jet in hot coflow configuration (case A) for unstructured (left) and block-structured (right) meshes, obtained using differential and algebraic test filters. Vertical dashed lines indicate mean values.

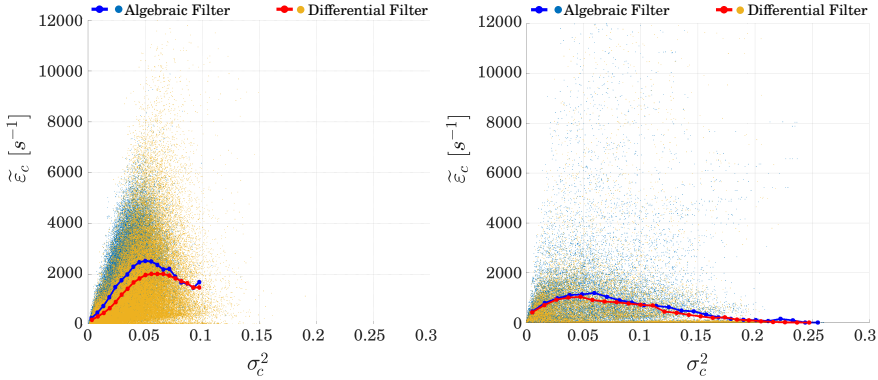


Figure 6.6: Scatter plots of subgrid scalar dissipation rate of progress variable, $\tilde{\epsilon}_c$ versus subgrid variance of c , σ_c^2 , as obtained on unstructured (left) and block-structured (right) meshes, for both algebraic and differential test filters. Conditional means are also shown.

dent from the figure. Some differences in the distribution of the modelling parameter β_c between algebraic and differential test-filter methods are visible already for the block-structured mesh case, Fig. 6.5 right. In particular, a clear peak is not distinguishable in the logarithmic plot in the case of the algebraic filter. Nevertheless, the mean value of β_c predicted in the two cases is similar. By looking at the scatter plots and conditional mean of SGS scalar dissipation rate in Fig. 6.6 (right), one can notice indeed that this quantity is predicted equivalently for any value of SGS variance. Similar scatter is also observed, which explains why the flow statistics predicted on the block-structured mesh are very similar when the two test filters are used, despite the differences observed in Fig. 6.5. A different relative behaviour is observed instead for the unstructured mesh cases. Here the distribution of β_c in Fig. 6.5 (left) leads to an overall lower mean value in the case of the algebraic filter, consistently with the instantaneous field contours observed for Fig. 6.3. By looking at the conditional means of subgrid SDR in Fig. 6.6 (left), one can notice that now this quantity is overestimated when the algebraic test-filter is used. This larger SDR justifies the lower SGS variances observed in the contours of Fig. 6.3, and thus the more upstream stabilization of the flame, with the use of the algebraic filtering.

From the above analyses one can conclude that, for conditions of relatively high turbulence (implying relatively wide turbulent kinetic energy spectrum), the algebraic test

filter provides similar results to the differential filter. Nevertheless, some different predictions are obtained on the unstructured grid, where the use of the differential filter leads to a more accurate flame lift-off height prediction compared to the algebraic filter strategy. This is attributed to the increased noise produced by interpolation operations for a fixed filter width, for such a mesh. For this reason, and by the investigation of the results presented, it is plausible to expect that as the mesh resolution converges towards DNS size (cell volume $\mathcal{V} \rightarrow 0$) and interpolation errors become less relevant, the two test filters might converge to the same result. In the next Section it will be shown that different considerations apply in conditions of weak turbulence.

6.3.2. WEAKLY-TURBULENT BLUFF BODY STABILISED FLAME

In [273] it was noted that a dynamic formulation for the estimation of β_c would not hold in conditions of weak turbulence due to the limited range of turbulence scales present. The weakly turbulent premixed case investigated experimentally in [75] (Case B in this work) is thus chosen to further assess the capabilities of the two test filters in predicting the the modelling constant β_c within the subgrid SDR model of Eq. 6.1. Only the block-structured mesh as discussed in Sec. 6.2 is used. The use of an unstructured mesh is expected in fact to affect the outcomes in terms of accuracy as observed for the jet flame in case B. Since relative differences in the flow field are already observed when using the two test-filters on the block-structured mesh for this case as will be discussed next, the use of an unstructured mesh for similar LES filter size is expected to amplify these differences and therefore this analysis is not repeated here.

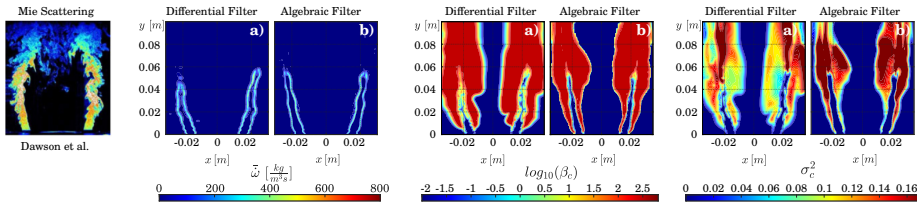


Figure 6.7: Comparison between instantaneous fields of filtered reaction rate (left), β_c parameter (centre) and SGS variance of progress variable (right), as predicted using the algebraic and differential filters, for Case B (bluff-body stabilised flame) on block-structured mesh. Mie scattering images taken from [75] are also shown on the left for reference.

Midplane contours of filtered temperature, β_c distribution (in logarithmic scale) and subgrid variance σ_c^2 as predicted by using algebraic and differential filter methods on the block-structured mesh are shown for the bluff-body case in Fig. 6.7. Unlike the case of the jet flame in hot coflow, here the two test-filter methods lead to different results also using the block-structured mesh. When the algebraic test filter is used, the dynamic procedure does not seem able to describe with sufficient resolution the local variations of the combustion model constant β_c across the flame region. This leads to significantly different distribution of subgrid variance, which in turns affects the resolved wrinkling of the flame as observed in the figure. By looking at the distribution of β_c in Fig. 6.8, one can notice that a well-defined peak value cannot be identified for the case of algebraic test-filter. Further inspection of the data shows that in many regions of the flame β_c

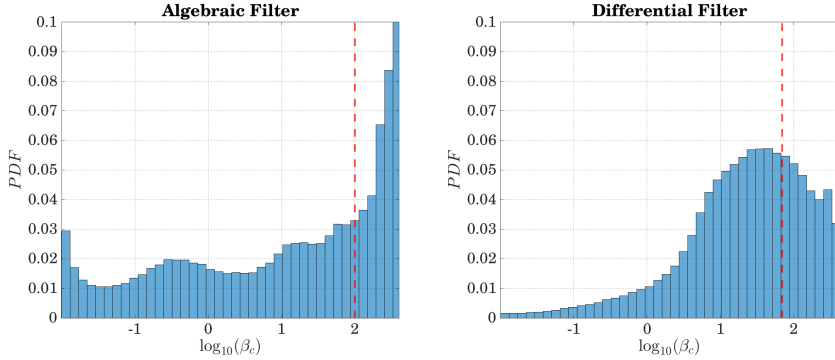


Figure 6.8: Distribution of β_c over the flame front in the bluff-body stabilised flame (case B) obtained using differential and algebraic test filters applied on block-structured mesh. Vertical dashed line indicate the mean value

6

oscillates between the imposed cutoff values, and $\beta_c \rightarrow 0$ in most of the domain (note that β_c in the numerical algorithm is truncated to $\varepsilon > 0$ to avoid a division by zero), implying a range of values across the flame is not predicted by the algebraic test-filter. This results in erroneous high values of the sub-grid SDR, and consequent low values of subgrid variance, which in turn implies the flame behaves in large extent as a laminar flame. This is not the case in the experiments for this configuration, as could be seen from the OH-LIF and Mie scattering images reported in [75] (See Fig. 6.7, left). Previous studies [246] highlighted the importance of the flame turbulence interaction, describing how the flame assumes a laminar-like behaviour close to the base of the bluff body and contributes to turbulence generation further downstream in the shear layer. In [246], from the comparison with the calculated non-reacting flow field, the flame appears to damp the weak turbulence generated in the shear layer around the bluff body, as a result of thermal expansion. On the other hand, the use of the differential filter results in a better calculation of β_c which now assumes a well-defined range of different local values across the flame front (Fig. 6.7), and a clear peak in its distribution is present (Fig. 6.8). Consequently, higher values of σ_c^2 are obtained in the flame region. Note that also in the present work the presence of the flame dumps the turbulence at the base of the bluff body, when compared to the non-reacting case (not shown). However, the formation of instabilities sustaining the turbulent structures in the shear layer can be observed further downstream in Fig. 6.7.

By looking at the scatter plots of subgrid SDR in Fig. 6.9, it is found that the conditional SDR is overestimated in the case of the algebraic test-filter at low values of sub-grid variance, while for values of σ_c^2 above about 0.04 algebraic and differential test-filters predict essentially the same result. This supports the argument that the two filters behaves differently in conditions of weak turbulence ($\sigma_c^2 \rightarrow 0$), and that the difference is caused by values of β_c saturating towards the lower cutoff limit at these conditions ($\beta_c \rightarrow 0$ implies larger values of $\tilde{\varepsilon}_c$). This behaviour, from the numerical point of view of the test-filter algorithm, is similar to that observed in Fig. 6.6 for the unstructured mesh. However, in that case low values of β_c were produced by noise arising from interpola-

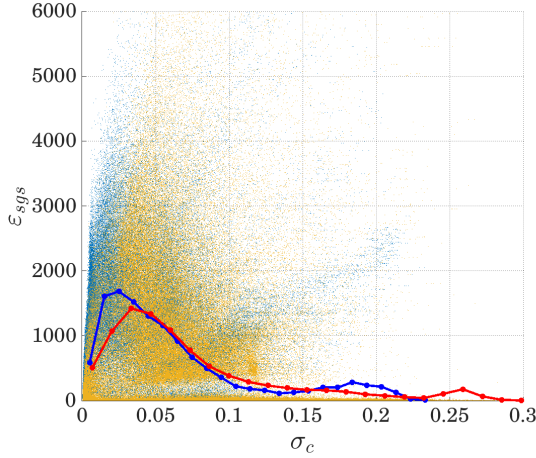


Figure 6.9: Scatter plots of subgrid scalar dissipation rate of progress variable, $\tilde{\epsilon}_c$ versus subgrid variance of c , σ_c^2 , as obtained on block-structured mesh for differential (●) and algebraic test filters (●). Conditional means are also shown: algebraic test filter (—), differential filter (—).

tion accuracy, resulting in overestimation of $\tilde{\epsilon}_c$ for a wider range of values of σ_c^2 . For the bluff body case investigated in this section, instead, overestimations of $\tilde{\epsilon}_c$ are observed only for relatively low values of σ_c^2 , indicating that the issue is in the estimation of the model constant in quasi-laminar regions. It is worth noting that additional tests were conducted (not shown) using a static approach with a value of β_c imposed as the mean of the values obtained from dynamic procedure. These tests resulted in a quite different flame structure as compared to the results from dynamic approach, indicating that imposing a single value for the combustion parameter is not trivial for this turbulence-evolving study case, thus stressing out the relevance of using robust dynamic approaches for this kind of combustion configurations.

6.4. SUMMARY

In this chapter, the use of a dynamic model was investigated for the closure of the subgrid scalar dissipation rate (SDR) of progress variable $\tilde{\epsilon}_c$, appearing in the transport equation of the progress variable subgrid variance σ_c^2 within the flamelet/presumed FDF LES framework for turbulent combustion. Two test-filtering strategies were compared: a standard algebraic filter approach and a differential filter based on a Fourier-like equation.

Large eddy simulations of two laboratory combustion systems, a lifted jet flame in hot coflow and a bluff-body stabilized premixed flame, demonstrated that the differential filter offers greater robustness across different conditions of turbulence intensities and mesh types. While both methods perform similarly under high turbulence levels on structured meshes, the algebraic filter is shown to be sensitive to mesh orthogonality and turbulence level, leading to degraded predictions under weak turbulence or on unstructured meshes. The differential filter, in contrast, consistently provides reliable

estimates of the model constant and better agreement with expected flame behavior, at the expenses of a modest increase in computational cost.

The findings highlight the importance of accurate subgrid variance modelling for flamelet based LES approaches with presumed FDF. The more robust dynamic model with differential filter is therefore used in each of the subsequent numerical studies in the present thesis. In the next chapter, the flamelet based LES framework with presumed FDF is extended to analyze differential diffusion effects in turbulent hydrogen flames.

7

DIFFERENTIAL DIFFUSION MODELLING

7.1. INTRODUCTION

This chapter focuses on differential diffusion modelling strategies within the flamelet-based LES with presumed FDF. As discussed in details in Chap. 2, hydrogen's high molecular diffusivity associated to sub-unity Lewis number in lean mixtures with air, results in redistributions of absolute enthalpy and mixture fraction along a laminar premixed unstretched 1D flamelet, whereas these quantities remain constant along the flame front for unity Lewis number conditions. In addition to these 1D effects, the higher hydrogen diffusion with respect to heat and the other species couples with flame stretch, resulting in further redistribution of local equivalence ratio and enthalpy, with consequent superadiabatic temperatures and reaction rate inhomogeneities. In particular, these two-dimensional effects may result in thermodiffusive instabilities arising from the coupling between differential diffusion and flame curvature, or in reaction rate increase with positive flame tangential strain rate (for negative values of the mixture Markstein length) [50, 54, 132]. Despite originating at molecular level, differential diffusion effects have been documented even under turbulent conditions [39, 52, 164, 165, 168, 223, 274]. These effects are not captured by conventional flamelet models that assume unity Lewis numbers for each species and therefore controlling variables. Nevertheless, these models have often been used for hydrogen flames under the assumption that turbulent transport dominates over molecular diffusion [178, 275, 276]. However, it remains unclear whether and under which conditions this assumption holds.

To address this, two differential diffusion models, originally developed in the context of DNS, are extended here to the LES framework with flamelet-based presumed FDF closure, to account for non-unity Lewis number effects on the diffusive fluxes of the controlling variables at the resolved level. As introduced in Sec. 3.2.3, model M1 is

Parts of this chapter have been published in *Combustion Theory and Modelling* 28 (6) (2024): 695-730 [101].

adapted from [124] and introduces a source term in the mixture fraction transport equation, while model M2 from [125, 134] applies corrections to the diffusive fluxes of mixture fraction, progress variable and enthalpy.

Two hydrogen combustion systems described in Chap. 4 are considered. First, a lean premixed flame in a slotted burner configurations [53] is simulated to assess the ability of the models to reproduce mixture fraction redistribution and the formation of thermally diffusive instabilities. Then, the lifted partially premixed flame in vitiated coflow [77], already studied in the previous chapters, is simulated, allowing the investigation of differential diffusion effects, accounted for at the thermochemistry level or at the resolved level, on flame stabilization mechanisms at higher turbulence intensity and partially premixed conditions.

7.1.1. FLAMELETS DATABASE

The thermochemical databases for the two study cases investigated in the present chapter are built using 300 premixed freely propagating laminar 1D flamelets with reactants equivalence ratios spanning the flammability range. For both cases temperature and species mass fractions in the reactants vary linearly with the mixture fraction, between their value in the oxidiser stream, where $z = 0$, to the value in the fuel stream, for which $z = 1$, as reported in Tables 4.1 and 4.2. Therefore, for the premixed slot burner case, all the flamelets have a constant reactants temperature of 300 K and the composition varies linearly between pure air and pure hydrogen, over a range of $z \in [0.007, 0.17]$. The stoichiometric condition is found at $z_{st} = 0.028$. For the partially premixed lifted flame case, the reactants temperature of the flamelets varies between 305 K in the fuel stream and 1045 K in the oxidiser stream (hot coflow). The reactants on the leaner flamelets are therefore at higher temperature and with a higher content of water, which is present in the coflow. In this case the mixture fraction spans a flammability range of $z \in [0.1, 0.75]$, with stoichiometric conditions at $z_{st} = 0.474$. It is worth noting that the high diffusivity of hydrogen can affect the inert mixing between fuel and oxidiser ahead of the flame, so that the mixture composition and enthalpy of the reactants may not vary linearly with mixture fraction. However, the inert jet/coflow mixing was shown in [77, 192] to be about linear with mixture fraction, due to the high content of nitrogen in both streams.

The high temperature and water content at low mixture fraction values results in a peculiar reaction rate map with a peak on the lean side, as shown in Figs. 7.1 and 7.2 b. Also, the effects of assuming non-unity Lewis number for each species in this database differ from the ones in the hydrogen/air case at constant temperature, shown earlier in Figs. 2.8-2.5. It can be seen from Fig. 7.2a that the mixture fraction decrease along each flamelet is lower than in the hydrogen/air case shown in Fig. 2.5, due to the relatively lower hydrogen content in the reactants associated with the presence of water, and predominant content of nitrogen. Moreover, Figs. 7.1 and 7.2b show that the inclusion of differential diffusion in the database results in a decrease of the reaction rate and its peak value for the lean flamelets, and a slight increase on the rich side. Also, when species non-unity Lewis number is considered in the manifold, the progress variable range over which the reaction occurs results to be slightly narrowed on the lean side as compared to the unity Lewis number case, while it appears broadened for rich mixtures. In a partially premixed case like the lifted flame in hot coflow, the flame stabilisation is

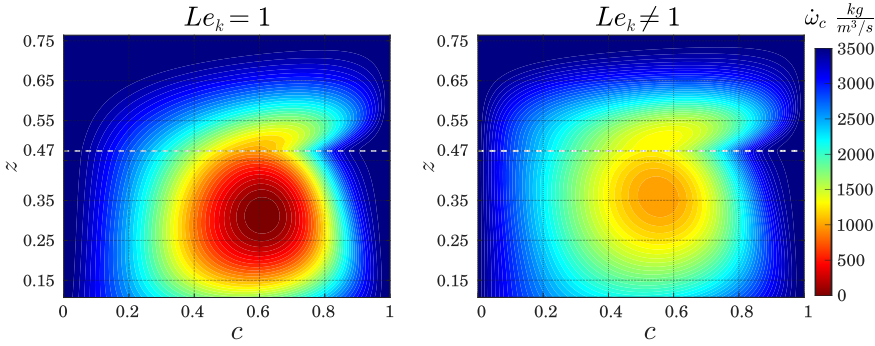


Figure 7.1: Contour plots of the scaled progress variable reaction rate in the c - z space for the flamelet database of the jet/coflow case with reactants conditions reported in Tab. 4.1. Flamelet calculations with unity Lewis number (left) and mixture averaged diffusion model (right). Results obtained using San Diego mechanism [270]. The stoichiometric condition, $z_{st} = 0.474$, is marked with the white dashed line.

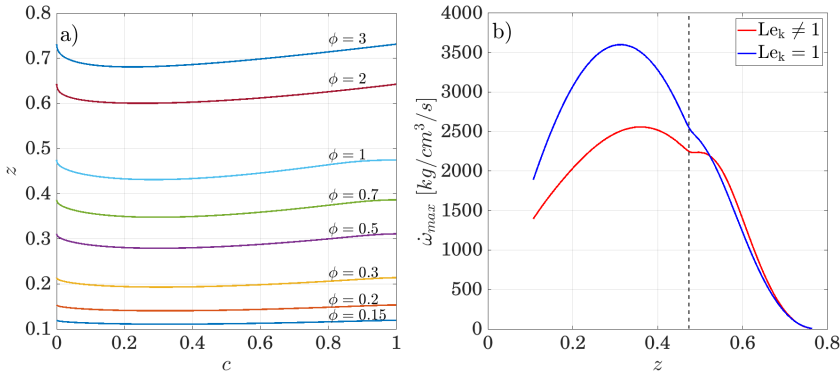


Figure 7.2: (a) Variation of mixture fraction in progress variable space across a freely propagating flame at different equivalence ratios, with the boundary conditions defined in Tab 4.1. (b) Maximum reaction rate at different reactants mixture fraction values obtained with and without differential diffusion modelling. Results obtained using the San Diego kinetic mechanism [270]. The stoichiometric condition $z_{st} = 0.474$ is marked as a vertical black dashed line

controlled by the equilibrium between convection and reaction rate associated to the local mixture fraction and progress variable values. Variations in these characteristic maps are therefore expected to affect the location at which the flame stabilises.

A parametric analysis in [260] further revealed the importance of the chosen kinetic mechanism on the lifted flame predictions. In the present work, the kinetic mechanisms DRM19 [277], Li *et al.* [278], Ó Conaire [279], and San Diego [270] were tested *a-priori* in the flamelet calculation and a sensitivity of the reaction rate map in terms of peak value and distribution in the progress variable/mixture fraction space was observed, in particular under the non-unity Lewis number assumption. Therefore, the effects of the inclusion of differential diffusion in the database can depend on the chosen kinetic mechanism. San Diego mechanism was selected for all the simulations of the partially

premixed case, following the aforementioned analysis and previous studies on hydrogen flames. Interested readers can find the comparisons of different mechanisms in Appendix B.2. For the premixed slotted burner the mechanism by Burke *et al.* [280] is used instead, in order to remain consistent with the reference DNS in [53].

7.2. NUMERICAL DETAILS

The Favre-filtered Navier Stokes equations including conservation of mass, momentum and absolute specific enthalpy (sum of sensible and formation enthalpies) are solved together with the transport equations of the controlling variables described in Sec. 3.2 using the low-Mach approximation and the finite volume method implemented in OpenFOAM v9. The pressure implicit with splitting operator (PISO) [281] algorithm is used for the pressure/velocity coupling and an external loop with at least 5 iterations per time step is used for the solution of the scalar transport equations. Second order central schemes are used for all convective terms, with flux limiters applied for the regions of high gradients across the flame. An implicit Euler scheme is used for temporal discretisation, following previous works [89, 241]. A constant time step is used to ensure a maximum CFL number below 0.35 everywhere in the computational domain. This corresponds to a timestep in the LES of $\Delta t = 2.0 \times 10^{-7}$ s for the lifted flame and $\Delta t = 1.0 \times 10^{-6}$ s for the slot burner. The subgrid scale stresses in the filtered momentum equation are closed using a one-equation model as in [89]. The one dimensional solver CHEM1D [141] is used for the flamelets computation, with the kinetic mechanisms described in Sec. 7.1.1. For the construction of the 4D table, $n_c = 100$ equispaced discretization points between 0 and 1 are used in the progress variable space, and $n_{\sigma_c} = 50$ points spanning between 0 and $\bar{c}(1 - \bar{c})$ are used for its subgrid variance space. The filtered mixture fraction space spans the flammability range, and a total of $n_z = 160$ and $n_z = 100$ equispaced discretization points are used for the lifted flame and the slot burner case, respectively. A total of $n_{\sigma_z} = 15$ points are used for the mixture fraction subgrid variance, spanning exponentially the range $[0, \bar{z}(1 - \bar{z})]$. Outside the flammability limits a linear interpolation of the tabulated quantities to their value in the fuel and oxidiser streams is performed.

The numerical domain for the lifted flame, shown in Fig. 4.1b, is a cylinder with a diameter of 183 mm (corresponding to 40 nozzle diameters D), which extends axially from the nozzle outlet to $50D$ downstream. The hot coflow enters the domain through an annular section extending radially from $0.5D$ to $20D$. The mesh resolution is chosen following previous LES works [192, 260] and consists of $N_x \times N_r \times N_\theta = 230 \times 60 \times 80$ cells in the axial, radial and azimuthal directions respectively, amounting to 897'000 cells in total. The cells are non-uniformly distributed so to cluster in the region of interest (up to $30D$ in the axial direction), and the spacing in the streamwise and radial directions, $\Delta_x \approx 0.6$ mm, $\Delta_r \approx 0.4$ mm, respectively, is of the order of the laminar flame thickness $\delta_l \approx 0.66$ -1 mm. Pope's 80% turbulent kinetic energy criterion [97] was applied on preliminary simulations to assess the quality of the mesh, as described in Sec 6.2. The ratio between modelled, k_{SGS} , and total turbulent kinetic energy (resolved plus SGS) was found below 0.2 in the region of interest. Boundary conditions for the lifted flame case are shown in Fig. 4.1. A turbulent inlet velocity profile is imposed at the nozzle exit, with synthetic turbulence imposed using the approach in [259]. The synthetic eddies generator takes a target of mean velocity profile, rms velocity profile and an integral length

scale as input. The measured average turbulent velocity axisymmetric profile reported in [131, 260, 268] is imposed at the nozzle outlet. The measured profile is scaled to ensure that the mass flow rate at the inlet of the domain equals that in the experimental case. The flame lift-off height was observed to be very sensitive to the turbulent inlet condition [260]. For this reason a preliminary analysis is carried out to ensure an accurate prediction of the jet spreading rate and its mixing with the coflow, and details of this analysis can be found in Appendix B.1. As a result of this analysis, other than the axial and radial rms velocity profiles, u' and v' , measured in [131], an integral length scale of $l_0 = 0.07D$ is imposed as target of the synthetic turbulence generator. Atmospheric pressure is imposed at the outlet, while zero-gradient conditions are imposed to outlet and lateral boundaries for all other scalars. Temperatures of 305 K and 1045 K are assigned at the jet and coflow inlets respectively, according to the experiment. The progress variable is set to zero at the inlets, and ignition is artificially imposed by creating a cylindrical sub region in the domain with $\tilde{c} = 1$. The mixture fraction is 1 at the jet inlet and 0 in the hot coflow. Each LES is run for a period of 4 flow-through times, defined as the time needed for a parcel of fluid travelling at the bulk speed on the centerline to reach a streamwise location of $40D$, approximately $t_{flow} \approx 16$ ms. Of these, one is used to pass the transient after ignition and the remaining three to collect statistics. Time-averaged data is further averaged azimuthally exploiting the axial symmetry of the domain.

The computational domain for the premixed slot burner case is shown in Fig. 4.2. The nozzle issuing the reactants has a height of $H = 8$ mm and a width of $4.5H$ in the z direction, and the rim has a thickness of 0.4 mm. A portion of the channel flow upstream of the nozzle exit, of length $2H$, is included in the domain. The domain is $12.5H$ long in the y direction and it extends for $15H$ downstream in the x direction. A structured hexaedral mesh is used with $N_x \times N_y \times N_z = 274 \times 140 \times 123$ cells in the three directions, respectively, amounting to a total of 4.8M cells. The cells are non-uniformly distributed to guarantee a size ranging from 0.2 mm to 0.5 mm in the flame region, where the estimated laminar flame thickness is $\delta_l \approx 0.66$ mm. In the y direction, 32 cells are placed across the channel width. The imposed boundary conditions are also shown in Fig. 4.2c. Atmospheric pressure with zero gradient velocity is imposed at the outlet, while symmetry conditions are imposed on all the lateral surfaces. The mixture fraction is imposed to $z = 0.0116$ ($\phi = 0.4$) at the inlets. The temperature is set to 300 K at the reactants inlet and to 1425 K at the products stream inlet. A uniform velocity of 3.6 m/s is imposed at the products stream inlet. A constant temperature of 300 K is imposed at the nozzle walls, together with no-slip conditions for the velocity field. The same strategy as for the lifted flame case is used to impose synthetic turbulence at the nozzle inlet. In this case, a preliminary LES of a developed turbulent channel flow, with velocity of $U_{bulk} = 24$ m/s, is performed to obtain average and rms velocity profiles to impose to the synthetic turbulent inflow generator. Only instantaneous fields are analysed in this case, therefore the LES are run for just two flow-through times of $t_{flow} = 5$ ms.

7.3. RESULTS

7.3.1. SLOT BURNER

First, the lean fully premixed slotted burner studied in [53] is simulated under the conditions reported in Tab. 7.1 employing the two differential diffusion modelling strategies introduced in Sec. 3.2.3 and summarized in Tab. 7.1. Differential diffusion effects were clearly observable in the DNS of this case [53], when compared to the equidiffusive case, for the occurrence of superadiabatic temperatures and self wrinkling due to thermo-diffusive instabilities, ultimately leading to a shorter flame length. The objective here is to investigate if the two modelling approaches are able to mimic these effects, in particular the coupling of curvature and mixture fraction redistribution at the resolved level, for an LES grid size in the order of the laminar flame thickness, at least from a qualitative point of view. In both models, the effects of differential diffusion are included at the thermochemistry level by assuming non unity Lewis number for every species, $Le_k \neq 1$, in the flamelet computation, using Eq. (2.16) to model diffusive transport. In the first model, M1_{RES}, a source term $\bar{\omega}_z$ is added to the mixture fraction transport equation, together with a modified diffusion coefficient D_z in line with the work in [124]. The mixture fraction source term is computed by using the resolved LES quantities in Eq. (3.22) directly. In the second approach, M2, the model proposed by Van Oijen and coworkers [125] is employed and extended to the LES context. A correction on the molecular diffusion flux is applied in this case to the transport equations of the controlling variables and enthalpy, as introduced in Sec. 3.2.5.

A qualitative comparison of instantaneous temperature and mixture fraction fields obtained using the two models is shown in Figs. 7.3 and 7.4, respectively, at random times. Both models appear to be able to reproduce the occurrence of super-adiabatic temperatures downstream of the flame front. These are predicted to be around 1600-1700 K by both models, in reasonable agreement with DNS results, reporting peak temperature values around 1700 K. The presence of temperatures higher than equilibrium (1425 K) can be only obtained by allowing local changes in the mixture fraction and using a thermochemistry database spanning a broader range of reactants mixture fraction values with $Le_k \neq 1$. Both models appear to be able to capture the coupling effect between flame front curvature and differential diffusion, giving origin to the development of thermo-diffusive instabilities in the form of bulges. From the contour plots in Fig. 7.4 it can be seen how the mixture fraction locally deviates from the nominal value of $z = 0.0116$ ($\phi = 0.4$) with a decrease upstream of the flame front and a re-increase towards the products. This also occurs in flat regions of the flame surface and is in line with what can be observed in 1D laminar flamelets in Fig. 2.8 and in [124]. In agreement

Table 7.1: Differential diffusion models used for the LES of the slot burner case [53].

	M1 _{RES}	M2
Flamelets	$Le_k \neq 1$	$Le_k \neq 1$
LES	correction of \bar{z} only Eqs. (3.21)-(3.23)	correction of \bar{c} , \bar{z} and \tilde{h} Eqs. (3.25)-(3.28)

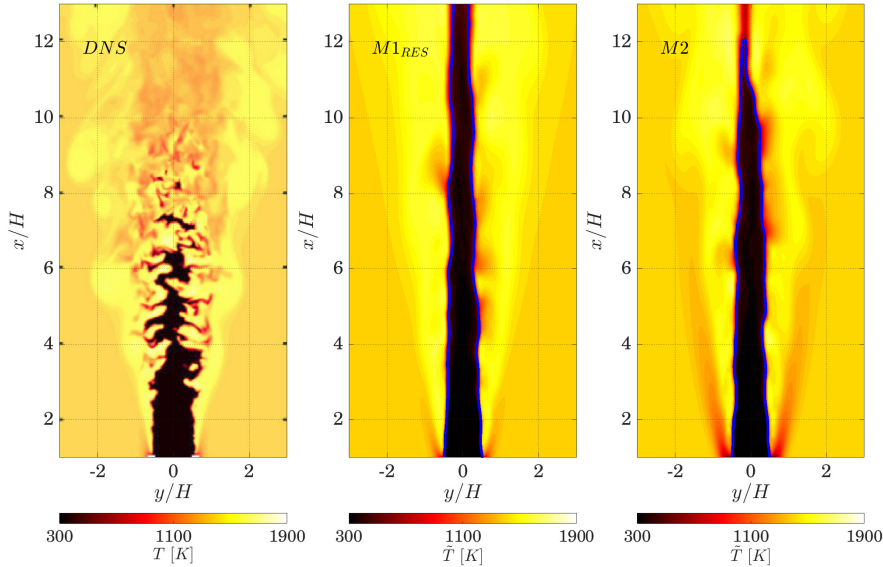


Figure 7.3: Midplane temperature contours from DNS [53] (left), and LES cases $M1_{RES}$ (centre) and $M2$ (right) of Table 7.1. Line: progress variable isoline $\tilde{c} = 0.5$ (—).

with DNS results and previous studies [149, 164], in the two LES cases a positive (convex) curvature towards the reactants is associated to a mixture enrichment and increase in temperature, while cusps lead to leaner mixture and to a reduction in temperature and reaction rate. Despite their different formulations, both models lead to very similar predictions in terms of flame front local curvature, broadening of mixture fraction range around the nominal value and super adiabatic temperature peaks, although model $M2$ predicts a slightly shorter flame. This can be assessed by looking at Fig. 7.3, where the flame front, identified by the progress variable isoline $\tilde{c} = 0.5$, shows a tip at around $13H$ for model $M2$, while it appears still open throughout the whole computational domain for model $M1_{RES}$. These results suggest that accounting for modification only in the mixture fraction field (model $M1_{RES}$) is sufficient to predict the correct coupling with curvature, at least for fully premixed cases without other sources of mixture fraction variations other than differential diffusion effects. Additional considerations will be provided for the partially premixed cases of Sec. 7.3.2.

Overall, the flame predicted by the two LES models appears less wrinkled than in the DNS. Although the coupling responsible for flame surface growth is qualitatively captured, at the present grid resolution the resolved wrinkling remains insufficient to reproduce the correct flame surface area and global consumption speed, ultimately leading to an overestimation of the flame length. In this comparison, one should note that the DNS data were not pre-filtered in Fig. 7.3, which partly explains why bulge formation in the LES occurs at larger scales than in the DNS. However, the observed behaviour is also to be attributed to the predicted growth of thermodiffusive instability at the resolved level.

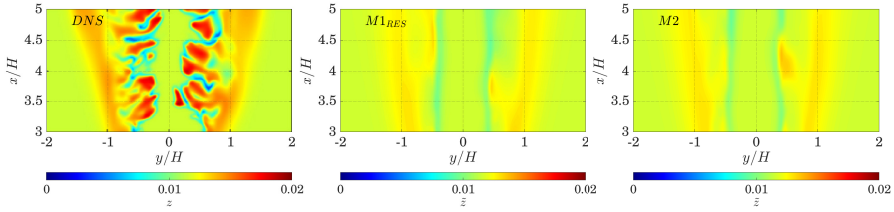


Figure 7.4: Midplane mixture fraction contours form DNS [53] (left), LES model M1_{RES} (centre) and LES model M2 (right) of Table 7.1.

In this regard, the LES filtering introduces a stabilizing effect dependent on the grid size which hinders the predicted self-wrinkling, as discussed in [282]. This highlights the need for subgrid modelling of differential diffusion effects. Such models should account for flame surface generation due to self-wrinkling induced by thermodiffusive instability and its interaction with turbulence at the subgrid level, together with the associated variations in filtered reaction rate and subgrid diffusive fluxes. The resulting subgrid surface generation should then feed back into the development of structures at the resolved scale.

In the considered presumed FDF LES approach, subgrid effects are only represented through the subgrid variance of the controlling variables, mainly c . This treatment primarily captures turbulence and filtering effects on the flame front, which tend to locally smoothen out the values of filtered reaction rate. However, the mechanism considered here differs, as differential diffusion may instead promote additional flame surface generation and thus locally increase the consumption speed. Recently, considerable research aimed at the development models for subgrid self-wrinkling induced by thermodiffusive instability. Examples include models developed for LES with thickened flame approaches [207], the scaling-law model proposed by Lapenna et al. based on stability analysis within a flame surface density closure framework [282], and DNS data-driven approaches [228] applied *a posteriori* within the FTACLES framework [283]. A detailed investigation of these aspects is beyond the scope of the present work, where the focus is limited to the prediction of mixture fraction and enthalpy redistribution at the resolved level. The incorporation of such models within the present flamelet LES framework may be explored in future work.

To further compare the influence of the two differential diffusion models on the predicted reacting states in the LES, scatter plots of filtered temperature versus mixture fraction are reported in Fig. 7.5, together with their conditional averages. Temperature values are reported only in the region of the flame, identified for simplicity here by $0.1 < \tilde{c} < 0.9$. The scatter plots are colored by the local flame front curvature in order to investigate the coupling between self wrinkling and diffusive transport. The filtered (resolved) curvature k is defined as [53] $k = \nabla \cdot \mathbf{n}$, where $\mathbf{n} = -\nabla \tilde{c} / |\nabla \tilde{c}|$ is the unit vector normal to the flame front and pointing towards the reactants. Scatter plots of mixture fraction versus progress variable are further reported in Fig. 7.5 (bottom), showing that both models appear capable to describe the mixture fraction decrease ahead of the flame front across the progress variable space and its return to the nominal value in the

products, $\tilde{z} = 0.0116$ (black dashed line in the figure). This effect of differential diffusion is also observable for an unstretched premixed flamelet (blue line in the figure) and is observed from the LES in the zero curvature burning states along the progress variable values in the same figure. Moreover, both models describe the interplay between flame front curvature and differential diffusion, which can be appreciated by the scatter of the mixture fraction values around the values corresponding to zero curvature states (green colored points). A positively curved flame front towards the reactants correlates to richer burning states, while negative curvature values (cusps) are associated to a decrease in mixture fraction, in line with DNS results. In particular, the LES is able to capture two features observed in the DNS [53] at high values of the progress variable $\tilde{c} > 0.8$, and associated with curvature effects:

- Burning states richer than the nominal mixture fraction, with an overshoot in the mixture fraction conditional average with respect to the nominal value, achieved through positive flame front curvature (red dots) and positive flame tangential strain,
- Burning states at mixture fraction values leaner than the laminar unstretched flamelet (blue line), as an effect of the negatively curved flame front sections (cusps, blue dots).

The same effects are also observed in the temperature scatter plots. The prediction of superadiabatic temperature is associated to the richer mixture reaching the equilibrium temperature. As qualitatively observed in Fig. 7.4, these rich burning states are caused by the coupling of mixture fraction diffusive flux and positive flame front curvature towards the reactants. In correspondence of flame cusps (regions of negative curvature towards the reactants) conditional temperature and reaction rate decrease instead.

Despite their different formulations, the two models give very similar predictions, with almost overlapping conditional averages. In particular, model M2 predicts states at slightly higher progress variable and temperature for mixture fraction values leaner than the nominal value, as compared to model M1_{RES}. These are associated to negative flame front curvature and suggest a more frequent occurrence of cusps predicted by model M2, which in turn can be explained by the correction in progress variable diffusion flux in model M2.

The analysis of the reacting states shows that both models of Table 7.1 are able to mimic qualitatively the differential diffusion effects on local redistribution of mixture fraction and, up to a certain extent, thermodiffusive instability, at the resolved level in a well-resolved LES of turbulent premixed flame. For such a case the corrections on the molecular diffusion in the controlling variables transport equations appears to be non-negligible with respect to the turbulent transport. As already observed from the contour plots in Figs. 7.3-7.4, the differential diffusion effects predicted by the two LES models appear to be milder than what observed from DNS results [53]. In general, the mixture fraction range around the nominal value is quite narrow and at low progress variable values the zero curvature burning states do not reach the lean mixture fraction values corresponding to the the laminar unstretched flamelet. This suggests that the corrected diffusive flux of the controlling variables imposed by the two models may be too mild, being it only dependent on the resolved curvature. As mentioned earlier, a model for the

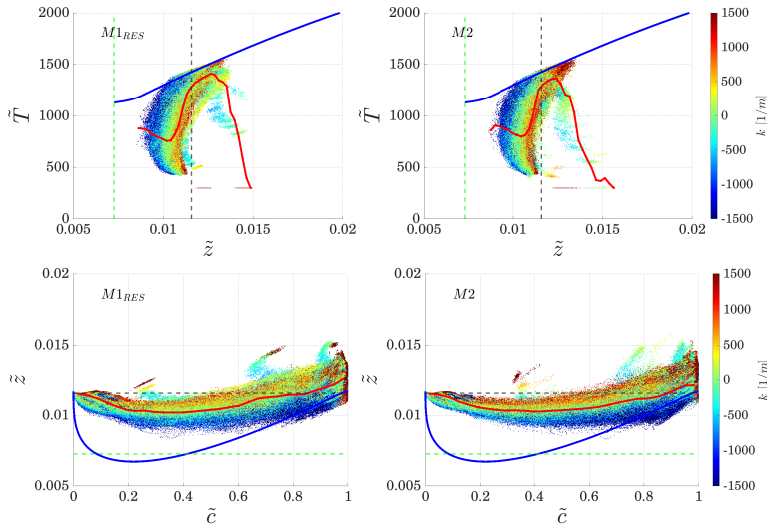


Figure 7.5: Scatter plots of filtered temperature versus filtered mixture fraction (top) and mixture fraction versus filtered progress variable (bottom) obtained from the LES of the premixed slot burner using the two differential diffusion approaches of Table 7.1. Only values within the flame, identified using $0.1 < \tilde{c} < 0.9$, are considered. The black and green dashed lines mark the nominal mixture fraction, $z_l = 0.0116$, and the lean flammability limit, $z_l = 0.007$, respectively. In the upper plots, the blue line represents the equilibrium temperature at different reactants mixture fraction values. In the bottom plots, the blue line represents the mixture fraction values along the progress variable computed for an unstretched laminar premixed 1D freely propagating flamelet at nominal reactants equivalence ratio $\phi = 0.4$, with mixture-averaged model to account for differential diffusion, see Fig. 2.8. The red line represents the conditional average.

7

interaction between curvature and differential diffusion at the subgrid level may provide higher resolved diffusive fluxes, ultimately leading to better LES predictions in terms of mixture fraction redistribution and flame front wrinkling. The effects of an increase of the diffusive fluxes corrections in model M2, are shown in a sensitivity analysis reported in Appendix B.3. In the next section, the differential diffusion models are tested on a partially premixed lifted flame at higher turbulence conditions, where variations of mixture fraction are also due to the turbulent mixing between jet and coflow and it is unclear whether this would hinder or strengthen the effects of differential diffusion.

7.3.2. LIFTED FLAME IN VITIATED COFLOW

FLAME STRUCTURE

The lifted flame in vitiated coflow [77] under the conditions reported in Tab. 4.1 is first simulated with the assumption of $Le_k = 1$ for all species k both in the thermochemical database and in the LES equations (MLe1 model in Tab. 7.2). In this case, the LES predicts a lifted flame stabilising at about $x = 10D$, as can be seen from both instantaneous and time averaged temperature contours in Fig. 7.6. In this setup the flame stabilisation is controlled by fuel/jet mixing until the mixture enters the flammability range and the flame stabilises in regions where the reaction rate and local convective transport balance each others. Flame stabilisation location and flame length can be further assessed

by looking at the average reaction rate contour plots, also shown in Fig. 7.6. A region of strong mean reaction rate, $\langle \widetilde{\omega}_c \rangle = 980 \text{ kg/m}^3/\text{s}$ is observed at the flame base, in correspondence of lean premixed conditions, $\langle \widetilde{z} \rangle = 0.25$. The inner part of the flame brush is observed instead to burn close to stoichiometric conditions or slightly rich, but with milder values of reaction rate. This stabilisation mode is consistent with other studies in literature [130], identifying a triple point at the base of the flame and an inner branch stabilizing in diffusion mode.

Turbulent mixing and reaction processes can be further assessed by comparing average and rms mixture fraction values along the centreline obtained from the LES with those from experimental measurements [260]. These comparisons are shown in Fig. 7.7. The central jet can be divided in a region of inert jet/coflow mixing, followed by a reactive zone and a downstream region where the products of combustion mix with the coflow stream. As the fuel jet spreads and mixes with the coflow, the predicted centreline mixture fraction decreases at the correct rate from $\widetilde{z} = 1$ at the fuel nozzle exit to around $\widetilde{z} = 0.8$ at flame anchoring point ($x = 10D$). At this location the flow accelerates due to thermal expansion and a decrease in the rate of jet spreading and centreline mixture fraction decay is correctly captured by the LES. Similarly, the mixture fraction rms along the centreline increases from the nozzle outlet due to turbulent mixing and reaches a local maximum in correspondence of the flame base, which is also well predicted by the LES. The average temperature values on the centreline in Fig. 7.7 as predicted by the LES are also in very good agreement with the experimental results. The rate of temperature increase in the streamwise direction due to inert jet/coflow mixing is well captured until the flame base location at $x = 10D$. The temperature then reaches a maximum value of 1500 K at the flame tip, followed by a slight decrease due to the mixing between the combustion products and the coflow stream. The temperature rms peak and its location are also predicted well by the LES. This quantity increases first due to turbulent inert mixing followed by a steeper gradient near the flame base, and then decreases downstream, where the mixture temperature becomes more homogeneous.

Computed radial profiles of average and rms temperature and mixture fraction are compared to experimental values in Fig. 7.8. A very good agreement between LES and experiments is observed for the average mixture fraction and its rms at any axial location, suggesting that the LES correctly captures the shear layer thickness and its development between jet and coflow. For the temperature profiles, a good agreement between LES results and experiments is found at $x = 8D$, where inert jet/coflow mixing takes place and a peak of rms temperature T_{rms} is observed on the shear layer. In the experiment the flame base is observed around $x = 11D$. The presence of the flame can be identified in these plots by the overshoot of temperature with respect to its value in the coflow stream. As can be observed from the figure at $x = 11D$, the LES slightly overpredicts the flame lift-off height, which also results in a more significant underestimation of temperature rms at $x = 11D$. For more downstream locations, however, both temperature and its rms are well reproduced by the LES, including the double peak in the $\widetilde{T}_{\text{rms}}$ profile observed at $x = 14D$, identifying inner flame branch and outer mixing layer between combustion products and hot coflow.

The above comparisons suggest that the premixed flamelets with presumed FDF approach without differential diffusion treatment is already satisfactory to predict the main

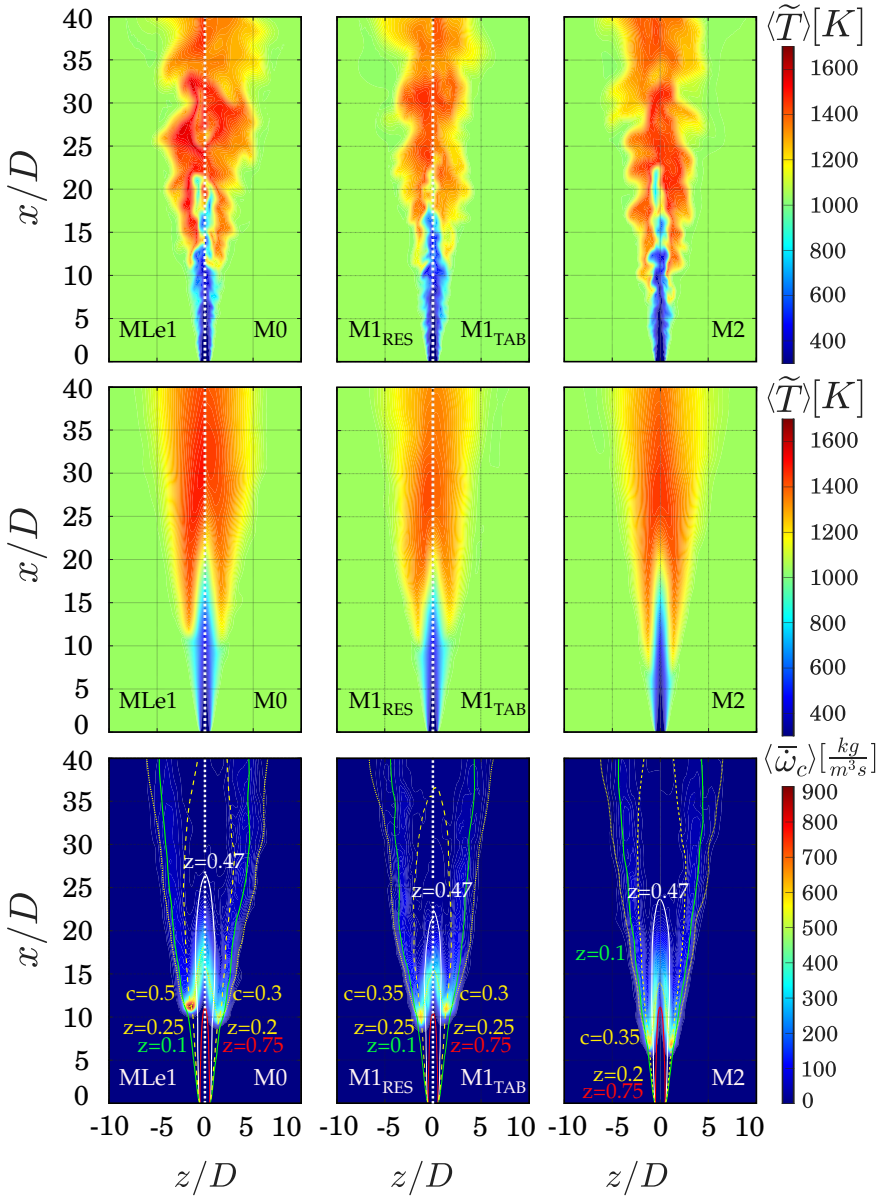


Figure 7.6: Mid-plane contours of instantaneous (top) and time-averaged (centre) temperature, and averaged filtered reaction rate (bottom) obtained from LES using the models for differential diffusion of Table 7.2. Solid isolines represent lean flammability limit ($-\langle \tilde{z} \rangle = 0.1$), rich flammability limit ($-\langle \tilde{z} \rangle = 0.75$), and stoichiometric condition (white line, $\langle \tilde{z} \rangle = 0.47$). Dashed isolines represent progress variable ($\langle \tilde{c} \rangle$) and mixture fraction ($\langle \tilde{z} \rangle$) at the location of maximum reaction rate.

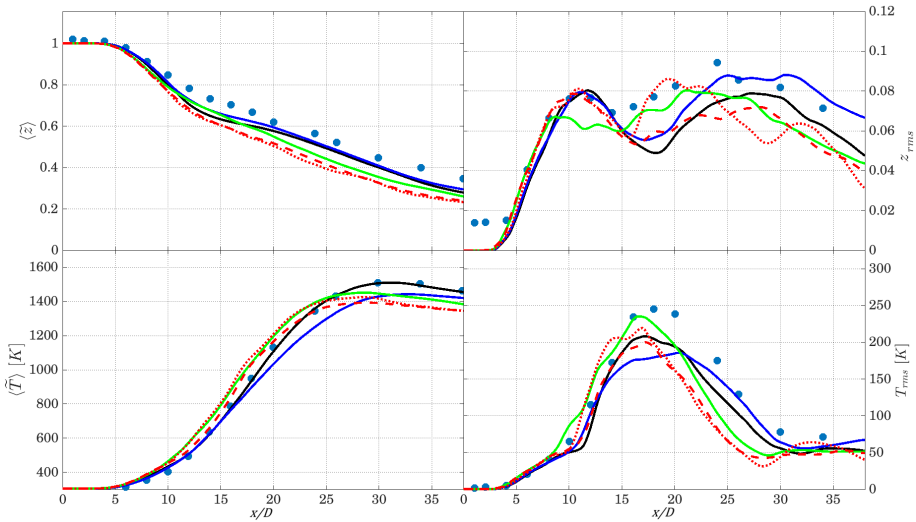


Figure 7.7: Centreline profiles of mean and rms temperature and mixture fraction. Symbols: measurements [77]. Lines: LES results from models MLe1 (—), M0 (—), M1RES (···), M1TAB (---), and M2 (—) of Tab. 7.2.

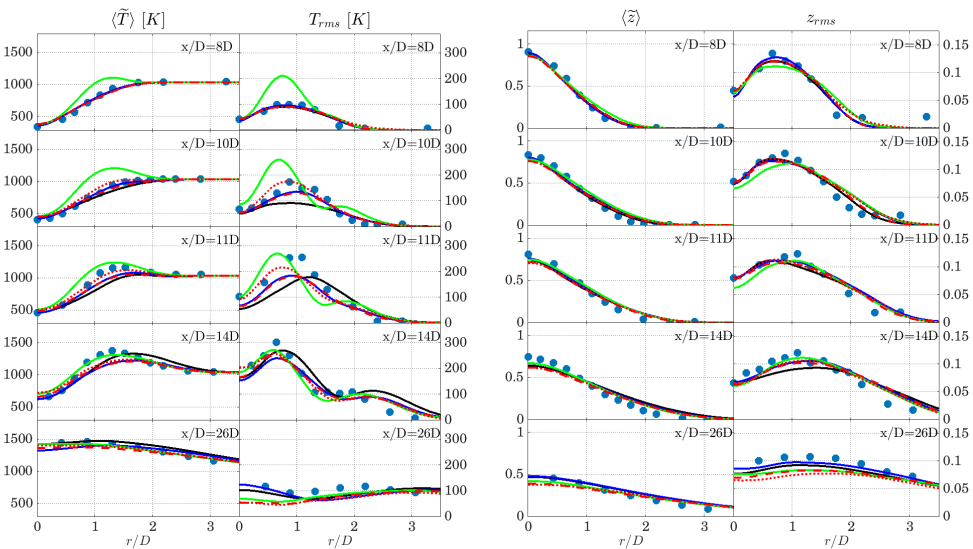


Figure 7.8: Radial profiles of time averaged and rms values of temperature and mixture fraction. Symbols: measurements [77]. Lines: LES results with model (—) MLe1, (—) M0, (···) M1RES, (---) M1TAB, (—) M2.

flame features for this test case. With respect to the slot burner analysed in Sec. 7.3.1, the lifted flame in this section is characterized by higher levels of turbulence and it is highly controlled by turbulent mixing, which might hinder the effects of differential diffusion observed in Sec. 7.3.1. The influence of differential diffusion modelling on the predicted flow field is investigated next to shed light on this point.

DIFFERENTIAL DIFFUSION MODELLING

Further simulations of the lifted flame were performed to assess the effects of differential diffusion models on the prediction of flame features. In addition to model MLe1 introduced earlier, four modelling approaches are tested and summarized in Tab. 7.2. Models M1_{RES} and M2 are the same used in Sec. 7.3.1 and listed in Tab. 7.1. In model M0 the flamelets database is built by considering non-unity Lewis number for every species, $Le_k \neq 1$, but no differential diffusion model is included in the LES transport equations. This way the influence of the thermochemistry on the results can be assessed, as it was shown in Fig. 7.1 that the reaction rate of progress variable varies significantly between the cases with $Le_k \neq 1$ and $Le_k = 1$. Model M1_{TAB} uses the model correcting mixture fraction diffusive flux as for model M1_{RES}, see Sec. 3.2.3, but the term $\bar{\omega}_z$ in Eq. (3.22) is computed from flamelets, pre-integrated and tabulated consistently with Eq. (3.6).

Mean centreline and radial profiles of temperature, mixture fraction and their rms as predicted by the five models of Tab. 7.2 are compared to experimental data in Figs. 7.7 and 7.8, respectively. The mixture fraction decay along the centreline, mainly associated to mixing between jet and coflow streams, is captured fairly well by all models. Interestingly, the models including differential diffusion at the resolved level M1_{RES}, M1_{TAB} and M2, predict a slightly steeper mixture fraction axial decay rate and temperature increase in the region upstream of the flame base, $4D < x < 10D$, as compared to models MLe1 and M0. This reveals that the predicted inert jet/coflow mixing is mildly enhanced by the modified diffusive terms in the controlling variable transport equations. For similar reasons a slightly steeper increase of mixture fraction rms is observed for models M1_{RES}, M1_{TAB} and M2. These differences in the inert mixing cause the flame to stabilise slightly more upstream in the cases with enhanced diffusive flux, which in turn results in the differences observed between the various models downstream of the flame stabilisation point ($x > 10D$).

The comparison between models M0 to MLe1 of Tab. 7.2 highlights the effect of including differential diffusion in the thermochemistry. As observed in Fig. 7.7, model M0 predicts the flame stabilisation point slightly more upstream, at $x \approx 10D$ as compared to $x \approx 11D$ predicted by model MLe1. Moreover, the flame for case M0 is slightly longer, see temperature contours in Fig. 7.6. Also, mean temperature along the centre-

Table 7.2: Differential diffusion (DD) models used for LES and flamelets.

	MLe1	M0	M1 _{RES}	M1 _{TAB}	M2
Flamelets	$Le_k = 1$	$Le_k \neq 1$	$Le_k \neq 1$	$Le_k \neq 1$	$Le_k \neq 1$
LES	no DD	no DD	\tilde{z} corrected Eq. (3.22) resolved	\tilde{z} corrected Eq. (3.22) tabulated	$\tilde{c}, \tilde{z}, \tilde{h}$ corrected Eqs. (3.25)-(3.28)

line increases at a slower rate for model M0 as compared to MLe1, and reaches a lower peak value. Similar considerations can be made by looking at radial profiles in Fig. 7.8. This different behaviour is explained by an overall reduction of reaction rate values when non-unity Lewis number is used in the flamelet database, as observed in Fig. 7.1. Nevertheless, model M0 also predicts the flame stabilisation point more upstream than model MLe1 as discussed earlier, which would suggest a higher reaction rate instead. This is explained as follows. Looking at Fig. 7.1, when differential diffusion is taken into account ($Le_k \neq 1$), the peak value of reaction rate decreases by about 30% as compared to the case at $Le_k = 1$, but its location also shifts towards the stoichiometric condition and lower values of progress variable, $c \approx 0.55$, in the $c - z$ space. For $c < 0.4$ the reaction rate in the case with differential diffusion is weaker on the lean side ($z < 0.25$) and stronger on the rich side ($z > 0.47$), as compared to the values for $Le_k = 1$. By looking now at the reaction rate contours in Fig. 7.6, one can notice that the intensity of the reaction rate at the flame base on the lean premixed side (towards the mixing layer between jet and coflow) decreases by around 47% for model M0 as compared to model MLe1, while it is about the same in the innermost rich region. The highest reaction rate at the flame base is found for $\langle \tilde{c} \rangle \approx 0.3$ in model M0 as compared to $\langle \tilde{c} \rangle \approx 0.5$ for model MLe1, and at slightly leaner conditions ($\langle \tilde{z} \rangle \approx 0.20$ as compared to $\langle \tilde{z} \rangle \approx 0.25$ in model MLe1). This causes the stabilisation point to slightly move radially outwards (leaner conditions and lower progress variable) where the lower jet velocities allows the flame to move upstream. In general, the main effect of including differential diffusion in the thermochemical database is an overall reduction of the reaction rates, in particular for lean states in the mixture fraction space, which for the investigated flame leads to lower temperature gradients as compared to the case without differential diffusion.

The comparison between models M1_{RES} and M1_{TAB} allows to assess the sensitivity of the source term $\dot{\omega}_z$ in Eq. (3.22) to its implementation in the LES. When this source term is tabulated (model M1_{TAB}), the flame is predicted to stabilise at $x \approx 11D$ (as compared to $x \approx 10D$ for model M1_{RES}), which is closer to what observed in the experiments and for model MLe1. As shown in Fig. 7.7, both models M1_{TAB} and M1_{RES} predict a steeper increase of temperature along the centreline with respect to model M0, and in better agreement with the experiments up to $x \approx 25D$. However, both models underestimate the maximum temperature and mixture fraction values as compared to the experiments. Similar considerations apply for the radial temperature profiles in Fig. 7.8. This behaviour is consistent with the reaction rate contours observed in Fig. 7.6, where one can observe that both models M1_{RES} and M1_{TAB} predict a maximum reaction rate at the flame base about 25% higher than that predicted with model M0. It is interesting to notice that the strongest reaction rate for models M1_{RES} and M1_{TAB} is found for values of progress variable similar to that observed for model M0, but at slightly richer conditions. This can only be associated to the different distribution of mixture fraction due to the introduction of the source term, since the same thermochemical database is used for models M0, M1_{RES} and M1_{TAB}. This results in a stronger mixing predicted by the latter two, which can be observed from the steeper decay of mixture fraction along the centreline observed in Fig. 7.7, and from the shorter jet core (see for example iso-line of mixture fraction at $\langle \tilde{z} \rangle = 0.47$ in Fig. 7.6). Overall, no significant differences are observed in the predictions from models M1_{RES} and M1_{TAB}, except for the aforementioned lift-off

height.

Final considerations are provided for model M2 of Tab. 7.2, which yields more significant differences with respect to the other models. In this case, the flame stabilisation point is predicted significantly more upstream, at $x \approx 5D$, as compared to the other models, as can be observed in Fig. 7.6. Nevertheless, a very good agreement in temperature and mixture fraction radial profiles, and their rms values, is still obtained at $x \geq 14D$, as observed in Fig. 7.8. Similarly to what observed for models M1_{RES} and M1_{TAB}, accounting for differential diffusion models at the resolved level leads to the prediction of steeper axial gradients of temperature (Fig. 7.7) as compared to model M0, where differential diffusion is only included through the thermochemical database. Furthermore, the flame predicted by model M2 presents a longer inner branch burning at rich conditions with respect to that predicted by the other models, as can be seen from the average reaction rate contour plots in Fig. 7.6. The peak value of reaction rate at the flame base for model M2 looks about the same of that predicted by models M1_{RES} and M1_{TAB}, where only the mixture fraction transport equation is corrected. The more upstream flame stabilisation location predicted by model M2 must therefore be explained by the combined correction on progress variable and mixture fraction transport equations. In particular, further investigations (not shown) indicate that the correction in model M2 leads to a higher radial mixture fraction diffusive flux, which slightly increases the local mixture fraction value on the leaner side of the jet/coflow mixing layer (see Fig. 7.8). Moreover, the increased progress variable diffusive flux modelled through the β_e gradient in Eq. (3.25) enhances the transport of progress variable across the flame, from products to reactants, leading to the stabilisation of the flame more upstream. This aspect is better investigated through the scatter plot analysis in the next section. Further sensitivity to the model parameters can be found in Appendix B.3.

7

7.3.3. FLAME BURNING STATES

Scatter plots of temperature, reaction rate and progress variable as predicted by the five LES models of Tab. 7.2 are shown in mixture fraction space in Fig. 7.9. The scatter plots are colored by the axial distance from the nozzle exit, $x/D = 0$, in order to distinguish between different regions in the domain. Conditional means are further reported in Fig. 7.10 for easiness of comparison between the various models. One can notice for all five models that equilibrium temperature is only reached at lean conditions (as also seen in experiments [77]). A peak temperature of 1600 K is predicted by model MLe1, consistently with the results described in Sec. 7.3.2 and in good agreement with experimental measurements [77]. The models M0, M1_{RES}, M1_{TAB} and M2, including differential diffusion in the thermochemical database, predict lower temperature values than model MLe1, in particular near stoichiometry and at rich conditions, which results from the lower reaction rate peak values in the thermochemical database. Model M2 predicts overall higher temperature values at stoichiometry and on the rich side, $\bar{z} > 0.47$. Moreover, burning states are found for this case up to $\bar{z} \approx 0.8$, which is a result of the more upstream stabilisation of the flame. This different behaviour for model M2 is a consequence of the corrected diffusion flux in the progress variable equation, which enhances the flux of progress variable across the flame front, from the outside (products) to the core of the jet (reactants), leading to the corresponding higher values of progress vari-

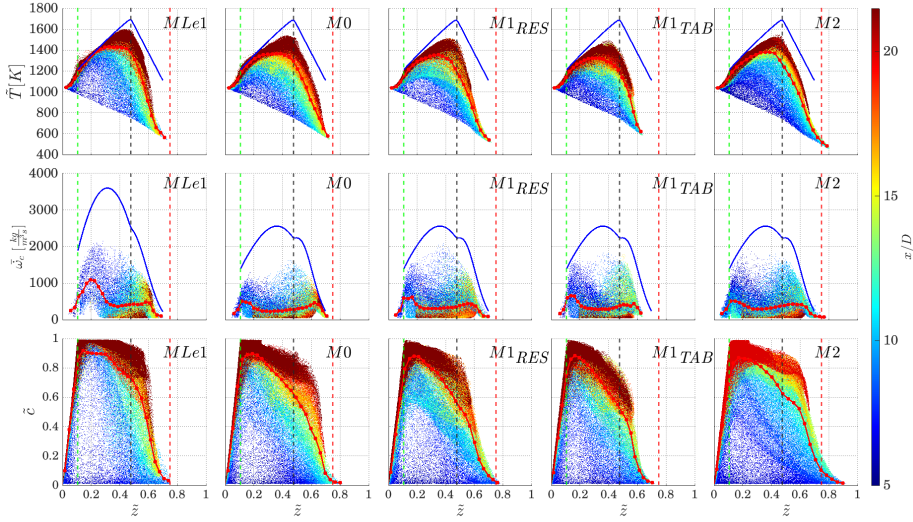


Figure 7.9: Scatter plots of temperature \tilde{T} (top), progress variable reaction rate $\tilde{\omega}_c$ (centre) and progress variable \tilde{c} , (bottom) versus mixture fraction \tilde{z} , coloured by the distance from the nozzle exit x/D . Only temperature values for $\tilde{c} > 0.1$ are shown to exclude unburnt conditions. Reaction rate values are only reported for the flame region, identified as the region where $0.1 < \tilde{c} < 0.9$. Vertical dashed lines refer to the flammability limits and the stoichiometric condition. Conditional averages (---), equilibrium flamelets temperature (---) and maximum reaction rate in the flamelet database (---) are also shown.

able near the rich flammability limits as compared to the other models (see scatter plots of progress variable). Note that the correction term is non zero also outside the flammability range. Also, fully burnt states are not observed on the rich side for all models due to the fact that quick turbulent mixing in the inner rich branch of the flame decreases the mixture fraction values as the reaction progresses.

Scatter plots of reaction rate are reported for $0.1 < \tilde{c} < 0.9$ and only show values higher than 2% of the maximum reaction rate in order to exclude points outside of the flame front. A bimodal behaviour is observed in the conditional mean of reaction rate where the two peaks identify respectively the lean premixed flame burning mode at the flame base ($x/D \approx 10$, blue color) and the rich inner branch of the flame extending to an axial location of $x/D \approx 20$. The comparison between the conditional means of the models with (M_0 , M_{1_TAB} , M_{1_RES} , M_2) and without (M_{Le1}) differential diffusion (see Fig. 7.10) reveals that the main difference in burning states is on the lean side, where the peak of conditional mean is stronger and observed at higher values of \tilde{z} in the case without differential diffusion. On the contrary, the value and location of the peak on the rich side is similar between the cases with and without differential diffusion. This also indicates that the stronger effect on the flame burning modes is given by the thermochemical database. In contrast, whether and how differential diffusion is taken into account at the resolved level seems to have negligible effect on the lean side of the flame, while some influence is observed on the rich side. In particular, including correction in the resolved diffusive fluxes seems to overall move the peak of reaction rate in rich premixed mode towards

leaner values, and this shift is less marked when corrections are applied to both fluxes of mixture fraction and progress variable (model M2). This might be due to the fact that model M2 predicts burning samples over a broader range of mixture fraction values in the rich side as compared to models $M1_{RES}$ and $M1_{TAB}$, as observed in Fig. 7.10.

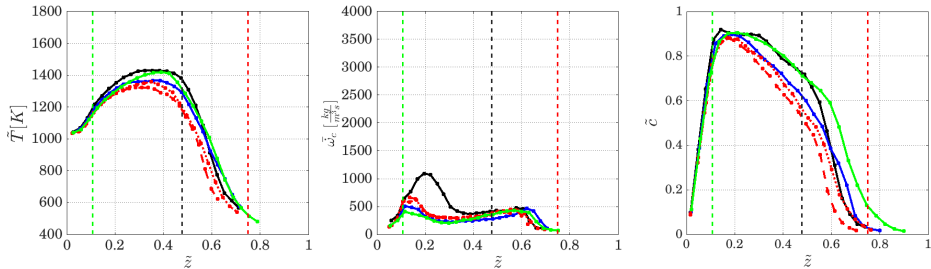


Figure 7.10: Conditional averages of temperature, reaction rate and progress variable in mixture fraction space, obtained from LES with models $MLe1$ (—), $M0$ (—), $M1_{RES}$ (···), $M1_{TAB}$ (- -) and $M2$ (—) of Tab. 7.2. Vertical dashed lines refer to the flammability limits and the stoichiometric condition.

7.4. SUMMARY

In the present chapter the effects of differential diffusion modelling (DD) within flamelet-based LES with presumed FDF of turbulent hydrogen combustion was investigated. Two representative cases were considered to evaluate the performance of DD models across different combustion regimes: a fully premixed, turbulent, thermo-diffusively unstable flame in a slot burner configuration, and a lifted partially premixed flame in a vitiated coflow.

In the first case, differential diffusion effects were introduced both in the thermochemical database and at the resolved LES level using two different correction strategies, one limited to the mixture fraction, model M1, the other also involving enthalpy and progress variable, model M2. These models successfully captured relevant features associated with thermo-diffusive instability, including flame front wrinkling, curvature-driven mixture fraction redistribution, and super-adiabatic temperature peaks. The similarity of results between the two modelling approaches, suggests that for fully premixed conditions (without enthalpy losses), a simple correction on the mixture fraction may be sufficient.

The second case presented a more complex scenario. Here, turbulent fuel-oxidiser mixing dominates the flame stabilization process, diminishing the relative impact of differential diffusion. In fact, first and second order statistics of temperature and mixture fraction are already in very good agreement with experimental measurements when differential diffusion is not taken into account neither at resolved nor at thermochemistry level. While the overall sensitivity to differential diffusion modelling is reduced compared to the premixed case, some effects are observable. Including differential diffusion only at thermochemical level does not affect jet/coflow mixing, but results in an overall reduction of the reaction rate and a consequent reduction of the temperature gradients. When the correction on the mixture fraction diffusion is included at the resolved level,

via model M1, the jet/coflow inert mixing appears mildly enhanced and an increase in the reaction rate at the flame base and temperature gradients is observed. When also the diffusion flux of progress variable is corrected at resolved level, model M2, the increased diffusion flux of progress variable from the products to the reactants causes an upstream shift of the flame stabilisation point as compared to the other tested models. The models for differential diffusion assessed in the present study were originally derived for premixed cases, where relatively small mixture fraction variations around the nominal value and well within the flammability range are expected. The analysis conducted in the present work suggests that additional treatment might be necessary in partially-premixed cases where the mixture fraction spans values across the entire flammability range.

In the present study the developed models were observed to qualitatively capture the effects of coupling between differential diffusion and flame front curvature within a perfectly premixed lean hydrogen-air flame. In the following chapter, the focus shifts on the coupling between non-unity Lewis number effects and flame tangential strain rate, and the predictive capability of the considered flamelet based LES with the implemented DD models is assessed. For this reason, a bluff body fully premixed turbulent hydrogen combustor is analysed, as the flame stabilises at significant tangential strain rate levels originating at the bluff body base.

8

DIFFERENTIAL DIFFUSION AND STRAIN COUPLING IN FLAMELETS/PRESUMED FDF LARGE EDDY SIMULATIONS

8.1. INTRODUCTION

As discussed in Sections 1 and 2 the application of flamelet based models to hydrogen combustion presents challenges relative to differential diffusion effects. These can be summarized as coupling with flame stretch leading to mixture fraction and enthalpy redistribution along the flame. Flame stretch can be caused by both curvature (induced by turbulent eddies or thermodiffusive instabilities) and tangential strain rate due to intense average velocity gradients or induced locally by turbulent structures. For hydrocarbon fuels studies like [239] and [285] have shown that the use of unstretched flamelets for the thermochemical database remains robust even under localized extinction events, as the effects of strain on quenching can be modelled by local interplay between reaction and convection [240]. Diffusively neutral flames ($\mathcal{L} \geq 0$) are weakly affected by strain in their consumption rate [54] and reaction rate reduction is only observed at high strain as quenching starts to occur. However, very lean hydrogen-air mixtures can have a negative Markstein length, which causes increasing reaction rate in response to positive tangential strain.

In the context of lean premixed hydrogen flames recent DNS studies [274] suggested that mixture fraction is the main controlling parameters for the description of the thermochemical states encountered in a thermo-diffusively unstable flame, rather than local strain or curvature. On the contrary, the *a priori* analysis conducted by Böttler et al.

Parts of this chapter have been published in Combustion Science and Technology, 1–17. [284].

[224] indicated that incorporating both strain and curvature variations in the flamelets database is necessary to capture all the thermochemical states. Nevertheless, in [224], the deviation of the reacting states predicted by the DNS from a flamelet database built only using unstretched flamelets at different mixture fraction was mostly associated to minor species, while smaller deviations were observed for main species, temperature and reaction rate.

In light of the above studies, it remains unclear whether the combined effects of strain and differential diffusion on the distribution of mixture fraction and reaction rate peak can be captured by the sole effect of resolved strain in an LES, and starting from a database of unstretched flamelets. To examine these aspects, the NTNU hydrogen unconfined bluff-body burner [255], described in Chap. 4, is chosen as a test case configuration. In particular, the work described in the present chapter aims to: (i) further validate the flamelet framework developed in the previous chapters for a bluff body stabilized hydrogen flame against available experimental data (PIV and OH*-chemiluminescence); and (ii) evaluate the model's ability in capturing differential diffusion and strain effects on the flame's behavior at the resolved level using a flamelet database built on unstrained flamelets.

8.2. SET-UP AND METHODOLOGY

The premixed bluff-body stabilized hydrogen flame developed at the Norwegian University of Science and Technology (NTNU), introduced in Chap. 4, is simulated here. The operating conditions considered for the present study are summarized in Tab. 8.1, along with the laminar flame properties corresponding to the nominal equivalence ratio $\phi = 0.4$.

For this analysis, the flamelet-based LES model with presumed FDF closure detailed in Sec. 3.2 and benchmarked in Chap. 6–7 is employed. This involves solving the Favre-filtered equations for continuity, momentum, absolute enthalpy (sum of formation and sensible enthalpies), controlling variables, and their subgrid-scale (SGS) variances. The SGS turbulence is modeled using a one-equation approach, solving an additional transport equation for the SGS turbulent kinetic energy k_{SGS} [95], see Eq. 2.58. The dynamic model described in Sec. 3.2.2 and applied in Chap. 6.2 is used for the SGS closure of the progress variable variance equation.

The flamelet database consists of 300 premixed, unstretched flamelets computed at varying equivalence ratios using the 1D solver CHEM1D [141], with Burke mechanism [280]. The flamelet database is parameterized using a scaled progress variable c based on the water mass fraction Y_{H_2O} , and Bilger's mixture fraction z [286]. Differential diffusion effects are accounted for at the thermochemistry level via a mixture-averaged diffusion model applied to the 1D flamelet solutions (see Eq. 2.16). At the resolved level, these

Table 8.1: Operating conditions for the NTNU bluff-body burner.

ϕ	\dot{m}_{mix} [kg/s]	P_{th} [kW]	s_l [m/s]	δ_l [m]	τ_f [s]
0.4	2.287×10^{-3}	3.5	0.21	6.5×10^{-4}	0.0031

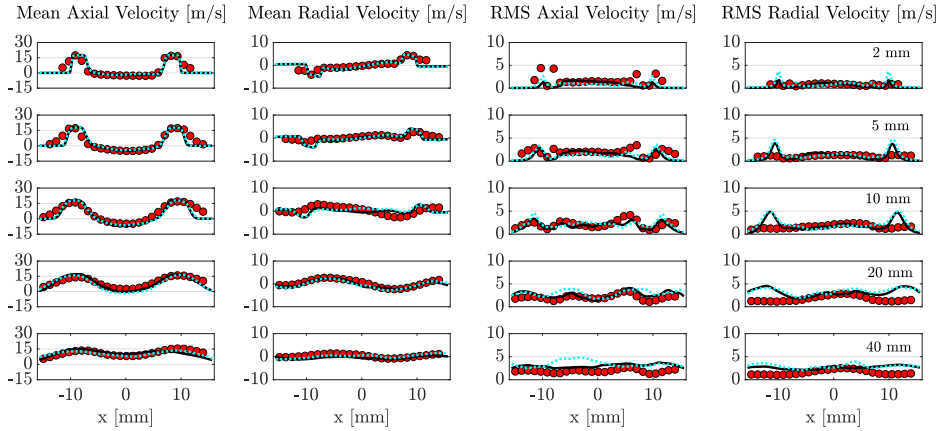


Figure 8.1: Radial profiles of axial and radial velocity, and their RMS, at different axial locations. (LES with $Le_k = 1$: \blacksquare , LES with $Le_k \neq 1$: \cdots , Exp \bullet)

effects are included through model M2 (see Sec. 3.2.3 and Chap. 7), which introduces corrections to the diffusive fluxes of both the controlling variables and absolute enthalpy, following the approach in [125].

The domain is discretized using 2 million hexahedral cells, and the boundary layer is refined to ensure a first cell center distance from the wall $y^+ < 1$ in wall units [93]. The quality of this mesh was assessed using the Cèlik criterion [287] in order to resolve at least the 80% of the kinetic energy throughout the computational domain. Fig. 4.4 (right) shows a cut plane of the computational mesh and summarizes the boundary conditions applied in the simulations. At the domain inlet, a mass flow rate of $\dot{m} = 0.00229$ kg/s with a value of mixture fraction of $z = 0.0125$ is imposed, which corresponds to the experimental equivalence ratio of $\phi = 0.4$. Total atmospheric pressure is imposed at the outlet.

The LES filtered equations are solved using the finite volume method in OpenFOAM 9. The Pressure-Implicit with Splitting of Operators (PISO) algorithm is employed for pressure-velocity coupling, and temporal discretization uses an implicit Euler scheme. Time integration is performed using constant time steps of 3×10^{-7} s and 6×10^{-8} s, maintaining the Courant number below 0.5 in all cells.

8.3. RESULTS AND DISCUSSION

8.3.1. VALIDATION AND FLAME STRUCTURE

Comparisons between LES and experimental measurements of time-averaged and RMS axial and radial velocity components at various streamwise (axial) locations are shown in Fig. 8.1. Both the cases with and without differential diffusion are reported, showing no significant differences in mean velocity flow field between the two models. The simulation results align well with the experimental data, particularly in capturing the peaks of

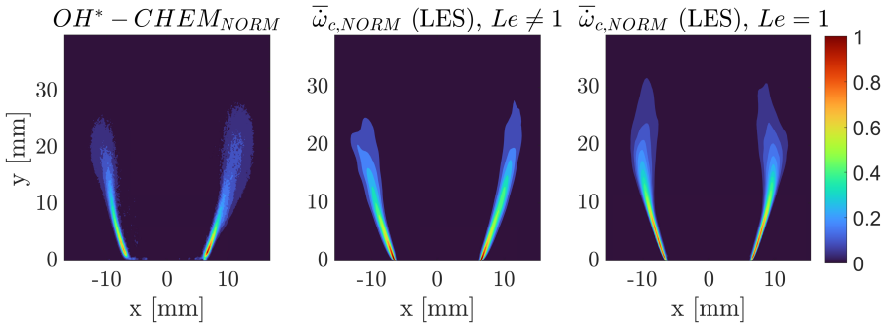


Figure 8.2: OH^* -Chemiluminescence from experiments [255] (left) and midplane contours of mean heat release rate obtained from LES results with (centre) and without (right) differential diffusion effects. All plots are normalized: experimental results have been normalized by their respective maximum OH^* -Chem value, while the numerical results have been normalized by the maximum value of the $Le = 1$ case.

both velocity components and RMS fluctuations. However, a significant overestimation of the RMS of radial velocity is observed in the shear layer region at a height of approximately $y = 20$ mm. This mismatch is attributed to an overestimation of combustion-induced turbulence at the bluff-body base. Supporting this interpretation, the RMS of radial velocity shows better agreement with experimental measurements in the corresponding non-reacting case (not shown). Also, comparisons of OH^* -Chemiluminescence measurements with the time averaged normalized reaction rate from LES, shown in Fig. 8.2, indicate that the LES accurately predicts both the shape and length of the flame. It can be further observed that the location of highest reaction rate moves towards the edge of the bluff-body and the flame gets shorter when differential diffusion effects are included in the model, and the comparison with experimental data improves in this case.

8

Further insight on the effects of differential diffusion is presented next. For an unstretched premixed flame, a decrease in mixture fraction is expected in the preheat zone ahead of the flame, followed by a re-increase in the flame region [153, 274]. This behaviour, categorized in Chap. 2 as a one-dimensional effect, is captured by the LES with differential diffusion model, as demonstrated in Fig. 8.3 by the presence of a region of mixture fraction with values around $\tilde{z} = 0.011$, which are lower than the nominal value $\tilde{z} = z_{nom} = 0.0125$. In fact, since the resolved curvature in this region is small and the positive resolved strain in the same region would increase the mixture fraction as compared to an unstrained case [153], the observed low values of \tilde{z} necessarily imply that one-dimensional effects of differential diffusion are captured in the LES. Besides, the LES with differential diffusion model also predicts a significant increase in mixture fraction in the post flame region ($\tilde{c} > 0.5$), above its nominal value. This increase is only possible due to the combined effects of stretch and differential diffusion (positive strain and curvature), as documented in previous studies [153, 274, 282]. This implies that the LES with unstretched flamelets thermochemistry can, at least qualitatively, mimic this interplay between resolved stretch and differential diffusion (two/three dimensional effect as categorized in Chap. 2). As a consequence of this enrichment, the LES also predicts superadiabatic temperatures, with peaks around $\tilde{T} = 1800K$ observed in the region of the

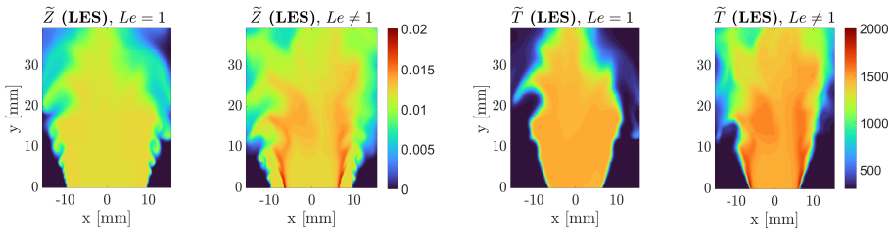


Figure 8.3: Midplane contours of instantaneous filtered mixture fraction (left) and temperature (right) obtained from the LES without ($Le = 1$) and with ($Le \neq 1$) differential diffusion model.

flame anchoring point (Fig. 8.3, right). These peaks are found to correspond to values of progress variable $\tilde{c} > 0.85$. Consistently, a redistribution of the reaction rate field is predicted with respect to the unity Lewis number case, with higher values concentrated close to the flame anchoring point, also resulting in a shorter flame as previously observed in Fig. 8.2.

The above analysis highlights significant effects of differential diffusion in the studied configuration. Nevertheless, the details of how the current modelling framework based on unstretched flamelets thermochemistry is capturing the interplay between stretch and differential diffusion is yet unclear. Insights on this aspect are provided in the next section.

8.3.2. AVERAGE RESOLVED STRETCH EFFECTS

In premixed flames, differential diffusion effects are tightly coupled with flame stretch K . This can be split into contributions of flame front curvature k_f and flame tangential strain S_t as in Eq. 2.39. In particular, flame curvature induced either by turbulence or by intrinsic thermodiffusive instabilities, is positively correlated with variations in mixture fraction, such that a convex curvature towards the reactants causes mixture enrichment upstream of the flame, while a cusp (concave towards reactants) produces a mixture fraction decrease [149, 164]. Similarly, positive flame tangential strain produces a mixture enrichment when coupled with differential diffusion [153]. The contours in Fig. 8.4 indicate a region of intense positive tangential strain rate $\langle \tilde{S}_t \rangle \sim 7500$ 1/s being generated at the edge of the bluff body, where the flame anchors, which is due to the interaction between the jet flowing around the bluff body and the region of hot gases recirculation. The same figure reports radial profiles of mean flame tangential strain in progress variable space for different axial locations. As one would expect, tangential strain decreases downstream. Its peak location, found for mean progress variable values $\langle \tilde{c} \rangle > 0.8$, is also found to shift towards the product side as one moves downstream. The effect of mean resolved strain on mixture fraction is also visible in Fig. 8.4. Consistently with the study in [153], higher levels of strain observed near the bluff body base limit the one-dimensional differential diffusion effects of mixture fraction decrease in the low progress variable region, and enhance its re-increase for higher values of \tilde{c} . This re-increase results in overshoot of mixture fraction above 50% in the region of higher strain, as compared to the nominal value. This in turns induces superadiabatic temperatures of the order of

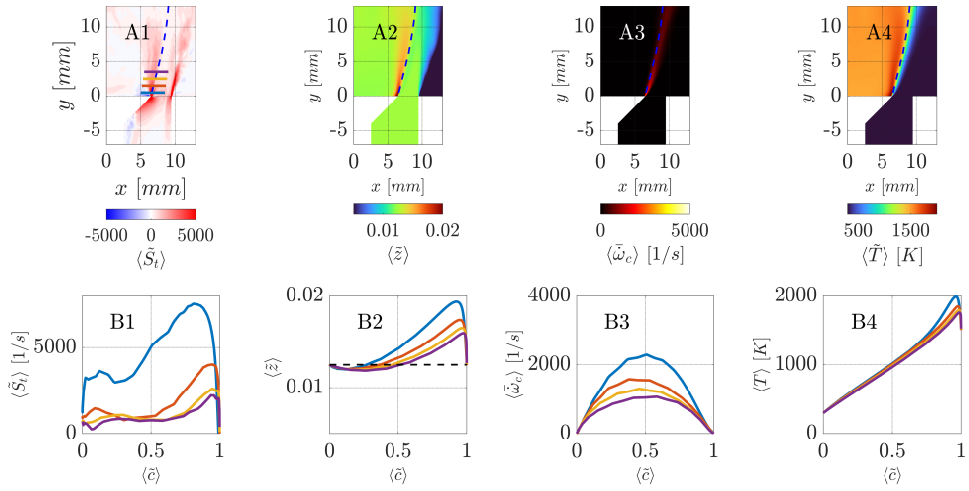


Figure 8.4: Top row, from left to right: Midplane contours of mean resolved tangential strain rate $\langle \tilde{S}_t \rangle$, mean mixture fraction, $\langle \tilde{z} \rangle$, mean progress variable reaction rate, $\langle \tilde{\omega}_c \rangle$, and mean temperature $\langle \tilde{T} \rangle$ obtained from LES with differential diffusion model. Isoline of mean progress variable $\langle \tilde{c} \rangle = 0.8$ is marked as a blue dashed line (---). Bottom row, from left to right: profiles of the same average quantities along the flame at the 4 axial locations marked in the A1 contour plot: $y = 0.5$ mm (—), $y = 1.5$ mm (—), $y = 2.5$ mm (—), $y = 3.5$ mm (—). The dashed line indicates the nominal mixture fraction value $z = 0.0125$.

$\langle \tilde{T} \rangle \sim 2000$ K. This phenomenon, which is linked to the relative magnitude of convective transport with respect to diffusive transport of mixture fraction due to differential diffusion in strained flames, is thus correctly captured by the LES at the resolved level. It is worth to notice that curvature is limited in the region of high strain near the flame anchoring point, as will be shown later. In the present configuration, unlike what was observed by Berger et al. [274] for the slot burner also simulated in Chap. 7, strain appears to dominate over curvature effects. The comparison of that combustion system with the present bluff-body further suggests that thermodiffusive instabilities, which played a major role in the slot burner [101, 274] for a similar equivalence ratio and massflow rates, are somewhat suppressed by the significant strain at the bluff-body base. Figure 8.4 also indicates that not only the peak reaction rate, but also the extent of the area underneath the curve (which is proportional to the consumption speed in physical space), increases in correspondence of regions of higher tangential strain rates (see radial profiles). This is an expected effect of reacting mixtures at negative Markstein lengths [54], and suggests that capturing the correct redistribution of mixture fraction might be sufficient, in the context of flamelets combustion modelling, to predict the correct increase in reaction rates. This is further confirmed by the fact that the flame shape and length, thus the consumption speed, predicted by the LES when differential diffusion is included are in better agreement with the experimental observations (see Fig. 8.2), than for the unity Lewis number case. On the other hand, one has to keep in mind that strain effects on reaction rate are also linked to enthalpy and radicals redistribution through the flame front as indicated in the *a priori* analysis of [224]. In the latter, however, errors were observed to remain below 10% in terms of major species, temperature, density and reaction

rates when using an unstretched flamelets database as compared to strained flamelets, with larger errors for minor species. Unfortunately, minor species mass fractions are not available for the considered experimental database for comparisons. Note that errors on minor species are commonly expected within flamelet-based approaches even for hydrocarbon flames, where additional transport equations and methods are often used to improve the accuracy of their predictions (e.g. see [135]).

The above results suggest that effects of strain in lean hydrogen flames can be predicted with unstretched flamelets thermochemistry, at least as long as most of the strain is resolved.

8.3.3. REACTING STATES

Figure 8.5 illustrates the joint probability density function of progress variable reaction rate $\bar{\omega}_c$ and progress variable \bar{c} at a random timestep. Only points on the flame with $\bar{\omega}_c > 1$ are considered. Consistently with what observed by Berger et al. [274] for a jet flame at the same equivalence ratio, differential diffusion effects (left) result in reaction rate values higher than those found in an unstretched 1D laminar flame, which is due to the effect of stretch on local enrichment. Since these states are significantly more abundant than states where the mixture fraction gets leaner, the global conditional average, $\langle \bar{\omega}_c | \bar{c} \rangle$, is also significantly larger than the one associated to unstretched samples only (red line), highlighting the significant effect of stretch on the reaction rate. Note that the latter curve still presents values larger than those for the unstretched laminar 1D flamelet (blue curve), due to the transport of mixture fraction from the enriched pockets from the nearby regions with non-zero stretch. Figure 8.5 (left) also indicates that increasing levels of tangential strain (dashed lines) yield an increase of conditional reaction rate, in agreement with the trends observed in [153]. These effects are completely absent when considering the case without differential diffusion (Figure 8.5, right), where the global conditional average matches the one obtained using unstretched samples only. Also, as expected, increasing levels of resolved strain does not affect the conditional reaction rate.

Figure 8.6 shows scatter plots of filtered mixture fraction \tilde{z} versus filtered progress variable \tilde{c} , at a random timestep, coloured by mean stretch, strain and curvature respectively. Global conditional averages as well as conditional averages obtained only using samples at zero stretch, strain or curvature are also shown. Stretch and tangential strain are normalized by the chemical time scale τ_f , and curvature is normalized by the laminar flame thickness δ_f , whose values are reported in Tab. 8.1. The plot on the left indicates a strong correlation between positive values of stretch and mixture enrichment. The global conditional average of mixture fraction versus progress variable shows the typical profile of a strained premixed 1D flamelet in counterflow configuration [153], as already observed in Fig. 8.4, with an initial decrease in mixture fraction with respect to the nominal value followed by a reincrease and eventual overshoot. The conditional average of unstretched reacting states, $\langle \tilde{z} | \tilde{c}, \bar{K} = 0 \rangle$ (red line), is observed to follow the profile of decreasing mixture for an unstretched 1D premixed flamelet (blue line), confirming that stretch is driving the deviation between the conditional average from LES states and unstretched flamelet values. Consistently with Fig. 8.5 and the results in [274], the values on the "unstretched" conditional average curve are higher than

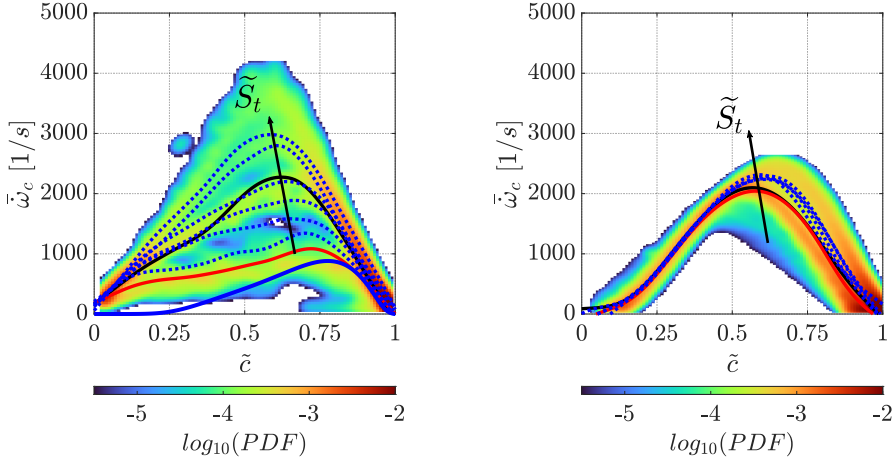


Figure 8.5: Joint probability density function of progress variable reaction rate versus progress variable at a random timestep. Both cases with (left) and without (right) differential diffusion are shown. Solid lines represent global conditional average $\langle \bar{\omega}_c | \bar{c} \rangle$ (—), conditional average restricted to unstretched reacting states $\langle \bar{\omega}_c | \bar{c}, \bar{K} = 0 \rangle$ (—), and the reaction rate for an unstretched 1D premixed laminar flamelet at the same equivalence ratio (—). Dashed lines indicate the conditional averages at fixed levels of tangential strain S_t .

those for the unstretched 1D flamelet. The two rightmost graphs in Fig. 8.6 further reveal that stretch effects are primarily driven by tangential strain in the present configuration, whereas curvature has a less pronounced influence. Indeed, one can notice that the conditional average at zero curvature, $\langle \bar{z} | \bar{c}, \bar{\kappa}_f = 0 \rangle$ (red line, rightmost graph), aligns with the global conditional average (black line). Furthermore, the conditional average at zero strain, $\langle \bar{z} | \bar{c}, \bar{S}_t = 0 \rangle$ (red line in the central graph), appears to align with the unstretched conditional mean (red line in the left graph). Nevertheless, flame curvature still maintains a mild positive correlation with mixture fraction variations, consistently with past observations [101, 274]. This milder influence of curvature effects as compared to previous studies is partly due to the fact that only modest strain levels were observed in these studies, and partly to the fact that the positive tangential strain itself at the flame anchoring location might be limiting the onset of thermodiffusive instabilities (observed instead in [274]), thus limiting the occurrences of strongly curved flame fronts [288]. As a final remark, Fig. 8.6 (central graph) further illustrates the conditional mean at zero curvature for increasing strain levels. This confirms the argument for Fig.8.5 that increasing strain intensifies the local enrichment, as observed in [153] for laminar strained flamelets, leading in turn to the increase of reaction rate.

To further characterize the influence of stretch, in Figure 8.7 the probability density functions of resolved stretch, tangential strain and flame curvature, with and without differential diffusion, are shown. One can notice that curvature has a zero mode (although the mean remains slightly positive due to a mild skewness to the right), which is believed to be the result of only turbulent eddies motion. On the contrary, the PDF of strain indicates the presence of two peaks, which are believed in turn to correspond to the effect of turbulent eddies and to the applied strain in the shear region where the

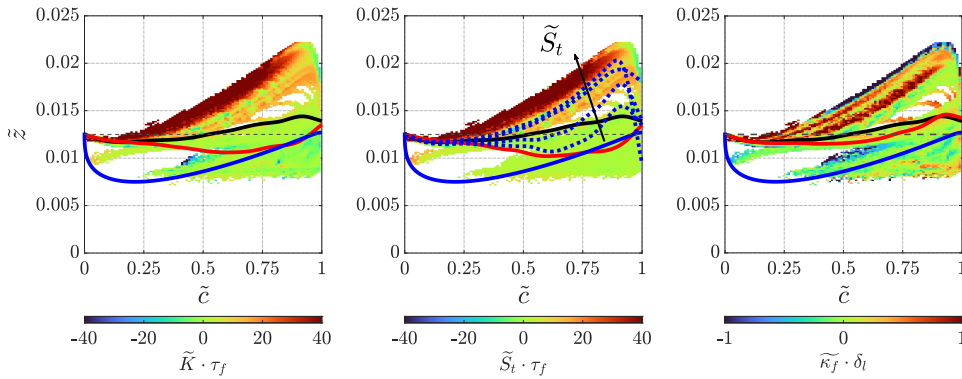


Figure 8.6: Scatter plots of mixture fraction versus progress variable in the flame region. Colours represent mean resolved normalized stretch (left), strain rate (center), and curvature (right). Global conditional averages $\langle \tilde{z} | \tilde{c} \rangle$ are marked as solid black line (—). The nominal mixture fraction is marked with a black dashed line (---). The mixture fraction from 1D unstretched premixed flamelet at the same equivalence ratio is plotted with a solid blue line (—). Red lines (—) indicate conditional averages obtained considering points at zero stretch, strain and curvature, respectively. The dashed lines (---) represent increasing levels of strain rate.

flame anchors (positive mode). This distribution is thus different to that observed in [274] where only a peak around zero strain was observed. It is interesting to note that the presence of differential diffusion causes an increase in the value of tangential strain associated with this second peak (strain itself intensifies), as well as an increased number of occurrences at this value. This is linked to the stabilization of the flame closer to the bluff-body edge characterized by higher strain levels and an overall shortening of the flame, and indicates that the hydrogen flame ‘chases’ the high strain region, due to the increase of reaction rate in response to strain.

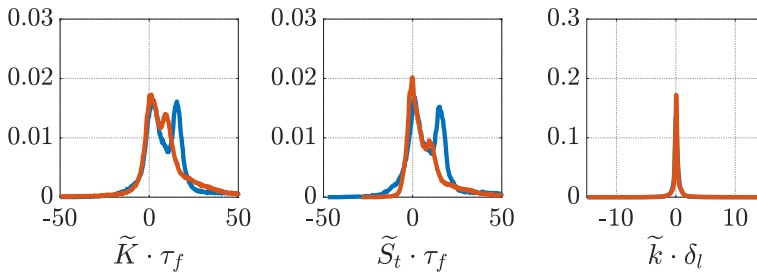


Figure 8.7: Probability density function of resolved stretch, strain and curvature, showing the comparison between the unity Lewis number case (—) and with differential diffusion (—).

8.4. SUMMARY

The differential diffusion model M_2 presented in Chap. 7, correcting for the diffusive flux of mixture fraction, progress variable and enthalpy was used to investigate the cou-

pling between differential diffusion and stretch in bluff-body stabilized lean premixed hydrogen flames. The LES was firstly validated against available PIV and OH* experimental data, showing accurate predictive capabilities, already without differential diffusion modelling. The differential diffusion model was shown to be able to predict the local redistribution of mixture fraction in regions of non-zero strain at the bluff body base, at the resolved scales. This redistribution was observed to cause a shift of the reaction source term peak towards the flame anchoring point, resulting in a shorter flame compared to the unity Lewis number case. Interestingly, the increased reaction rate induced by positive flame tangential strain (due to negative Markstein length) was correctly captured by the sole use of unstretched flamelets thermochemistry. This requires that the diffusive flux of the controlling variables is appropriately corrected to account for differential diffusion and that most of the strain rate is resolved.

The LES framework benchmarked in the first part of this thesis was proven to give satisfactory predictions of hydrogen turbulent flames under various combustion regimes. Moreover, the implemented differential diffusion model was proven to give physical predictions of differential diffusion coupling with resolved curvature and strain rate. The LES framework is subsequently employed for the numerical analysis of a practical swirl-stabilized combustor, as presented in Part II.

II

LES STUDY OF THE TU DELFT SWIRL STABILIZED COMBUSTOR

9

INVESTIGATION OF MIXING IN A JET IN SWIRLING CROSS-FLOW CONFIGURATION

9.1. INTRODUCTION

As discussed in Chap. 1, lean premixed combustion is a promising strategy to reduce fuel consumption and NO emissions by lowering flame temperatures, thereby enabling more sustainable combustion for gas turbines technology [289]. In particular, fuel-flexible combustion systems, capable of operating on both carbon-based fuels and hydrogen or any mixture of the two, have gained significant attention across various industries, offering a broader operability range, even in scenarios where hydrogen is not consistently available. These are the focus of the present study which investigates the TU Delft swirl-stabilized combustor with axial air injection, introduced in Chap. 4, a laboratory-scale technically premixed combustor suitable for advancing fuel-flexible combustion systems in aeronautical applications [25].

Mixing quality is a critical parameter for achieving spatially uniform flame temperatures and, consequently, low NO emissions. Preliminary numerical studies revealed a lack of mixture homogeneity at the combustion chamber inlet for the considered operating chosen as reference in experiments [290–292]. Experimental measurements in [68] highlighted that flame stabilization and NO emission trends vary depending on the fuel composition and use of axial air injection (AAI), suggesting that non-uniform mixing significantly influences both flame shape and emissions. This chapter focuses on investigating the mixing process in detail.

The use of hydrogen based fuel, with its significantly higher flame speed compared to hydrocarbon fuels, presents increased risk of flashback and thermoacoustic instabilities when homogeneously premixed within the injector [293], as discussed in Chap. 1. To

Parts of this chapter have been published on International Journal of Hydrogen Energy 141 (2025): 176-192.

mitigate these risks and ensure stable combustion with high hydrogen content, strategies aim to minimize the volume of flammable mixture present in the injector. This is typically achieved through late-stage fuel injection and rapid mixing. An example is Lean Direct Injection (LDI) [37, 38], where fuel is injected directly into the combustion chamber and mixes rapidly with abundant air, often in a swirling flow to improve flame stability. Other approaches include partially premixed strategies with delayed hydrogen injection [294–296], and technically premixed combustors featuring dedicated mixing sections with flashback mitigation measures, such as in [49, 297] or within the TU Delft swirl-stabilized combustor examined in this work [68].

A widely adopted method for achieving effective and quick mixing is the jet-in-crossflow (JICF) configuration, where fuel is injected transversely into an oxidiser stream [298, 299], commonly seen for gas turbine injectors [300, 301]. Four characteristic flow structures typically arise in an axial JICF setup [302]: (1) horseshoe vortices originating from the jet issuing base, (2) windward shear layer vortices due to Kelvin-Helmholtz instability, (3) a far-field counter-rotating vortex pair (CVP), and (4) wake region downstream of the jet, with upright vortical structures in the jet's wake forming from cross-flow boundary layer vorticity. Among these, the CVP plays a crucial role for jet-crossflow mixing by entraining crossflow fluid into the jet [303, 304].

Mixing behavior in JICF configurations is strongly influenced by geometric parameters such as nozzle shape [305, 306] and injection angle [307], as well as flow parameters including the jet-to-crossflow density ratio $S = \rho_{\text{jet}}/\rho_{\text{crossflow}}$, velocity ratio $R = U_{\text{jet}}/U_{\text{crossflow}}$, momentum flux ratio $J = SR^2$, and Reynolds number Re [298, 308, 309]. Among these, J has been recognized as the dominant factor controlling mixing performance [310, 311]. Effective mixing typically requires $J > 25$, and in some cases, $J > 100$ [310]. At very high J values, the jet behaves similarly to a free jet in static environment, just slightly bent by the incoming crossflow, while at low J ($J < 1$), the jet tends to remain attached to the wall, feature leveraged in film cooling applications [312, 313]. The high diffusivity of light fuels such as H_2 is expected to further impacts mixing dynamics [314].

Swirling crossflows, commonly used in modern gas turbines for flame stabilization [58, 85, 301, 315], introduce additional complexity to the JICF mixing process. Unlike axial flows, swirling flows involve a tangential velocity component and a radial pressure gradient. Early investigations employing helium jets into swirling crossflows [316, 317], used to replicate density effects of light fuels, revealed that swirl significantly reduces jet penetration depth (by up to a factor five at a swirl number $S_w = 2.25$). However, helium's lower density compared to air leads to differential centrifugal effects that promote outward air transport and inward transport of the fuel jet fluid, partially compensating for reduced penetration [317]. For momentum flux ratios in the range $0.28 \leq J \leq 12.6$, jets were observed to follow spiral paths aligned with the swirl direction. More recent studies [318] explored hydrogen jets in swirling crossflows, finding that increased swirl number affects mixing by inducing central recirculation zones and modifying the shear layer distribution, at the exit of premixing sections. Additionally, momentum flux ratio was shown to influence both the penetration depth and the homogeneity of the resulting mixture.

While both swirling flows and JICF configurations have been studied extensively in isolation, the understanding of combined effects of swirl and jet in crossflow injection,

particularly under fuel-flexible conditions, remains limited. In particular, no studies have accounted for the effects of varying fuel densities on the mixing process, nor has a systematic methodology been established to investigate these effects experimentally and numerically. Understanding how fuel composition and injection parameters affect mixture homogeneity conditions prior combustion is crucial for predicting NO emissions and assessing flashback risk in technically premixed, swirl-stabilized combustors.

In the present chapter the mixing characteristics of the jet in swirling cross-flow configuration in the dual-fuel (CH_4/H_2) technically premixed TU Delft combustor [68], is analysed with LES, complementing the experimental work presented in [319]. In these experiments, helium/air mixtures are employed as surrogates for CH_4/H_2 blends, with adjusted helium-to-air ratios to match the density of the actual fuel mixtures. The mixing process and velocity fields are visualized by seeding the fuel stream with droplets before injection in the optically accessible mixing tube. The LES simulations validate this surrogate approach and further characterize the mixing behavior and homogeneity levels across different fuel compositions. A detailed decomposition of the transport processes, including convection, molecular diffusion, and turbulent subgrid transport (diffusion), is also presented to quantify their respective roles in mixture formation. These insights support the interpretation of flame stabilization and emission trends observed in the experiments of [68].

9.2. METHODOLOGY

9.2.1. JOINT EXPERIMENTAL AND NUMERICAL METHODOLOGY DESIGN

The present study investigates the fuel/air mixing process within the TU Delft swirl stabilized combustor, which features a jet in swirling cross-flow fuel injection configuration. A schematic of the set-up is provided in Fig. 4.5 in Sec. 4. The study focuses on the case with geometric swirl number [256] of $S_{w,\text{geom}} = 1.1$ at the conditions outlined in [68], where the burner operates under different CH_4/H_2 mixtures with a constant thermal power $P = 12\text{ kW}$ and a constant mass flow rate of air $\dot{m}_{\text{air}} = 5.38\text{ g/s}$ (see Tab. 9.1).

CH ₄ /H ₂ reacting case at $P = 12\text{ kW}$					
Tag	XH ₂	\dot{m}_{H_2} [lpm]	\dot{m}_{CH_4} [lpm]	LES	d_{fuel} [mm]
A	0	0	21.21	✓	3.50
B	0.4	11.17	16.76	✓	3.50
C	0.8	39.2	9.13		3.50
D	1	71.8	0	✓	3.50

Table 9.1: Fuel mixtures and injector diameters for the reference (CH_4/H_2) cases at $p = 1\text{ atm}$ and $T = 288.15\text{ K}$

In the experimental campaigns conducted in [68], fuel-air mixing is studied using a non-reactive surrogate gas to eliminate the complexities associated with handling reactive gases. Helium has previously been proposed as a surrogate for H_2 . Although it does not replicate fully the diffusive characteristics of H_2 within oxidizers, previous results suggest that it exhibits a similar global mixing behaviour [320]. Helium/air mixtures are used as a surrogate for CH_4/H_2 mixtures, matching both the density and injection velocity of the jet [308], while maintaining the same fuel inlet diameter. Therefore, the helium

He/air surrogate					
Tag	\dot{m}_{He} [lpm]	\dot{m}_{air} [lpm]	LES	Exp	d_{fuel}
A _s	11.01	10.58		✓	3.50
B _s	22.27	7.82		✓	3.50
C _s	42.87	2.25		✓	3.50
D _s	71.80	0	✓	✓	4.07

Table 9.2: He/air mixtures and injector diameters for the surrogate cases at $p = 1$ atm and $T = 288.15$ K.

mole fraction in the surrogate fuel stream corresponding to a reference case with a given hydrogen mole fraction of X_{H_2} is computed as:

$$X_{\text{He}} = X_{\text{H}_2} \frac{\rho_{\text{H}_2} - \rho_{\text{CH}_4}}{\rho_{\text{He}} - \rho_{\text{Air}}} + \frac{\rho_{\text{CH}_4} - \rho_{\text{Air}}}{\rho_{\text{He}} - \rho_{\text{Air}}} \quad (9.1)$$

To represent the 100% H₂ case using helium (He) as a surrogate, it is not possible to match the fuel density, since He is approximately twice as dense as H₂. Therefore, to maintain the same momentum flux ratio J , the volumetric flow rate of the fuel stream is kept constant between H₂ and He, and the fuel inlet diameter is increased when using He. Tab. 9.1-9.2 show the fuel compositions for the reference cases (Tag A - D), experimentally studied under reacting conditions in [68], and the corresponding fuel surrogates (Tag A_s - D_s) for the non-reacting experiments in [319].

The momentum flux ratio between transverse jets and swirling cross-flows J_{swirl} is a relevant parameter for the presented analysis and is defined as follows [318]:

$$J_{\text{swirl}} = \frac{\rho_{\text{jet}} \cdot U_{\text{jet}}^2}{\rho_{\text{air}} \cdot U_{\text{air}}^2 \cdot (1 + 4 \cdot S_w^2)}, \quad (9.2)$$

where ρ is the density and U the axial velocity. In this chapter, U_{air} is taken as the bulk velocity of the swirling air, due to the complex velocity distribution at the swirler outlet.

Fig. 9.1a shows the momentum flux ratio J_{swirl} by varying the percentage of H₂ in the fuel X_{H_2} for the reacting cases (CH₄/H₂, blue line) and its surrogate (He/air, green dotted line). It can be seen that the curves of the two mixtures are about overlapping, since the density is kept constant between the fuel mixture and the surrogate fuel and the fuel ports diameter is increased in the 100% He surrogated case D_s. For both, the momentum flux ratio increases up to $X_{\text{H}_2} = 0.8$, and afterwards drops again slightly. Fig. 9.1b shows the corresponding Reynolds numbers. Due to the higher viscosity of Helium compared to H₂ and CH₄, some discrepancies are observed in the Reynolds numbers between the methane-hydrogen mixtures and their surrogate at the same value of J_{swirl} (blue and green data). However, for all investigated cases, the flow remains in the laminar or transition regime. Therefore, the change in Reynolds number is not anticipated to affect the mixing substantially.

The investigation of the mixing process in [319] is carried out within a combined numerical and experimental framework. The experiments were performed in a replica of the TU Delft partially premixed CH₄/H₂ swirl-stabilized burner [68], featuring the same stainless steel axial swirler and an optically accessible mixing tube and combus-

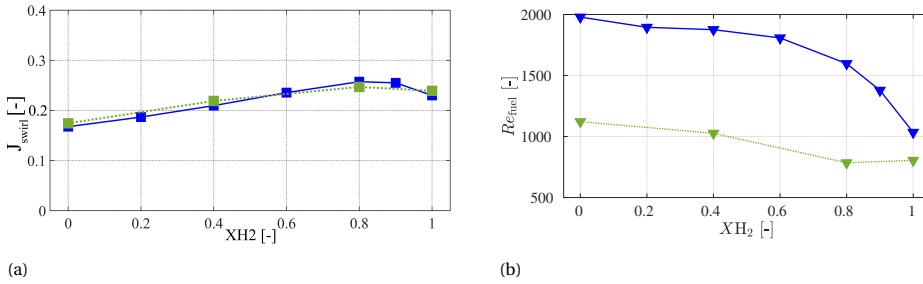


Figure 9.1: (a) Momentum flux ratio and Reynolds number (b) for CH₄/H₂ mixtures (—) and the surrogate conditions (---) in the fuel stream.

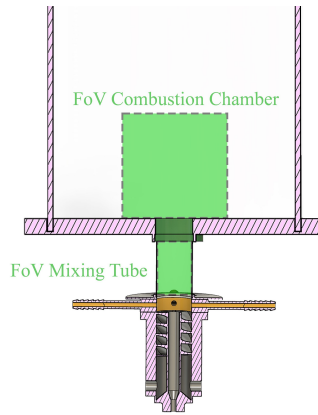


Figure 9.2: Field of view for the optically accessible combustion chamber and mixing tube

tion chamber. Particle Image Velocimetry (PIV) data are available, and the mixing process was analyzed using Mie scattering images acquired within the mixing tube. Only the fuel stream was seeded, so the Mie scattering signal serves as an indicator of the mixing level between fuel and air. Specifically, the surrogate fuel stream (He/air) was seeded with DEHS droplets. Post-processing of the Mie-scattered images using particle counting techniques described in [319] enabled visualization of the fuel–air mixing. The field of view of the experimental measuring techniques is shown in Fig. 9.2

In the present chapter, the 100% helium case (Ds in Tab.9.2) is first simulated using LES to validate the numerical model through comparison with experimental measurements. Subsequently, LES is used to analyze cases with different CH₄/H₂ fuel compositions (cases A, C, and D in Tab.9.1). A comparison between case D and its surrogate case Ds serves to evaluate the suitability of helium as a tracer to represent the macroscopic mixing behavior of hydrogen, thereby validating the experimental methodology and identifying its limitations.

The numerical results provide detailed quantitative information on the fuel mass fraction distribution within both the mixing tube and the combustion chamber. Mixing

quality is analyzed for each of the investigated fuel mixtures, and the resulting trends are compared with those obtained from the surrogate experimental cases. Further insight into the mixing process is obtained by analyzing the individual terms in the mass fraction transport equation, allowing assessment of the relative roles of convection, molecular diffusion, and turbulent transport for the various species involved.

The mixing quality in both the experimental and numerical studies is evaluated using the spatial unmixedness parameter U_s , which quantifies the degree of non-uniformity in fuel distribution across a given plane. It is defined as [321]:

$$U_s(y) = \frac{\langle (\overline{C(x,y)} - \langle \overline{C(y)} \rangle)^2 \rangle}{\langle \overline{C(y)} \rangle \cdot (1 - \langle \overline{C(y)} \rangle)}. \quad (9.3)$$

In the present chapter, \overline{C} represents the temporal average, while $\langle C \rangle$ denotes the spatial average of the fuel concentration C . The numerator expresses the spatial variance of C , and the denominator normalizes this variance by the theoretical maximum. In the LES simulations, C corresponds to the fuel mass fraction Y_{fuel} , whereas in the experiments, it corresponds to the particles concentration. Since three-dimensional data are not available from the experiments, the degree of mixing is evaluated using planar distributions of C in both experimental and numerical datasets. The parameter U_s ranges from 0 for a perfectly premixed condition to 1 for a completely unmixed case.

In addition to this scalar metric, spatial distributions of the normalized fuel concentration are used to visualize how the fuel is distributed across the measurement plane.

$$C^*(x, y) = \overline{C(x, y)} / \langle \overline{C(y)} \rangle \quad (9.4)$$

C^* is a useful parameter to compare cases with substantially different fuel compositions, as the fuel mass fraction is locally normalized by its spatial average at each stream-wise location.

LES MODELLING

The mixing process within the TUDelft combustor is simulated with Large eddy simulation (LES) paradigm. The considered fluid is a multicomponent mixture whose composition, and therefore density, vary through the mixing process. To deal with non-constant density, the Favre-filtered (density-weighted) formulation of the Navier-Stokes equations (see Chap. 2, Sec. 2.9.1) is employed.

The dynamic viscosity for each species μ_k is calculated as a polynomial function of the logarithm of temperature, T , using the species transport properties according to the San Diego chemical mechanism in [143]. From the μ_k values, a simple mass fraction based average is applied to determine the dynamic viscosity of the whole mixture, μ . The subgrid-scale viscosity, μ_{SGS} , is modelled through a one-equation approach [95], where an equation for the subgrid-scale turbulent kinetic energy k_{SGS} is resolved, see Eq. 2.58. This turbulence model is particularly well-suited for flows with anisotropic turbulence, such as the present case involving swirling motion and transverse injection. The solution of a transport equation allows to capture the dynamic behaviour of the subgrid turbulence field with its spatial inhomogeneities and temporal variations.

To analyse the mixing process, an additional transport equation is resolved for the mass fractions Y_k of each species composing the mixture (i.e. N_2 , O_2 , H_2 , He , CH_4).

Setting to zero the source term associated to chemical reactions, the transport equation reduces to a convection-diffusion equation:

$$\frac{\partial(\bar{\rho}\widetilde{Y}_k)}{\partial t} + \frac{\partial(\bar{\rho}\widetilde{u}_j\widetilde{Y}_k)}{\partial x_j} = \frac{\partial}{\partial x_j} \left[\left(\overline{\rho D_k^m} + \frac{\mu_{SGS}}{Sc_t} \right) \frac{\partial\widetilde{Y}_k}{\partial x_j} \right] \quad (9.5)$$

The effective diffusion coefficient on the right-hand side term consists of two contributes: one representing species transport due to molecular diffusion and another accounting for subgrid convective transport. The latter is modeled as an additional diffusion term with a diffusion coefficient $\rho D_t = \mu_{SGS}/Sc_t$. A constant SGS Schmidt number is used for all the species, set to $Sc_t = 0.7$. A mixture-averaged model following Fick's law approximation [149] is employed to determine the molecular diffusion coefficient of each species k with respect to the mixture, see Eq. 2.15:

$$D_k^M = \frac{(1 - Y_k)}{\sum_{j \neq k}^N X_j / D_{kj}}, \quad (9.6)$$

where X_k are the species mole fractions, and D_{kj} are the binary diffusion coefficients for each species pair, expressed as a logarithmic polynomial function of temperature, employing the transport parameters in the San Diego kinetic mechanism [143]. This approach ensures that the diffusion coefficient of each species varies in time and space according to the local mixture composition. Unlike the equi-diffusivity assumption, it captures inter-species diffusion more accurately and accounts for its effects on resolved scales mixing, including, for example, separation phenomena in multicomponent fuels.

An energy conservation equation is also solved, as no incompressibility assumption is made. A filtered transport equation for the sensible enthalpy \widetilde{h}_s is therefore solved, where the thermal diffusivity is computed analogously to the dynamic viscosity and the turbulent Prandtl number is taken equal to $Pr_t = 0.85$. The equation set is closed through the filtered ideal gas equation of state and the thermodynamic relation $\widetilde{h}_s = \int_{298.15\text{K}}^{\widetilde{T}} \widetilde{C}_p(T') dT'$, where C_p is the mixture's specific heat at constant pressure, computed through Janaf polynomials [143].

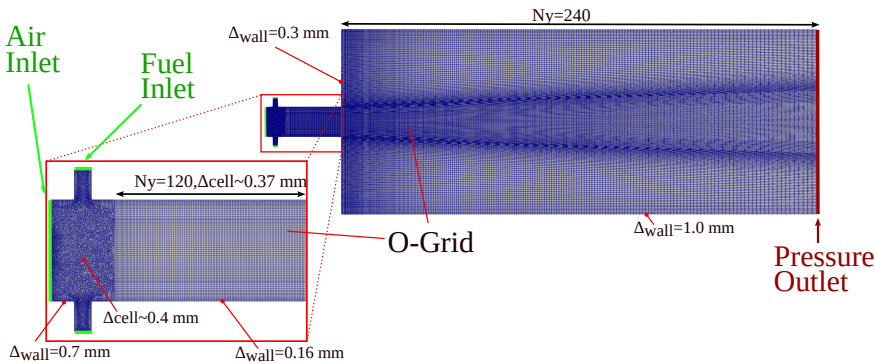


Figure 9.3: Sketch of the computational grid

The numerical domain, illustrated in Fig. 9.3, includes the combustion chamber, the mixing tube, and the fuel ports, according to the geometry detailed in Chap. 4. The swirler is excluded from the calculation to reduce the computational cost and a synthetic turbulence generator [259] is employed to mimic the turbulent swirling flow delivered at the swirler exit, as described next. A hybrid structured/unstructured meshing approach is used, to exploit the advantages of hexahedral elements in terms of cell skewness and non-orthogonality minimization, but retaining the flexibility of tetrahedral cells to discretize the regions with more complex geometry. The mixing tube is discretized through an O-grid where the hexahedral cells have a characteristic size of $\Delta_{\text{cell}} = 0.3\text{ mm}$ to 0.4 mm . A non-uniform spacing is imposed to refine the wall region, where the first cell height is set to $\Delta_{\text{wall}} = 0.16\text{ mm}$ corresponding, adopting viscous scaling [93], to $y_{\text{wall}}^+ < 10$ under fully developed flow. The O-grid extends to the combustion chamber, maintaining a cell size of $\Delta_{\text{cell}} = 0.3\text{ mm}$ to 0.4 mm in the mixing tube exit region, and merges with an additional annular structured block. An unstructured block with tetrahedral cells with a characteristic size of $\Delta_{\text{cell}} = 0.4\text{ mm}$ is used in the region connecting the fuel ports to the mixing tube. A wall refinement is obtained here through hexahedral layers achieving a first cell height of $\Delta_{\text{wall}} = 0.07\text{ mm}$. The total cell count is 4.45 M.

The mesh quality was assessed a-posteriori through Pope's criterion [97], verifying that the subgrid turbulent kinetic energy represented less than the 20% of the total turbulent kinetic energy (resolved plus subgrid) $k_{\text{SGS}} < 20\%TKE = 20\%(K_{\text{res}} + k_{\text{SGS}})$ in the region of interest. Additionally, a mesh sensitivity analysis was conducted by performing an LES simulation of case D_s on a finer, fully block-structured grid containing 12.73 million hexahedral elements, which discretized the entire domain, including the swirler, which corresponds to the one employed later in Chap. 10. A comparison of the predicted time average velocity and species mass fractions fields (not shown) confirmed that the LES results are mesh insensitive for macroscopic quantities.

The same simulation was used to characterize the turbulent flow field at the swirler exit and provide accurate inlet conditions for the simulations where the swirler is excluded from the computational domain. Time-averaged fields of the three velocity components U_j and the six components of subgrid velocity variances (and covariances) $\overline{u'_i u'_j}$ were extracted on a surface at an axial location of $x = -60\text{ mm}$ and imposed as target conditions to a synthetic turbulence generator [259], along with an integral turbulent length scale of about $l_t \approx 1/3D_h$, where $D_h \approx 6\text{ mm}$ is the hydraulic diameter of a single swirler vane. The synthetic turbulence generator produces time-varying inlet velocity values at every face of the air inlet patch (see Fig. 9.3), ensuring that the first and second-order time statistics of the generated velocity field match the prescribed target values. The velocity field statistics obtained from the simplified geometry were compared against those from a refined mesh with the swirler fully resolved. The comparison confirmed that the synthetic turbulence method accurately reproduces the relevant turbulent features in mixing tube and combustion chamber, thereby validating its use. A constant mass flow rate at a temperature of $T = 288.15\text{ K}$ is applied at the fuel ports, consistently with the considered operating conditions, reported in Tabs. 9.1-9.2. Zero pressure gradient is imposed to every inlet. Zero normal gradient velocity and wave transmissive pressure boundary conditions are imposed at the domain outlet to miti-

gate the reflection of pressure waves back to the swirler, with atmospheric pressure set at a distance $l = 3$ m from the combustion chamber outlet [322–324]. No-slip conditions are applied to the velocity at the walls and zero-gradient to other quantities. In regions where the wall refinement is insufficient to resolve the boundary layer, Spalding wall functions are employed to approximate the subgrid turbulent viscosity [269]. As mentioned in Sec 9.2.1, the thermochemical properties of the considered species are taken accordingly to the San Diego kinetic mechanism [143].

In the present set-up, preliminary LES showed a wide range of residence time values in the different regions of the computational domain, depending on the various flow features, such as the recirculation zones originating in the combustion chamber, as described more in details in Chap. 10. For this reason, each simulation is initialized from an LES solution evolved for $t_{\text{chamb}} = 1.5$ s, which is the total amount of time necessary for a fluid parcel to travel from the swirler ports to the outlet of the combustion chamber, in order to obtain a fully developed air flow field. A smaller characteristic time $t_{\text{flow}} = 0.1$ s is chosen, coinciding with the flow residence time at the mixing tube exit, at a location of $y = 25$ mm. Therefore, each LES is run for one characteristic time for further fuel stream development after the initialization, and for additional $2 t_{\text{flow}}$ to acquire statistics, for a total of $t_{\text{tot}} = 0.3$ s. On the 4.45 M mesh, without resolving the swirler, a typical simulation requires 30'000 CPU-hours to compute one characteristic time t_{flow} , compared to the 50'000 required on the complete 12.73 M mesh including the swirler. The LES settings are summarized in Tab. 9.3.

Parameter	Value	Parameter	Value
n_{cells}	4.45 M	Δ_{cell}	0.3–0.4 mm
y_{wall}^+	< 10	Wall functions	Spalding [269]
Δt	2×10^{-7} s	Solver	reactingFoam compressible
CFL_{max}	0.5	Time integration	Second-order implicit backward
t_{tot}	0.3 s	Subgrid turbulence model	One-equation k_{SGS} [95]
t_{flow}	0.1 s	Computational cost	30k CPU-hours/ t_{flow}

Table 9.3: LES simulation settings

9.3. RESULTS

9.3.1. FLOW FIELD ANALYSIS

Case D_s (surrogate case for $\text{XH}_2 = 1$) is first simulated numerically and the predicted velocity fields are compared to the experimentally measured flow field to validate the numerical model. Fig. 9.4 shows contour plots of axial (U) and transversal (V) velocity field in the mixing tube and combustion chamber, numerically predicted via LES and experimentally measured via PIV.

In agreement with experiments, the LES is capable to correctly predict the vortex break down at the transition from the mixing tube to the combustion chamber. As it enters the combustion chamber, the swirling flow forms a jet opening under the effect of the sudden cross section expansion and centrifugal forces.

The combined effect of adverse axial pressure gradient due to sudden cross section

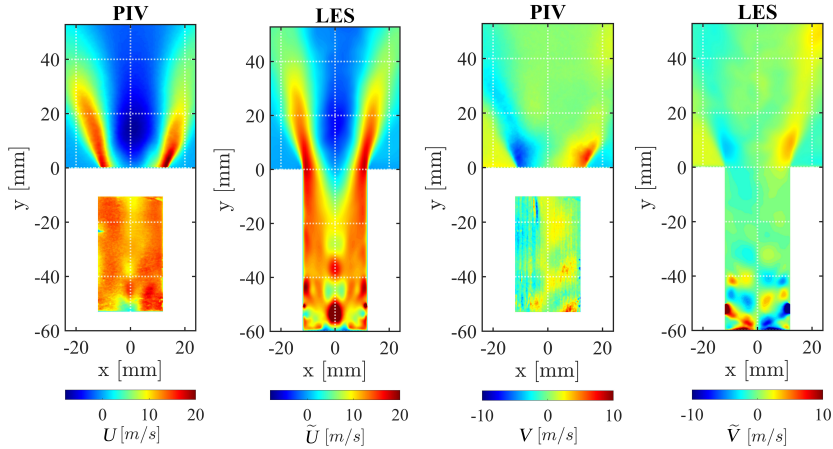


Figure 9.4: Average streamwise velocity flow field (a) and average transversal velocity flow field (b) in the mixing tube and combustion chamber obtained experimentally by PIV (left) and numerically (right) for case D_s , Tab. 9.2.

expansion and low pressure at the core, due to the swirling flow, induces the formation of a central recirculation zone (CRZ). At the considered swirl number conditions, the CRZ is not fully contained in the combustion chamber, but it is observed to form in the last section of the mixing tube, which could not be captured via PIV because of the baseplate. The LES predicts the location of the stagnation point at an axial location of $y \approx -5$ mm. Even if not optically accessible, the PIV flow field suggests that the stagnation point is located between $-10 \text{ mm} < y < -5 \text{ mm}$, coherently with the LES.

The axial and radial velocity fields predicted by the LES show the presence of secondary flow patterns at the mixing tube core (see Fig. 9.4 LES). A wake region with almost zero axial velocity and intense inward radial velocity forms downstream of the central AAI duct at the swirler exit $y \approx -60$ mm, as the high velocity stream from the swirler vanes flows towards the mixing tube center to fill this low momentum region. The combined effect of radial velocity due to this wake region and the centrifugal force due to swirl gives origin to alternating regions of high and low axial and inward-outward radial velocity, identifying secondary recirculating structures. The same features can be qualitatively observed from PIV measurements, in particular the presence of low axial velocity at a location about $y \approx -50$ mm, and the alternating radial velocity pattern.

Numerically computed and experimentally measured radial profiles of average velocity in the combustion chamber are quantitatively compared in Fig. 9.5. A good prediction of the peak values in both the axial and transversal velocity components is observed. Close to the mixing tube outlet ($y = 8$ mm), the LES correctly predicts the peak axial velocity value within 9%, and the peak transversal velocity value within 6%. The jet opening is slightly underpredicted by the LES ($\text{LES} = 22^\circ$, $\text{Exp} = 25^\circ$), as reflected in the prediction of the radial location of the velocity peaks for both components across all axial positions. Some asymmetry is noticed in the experimental values, which introduces discrepancies with numerical results on the right side of the observed window.

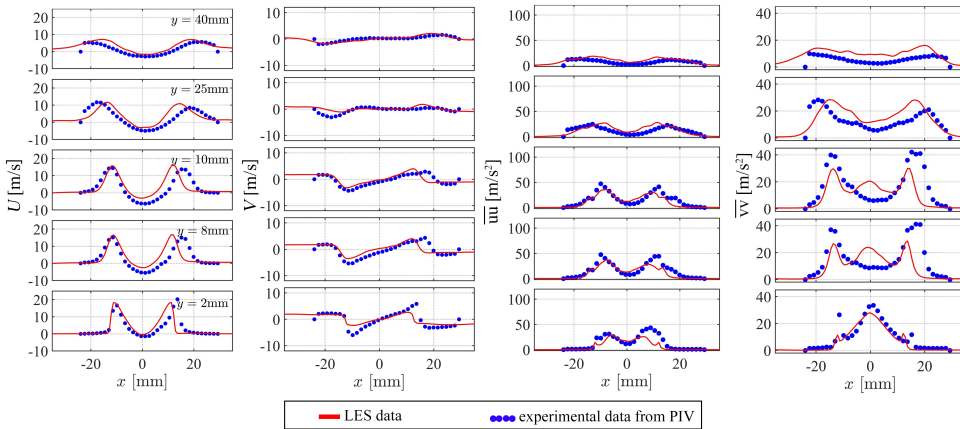


Figure 9.5: From left to right: radial profiles of axial (U) and transversal (V) velocity and variance of axial ($\overline{u'u'}$) and transversal ($\overline{v'v'}$) fluctuating velocity components from LES (—) and experiments (•••) at different streamwise locations y (rows).

The backflow velocity along the centerline is also well predicted by the LES, with an underestimation of its magnitude near the mixing tube exit at $y \approx 0$ mm. Higher-order statistics show good agreement, highlighting the LES's ability to predict turbulence intensity in the shear layers. The radial profile of the predicted axial velocity variance, $\overline{u'u'}$, qualitatively follows the distribution observed experimentally, with a correct prediction of the radial location of the peak values. Close to the mixing tube exit, $y = 2$ mm – 8 mm, the LES predicts the peak velocity within 20% accuracy, while further downstream the accuracy increases to 7%. For transverse velocity variance $\overline{v'v'}$, the LES correctly predicts the three-peaks radial profile observed experimentally at the mixing tube exit. The peak located on the centerline corresponds to the stagnation point upstream of the central recirculation zone and is underpredicted by the LES by 15%. Shortly downstream, $y = 8$ mm, the radial variance profile $\overline{v'v'}$ transitions to a two-peak shape, corresponding to the two branches of the opening jet. The LES correctly captures this shape from $y = 25$ mm on, but a peak on the centerline is still visible up to $y = 10$ mm, which is related to differences in the prediction of the CRZ axial location and jet opening angle.

Overall, the LES appears capable to capture the main flow features, including the vortex breakdown and the opening angle of the swirling jet, despite minor underpredictions in the peak velocity values.

9.3.2. MIXING PROCESS ANALYSIS

The fuel injection and mixing processes are investigated in this section. In Fig. 9.6 the development of the jet in swirling cross-flow structures is visualized through iso-surfaces of helium mass fraction as predicted by the LES for the same case D_s . The injected fuel stream is observed to follow a helical path as it mixes with the swirling flow. Interestingly, the positive and negative axial velocity values on the iso-surfaces reveal the presence of four counter-rotating vortex pairs, which consistently originate at the four fuel ports.

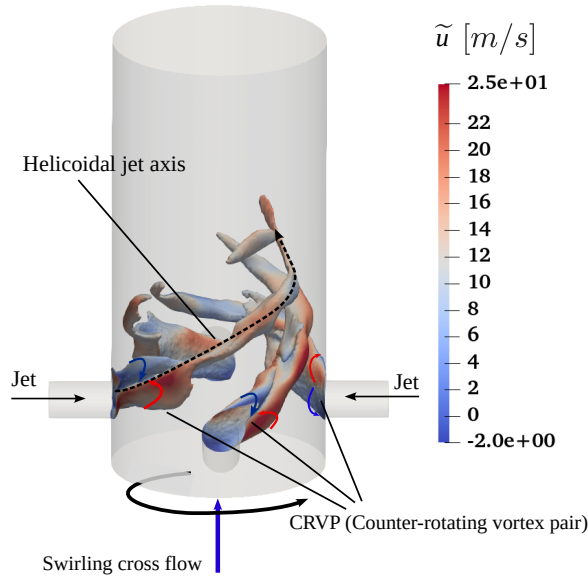


Figure 9.6: Visualization of helium jets in swirling cross-flow structures in the mixing tube as predicted by LES of case D_s by instantaneous iso-surfaces of helium mass fraction $Y_{\text{He}} = 0.25$, colored by axial velocity \tilde{u} .

These structures, formed by the pressure difference between the windward and leeward sides of the jet relative to the incoming swirling flow, are a characteristic feature of jets in cross-flow, as widely documented in the literature [302, 318, 325].

Fig. 9.7a shows the normalized fuel concentration C^* obtained from particle tracing in the helium fuel stream for the case D_s . The highest scattering intensity is observed at a location of $y \approx 50$ mm close to the fuel ports, where the fuel stream issues into the mixing tube and penetrates the swirling flow towards the centreline due to its radial injection momentum. The intensity magnitude and radial gradients of C^* clearly decrease in the streamwise direction as the fuel stream mixes with the swirling air stream. At the end of the experimental field of view ($y \approx -15$ mm), C^* drops to about 1 near the outer walls, while almost no particles are observed at the core, where C^* is still around 0.5. This stratification results from the combined effects of particle convection towards the center, driven by the radial injection momentum and associated to the jet in cross-flow development, and outward transport caused by centrifugal forces and radial velocity components, as analyzed in subsequent sections.

The time averaged field of helium mass fraction Y_{He} as predicted by the LES of case D_s is also reported in Fig. 9.7b and compared to C^* obtained from experiments. Coherently with what observed through particle tracking, high values of helium mass fraction are observed in correspondence of the fuel ports, with a decrease downstream as the helium jets spread and mix with the swirling cross-flow.

Closely downstream of the fuel ports, the numerical results reveal a pattern of isolated spots with high helium concentration, corresponding to the sectional view of the helical structures shown in Fig. 9.6. The same spots cannot be observed as clearly from

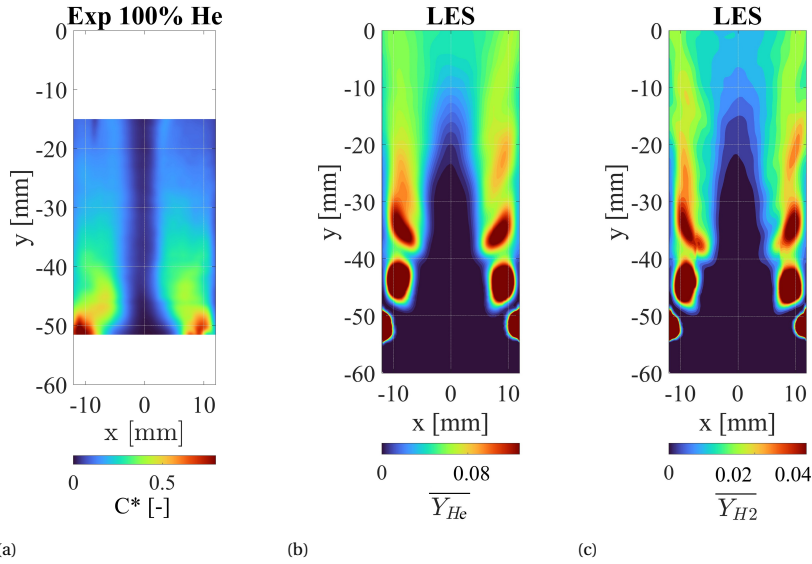


Figure 9.7: (a) Experimentally obtained C^* of case D_s at J_{low} , (b) Helium mass fraction of case D_s at J_{low} (c) H_2 mass fraction of the reacting case D.

experimental imaging in Fig. 9.7a, possibly due to insufficient resolution to capture these patterns. On the other hand, this could suggest an under-prediction of turbulent mixing in the LES, and therefore a persistency of the coherent jet structures described in Fig. 9.6 up to an axial location of $y \approx -30$ mm (memory effect) [326, 327]. In this regard, the LES predicts a weaker mixing than experimentally visualized in the first part of the mixing tube up to $y \approx -30$ mm. Downstream, stratification becomes more pronounced than in the LES, which may be due to the centrifugal separation effect. The particles tend to concentrate closer to the wall, having higher mass than the gas they track, for which instead a transport equation is solved in the LES. As observed experimentally, a stratification of fuel is evident between the mixing tube wall and the central lean core. This region appears wider in the LES predictions compared to the experiment up to $y \approx -25$ mm. From $y \approx -20$ mm the central unmixed core exhibits a similar width in both the LES predictions and experimental measurements. The LES further predicts some mixture stratification at the mixing tube exit, with helium mass fraction values of $Y_{He} \approx 0.04$ close to the wall and $Y_{He} \approx 0.0286$ at the mixing tube core, which are about 10% higher and 21% lower than the nominal value of 0.0362, respectively.

9.3.3. SUITABILITY OF HE AS A H_2 SURROGATE

The time-averaged H_2 mass fraction Y_{H_2} field, as predicted by the LES of case D, is also reported in Fig. 9.7c and compared to the helium mass fraction field from case D_s , in order to assess the suitability of Helium as a surrogate gas to predict the mixing behavior of H_2 in the present configuration. As already shown in Tab. 9.2, fuel ports in case D_s have larger diameter than case D, to achieve the same fuel jet momentum. The two

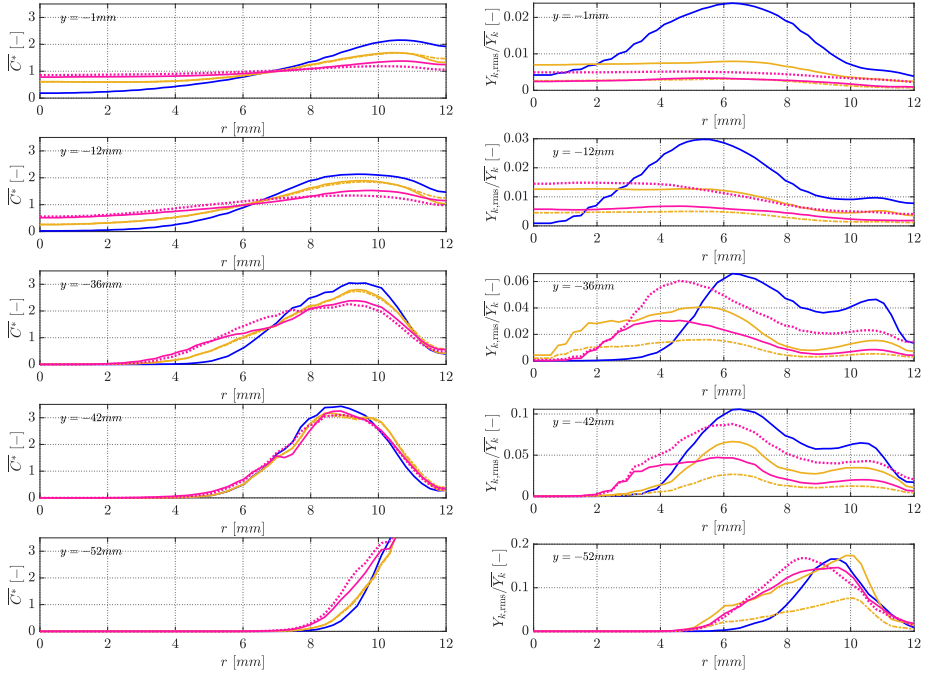


Figure 9.8: Radial plots of time averaged normalized fuel mass distribution C^* (left) and fuel mass fraction temporal rms normalized by its local time averaged value $Y_{k,rms}/\bar{Y}_k$ (right). LES results for case A $X_{H_2} = 0$ (—), case C $X_{H_2} = 0.8$ (Y_{CH_4} (—)) and Y_{H_2} (---), case D $X_{H_2} = 1$ (—) and surrogate case D_s (· · · ·).

cases display very similar mixing features, such as the fuel jet penetration and spread rate in the swirling cross-flow, the length of the lean core and mixture homogeneity at the mixing tube exit, where the H_2 mass fraction approaches its nominal value of 0.0184. Higher stratification is observed for H_2 in case D with respect to He in the surrogate case D_s towards the mixing tube exit. This results in higher mass fraction values than the nominal at the walls $Y_{H_2} \approx 0.022$ and 30% leaner than the nominal value at the core $Y_{H_2} \approx 0.013$. This suggests a slightly worse mixing of the H_2 case D as compared to the surrogate case D_s with helium.

A more quantitative description of mixing process and comparison of the two cases D and D_s is provided in Fig. 9.8 showing the radial profiles of time-averaged normalized mass fractions of the fuel agent C^* (left) and the rms mass fraction values (right) at different axial locations. The pink lines represent case D (solid) and case D_s (dashed). Results are azimuthally averaged and plotted against the radial coordinate r . In the upstream part of the mixing tube $y = -52$ mm, the profiles illustrate the radial penetration of the fuel stream driven by the radial injection momentum. The rms profiles shows a peak at a radial location $r \approx 8$ mm to 10 mm, corresponding to the region of steepest radial C^* gradients and identifying the mixing layer between the fuel stream and the incoming swirling air. At $y = -42$ mm, the normalized mass fraction value of both helium (case

D_s) and hydrogen (case D) reaches a peak of approximately $C^* \approx 3$ at a radial location of $r = 9$ mm, marking the most inward fuel reach due to radial injection momentum. Further downstream, the profile spreads both inwards towards the mixing tube core and outward towards the wall as the fuel mixes downstream. The peak radial location shifts outwards, indicating fuel stratification towards the wall, while its magnitude decreases. Consistently, the rms profiles display a double-peak structure from $y = -43$ mm downstream. The inner peak, higher in magnitude, corresponds to the intense mixing layer on the windward side of the fuel jet, where it interacts with the cross-swirling air flow. In contrast, the outer peak, which has a lower rms value, corresponds to the less intense mixing layer on the leeward side, where fuel spreads outward towards the wall. Eventually, the mass fraction profile tends to approach $C^* = 1$, as the mixture becomes homogeneous. Consequently, the rms values diminish, and the double-peak structure transitions into a single peak, eventually flattening out.

The Helium mass fraction profiles in case D_s (pink dashed line) closely match the H_2 profiles of case D (pink solid line), especially close to the mixing tube exit. At these locations, case D shows slightly higher peaks of C^* than case D_s suggesting more stratification when using H_2 , consistently with the contour plots in Fig. 9.7c. At more upstream locations ($y = -36$ mm and $y = -52$ mm), higher He normalized mass fraction values with respect to H_2 are observed in a region between 5 and 9 mm from the centreline, suggesting a quicker penetration of helium towards the core of the swirling cross-flow, as confirmed by the higher rms values of Y_{He} than Y_{H_2} at these locations. This is possibly associated to the overall slightly higher injection momentum of helium, as shown in Fig. 9.1a, and may explain the ultimately more homogeneous mixture obtained for case D_s .

In summary, the LES results for case D_s demonstrate strong validation of the numerical model when compared to experimental data, showing accurate predictions of the velocity field and reasonable agreement in describing the mixing process. Furthermore, the numerical results from cases D and D_s confirm that helium serves as an effective surrogate for H_2 in replicating the mixing behavior under the present operating conditions, thereby supporting the validity of the experimental methodology. Building on this validation, the following section explores the impact of variations in fuel composition on mixing characteristics, maintaining constant operational power and air mass flow rate, through both numerical and experimental approaches.

9.3.4. EFFECT OF FUEL COMPOSITION ON FUEL-AIR MIXING

Fig. 9.9a presents the spatial unmixedness U_s (Eq. 9.3) along the mixing tube for various surrogate fuel compositions, determined from post-processed Mie-scattering images of the cases in Tab. 9.2. The spatial unmixedness, calculated using Eq. 9.3, is evaluated at multiple y -locations to assess mixture homogeneity and its streamwise evolution, which reflects the rate of mixing. For cases A_s , B_s , and C_s representing CH_4/H_2 fuel mixtures of increasing H_2 content (0%, 40% and 80% H_2 in volume, respectively), the unmixedness at the most upstream location ($y = -50$ mm) consistently measures approximately $U_s \approx 0.24$. At $y = -15$ mm, a distinct correlation between higher helium content and better mixing quality is observed. At this location, cases A_s and B_s , representing a methane mass fraction above 90 % in the fuel stream, yield nearly identical unmixedness values of

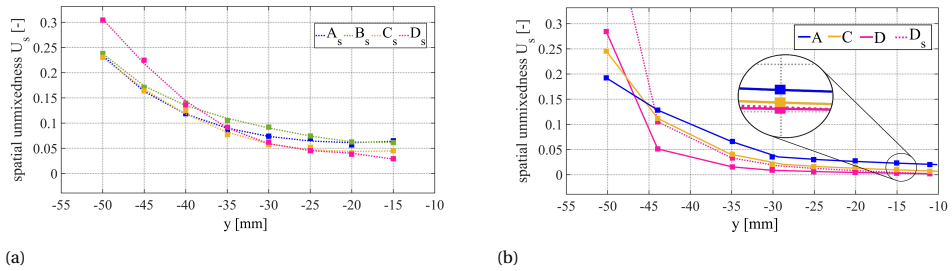


Figure 9.9: Spatial unmixedness at different y locations for different fuel compositions (—) and its surrogates (····): $X_{H_2} = 0$ (—), $X_{H_2} = 0.4$ (—), $X_{H_2} = 0.8$ (—) and $X_{H_2} = 1$ (—) calculated from experimental data (a) and numerical data (b).

$U_s \approx 0.055$, while case C_s (representing 66% methane by mass) achieves a slightly lower value of $U_s \approx 0.05$. In comparison, the full helium case (case D_s), which serves as a surrogate for pure H_2 fuel stream, exhibits the highest initial unmixedness value of $U_s \approx 0.3$ and experiences a more rapid mixing, with respect to the other tested fuel compositions, reaching the lowest unmixedness value $U_s \approx 0.025$ at the tube exit.

The same analysis is performed using LES (Fig. 9.9b), simulating the actual CH_4/H_2 fuel mixtures (cases A, C and D) alongside with the 100% helium case (case D_s). The simulations confirm the experimental findings, clearly highlighting that higher H_2 content in the fuel stream corresponds to higher upstream unmixedness, close the fuel injection ports, but it also promotes faster mixing along the tube, leading to a higher degree of mixing. This behavior may be attributed to a more inward penetration of the fuel stream towards the central core in the upstream regions, which increases unmixedness initially but accelerates mixing and enhances homogeneity further downstream. This is confirmed by the results in Fig. 9.8, where close to the fuel ports location $y = -50$ mm, higher H_2 content in the fuel mixtures results in higher C^* values closer to the mixing tube core ($r \approx 6$ mm to 10 mm). Consistently, the inner rms peak, which identifies the mixing layer, shows higher values with increasing H_2 content and its radial location shifts closer to the mixing tube axis. Fuel penetration is primarily influenced by the initial fuel jet radial momentum and fuel diffusion. Moreover, in a swirled configuration, centrifugal forces act differently on two streams of different density, so that the air stream is pushed outwards more than the lighter fuel stream. This effect is more pronounced upstream in the mixing tube, where density gradients are stronger due to unmixedness, and it contributes to better mixing for lighter fuels. At the mixing tube exit, case A (100% methane) exhibits more significant fuel stratification, with a peak value $C^* \approx 2$, whereas case D shows a more homogenous mixture with $C^* \approx 1$.

Both LES and experiments show that unmixedness decreases sharply between $y = -50$ mm and $y = -30$ mm, followed by an asymptotic trend downstream, suggesting that most of the mixing occurs in the upstream region of the mixing tube and residual unmixedness stratification persists further downstream. This is coherent with Fig. 9.8 where the C^* and rms profile spread out between -52 mm to -36 mm while showing minimal changes downstream. Further mixing cannot occur due to balance between convective centrifugal transport and inward diffusion as further clarified by LES results in

the next section. Therefore, when fixing the air mass flow rate and power setting, stratification appears inherent to the fuel properties and its injection momentum (which is constrained by the operating conditions in the considered geometry).

Despite the similarities between LES and experiments, LES predicts lower unmixedness values at the tube exit compared to experiments, suggesting better mixing performance for all investigated cases. This discrepancy arises from differences in measurement methods. While LES resolves the actual fuel gas distribution, experimental measurements rely on seeding the fuel stream with droplets. The discrepancies between LES and experimental data may be related to limitations of the DEHS droplets in representing the inertial and diffusive behavior of the gaseous fuel.

Nevertheless, both methods successfully capture the overarching trends, demonstrating that higher H_2 content consistently results in lower unmixedness values at the tube exit and that most of the mixing takes place in the first half of the mixing tube. To further explain the observed trends, a detailed analysis of radial fluxes in the transport equations is conducted next, followed by a comparative budget analysis of the transport terms across different fuel compositions.

9.3.5. RADIAL SPECIES FLUXES

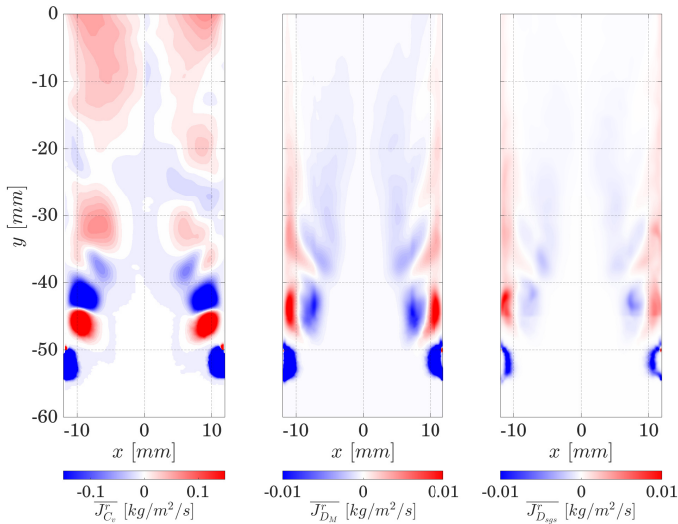


Figure 9.10: Time averaged radial flux of Helium due to convective, molecular diffusive and turbulent diffusive transport as computed from the LES of case D_s .

LES data in the mixing tube are further elaborated to provide a comprehensive overview of the mixing mechanisms in the present set-up. To this scope, the helium case D_s is taken as a reference and the radial fluxes of helium mass fraction are computed. With reference to the filtered transport equation in Eq. 9.5, the radial fluxes are computed as:

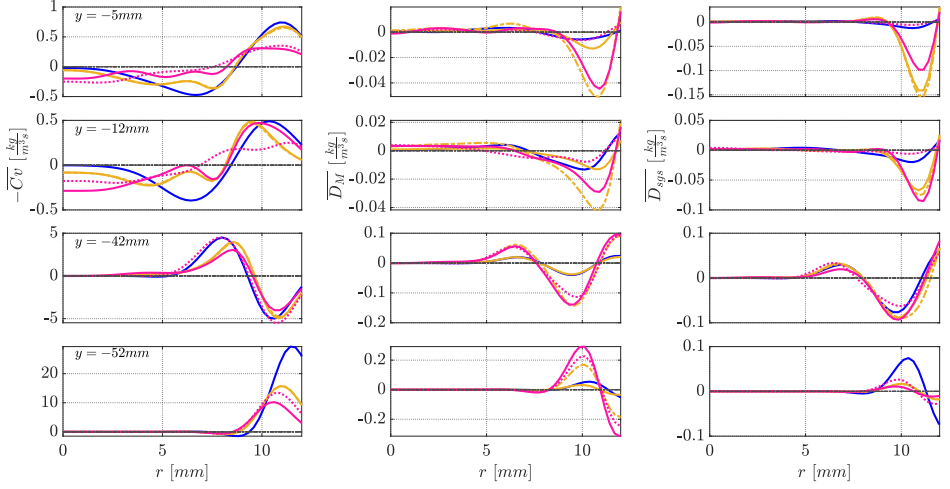


Figure 9.11: LES results for case A $X_{H_2} = 0$ (—), case C $X_{H_2} = 0.8$ (Y_{CH_4} (—) and Y_{H_2} (---)), case D $X_{H_2} = 1$ (—) and surrogate case D_S (· · · ·).

$$J_{C_v}^r = \overline{\rho \widetilde{u}_r \widetilde{Y}_{He}} \quad J_{D_M}^r = -\overline{\rho D_{He}^m} \frac{\partial \widetilde{Y}_{He}}{\partial r} \quad J_{D_{SGS}}^r = -\frac{\mu_{SGS}}{Sc_t} \frac{\partial \widetilde{Y}_{He}}{\partial r}, \quad (9.7)$$

where convection $J_{C_v}^r$ is linked to the local helium mass fraction and radial velocity component values, while molecular diffusion $J_{D_M}^r$ and subgrid turbulent transport $J_{D_{SGS}}^r$ are driven by the mass fraction gradients. Fig. 9.10 reports the contour plots of the time averaged radial fluxes. The convective flux accounts for the majority of the transport near the fuel ports ($y = -52$ mm), where the initial jet momentum drives the fuel into the swirling flow up to a radial location of $x = 10$ mm. The secondary recirculating flow described in Fig. 9.4 and the characteristic helicoidal fuel stream structures with counter-rotating vortex pair (Fig. 9.6) give origin to peculiar alternating inward and outward convective flux patterns. The radial velocity component is quickly redirected by the incoming swirled cross-flow into stronger streamwise and tangential components, as the flow in the mixing tube transitions to a homogeneously swirling state (Fig. 9.4). Consequently, the convective flux decreases to a value below 0.05 at an axial location around $y \approx -35$ mm, and the inward (negative) convective flux fades. Further downstream, the inward component is almost completely suppressed along with the weakening of secondary recirculation zones (Fig. 9.4), leaving a residual outward flux from $y = -30$ mm downstream. This outward flux intensifies near the outlet, as the mixture must flow around the central recirculation zone located close to the mixing tube outlet, Fig. 9.4.

Analyzing the diffusion fluxes reveals that the molecular diffusion intensity is comparable to that of turbulent diffusion (in the case of helium), emphasizing the importance of accurately modeling molecular diffusion. At most locations (e.g. $y > -50$ mm), the turbulent diffusion value is even smaller than the molecular diffusion, suggesting good mesh resolution and low turbulence level due to the very low Reynolds numbers of the

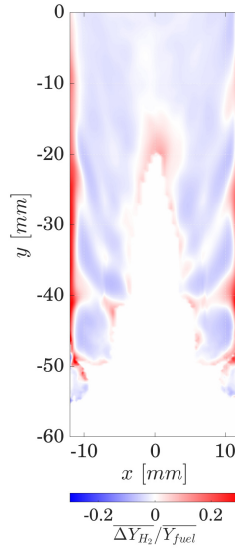


Figure 9.12: Local variation of hydrogen mass fraction in the fuel composition at a random time for case C.

fuel stream ($Re \approx 800$). The diffusion flux patterns follow mass fraction gradients, with the strongest intensity occurring in the shear layer. In particular, negative diffusive flux (inwards) is observed towards inner radial regions, in correspondence of the windward mixing layer between fuel jet and cross-flow, previously identified in Fig. 9.8 with the inner rms peak and maximum mass fraction gradient. Analogously, at a streamwise location of $y \approx -45$ mm, positive diffusive flux, spreading fuel towards the outer boundary layer is observed, which is associated with the leeward mixing layer. Consistently with previous observations, most of the mixing appears to occur upstream of $y = -30$ mm, where convection and diffusion fluxes remain strong due to residual radial velocity components (from fuel injection or recirculation) and significant fuel mass fraction gradients are present. Downstream of $y = -30$ mm, these gradients smooth out (as seen in Fig. 9.8) and the inward radial momentum dissipates, resulting in significantly milder mixing. At these locations, the primary factor contributing to the described fuel stratification is the predominance of outward convection (driven by the presence of the central recirculation zone at the mixing tube exit), while diffusion diminishes due to the mitigated mass fraction gradients associated to the increasingly homogeneous mixture.

9.3.6. RADIAL TRANSPORT BUDGET ANALYSIS

Next, a budget analysis is carried out to evaluate the strength of transport terms for different fuel compositions and compare them. Considering the time-averaged form of Eq. 9.5, and assuming the time derivative is zero due to steady-state flow, the transport terms given by the local divergence of species fluxes ($-\nabla \cdot J_k$) must balance, such that:

$$-C_{\nu,k} + D_{M,k} + D_{SGS,k} = 0, \quad (9.8)$$

being $-C_{v,k}$, $D_{M,k}$ and $D_{SGS,k}$ the species k transport terms appearing in Eq. 9.5 associated to convection, molecular and subgrid transport, respectively. Considering only the radial contribution of the three radial fluxes to the transport budget of a species k , these terms are computed as follows:

$$C_{v,k}^r = \frac{\partial}{\partial r} (\bar{\rho} \bar{u}_r \bar{Y}_k) \quad D_{M,k}^r = \frac{\partial}{\partial r} \left(\bar{\rho} D_k^m \frac{\partial \bar{Y}_k}{\partial r} \right) \quad D_{SGS,k}^r = \frac{\partial}{\partial r} \left(\frac{\mu_{SGS}}{Sc_t} \frac{\partial \bar{Y}_k}{\partial r} \right) \quad (9.9)$$

The time averaged radial profiles of the budget terms in Eq. 9.9 are reported in Fig. 9.11 for different streamwise locations. These terms are normalized by the spatial average of the fuel mass fraction at each y -location to express the transport terms relative to C^* , thereby highlighting the relative significance of each term with respect to the local level of unmixedness. Negative values of the budget term indicate that convection or diffusion are transporting fuel away from a specific radial location, whereas positive values represent transport towards that location.

Consistently with Fig. 9.10, at the fuel port exit, convection accounts for most of the radial transport since the fuel is injected into the mixing tube with its initial radial momentum. Case A (blue line) exhibits the highest peak value of the convective transport term due to the higher mass flow rate of methane compared to the other cases (see blue line, left column last row in Fig. 9.11). However, cases with higher H_2 content (yellow line C and pink line D) exhibit a further fuel entry towards the center of the mixing tube, as indicated by a more inward peak location in the convection profile and a wider distribution of nonzero values extending further inwards. This behavior, consistent with the trends described earlier (Figs. 9.8-9.9b), is associated with the higher fuel momentum in these cases.

Further downstream, at $y = -42$ mm, the convection term continues to transport fuel radially inwards for all the cases, from $r = 4$ mm (peak of negative budget value) to $r = 8$ mm to 9 mm (peak of positive budget value). As expected, the convection term has lower values here than at the fuel ports, where the radial velocity due to the injection is at its maximum. At this downstream location, convection is primarily driven by radial velocity induced by the secondary recirculations described earlier (Fig. 9.4).

The diffusive transport (both molecular and turbulent) displays a double-peak profile (middle and right column in Fig. 9.11), indicating fuel transport via diffusion from $r \approx 9$ mm to 10 mm (where the maximum fuel mass fraction appears, as shown in Fig. 9.8 and Fig. 9.7) both towards the mixing tube core (up to $r = 4$ mm) and outwards into the boundary layer, as previously described. Although diffusive transport is two orders of magnitude weaker than convection, it still promotes fuel transport towards the center at each streamwise location. Notably, in cases C and D, the molecular diffusion of H_2 has similar magnitudes as turbulent diffusion, and between $r = 4$ mm and $r = 6$ mm, it becomes comparable to convection.

Towards the mixing tube exit ($y = -12$ mm and $y = -5$ mm), the intensity of convection is drastically reduced by an order of magnitude for all the cases. Here, radial transport is primarily driven by outward radial velocity associated with vortex breakup and the presence of the central recirculation zone (CRZ) at the tube exit (Fig. 9.4). At this location, convection appears to promote stratification, while diffusion opposes it.

In facts, H_2 and helium (cases D and D_s) are less subject to outward radial convection as compared to methane and H_2/CH_4 mixtures (case A and C) due to their lower density, while their molecular diffusion remains significant, ultimately displaying the lowest levels of unmixedness and stratification.

Interestingly, Fig. 9.11 demonstrates how the species in a multicomponent fuel are subject to different transport mechanisms. Specifically, in case C ($X_{H_2} = 0.8$), hydrogen's diffusive transport (yellow dashed line) exhibits peak values approximately 50% higher than methane's diffusive transport (yellow solid line). Conversely, convective and turbulent diffusion transport are nearly identical for the two species. The effects of these differences in diffusivity are illustrated in Fig. 9.12, which shows the local drift in the hydrogen-to-fuel mass fraction ratio relative to its nominal value at injection, thereby highlighting the CH_4/H_2 separation within the fuel mixture. Hydrogen diffuses more significantly than methane across the upwind and leeward mixing layers, both reaching deeper into inner mixing tube core and forming a hydrogen-rich zone (red values) at the boundary layer, where molecular diffusion dominates over turbulence. In this region, the hydrogen percentage relative to the local fuel mass fraction is predicted to increase by up to 25%. This highlights potential risks associated with boundary flashback when employing methane-hydrogen fuel mixtures in the studied configuration.

9.4. CONCLUSIONS

The present chapter describes the numerical LES analysis of the mixing behaviour of a jet in swirling cross-flow configuration representative of the injector of a lab-scale technically premixed, swirl-stabilized burner, complementing the experimental approach proposed in [319]. In [319] Mie scattering images of the seeded fuel stream enable particle count techniques to evaluate the degree of mixing, while Large Eddy simulations (LES) solving species transport equations are used in the presented study to investigate the problem numerically. The analysis focuses on the influence of fuel composition on the mixing process. Mixing performance is evaluated using a spatial unmixedness parameter U_s , and by examining the radial profiles of species mass fractions obtained from numerical simulations. To represent CH_4/H_2 fuel mixtures, helium/air mixtures with varying helium concentrations are employed, with the suitability of helium as a surrogate for H_2 validated through numerical simulations. The key conclusions are as follows:

1. Helium is validated as a reliable surrogate for hydrogen for assessing macroscopic fuel-air mixing trends in partially premixed swirl-stabilized injectors. A suitable strategy to use helium is to keep the momentum flux ratio J_{swirl} constant. Due to the higher helium density, equal jet momentum (at constant mass flow rate) has to be achieved by adjusting the fuel inlet diameter.
2. In fuel blends of CH_4 and H_2 , the higher diffusivity of H_2 into air with respect to CH_4 can result in a H_2 rich region at the mixing tube wall near the entrance in the combustion chamber, exacerbating potential criticalities related to boundary layer flashback.
3. For similar values of J_{swirl} , decreasing the density of the fuel stream improves mixing. Convection dominates mixing near the injection ports, but it drives outward

fuel stratification downstream, near the mixing tube exit. In contrast, molecular diffusion transports fuel species across the jet's windward and leeward shear layers, enhancing mixing towards the mixing tube center at all streamwise locations. H_2 and He undergo less downstream stratification because of their lower density and higher molecular diffusivity compared to CH_4 , both improving mixing.

9.5. OUTLOOK & CONSIDERATIONS

The non-reacting results indicate that increasing the H_2 content improves mixing in fuel-flexible (CH_4/H_2) combustion systems with a jet-in-cross-flow configuration. Enhanced mixing with higher H_2 content could contribute to reduced NO_x emissions, assuming constant adiabatic flame temperature, by lowering the operating equivalence ratio. However, due to H_2 's significantly higher flame speed, the flame may anchor further upstream in regions where the fuel and air are less premixed, potentially increasing NO_x levels. As such, direct estimation of NO_x from non-reacting mixing data alone is challenging.

While non-reacting studies provide valuable trends, they may not fully capture the behavior under reacting conditions. Nevertheless, they offer useful insights into mixing characteristics and flame anchoring behavior. In the next chapter, reacting conditions are investigated through flamelet model, where no direct transport equation for each species is solved, and the influence of fuel stratification on flame stabilization and emissions is investigated in details.

10

LES ANALYSIS OF THE TU DELFT SWIRL-STABILIZED COMBUSTOR

10.1. INTRODUCTION

This chapter focuses on the LES analysis of the TU Delft swirl-stabilized combustor [68] under reacting conditions. Building upon the preliminary non-reacting simulations with detailed species transport to assess mixing quality, presented in Chapter 9), this study shifts the focus towards a computationally efficient, yet physically accurate modeling strategy for hydrogen combustion under laboratory scale application conditions.

LES of swirl-stabilized technically premixed combustors have been extensively performed for hydrocarbon fuels, both in laboratory scale configurations and setups close to practical gas turbine applications. An extensive review of LES models, best practices and state of the art of gas turbine test cases are given in [195]. Many of them have been carried out using LES models solving for detailed species transport, which offers a very high level of details in the description of a broad range of physical features, i.e. turbulent mixing, heat loss, strain-flame interaction, and pollutant formation. Among these are for example the thickened flame model (TFM) with detailed (or reduced) chemistry, which has been largely employed for the LES of swirled hydrocarbon combustors at conditions relevant for gas turbines [87, 195, 328–330]. Alternatively, flamelet-based models have also been successfully applied with advantages in terms of robustness and computational cost. For instance, the filtered tabulated chemistry (FTACLES) model [107], or flamelet based chemistry tabulation with presumed FDF closures [65, 89, 136, 331], have provided accurate predictions in swirl-stabilized combustors with hydrocarbon fuels.

In contrast, the LES study of hydrogen swirled combustors under practical operating conditions is still at an early stage. This is firstly due to the fact that experimental test cases have only recently been developed [58, 296, 297, 332]. Methane-hydrogen blends are often used as intermediate cases to progressively approach the behavior of pure hydrogen flames [295], and these blends have been numerically investigated in several studies [333, 334]. Secondly, extending LES to pure hydrogen flames remains particu-

larly challenging due to the differential diffusion (DD) effects, as extensively reviewed in Chaps. 1–2. It remains unclear whether in practical hydrogen combustors, including swirl-stabilized configurations, differential diffusion effects are relevant under highly turbulent conditions and different premixing levels (perfectly premixed, technically premixed, partially premixed), therefore requiring modelling at a resolved and subgrid level in LES.

Early LES of swirl-stabilized technically premixed combustors burning pure hydrogen relied on detailed chemistry. In these approaches, differential diffusion effects can be included at a resolved level by assigning an individual diffusion coefficient to each species in their transport equation, based on local composition and thermochemical state (see Sec. 2.1.2). Using this strategy, several recent studies have successfully simulated swirl-stabilized hydrogen flames with detailed chemistry and thickened flame models (TFM) including differential diffusion [44, 58, 335]. In technically premixed cases, with non perfectly homogeneous mixture, DD effects were found to be limited [44], although influencing the local mixture composition and nitric oxide NO formation. In contrast, fully premixed lean hydrogen swirl combustors have shown clear evidence of thermodiffusive instabilities when simulated with thickened flame models and detailed species transport, confirming the importance of DD modeling in these regimes [336].

As reviewed in Chapter 2 significant effort has gone into developing differential diffusion models for flamelets-based LES at the resolved level [39, 133, 225], tested primarily on canonical flames, and the need of subgrid models has been also addressed in literature [39, 282]. As a result, the application of flamelet-based LES to hydrogen swirled combustors, relevant for practical applications, is still limited. In swirl-stabilized configurations, flamelet-based simulations of methane–hydrogen blends have neglected DD, but nevertheless achieved good agreement with experiments [337]. Similarly, LES of technically premixed swirl combustor fueled with 100% hydrogen [297] omitted DD effects but still reproduced experimental data with good accuracy, as turbulent mixing dominated over molecular diffusion [178]. In the same experimental setup studied in [178, 297], LES results obtained with a flamelet model neglecting differential diffusion were compared against TFM simulations imposing species-specific diffusion coefficients in [338]. The effects of differential diffusion were found to be secondary to turbulent transport, in line with what observed in [44], but still noticeable in reacting regions. Recent work [226, 227] has initiated a more detailed study of DD effects in flamelet-based LES of lean perfectly premixed swirled hydrogen flames, showing good agreement with experimental observations and the correct prediction of thermodiffusive instabilities, whose prediction is fundamental for the correct description of stabilization and structure of these flames.

The study presented in this chapter contributes to this ongoing research by applying for the first time the in-house flamelet/presumed FDF LES model, developed and validated in Part I of this thesis, for the analysis of the TU Delft swirl combustor introduced in Chap. 4, operated with 100% hydrogen fuel. Previous investigations of this combustor focused only on methane–hydrogen blends, employing either a thickened flame model with detailed chemistry [290, 291, 339] or a flamelet/presumed FDF framework [292]. The LES model is firstly validated against experimental data at a baseline operating point, with low hydrogen content fuel blend, to assess its performance in predicting

non-reacting and reacting flow fields, flame stabilization behavior, and NO_x emissions, partly explored previously in [292]. Next, the combustor is simulated at the same power and air mass flow rate conditions as the baseline set point, but with 100% H_2 fuel. This case, which has shown propensity to flashback in experiments, is used to evaluate the influence of heat loss modelling on flame stabilization near flashback conditions. In addition, an ultra-lean operating point at the same power setting with increased air mass flow rate is numerically explored. The LES analysis of this regime, which has not yet been experimentally studied, provides a preliminary assessment of flame stability limits, emission characteristics, and the influence of mixture inhomogeneities under near-extinction conditions.

The main objectives of this chapter are to:

- Quantitatively assess the effects of mixture stratification on flame anchoring, stabilization, and NO_x emissions;
- Characterize the flame stabilization in near-flashback conditions assessing the relevance of heat loss modeling;
- Evaluate differential diffusion effects and their interaction with local flame strain in technically premixed hydrogen flames, assessing their relevance compared to turbulent mixing and fuel stratification in terms of temperature and emissions

The results obtained in this chapter contribute to a better understanding of hydrogen combustion dynamics in swirled configurations. The analysis further supports the interpretation of experimental findings reported in [68] and provides detailed insights that complement and extend the experimental database.

10.2. OPERATING CONDITIONS

The geometrical details and available experimental measurements of the TU Delft swirl-stabilized technically premixed combustor were introduced in Chapter 4 and described in [68]. For the present analysis, the swirler with geometric swirl number $Sw = 1.1$ is selected, at a reference operating power of 12 kW and a total air mass flow rate of $\dot{m}_{\text{air,tot}} = 5.38 \text{ g/s}$, consistent with the experimental investigations by Link and co-workers [68, 113, 319], as well as previous numerical analyses [290–292, 339]. A summary of the operating conditions for the simulated cases is provided in Tab. 10.1. An inlet temperature of 300 K and ambient pressure of 101325 Pa are assumed for all the simulations.

An operating condition featuring fuel composition of 25% H_2 and 75% CH_4 in volume is selected (case 25H2) for model validation, given the improved flame stability observed experimentally compared to the pure CH_4 case. To achieve the 12 kW power output, a fuel mass flow rate of $\dot{m}_{\text{fuel}} = 0.228 \text{ g/s}$ is imposed, resulting in a nominal equivalence ratio of $\phi_{\text{nom}} = 0.65$ and a corresponding mixture fraction of $z_{\text{nom}} = 0.04$, according to Bilger's definition [139] reported in Eq. 2.33. This configuration leads to an adiabatic flame temperature of approximately 1980 K. For this fuel composition, the stoichiometric mixture fraction is $z_{\text{st}} = 0.053$.

The same power and air mass flow rate set point is considered for the 100% H_2 cases, for consistency. At the nominal condition (100H2_{nom} in Table 10.1) a fuel mass flow rate

of 0.1 g/s is employed, resulting in a nominal equivalence ratio of $\phi_{\text{nom}} = 0.63$. Experimental observations indicated instability at this operating point, with a strong flashback propensity. Experimentally, a minimum axial air injection of 20% was necessary to achieve a flashback-free flame at the considered operating conditions.

As will be discussed in Sec. 10.6, flashback is observed in the LES results for the nominal case with 100% H₂ (100H_{2, nom} of Tab. 10.1), when heat losses are not considered in the model. In order to investigate a stable case at the 100% H₂ fuel condition, further LES are thus conducted where flashback is avoided by selecting an ultra-lean operating point. This is achieved by maintaining a fixed power output (12 kW) while increasing the air mass flow rate by 86%, which results in a nominal equivalence ratio of $\phi_{\text{nom}} = 0.34$ and an adiabatic flame temperature of approximately 1390 K. Although no experimental measurements are available for this condition, the analysis on the LES results is relevant to assess flame stability, mixing efficiency and emission minimization under ultra lean conditions in the investigated combustor.

A total of five LES is carried out. The case with 25% H₂ content in the fuel blend is simulated first in order to validate the flamelet model and get insights on the main physical features of the combustor. Four additional LES are performed for the cases with 100% hydrogen fuel. First, the nominal case (100H_{2, nom}) is simulated neglecting differential diffusion modelling and focusing on the effects of heat loss. Next, a baseline LES (100H₂) is conducted for the ultra-lean operating condition, again neglecting differential diffusion and without axial air injection (AAI). To isolate the impact of AAI on mixing, flame structure, and emissions, a third simulation (100H₂AAI) is carried out for the same ultra-lean condition, imposing 10% AAI. Finally, the ultra-lean case is simulated without AAI but including differential diffusion modelling (100H₂DD), enabling an evaluation of its role in flame dynamics and emission characteristics.

Case		25H ₂	100H _{2, nom}	100H ₂	100H ₂ AAI	100H ₂ DD
$\dot{m}_{\text{air, tot}}$	[g/s]	5.38	5.38	10.0	10.0	10.0
AAI	[%]	0	20%	0%	10%	0%
\dot{m}_{fuel}	[g/s]	0.228	0.1			
P	[kW]	12	12			
$X_{\text{H}_2, \text{fuel}}$		0.25	1			
$X_{\text{CH}_4, \text{fuel}}$		0.75	0%			
ϕ_{nom}		0.65	0.63	0.34		
z_{nom}		0.04	0.018	0.01		
$T_{\text{ad, nom}}$	[K]	1980	1890	1390		

Table 10.1: Operating conditions of the simulated test cases.

10.3. NUMERICAL SET UP

The in-house flamelet-based LES model with presumed FDF, described in Sec. 3.2 and previously applied in Chapters 6, 7, and 8, is here employed to simulate the TU Delft swirl-stabilized combustor. The Favre-filtered Navier–Stokes equations, i.e. conservation of mass, momentum, and absolute specific enthalpy (sum of sensible and forma-

tion enthalpies) are solved using the low-Mach number approximation and the finite volume method within OpenFOAM v9. Additionally four Favre-filtered transport equations are solved within the combustion model for the two controlling variables (progress variable \tilde{c} and mixture fraction \tilde{z}) and their SGS variances. The PIMPLE algorithm is used for the solution, where the pressure–velocity coupling is handled using the PISO algorithm [281] and an external loop performing at least three iterations per time step is used to solve scalar transport equations. Convective and diffusive terms are discretized using second-order central schemes, and time integration is carried out with an implicit Euler scheme. A constant time step of $\Delta t = 1.0 \times 10^{-6}$ s is used, ensuring a maximum CFL number below 0.1 throughout the swirler, mixing tube, and flame region. Subgrid-scale stresses and scalar fluxes are closed using a one-equation model for subgrid viscosity μ_t [95, 102, 176], as detailed in Chap. 3.

Nitric oxide NO formation is investigated by integrating the transport model described in Sec. 3.2.5 into the baseline flamelet framework. A transport equation for NO mass fraction is solved, with the formation rates tabulated as a function of the controlling variables (progress variable and mixture fraction), and their SGS variances.

To assess the influence of heat losses on flame stabilization in near-flashback conditions, the correction model described in Sec. 3.2.4, similar to that in [251], is employed, imposing isothermal wall conditions and locally computing an enthalpy defect relative to the adiabatic case. In Sec. 10.7.2, differential diffusion effects are examined in the 100H2DD simulation. For this purpose, the M_2 model introduced in Chap. 7 and tested under strained conditions in Chap. 8 is adopted, as it corrects for differential diffusion terms in the transport equations of both controlling variables and enthalpy.

The one-dimensional solver CHEM1D [141] is used to construct the thermochemical database from unstretched 1D premixed laminar flamelets. Approximately 300 flamelets at a reactant temperature of 300K and atmospheric pressure are computed. The flammability range spans $z \in [0.017, 0.218]$ for the fuel blend case with 25% H_2 (25H2), and $z \in [0.007, 0.017]$ for all cases reported in Tab. 10.1 with 100% hydrogen fuel (100H2). A scaled progress variable c based on combustion products of water mass fraction Y_{H_2O} and carbon dioxide Y_{CO_2} is used for the case with the fuel blend of 25 % hydrogen 75% methane (in volume). For the pure hydrogen cases, a progress variable based on combustion products, i.e. only Y_{H_2O} , is also adopted to ensure consistency with the methane/hydrogen blend case and the analysis and validation presented in Chap. 7 for partially premixed hydrogen flames. This choice is further supported by previous studies on hydrogen swirl combustors under globally lean conditions [178], where a detailed comparison of different progress variable definitions showed that using Y_{H_2O} provides a suitable parametrization of the thermochemical quantities.

For the 100H2DD case of Tab. 10.1, a mixture-averaged transport model is used to include differential diffusion in the resolution of the 1D flamelets, as introduced in Sec. 2. In all other cases, a constant unity Lewis number is assumed for each species. When heat loss modeling is applied, 10 additional flamelet manifolds are computed with reactant temperatures ranging linearly from 200K to 400K. These are used to derive a correction factor for the reaction rate, as described in Sec. 3.2.4. For the 25H2 case, the GRI3.0 mechanism [142] is used, as the fuel is predominantly methane. and GRI3.0 is often used in similar studies for methane fuel. For all cases involving 100% H_2 , the San Diego

mechanism [143] is employed, as it was specifically developed and validated for hydrogen flames [340]. This choice aligns with previous studies on pure hydrogen swirled combustion [58, 341] and ensures consistency with the analysis in Chapter 7, where the mechanism was further assessed for partially premixed hydrogen flames. This is coupled with the nitrogen chemistry mechanism employed in [44] for accurate prediction of NO formation.

The computational domain, illustrated in Fig. 10.1, includes the combustion chamber, mixing tube, and swirler, based on the geometry described in Chap. 4. A fully block-structured hexahedral mesh is constructed using the software Pointwise [342]. This approach ensures fine resolution in the flame region and near-wall areas while minimizing skewness, non-orthogonality and total cell count. This is crucial given the long residence times and associated computational cost, as discussed in the next section. A total of $N_\theta = 236$ points is distributed in the azimuthal direction while $N_y = 180$ points are used in the axial direction for the combustion chamber, with 120 points concentrated in the most upstream region of the combustion chamber ($0 < y < 100$ mm), see Fig. 10.1, to refine the flame region. The typical mesh spacing in the flame region is $\Delta y \approx 0.05$ mm in the radial direction and $\Delta y \approx 0.3$ mm in the axial direction is achieved in the jet and flame region. This corresponds to characteristic cell size of approximately $0.225 \delta_L^0$ laminar flame thickness for the nominal 100H2 case of Tab. 10.1, $0.45 \delta_L^0$ laminar flame thickness for 100H2_{nom} case and $0.15 \delta_L^0$ for case 25H2. In the mixing tube $N_y = 180$ points are used axially to obtain a cell size of 0.25 mm. A wall-normal mesh spacing of $\Delta_{\text{wall}} = 0.03$ mm is used in mixing tube and combustion chamber base plate, achieving a first cell center distance from the wall of $y^+ \approx 5$, in wall units [93], computed after steady state flow is reached within the computational domain. This is defined as $y^+ = y u_\tau / \rho$, where y is the distance from the wall and u_τ is the so-called friction velocity, computed from the shear stress at the wall τ_{wall} as $u_\tau = \sqrt{\tau_{\text{wall}} / \rho}$. In the swirler, a typical cell size of 0.3 mm and wall-normal mesh spacing of 0.1 mm are used, achieving a wall first cell height of $y^+ \approx 8$. The total cell count amounts to 12.7 M points. The Pope criterion [97] is evaluated for case 25H2 of Tab. 10.1 under reacting and non-reacting conditions to ensure a sufficient mesh resolution. This allowed to verify that at least 80% of the total turbulent kinetic energy is resolved everywhere in the domain.

Preliminary LES results obtained with the flamelet/ presumed FDF model for the non-reacting 25H2 case of Tab. 10.1 are compared to the results obtained on a coarser mesh (4.45 M elements, excluding the swirler from the domain) for non-reacting mixing studies described in Chap. 9. The comparison reveals that time averaged and rms quantities are insensitive to mesh refinement, confirming grid-insensitive results. The present analysis is carried out on the finer mesh 12.7 M.

The boundary conditions are specified as follows. At the domain inlets, mass flow rates are specified according to Tab. 10.1. Mixture fraction values of $z = 0$ are imposed at the swirler ports and at the AAI port and $z = 1$ at the fuel ports, both at 300 K. A zero-gradient condition is used for pressure at the inlet. At the outlet, wave-transmissive boundary conditions are applied to prevent spurious reflections of pressure fluctuations and associated velocity field oscillations, prescribing atmospheric pressure at a far field location of $l_\infty = 3$ m downstream of the domain outlet [322–324]. A zero-gradient condition is imposed for every other scalar at the outlet. No slip condition is imposed at the

wall and Spalding wall functions are used for SGS viscosity [269]. Zero-gradient boundary condition is imposed at the walls for every scalar, including pressure. All walls are assumed adiabatic by default; however, to assess flame flashback sensitivity to wall temperature in Sec. 10.6, a limit case with walls at 300 K is also simulated.

The computational cost is of 383 CPU hours per 1 ms of simulation, in a reacting cases and 215.6 CPU hours per ms in non-reacting case. The choice of total simulation times is described in the next section.

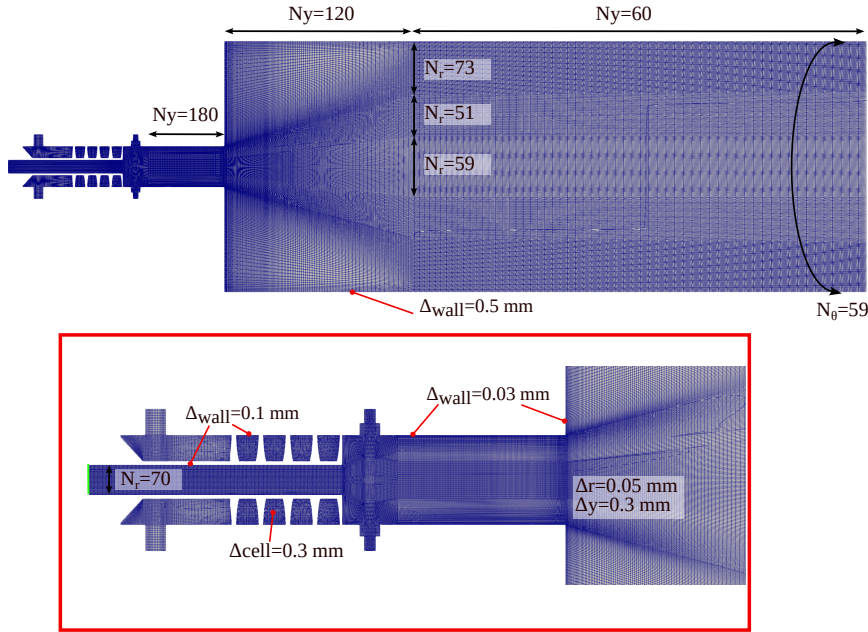


Figure 10.1: Planar section of the computational domain, discretized through a fully block-structured hexahedral grid.

10.4. PRELIMINARY RESIDENCE TIME ESTIMATION

A preliminary analysis is conducted to evaluate the characteristic flow time scales within the swirled combustor and to determine a suitable simulation time for flow development and statistics acquisition. A first estimate of the combustion chamber flow-through time, based on bulk velocity and average density, gives 1.34 s for case 25H2 under non-reacting conditions and when combustion is included, thermal expansion reduces it to 0.22 s. However, the chamber flow presents complexities associated to the recirculation zones. Therefore, a more accurate estimation of the flow-through time and residence times within the various zones of the combustion chamber is obtained by solving the filtered transport equation for the local flow age τ [343]:

$$\bar{\rho} \frac{D\tilde{\tau}}{Dt} = \nabla \cdot [(\bar{\rho}\mathcal{D} + \frac{\mu_t}{Sc_t})\nabla\tilde{\tau}] + \bar{\rho}, \quad (10.1)$$

which takes the form of a convection/diffusion equation with an additional unity source term. In the previous, D/Dt denotes the material derivative, \mathcal{D} is the mass diffusion coefficient, taken equal to the thermal diffusion coefficient α , μ_t is the subgrid viscosity computed according to the turbulence model adopted in the LES and Sc_t is the SGS Schmidt number, taken equal to 0.7.

Figure 10.2 shows instantaneous and average midplane contours of local flow age for case 25H2 in both non-reacting and reacting conditions. For the non-reacting case, the flow age at the combustion chamber exit is about $\tau \approx 1.6$ s, resulting in a longer flow through time than what obtained via simple bulk velocity estimation. The analysis also reveals the broad range of characteristic time scales across the combustion chamber. Residence times are $\tau \approx 150$ ms in the central recirculation zone (CRZ), $\tau \approx 550$ ms in the outer recirculation zone (ORZ), and similarly long downstream of the CRZ at $y \approx 50$ mm. With combustion, the flow-through time decreases by about 80% to 300 ms due to thermal expansion and estimates via bulk velocity are underestimated also for the reacting case. A clear distinction between residence times in the various combustion chamber between regions persists in the reacting case, with roughly $\tau \approx 20$ ms in the CRZ and $\tau \approx 120$ ms in the ORZ.

These results highlight some practical challenges for LES, related to the broad time scales separation and the long residence time in some regions. Given the computational cost of the LES code reported in the previous section, a complete flow through time for the reacting case results in 115 K CPU hours, on the considered 12.7 M elements mesh. To mitigate this high computational cost, a single non-reacting initialization run is performed for about 1.5 s (323.4 K CPU-hrs), ensuring reasonably developed flow at the exit and in the ORZ. Once a stable downstream pressure and non-zero exit velocity are reached, it is assumed that the slow downstream flow has limited influence on the near-jet region of interest (in correspondence of the flame location). Accordingly, a characteristic time for the jet region, taken as the residence time just downstream of the CRZ at $y = 100$ mm, is adopted. For reacting cases, this gives $\tau_{\text{flow}} \approx 50$ ms. Reacting simulations are therefore advanced for about ≈ 240 ms, corresponding to $1.5 \tau_{\text{flow}}$ for ignition washout and $3.3 \tau_{\text{flow}}$ for statistics collection, at a cost of 92.7 k CPU-hours per case.

While this strategy reduces computational cost by neglecting the slow far-downstream flow, the ORZ remains a critical region. Due to its long residence time and proximity to the jet, accurate simulation of its development is essential for correctly capturing vortex breakdown dynamics and flame stabilization in the central region, as further discussed in Sec. 10.5.1.

10.5. 75% CH₄ -25% H₂ CASE

10.5.1. NON-REACTING CASE

The swirl-stabilized combustor is first simulated under non-reacting conditions to provide validation of the flamelet-based LES model on the present configuration. Operating condition 25H2 from Table 10.1 is selected as the baseline case, featuring a fuel mixture with 25% hydrogen and 75% methane by volume and a total air mass flow rate of 5.38 g/s, the case is simulated without any axial air injection. Numerical and experimental analysis within the study presented in Chap. 9 indicated that, within the considered range

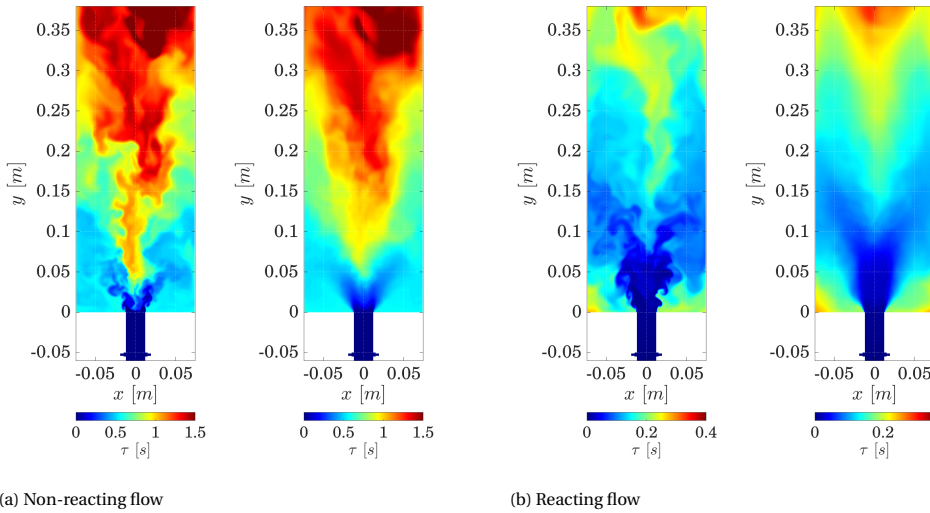


Figure 10.2: Midplane contour plots of instantaneous and average local flow age computed for case 25H2 of Tab. 10.1.

of fuel injection momentum, the flow field in the combustion chamber is primarily governed by the air mass flow rate and the level of axial air injection, rather than fuel mass flow rate and momentum. Therefore, the numerical results can be meaningfully compared with the non-reacting experimental PIV measurements from case A_s in Chapter 9 and in [319], which shares the same air mass flow conditions but considers a surrogate fuel mixture composed by helium and air with slightly different molecular properties.

The comparison between predicted and experimentally measured velocity fields is shown through contour plots and radial profiles of time-averaged axial and transverse velocities in Figs. 10.3-10.4. The LES reproduces with good qualitative agreement the flow features observed experimentally, such as the jet opening angle, the central recirculation zone (CRZ), and the outer recirculation zone (ORZ). However, the PIV results show a slightly wider jet spread and the formation of the CRZ at a more upstream location than what predicted numerically. In the experimental measurements, the leading edge of the CRZ is located in correspondence of the mixing tube exit $y = 0$ mm, while in the LES it is located around $y = 5$ mm. Moreover, the LES predicts a weaker CRZ with minimum backflow velocities of $\langle \bar{u} \rangle = -6$ m/s at a location of $y = 17$ mm, 14% lower than the experimentally measured minimum velocity of -7 m/s at a location of $y = 14$ mm. This discrepancy may be attributed to a lower effective swirl number predicted by the LES, possibly originating from geometric differences between the experimental hardware and the simulated model. On the other hand, the jet opening, and hence the formation and strength of the CRZ, could be influenced by the development of the ORZ and the flow field in the region right downstream the CRZ, e.g. $y \approx 55$ mm. As shown in Fig. 10.2, these regions exhibit significantly higher residence times compared to the jet region and a longer simulation time may be required for the LES to fully capture the flow de-

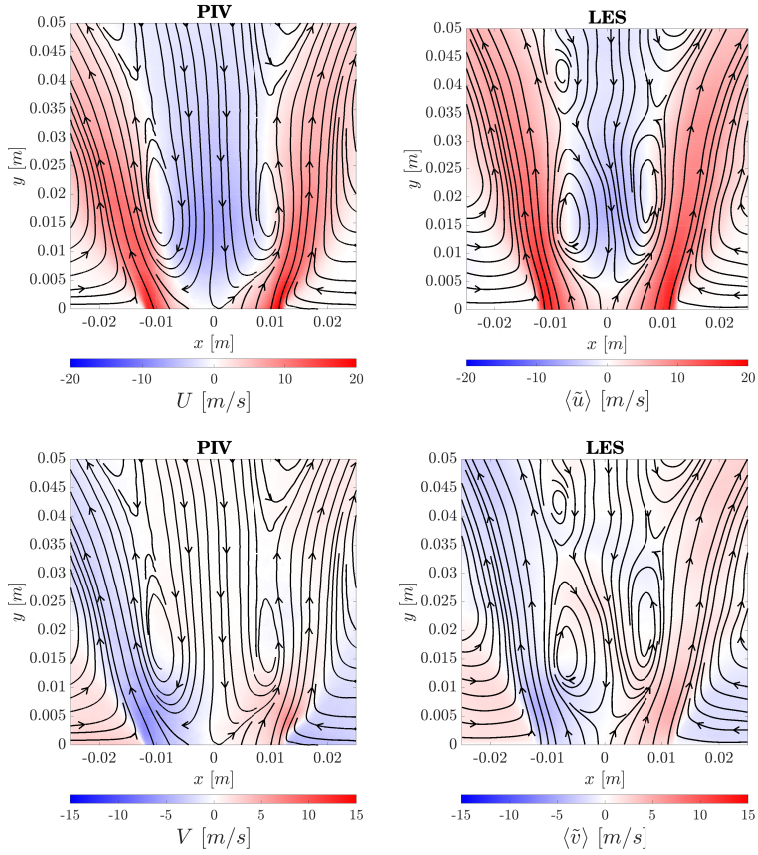


Figure 10.3: Midplane contours (with streamlines in black) of axial (top) and transversal (bottom) average velocity fields obtained from PIV measurements of the surrogate case corresponding to 0% H₂ in Chap. 9 (left) and LES results for the non-reacting 25H₂ case of Tab. 10.1 (right).

velopment there. However, was not possible due to computational limitations and the current level of agreement is considered acceptable for the purpose of this study.

A quantitative comparison of the radial profiles further confirms the good agreement between numerical predictions and experimental data. The axial velocity peak is accurately predicted by the LES at each axial location considered in Fig. 10.4, with an over-estimation error below 15%. The LES underestimation of the backflow velocity is visible up to $y = 10$ mm. The under-prediction of the jet opening can be seen from the radial location of axial and transversal velocity peak, which appears underestimated from the LES. The value of transversal velocity peak is lower in the LES, another hint of an under-prediction of swirl number, or correct development of the vortex breakdown. In the ORZ the transversal velocity appears well predicted.

The predicted variances are also in reasonably good agreement with the experiments, indicating that the turbulent characteristics of the swirling flow are well captured. Near

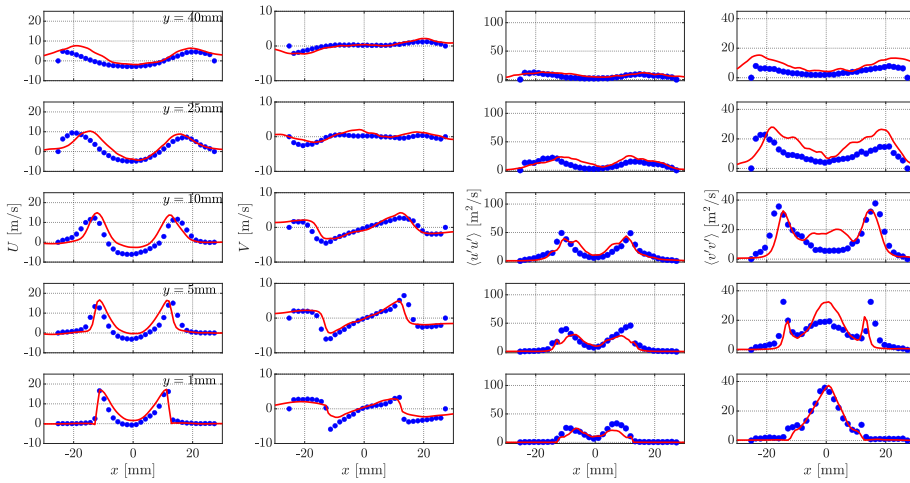


Figure 10.4: Radial profiles of average velocity and velocity variance as predicted by LES (—) of non-reacting case 25H2 of Tab. 10.1 and measured by PIV (•) for the surrogate case corresponding to 0% H₂, in Chap. 9.

the exit of the mixing tube, the axial velocity variance exhibits a double-peak radial profile. These peaks correspond to the inner shear layer, while the outer shear layer (OSL) displays lower velocity variance values. The radial location of the variance peak in the LES is closer to the centerline, if compared to experiments, resulting from the prediction of a narrower CRZ. Peak values are underestimated near the mixing tube exit, but the error diminishes further downstream. The transversal velocity variance features a triple-peak profile near the exit. The two outer peaks correspond to the outer shear layer, while the central peak is associated to lateral fluctuations of the CRZ leading point. This can be associated with the interaction between the CRZ and the precessing vortex core (PVC), as discussed in Sec. 10.5.3. Similarly to what observed in chap. 9 the presence of this central peak persists in the LES up to $y = 10$ mm while the experiments show a decreasing peak variance value at $y = 5$ mm, compared to the mixing tube exit $y = 1$ mm and the absence of the central peak from $y = 10$ mm downstream.

The comparison of LES results for the non-reacting case against available experimental data, showed overall good agreement, thereby providing confidence that the LES model, with tabulated thermochemical mixture properties, correctly captures the flow fields and turbulent features within the combustor. In particular, the processes of fuel/air mixing, turbulence generation in the injector, and vortex breakdown within the combustion chamber appear to be well represented. The observed discrepancies are minor; however, further investigation is necessary, especially regarding simulation time for ORZ development and a thorough verification of the geometrical consistency of the manufactured hardware. Building on this foundation, the next section examines the reacting case, leveraging the confidence gained in the model's ability to reproduce the turbulent flow field accurately.

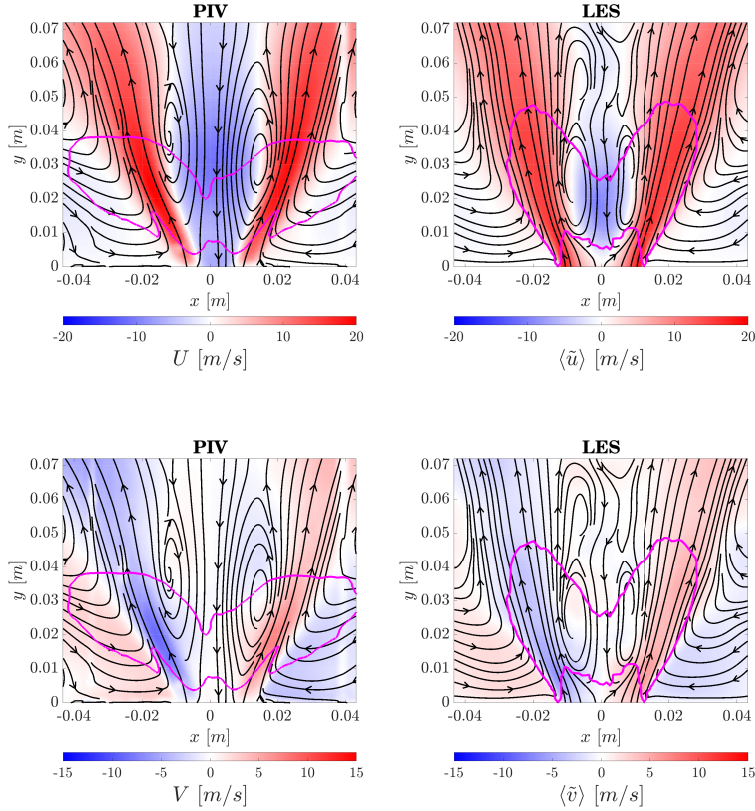


Figure 10.5: Midplane contours (with streamlines in black) of axial (top) and transversal (bottom) average velocity fields obtained from PIV measurements and LES of case 25H2 of Tab 10.1 under reacting conditions. The magenta isolines (—) represents 10% of the maximum OF-PLIF signal in the experiments (left) and the 2% of the maximum time-averaged reaction rate ($\overline{\omega}_c$) from LES (right).

10.5.2. REACTING CASE: FLOW FIELD AND FLAME TOPOLOGY

The test case 25H2 from Tab. 10.1 is simulated under reacting conditions. The predicted flow field and flame topology are analyzed and compared against available PIV data and OH-PLIF measurements provided by Link and coworkers, [319]. The velocity field obtained from PIV measurements and predicted by LES is shown in Fig. 10.5. Compared to the non-reacting flow fields reported in Fig. 10.3, the presence of the flame leads to flow acceleration due to thermal expansion in both the streamwise and radial directions. This, in turn, strengthens the recirculation zones, with the measured peak backflow velocity in the central recirculation zone increasing from -7 m/s in the non-reacting case to about -10.6 m/s in the reacting case. The CRZ in the reacting case appears longer in the streamwise direction, and the point of minimum velocity is observed to move downstream of 16 mm with respect to the non reacting case (now located at $y = 30$ mm),

while the CRZ leading point shifts upstream towards the mixing tube, and it is not visible within the PIV measurement window. Moreover, an increase in the transverse velocity peak is observed, but an overall reduction of the jet opening angle, due to the increased axial velocities in the reacting case, as compared to the non-reacting case. The LES captures these physical effects reasonably well, correctly predicting the increased axial and transverse velocities, together with a stronger CRZ. A reduced jet opening angle is predicted, aligning well with experimental measurements. This can be traced by means of the angle of outer shear layer, region of maximum velocity radial gradients. This can be roughly visualized with the region of transition from zero to positive axial velocity and from inwards to outwards radial velocity (white region in Fig. 10.5, bottom panels), and corresponds to the location where the average streamlines bend from transversal to axial direction. The computed streamlines also show very good qualitative agreement, with the ones derived from experimental data.

Some differences are notable in the inner shear layer, (identifiable as the axial velocity inversion region, inner white region in Fig. 10.5, top row) and the CRZ development. The LES predicts a narrower, and shorter central recirculation zone. The predicted point of minimum back flow velocity (-9.5 m/s) is located at $y = 17$ mm, unaltered with respect to the non reacting case, and 13 mm more upstream than experimentally measured. The leading point of the CRZ is predicted at about $y = 2$ mm, while it results outside of the PIV measurement window in the experiment. Downstream of the CRZ, $y \approx 50$ mm, PIV shows a significant backflow region on the centerline $U \approx -6.5$ m/s, which in LES appears narrower in the radial direction and exhibits weaker backflow $\langle \tilde{u} \rangle \approx -1$ m/s. As previously discussed for the non-reacting case, the correct prediction of the CRZ may be affected by the full development of the flow in the outer recirculation zone (ORZ), characterized by high residence time (see Fig. 10.2). This may require to run the LES for longer time, which was not possible due to computational limitations.

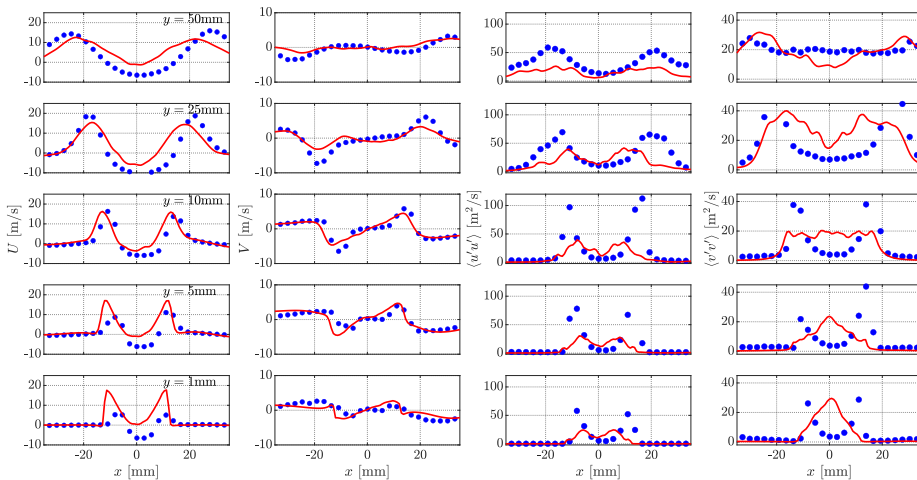


Figure 10.6: Radial profiles of average velocity and velocity variance from PIV measurements (●) and LES results (—) for case 25H2 of Tab. 10.1 under reacting conditions.

A quantitative comparison of measured and computed radial profiles of mean velocity is provided in Fig. 10.6. Excellent agreement between LES and PIV is observed in the prediction of axial velocity peaks at $y = 10$ mm and transverse velocity peaks at $y = 5$ mm and $y = 10$ mm, with errors below 10%. The position of the outer shear layer, identified by the points of maximum radial gradient of axial and transverse velocity, is predicted fairly well at all the considered axial locations. Similarly, the position of the inner shear layer (ISL) is correctly captured up to $y = 10$ mm. At more downstream locations $y \geq 25$ mm the relative radial distance between the average velocity peaks predicted by the LES is underestimated in comparison to PIV measurements, due to the narrower predicted CRZ, as previously observed in Fig. 10.5. The LES overestimates the axial jet velocity by up to 45% in the region at the mixing tube exit ($0 < y < 5$ mm) and underestimates it by up to 22% in more downstream regions ($y > 25$ mm). These discrepancies can be attributed to differences between the flame anchoring location observed experimentally and that predicted by the LES, as discussed next. The centerline backflow velocity is underestimated by the LES at each considered axial location. According to PIV measurements, the CRZ induces backflow velocities of about $U \approx -6.7$ m/s up to the very exit of the mixing tube, whereas LES predicts zero axial velocity at the $y = 0$ mm and significant backflow starting only from $y = 10$ mm.

Radial profiles of velocity variances are investigated next. PIV data shows that the presence of the flame results in increased velocity variances in axial and transversal direction in correspondence of the regions of inner and outer shear layers, when compared to the results for the non-reacting case shown in Fig. 10.4. This effect is less pronounced in the LES results, where the value of the peak velocity variance is approximately half of what experimentally measured. The radial profile of transversal velocity variance predicted by LES displays a single central peak up to locations $y = 5$ mm, similarly to what observed numerically and experimentally for the non-reacting case, see Fig. 10.4. Conversely, PIV measurements show that this central single-peak profile disappears under reacting conditions and a double peak profile is observed at each streamwise location within the combustion chamber. As mentioned in the previous section, the central peak in transversal velocity variance is linked to the location of the CRZ leading point. Experimentally, this point shifts significantly upstream under reacting conditions, exiting the combustion chamber ($y < 0$ mm). Consequently, the central peak is absent in PIV data. In the LES, however, the CRZ leading point remains near the mixing tube exit ($y = 2$ mm), which explains why the central peak persists in the predicted profiles.

The flame shape and position is analysed comparing numerical results with experiments. Experimentally, the flame is visualized by means of OH-PLIF intensity data available from the experimental campaigns in [68]. The OH-PLIF intensity normalized by its maximum value $I_{\text{OH}}/\max(I_{\text{OH}})$ is shown in Fig. 10.7 and an isoline marking 10% of the maximum intensity value is superimposed to the PIV measured velocity fields in Fig. 10.5. For LES, the reacting region is identified by an isoline of progress variable reaction rate at 2% of its maximum value. As seen in Fig. 10.5, the flame brush displays an M-shape in both LES and experiments, with an outer branch stabilized along the outer shear layer and an inner branch stabilized within the CRZ. The predicted reacting region in LES is qualitatively similar to the experiment. However, from LES results the flame appears slightly longer than the one observed experimentally, reaching $y = 48$ mm com-

pared to $y = 38$ mm in experiments, and appears narrower. While the flame predicted by the LES follows the jet opening, remaining within the region delimited by the OSL, the flame observed experimentally appears wider in the radial direction, exceeding the outer shear layer and reaching radial positions of $x = \pm 40$ mm.

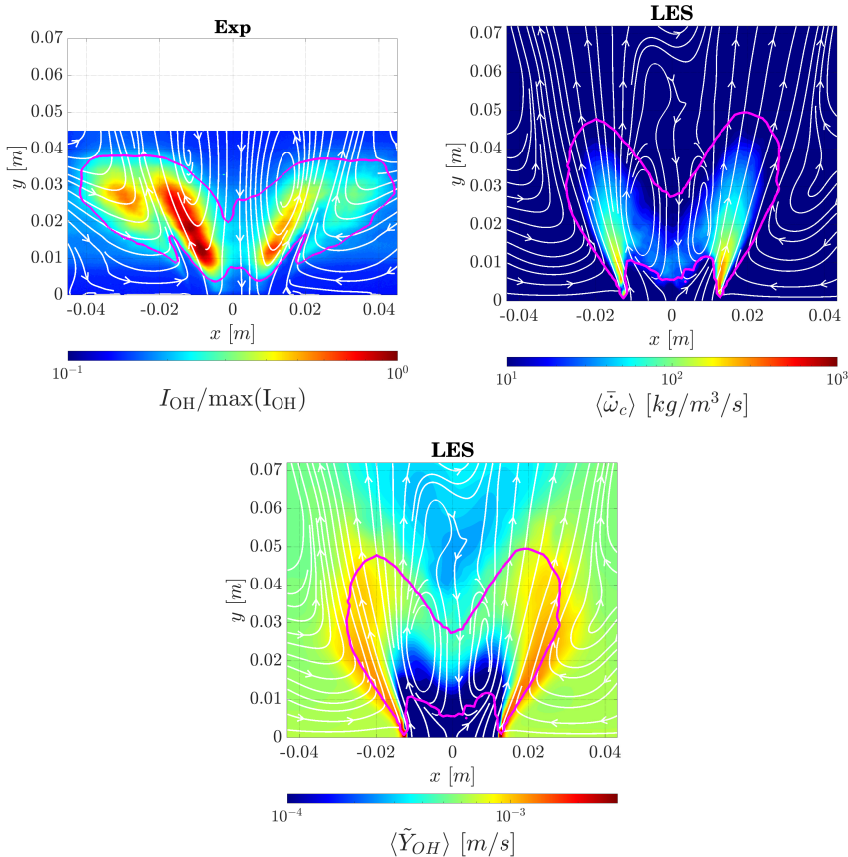


Figure 10.7: Midplane contour plots (with streamlines in white) for reacting case 25H2 of Tab. 10.1: normalized OH-PLIF signal intensity from experimental campaigns (top left), mean progress variable reaction rate (top right) and mean OH mass fraction (bottom) from LES computations. The legend for the magenta solid line (—) is defined as in Fig. 10.5.

Despite the similarity in flame shape, notable differences in flame structure exist between the LES predictions and experimental observations. In Fig. 10.7, the highest OH-PLIF signal intensity in the experiments is localized in the central recirculation zone (CRZ), aligning with the inner shear layer. The OH-PLIF signal is significantly weaker along the outer flame branch (along the outer shear layer), suggesting that the flame is quenched at the rim of the mixing tube ($y = 0$ mm, $x = \pm 12$ mm), resulting in a lifted flame with lift-off height of approximately $y = 10$ mm. In contrast, contour plots of progress variable reaction rate and OH mass fraction from LES calculations (both shown

in logarithmic color scale to highlight the inner flame branch) indicate maximum reactivity in the outer shear layer and significantly lower reactivity in the CRZ. In this case the flame is attached to the mixing tube rim, resulting in intense OH production in this region.

The discrepancy between the attached flame predicted by LES and the experimentally observed lifted flame can be explained by mechanisms reported in the literature for similar swirled configurations [44, 87, 170, 328, 339, 344], which highlights that the high strain rate at the injector rim and heat losses at the combustor walls significantly affect the flame structure and stabilization. Benard et al. [87] highlighted how for a 100% methane fuel case the strain level at the injector rim controlled the amount of cooled products recirculated towards the flame zone, determining extinction. On the other hand, lean fuel-air mixtures with high hydrogen content can exhibit negative Markstein length, which determines an increase of the consumption speed under strain and favors an attached flame [170, 344]. This is consistent with the experimental observations shown in [68] for the present set up, where increasing hydrogen content in the fuel blend lead to a decrease in the lift off height of the outer flame branch and an attached flame under 100% hydrogen fuel conditions. As shown in Chap. 8, effects of strain on negative Markstein length mixtures can be partly captured at the resolved level, by means of the differential diffusion models implemented in the baseline LES code (chapter 7). Furthermore, the long residence time in the outer recirculation zone favors heat loss from the combustion products to the quartz chamber walls (at a temperature of about 600 K) and base plate (which reaches temperatures between 450 K and 500 K during experimental measurements). As these gases get recirculated towards the flame base they can quench the outer flame branch causing it to lift [344]. The absence of an accurate model for heat loss in the in-house LES model and the uncertainties on the experimental thermal boundary conditions, hinders the correct prediction of the flame shape and stabilization. The role of heat losses in this configuration, detailed in [339], may explain the observed quenching of the outer flame branch in the experiment. An analysis on the effects of heat losses is later presented in Sec. 10.6 for the 100% hydrogen fuel case.

In the experimental data, the inner branch forms a steeper angle, with the turbulent flame brush following the inner shear layer, Fig. 10.7. The acquisition window for OH-PLIF images extends only up to $y = 5$ mm, but based on the OH intensity and CRZ structure shown in Fig. 10.5, the inner branch is likely to extend into the mixing tube, following the inner shear layer. Whether combustion occurs along the centerline inside the tube remains uncertain and depends on local fuel-air mixing, as discussed in the following paragraphs, and hot gas recirculation. In the LES the inner flame brush aligns with the inner shear layer and follows the zero axial velocity region around the CRZ leading point (see Fig. 10.5). From LES results the CRZ leading point and consequently the inner flame branch appear entirely located downstream of the mixing tube, in contrast with experimental observations. The inner branch appears thickened due to the intense turbulent fluctuations in the CRZ leading point (as further discussed later in Sec. 10.5.4), linked to the peaks in transverse velocity variance observed in Fig. 10.6 and the precessing vortex core (PVC) interaction with CRZ, to be further discussed in Sec. 10.5.3. The mismatch between LES and experimental results may stem from an underprediction of recirculation strength and the CRZ position, consistent with observations from the non-

reacting case. However, the flame structure and flow field, including CRZ position and backflow intensity, are strongly interdependent. Therefore, the overall misprediction of the flame on the outer branch may affect the predicted positioning of the CRZ, and consequently the stabilization of the inner flame branch.

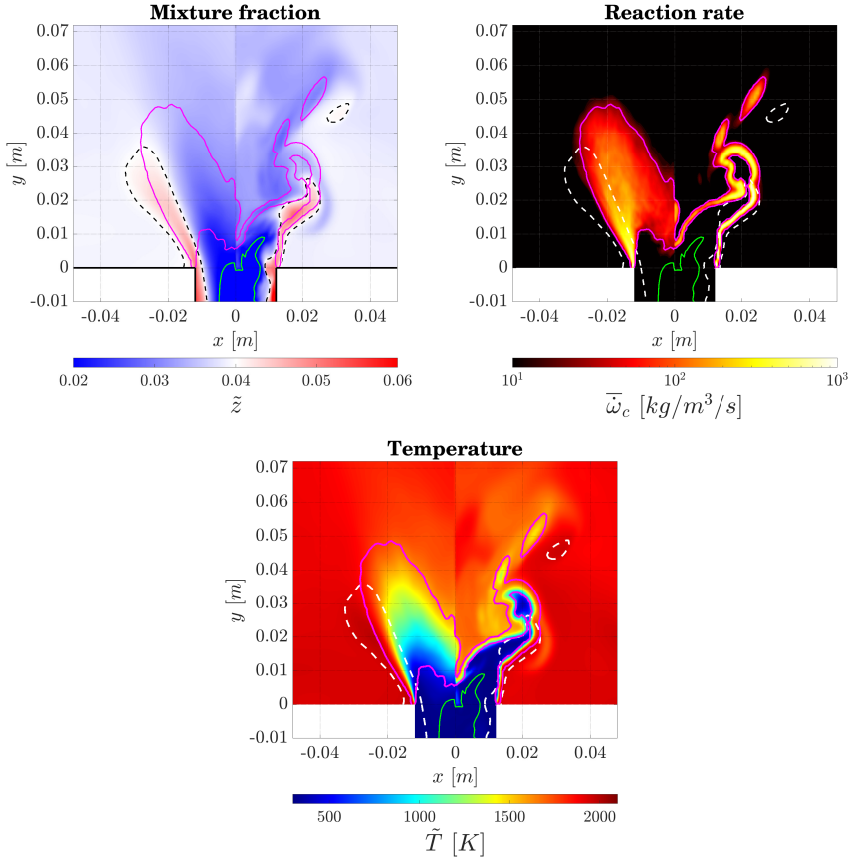


Figure 10.8: Midplane contour plots from LES results of 25H2 of Tab. 10.1 under reacting conditions: mixture fraction (top left), mean progress variable reaction rate (top right), Temperature (bottom). Time averaged (left halves) and instantaneous (right halves) quantities. Isolines of mixture fraction at nominal value $z_{\text{nom}} = 0.04$ (), lean flammability limit $z_{\text{lean}} = 0.017$ (—), and progress variable reaction rate isoline at 2% of its maximum value (—).

Further insights into the stabilization mechanism can be derived from the instantaneous and time-averaged contour plots of mixture fraction, temperature, and progress variable reaction rate as predicted by LES and reported in Fig. 10.8. In these plots, the dashed contour line marks the nominal mixture fraction value of $z_{\text{nom}} = 0.04$ ($\phi_{\text{nom}} = 0.65$), therefore enclosing regions of mixture richer than the nominal condition. A solid magenta line indicates the flame region, similarly to the previous figures.

The mixture fraction plot confirms strong radial fuel stratification, with mixture richer

than nominal (red color) accumulating near the mixing tube walls, as anticipated in Chap. 9. The flame thus stabilizes in a non-uniform equivalence ratio field, which affects its structure. In particular, the outer branch burns under conditions consistently richer than the nominal mixture fraction, explaining the high reaction rates observed at the mixing tube rim and the LES prediction of an attached M-flame, in contrast with the experimental observations. The instantaneous reaction rate snapshot at a given time-step (right-top panel, left) shows that the outer flame branch remains entirely within the richer region, marked by the dashed isoline, up to a location of $y = 25$ mm. Similarly, the instantaneous and average thermal field show temperature peaks around 2000 K at these locations, which exceed the adiabatic flame temperature corresponding to the nominal equivalence ratio (1927 K). These hot products at richer mixture fraction then mix with colder products ($\tilde{T} = 1927$ K) in the post flame region, i.e. the region enclosed by the dashed line, located outside of the magenta iso-line. The outer branch can be viewed as stabilizing in counterflow configuration against recirculated products at the nominal adiabatic flame temperature and mixture fraction.

The inner flame branch exhibits significantly leaner composition than the outer flame branch attaching to the injector rim. Fig. 10.8 (top-left) shows that, at the mixing tube core, the mixture fraction at the combustion chamber inlet is below the lean flammability limit $z_{\text{lean}} = 0.017$, indicated by the green solid line. In this region combustion occurs just above the flammability limit, as the flame receives richer fresh reactants from the inner shear layer between the CRZ and the opening jet [318]. At about $y = 5$ mm, the mixture becomes reactive enough to sustain combustion in the low velocity regions at an effective mixture fraction of $\tilde{z} \approx 0.03$. Also on the inner branch the flame stabilizes in counterflow configuration, supported by hot reacted products at mixture fraction close to nominal values recirculated by the CRZ. In this region the temperature ($\tilde{T} \approx 1500$ K) is lower than the nominal adiabatic flame temperature, and lower average temperature gradients than in the outer branch are observed. For the same reason, the inner branch displays an order of magnitude weaker reaction rate than the outer branch.

10.5.3. PRECESSING VORTEX CORE (PVC) DYNAMICS

The analysis of the time evolution of velocity and pressure fields reveals the presence of a precessing vortex core (PVC), i.e. a helical vortical structure in precession motion with respect to the combustor central axis, described in various studies in literature [85, 88, 178, 345–347]. This is visualized in Fig. 10.9 by means of a pressure isosurface of $\bar{p} = 101200$ Pa, colored by the local mixture fraction value \tilde{z} . The blue color indicates a mixture fraction below 0.02, meaning that the vortex core contains almost pure air. The helicoidal structure develops axially starting from the swirler exit at $y = -60$ mm and it follows the jet opening in the combustion chamber. It is thus observed to wrap around and interact with the central recirculation zone (CRZ) and the flame front within the combustion chamber, which in Fig. 10.9 is identified by an iso-surface and a red iso-line of progress variable $\tilde{c} = 0.5$.

The precessing motion of the vortex core is tracked by means of time series of the pressure field on a cross-section close to the mixing tube exit ($y = -1$ mm), and identifying the location of the point of minimum pressure at each time step. The sine of the azimuthal coordinate of the pressure minimum θ_{PVC} is plotted as time series in Fig. 10.10,

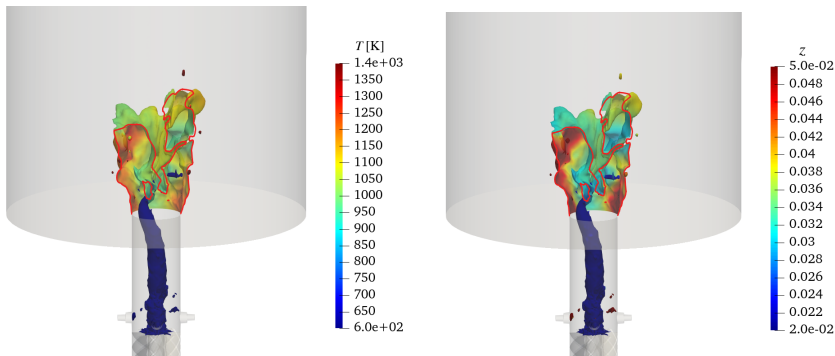


Figure 10.9: Three-dimensional representation of the PVC structure by means of instantaneous pressure iso-surface at $\bar{p} = 101200$ Pa colored by the instantaneous mixture fraction value \bar{z} (blue central structure). The flame surface is visualized by means of iso-surface and iso-line (→) at progress variable $\bar{c} = 0.5$. Flame surface coloured by: temperature values (left) and mixture fraction values (right).

blue line. The location of the minimum pressure point on the $z-y$ cross plane precesses around the mixing tube axis with a period of about $T_{PVC} \approx 4.3$ ms. The θ_{PVC} signal is acquired at a sampling frequency of $f_s = 20$ kHz over a time window of 75 ms, corresponding to approximately 17 times the PVC precession period T_{PVC} . The fast fourier transform (FFT) analysis of the $\sin(\theta_{PVC})$ signal, reveals a clear dominant mode at a frequency of $f_{PVC} \approx 233$ Hz, corresponding to a Strouhal number of $St = f_{PVC} D_{MT} / U_{bulk} = 0.5$, where D_{MT} is the mixing tube diameter and U_{bulk} is the bulk velocity in the mixing tube. This value is reasonably close to the one computed in [290] and measured experimentally in [348] for the non reacting case at the same air mass flow rate.

The pressure field on the cross section at $y = -1$ mm is phase averaged at a frequency of 233 Hz and reported in Fig. 10.11. The precession motion of the point of minimum pressure around the mixing tube geometrical axis at a radial coordinate of about 5 mm is clearly visible at the considered frequency as its azimuthal location shifts by 90° at the different cycle phases. This point of pressure minimum is associated with a point of zero in-plane velocity (center of the swirling motion, identified by means of the phase-averaged streamlines) located at a slightly inward radial location 3 mm. As the vortex core precesses, it induces an azimuthal acceleration in the flow region between the closest wall portion and the center of rotation, as seen from a reduced spacing between average streamlines, and a deceleration on the diametrically opposite sector.

As already noted in [339], the PVC is observed to induce periodic oscillation in the mixture fraction field. The point of minimum mixture fraction is tracked and its azimuthal position is represented in time in Fig. 10.10, red line. A clear periodic oscillation exactly in phase with the location of minimum pressure is observed. In facts, due to the jet in cross flow fuel injection, the mixing tube core presents the lowest mixture fraction and it is mostly composed by air. With its precessing motion, this air core creates asymmetry in the mixture composition entering the combustion chamber, resulting in oscillations in flame positioning, shape and temperature distribution. This is visible from Fig. 10.9, where the flame front is visualized by a reaction rate isosurface colored by mixture fraction (left) and temperature (right). The flame surface closest to the PVC

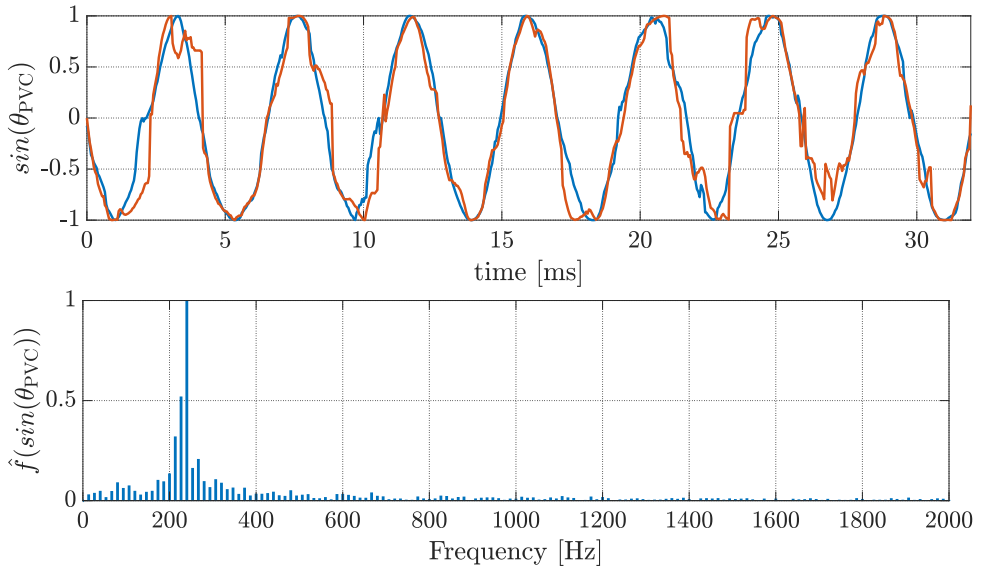


Figure 10.10: Top panel: time series of the azimuthal location of the point of minimum gauge pressure (—) and mixture fraction (—) at a location of $y = -1$ mm. Bottom panel: single sided normalized amplitude spectrum of the sine of the azimuthal coordinate of the point of minimum pressure as a signal in time, obtained by fast Fourier transform (FFT).

shows a decreased mixture fraction value (towards blue color) and reduced temperature compared to the rest of the flame. In Fig. 10.11 this is clearly visualized by phase averaged mixture fraction field at the mixing tube exit ($y = -1$ mm). A clear region of low mixture fraction (with a value close to zero, indicating pure air) is observed to precess at the same frequency of the pressure minimum and it trails in the azimuthal direction behind the center of rotation visualized by the streamlines. A region of mixture fraction richer than the nominal value z_{nom} is induced in the diametrically opposite sector.

Phase-averaged fields are also reported on the axial x - y -plane in Fig. 10.12. From contour plots of gauge pressure, the helical path of the PVC is visible starting from $y \approx -20$ mm and developing in the combustion chamber, where it completes roughly one visible turn. On the mid-plane section the helicoid structure appears as two low pressure spots alternating on the left and right side of the central axis. A clear precession motion is visible from the coherence of the phase averaged plots at the considered frequency. The phase averaged streamlines visualize the vortical motion induced around the helical PVC axis, as described thoroughly in [345]. In the central panel, the interaction of the PVC with the CRZ is visualized. As seen in Fig. 10.9, the helical vortex core path wraps around the CRZ in the combustion chamber as the jet opens. The shape of the CRZ is deformed by the local velocity field induced by the PVC. The leading point of the CRZ is observed to precess in phase with the PVC which appears as an oscillating lateral motion on the axial plane. This induces a periodic precession motion in the flame inner branch, which is bounded to stabilize on the inner shear layer.

As a result of the oscillating mixture fraction field, the temperature field presents a

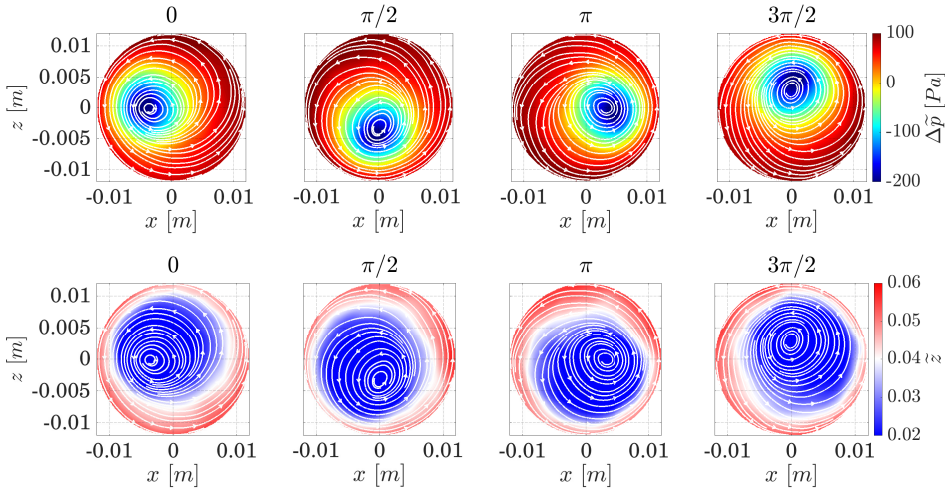


Figure 10.11: Cross-plane contours of phase-averaged (with respect to the PVC frequency of $f_{\text{PVC}} = 233$ Hz) fields of gauge pressure $\Delta \bar{p} = \bar{p} - p_{\text{atm}}$ (top panel) and mixture fraction \bar{z} (bottom panel) over a mixing tube cross section located at $y = -1$ mm. Phase averaged streamlines are reported in white.

periodic behaviour, with high temperature regions following the helical path of the high mixture fraction sections at the mixing tube exit shedding downstream in the combustion chamber. This is observable in the bottom panel of Fig. 10.12, showing alternating high temperature spots at 2000 K, higher than the nominal 1700, trailing downstream in phase with the PVC motion. The vortical velocity field induced by the helicoidal structure induces a roll up of the flame around the vortex core, similarly to what described in [88, 347].

This analysis highlights the origin of intrinsic periodic dynamics where the velocity field couples with mixing and temperature field. The use of axial air injection, which will be explored in sec. 10.7.1, was observed to fully suppress the PVC dynamics, resulting in a symmetric flame.

10.5.4. REACTING STATES AND EMISSIONS

At the considered set point (25H2 of Tab. 10.1), the TU Delft swirled combustor does not operate under uniform conditions. Instead the reacting mixture spans a broad range of combustion regimes determined by the local mixing and turbulence levels in the different zones of the combustor. Therefore, an analysis of the reacting states is carried out to quantitatively characterize the combustion process together with the formation of nitric oxide NO. The thermochemical states within the mean flame brush ($0.1 < \langle \bar{c} \rangle < 0.9$) are retrieved from time-averaged LES results and plotted on the Borghi-Peters diagram [138] in Fig. 10.13. The characteristic turbulent velocity is estimated as $u' = \sqrt{2/3} k$, where the local turbulent kinetic energy k is obtained from the resolved velocity fluctuations and the subgrid-scale turbulent kinetic energy k_{SGS} computed accordingly to the SGS turbulent model: $k = 0.5 \sum_{i=1}^3 \langle (\bar{u}_i - \langle \bar{u}_i \rangle)^2 \rangle + k_{\text{SGS}}$. A reference characteristic turbulent length

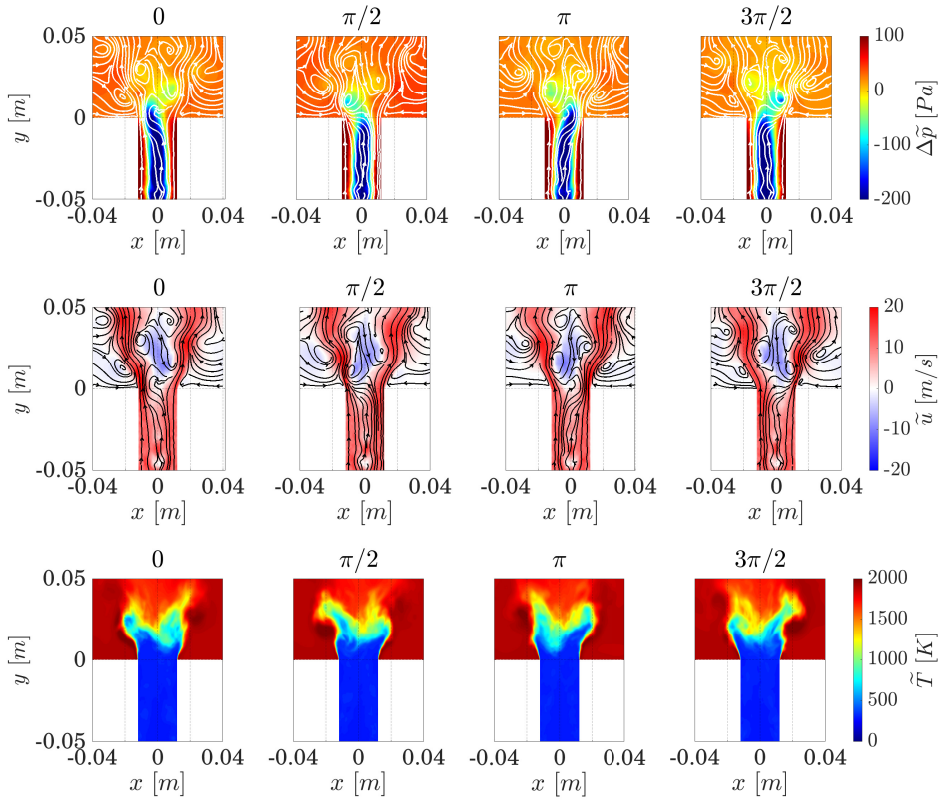


Figure 10.12: Midplane contours of phase-averaged (with respect to the PVC frequency of $f_{\text{PVC}} = 233$ Hz) fields of gauge pressure $\Delta\bar{p} = \bar{p} - p_{\text{atm}}$ (top row), axial velocity \bar{u} (center row) and temperature \bar{T} (bottom row). Phase averaged streamlines are reported in white.

scale is set to the mixing tube radius ($l_t = 12$ mm), after visual inspection of instantaneous values of fluctuating velocity components in the flame region. The local laminar flame speed and thickness are estimated from the one-dimensional unstretched premixed flamelet calculations at the local equivalence ratio and reactants temperature of 300K. The scatter plot is colored by mixture fraction: grey points represent the nominal mixture fraction value, while blue and red indicate leaner and richer compositions, respectively.

A clear correlation is observed between the mixture fraction and the Karlovitz number. The lean reacting mixture (shown in blue in Fig. 10.13), associated with the inner flame brush in the central recirculation zone and the inner shear layer (see Fig. 10.8), reaches the highest Karlovitz numbers ($Ka \approx 12000$). This is due to the combination of long chemical timescales, linked to the low equivalence ratio, and elevated turbulence in the inner shear layer, with additional velocity fluctuations induced by the PVC. These points in the CRZ also exhibit the highest turbulent Reynolds numbers ($Re_t \approx 700$). Con-

versely, richer reacting mixture (shown in red in Fig. 10.13), corresponding to the reacting region in the outer shear layer, displays the lowest Karlovitz numbers ($Ka \approx 2$). At these richest conditions ($z \approx 0.05$), the flame reaches its minimum thickness, so that $l_t \approx 27.5\delta_L^0$ (vertical dashed line). These trends are consistent with the average flame brush structures observed earlier from the average contour plots in Fig. 10.8: the inner flame branch is broad and highly wrinkled due to strong velocity fluctuations in the CRZ, while the outer flame branch attaching to the injector rim is thinner, due to both shorter chemical time scales and lower turbulence intensity.

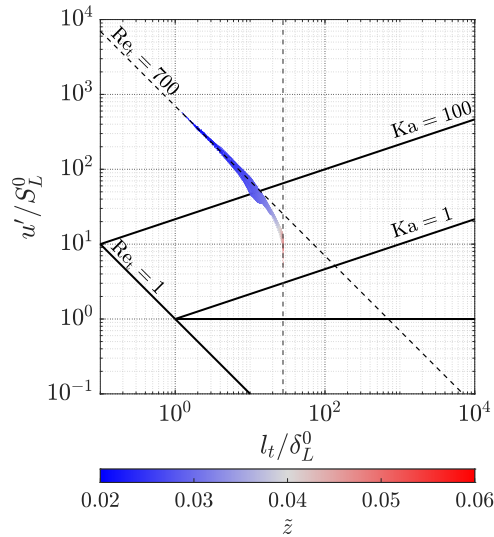


Figure 10.13: Reacting states computed from time-averaged LES results and reported on the the Borghi-Peters diagram [138]. Data points are collected within the mean turbulent flame brush, identified by the progress variable interval $0.1 < \langle \tilde{c} \rangle < 0.9$, and colored by the mean mixture fraction value (\bar{z}). Black dashed lines (---): iso-line of turbulent Reynolds number $Re_t = 700$ (oblique) and $l_t = 27.5 \delta_L^0$ limit (vertical).

The mixture inhomogeneity and its effect on the reacting states are further characterized by means of the joint probability density function (JPDF) of temperature and mixture fraction across the flame front ($0 < \tilde{c} < 1$) at a random time step, reported in Fig. 10.14. Conditional mean values of temperature over mixture fraction are also plotted for different intervals of progress variable in black. The significant stratification of reactant mixture fed into the flame is evident at low progress variable, where the mixture fraction spans a wide range of values around the nominal condition, from $\bar{z} = 0.011$ up to $\bar{z} = 0.062$, exceeding the stoichiometric value. As the reaction progresses, the mixture fraction distribution narrows towards the nominal value, with fully reacted states concentrated in the range $\bar{z} \in [0.03 - 0.05]$, see the highest JPDF values (shown in red in Fig. 10.14) for $\tilde{c} \rightarrow 1$, leading to a range of temperature values in the products $\tilde{T} \in [1450, 2150]K$. This is due to the fact that the stratified mixture at different equivalence ratios and reaction progress levels continues to mix while burning along the inner and outer shear layers.

Most reacting states are observed to burn leaner than the nominal mixture fraction

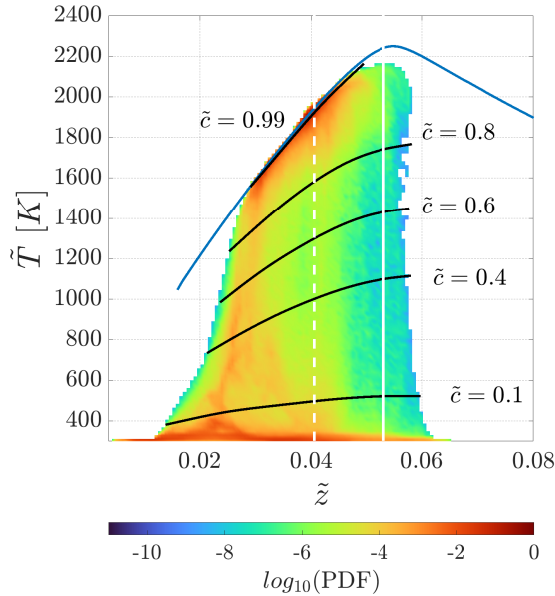


Figure 10.14: Joint probability density function (JPDF) of temperature \tilde{T} and mixture fraction \tilde{z} at a representative time instant. Adiabatic flame temperature versus mixture fraction computed from unstretched laminar premixed 1D flamelets is reported as a blue line (—). The dashed and solid vertical white lines indicate the nominal mixture fraction value $z_{\text{nom}} = 0.04$ and the stoichiometric condition $z_{\text{st}} = 0.053$, respectively. Conditional means of temperature versus mixture fraction at different progress variable values $\langle \tilde{T} | \tilde{z} \rangle_{\tilde{c}=c^*}$ are also reported as black solid lines.

value, as indicated by the highest JPDF values (on the left of the dashed line, Fig. 10.14), and they correspond to the points in the inner flame branch. Here, ultra-lean fresh gases from the mixing tube core mix with partially reacted products from richer regions via the inner shear layer or recirculated within the CRZ (see Fig. 10.8). Consequently, both mixture fraction and progress variable increase across the flame in this region, with final temperatures remaining below the nominal adiabatic value of 1927 K. Conversely, the outer flame branch, associated with mixture fractions richer than nominal, shows fewer occurrences, i.e. lower JPDF values. In this region, the mixture enters the flame under significantly richer conditions than the nominal equivalence ratio (up to $\tilde{z} = 0.06$, $\tilde{\phi} = 1.14$). As combustion proceeds, the mixture fraction decreases due to recirculation of products at lower mixture fraction from the ORZ towards the flame, and continuous mixing with the leaner jet core, see Fig. 10.8 top-left. These richer samples yield localized temperature peaks at the flame base near the mixing tube rim, exceeding the nominal adiabatic flame temperature by up to 250 K, consistently with observations in Fig. 10.8. Similar distributions of reacting states have been reported for other technically premixed combustors in the literature [44, 338]. However, in those cases, the stratification pattern is reversed, with the lean branch located on the outer side due to coaxial fuel injection near the mixing tube axis.

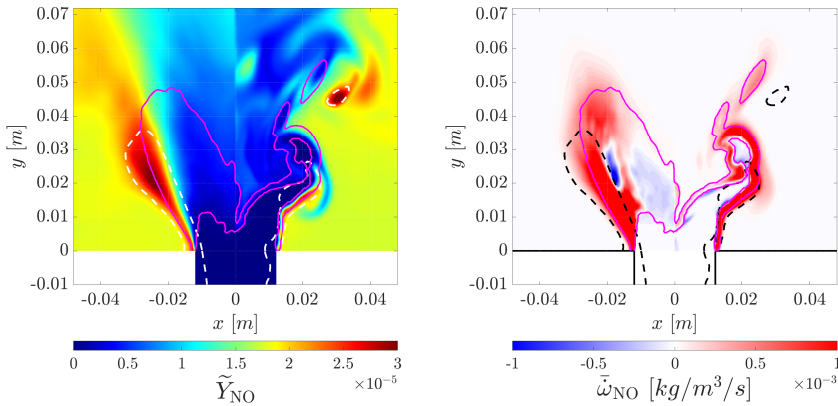


Figure 10.15: Average (left halves) and instantaneous (right halves) midplane contour plots of nitric oxide mass fraction Y_{NO} (left panel) and source term $\bar{\omega}_{NO}$ (right panel), as computed with LES of case 25H2 of Tab. 10.1. Line legend is as for Fig. 10.8.

The described inhomogeneities in mixture composition and the presence of localized temperature peaks significantly influence the formation of nitric oxide NO. Fig. 10.15 presents both time-averaged and instantaneous contours of nitric oxide mass fraction Y_{NO} and formation/consumption rate $\bar{\omega}_{NO}$. The highest formation rates are found along the outer flame branch (see right panel), where the mixture fraction is the richest and peak temperatures above 1800 K enable NO formation through the thermal (Zeldovich) pathway [43, 44, 328]. In this region, the non-zero source term extends beyond the outer magenta line, highlighting the continued NO formation within the products in the post-flame region. Because of its long chemical timescales, NO is convected downstream as it forms along the outer flame branch and a maximum Y_{NO} between $y \approx 15\text{--}30$ mm and $x = -25$ mm in the time-averaged fields. This region is encompassed by the dashed line, signifying products richer than the nominal mixture fraction value. Outside the dashed line, these rich products with high NO content mix with gases at the nominal mixture fraction, causing NO concentration to decrease. In contrast, the inner flame branch shows negligible NO formation, about an order of magnitude lower than in the outer branch. This is due to the leaner mixture composition and lower temperature which falls below 1800 K (see Figs 10.8-10.14), hindering the thermal NO formation.

It is important to note that, although a transport equation is solved for NO, its reaction rate is still retrieved from flamelet tabulation. The flamelet database is generated from 1D premixed flamelets where NO is absent from the reactants. The sink term in the database, arises from the presence of NO in upstream flame region, as seen in Fig. 3.2, which starts to form on the flame front and diffuses towards the reactants [135, 191]. In reality, NO formed under varying composition conditions and recirculated into the CRZ can significantly influence the real local formation or consumption, a process that would require detailed chemistry mechanisms to be fully captured [328, 349]. Nevertheless, LES based on flamelet tabulation provides a reasonable representation of the underlying physics.

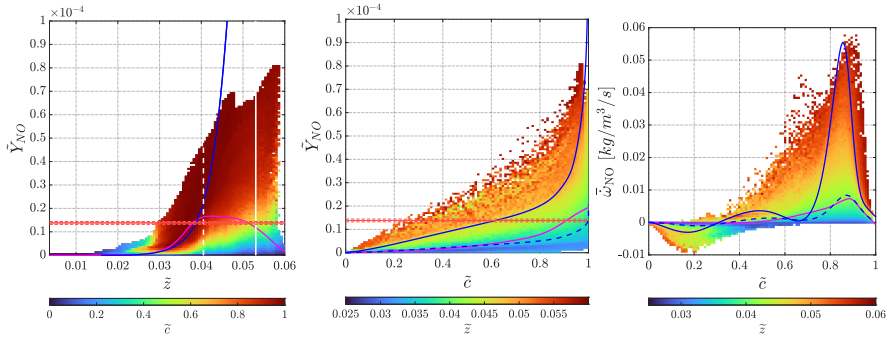


Figure 10.16: **Left:** scatter plots of nitric oxide mass fraction versus mixture fraction, colored by conditional progress variable values. Lines: (—) conditional mean $\langle \tilde{Y}_{\text{NO}} | \bar{z} \rangle$, (—) equilibrium Y_{NO} as computed from premixed unstretched 1D flamelets. **Center:** scatter plots of nitric oxide mass fraction versus progress variable, colored by conditional mixture fraction values. Lines: (—) conditional mean $\langle \tilde{Y}_{\text{NO}} | \tilde{c} \rangle$. Y_{NO} values along a premixed unstretched 1D flamelets at stoichiometry (—) and nominal equivalence ratio (---) are reported as reference. **Right:** Same as center for NO source term $\tilde{\omega}_{\text{NO}}$.

The NO concentration is further examined in relation to the reacting states using an instantaneous plot of NO mass fraction versus mixture fraction, colored by the conditional progress variable, shown in Fig. 10.16 (left). In the outer flame branch, where the mixture is richer and exceeds stoichiometric conditions (right of the white solid line), peaks of $\tilde{Y}_{\text{NO}} \approx 8 \times 10^{-4}$ are observed. These rich reacting samples, however, do not reach the high Y_{NO} theoretical equilibrium value (derived from 1D flamelet computations and marked as a blue line), because mixing with recirculated products at lower mixture fraction, temperature, and NO concentration in the ORZ interrupts complete NO formation. Conversely, leaner samples (to the left of the white dashed line) at high progress variable exhibit NO levels above equilibrium. These are associated to the recirculation of NO formed in richer regions into the leaner inner flame branch via the CRZ, in line with the mechanism described in [349].

Figure 10.16 (center) shows instantaneous \tilde{Y}_{NO} values as a function of the progress variable \tilde{c} , colored by conditional mixture fraction \bar{z} . Results from an unstretched 1D flamelet at the nominal equivalence ratio are included as a blue dashed line for comparison. Results highlight that mixture inhomogeneities introduce scatter in the NO distribution, leading to values significantly above those predicted for a flamelet at the nominal equivalence ratio. A clear correlation of NO concentration with mixture fraction is evident across all progress variable values. In richer samples, an exponential increase of NO with \tilde{c} becomes pronounced, particularly for $\tilde{c} > 0.8$ (high-temperature conditions), as the higher flame temperatures enable NO formation via Zeld'vich pathway [43, 44, 329]. Flamelet results at stoichiometry are also shown for reference (blue solid line). The conditional average of NO versus progress variable (magenta line) closely follows the nominal 1D flamelet prediction up to $\tilde{c} \approx 0.5$. Deviations appear beyond $\tilde{c} \approx 0.5 - 0.8$, due to the exponential increase in NO formation at richer mixture fractions. Closer to the products $\tilde{c} \rightarrow 1$, the values remain slightly below the flamelet equilibrium level at the nominal equivalence ratio. This indicates that overall emissions are governed primarily by flame regions burning at nominal or leaner equivalence ratios, where NO is even consumed in

the CRZ, while the rich outer regions show high NO concentration but without reaching the high theoretical equilibrium value associated to the thermal pathway. Secondly, although mixture inhomogeneities generate local peaks of NO, they do not strongly affect the final product concentrations, which remain close to the equilibrium value predicted at the nominal equivalence ratio.

The instantaneous NO source term, $\bar{\omega}_{\text{NO}}$, is shown in Fig. 10.16 (right) as a function of the progress variable, colored by conditional mixture fraction. The conditional averages of $\bar{\omega}_{\text{NO}}$ over progress variable closely follow the predictions from a 1D unstretched laminar flamelet at the nominal equivalence ratio, similarly to what observed for Y_{NO} . However, the peak in $\bar{\omega}_{\text{NO}}$ at $\tilde{c} \approx 0.9$ is lower than the corresponding flamelet value, reflecting the dominant influence of the inner flame branch, which burns significantly leaner than nominal conditions. Mixture fraction stratification introduces substantial scatter around these values, with local peaks in both formation and consumption rates that exceed those predicted for the nominal case. For reference, the reaction rate of a 1D flamelet at stoichiometry is included as a blue line. The plot also confirms that NO consumption occurs at low progress variable across a range of mixture fractions, as qualitatively observed from Fig. 10.15. Near stoichiometric conditions ($\tilde{z} \approx 0.054$), a negative peak of about 17% of the maximum positive formation rate is observed.

Nitric oxide concentration measurements are available from a gas analyser placed on the centerline at the combustion chamber outlet, obtained within the experimental campaigns in [68]. To gain a global measure of the NO emissions from the LES for the present configuration a control cross plane is selected at a location $y = 100$ mm, where the residence time is about $\tau = 50$ ms, which ensures at least two flow-through times at this location during the available simulation time. LES results about NO emissions at the control plane are summarized in Tab. 10.2. An average NO concentration of 14.23 ppm is computed at the control section. This results in just a 12% overestimation with respect to the experimentally measured value of 12.67 ppm (± 0.53 standard deviation), which can be considered a reasonably good agreement according to the state of the art in NO prediction through LES [44, 328]. Both experiments and simulation result in NO emission below the equilibrium values of $X_{\text{NO,nom}} = 18$ ppm, which can be due to the fact that large portion of the flame burns leaner than the nominal condition within the CRZ. At the same time, the overestimation in the LES could be due to the prediction of a fully reacting rich outer flame branch, which is completely quenched by heat loss and strain in the experiments. The emission index is computed as $\text{EI}_{\text{NO}} = \dot{m}_{\text{NO}} / \dot{m}_{\text{fuel}} = 0.351 [\text{g}_{\text{NO}} / \text{kg}_{\text{fuel}}]$ and the values are in line with numerical and experimental analysis of analogous technically premixed swirled combustors in literature [44, 297, 328]. The NO concentration adjusted at 15% O₂ is also computed resulting in 5.546 ppm, close to the experimental values obtained in [68] for the present setup.

Overall, the presented analysis highlights the broad range of combustion regimes within the TU Delft combustor at the investigated operating conditions. Inhomogeneity in fuel-air mixedness leads to localized scatter in NO formation and NO concentration peaks, but overall the emissions levels remain close to those predicted for a flame at the nominal equivalence ratio, with a slight dominance of the lean burning regions reducing the overall emission. For the considered operating conditions, the outer flame branch is suppressed in experiments due to heat losses. Nevertheless, the LES results highlight

the critical role of the rich outer flame branch in pollutant formation and emphasize the sensitivity of emission levels to flame positioning and fuel stratification. These insights are particularly relevant for design: for example, higher operational wall temperatures may enable flame reattachment [344], leading to increased emissions, which must be accounted for in combustor development. Similarly, increasing the hydrogen content leads to a sustained outer flame branch (with possible reattachment), as shown in [170] and in [68] for the present set-up, which tends to burn under richer conditions and lead to higher emissions levels, as observed experimentally in [68]. In this context, the present numerical analysis provides a framework for interpreting such experimental trends and emphasizes the need to accurately model fuel-air mixing, heat loss and to experimentally characterize thermal boundary conditions when investigating emissions in technically premixed swirled combustors.

Case	Exp [ppm]	X_{NO} [ppm]	NO@15%O ₂ [ppm]	\dot{m}_{NO} [g/s]	EI _{NO} [g _{NO} /kgf]
25H2	12.67 ± 0.53	14.23	5.546	8.00 × 10 ⁻⁵	0.351

Table 10.2: NO emissions data as experimentally measured through gas analyzer on the centerline at combustion chamber exit [319] and numerically predicted at a control plane $y = 100$ mm for case 25H2.

10.6. 100% H₂ CASE: NEAR-FLASHBACK CONDITION

In this section the focus is on the 100% hydrogen fuel case at the nominal thermal power and total air mass flow rate (case 100H_{2,nom} of Tab. 10.1). Experimental campaigns in [68] showed that increasing hydrogen content in the fuel mixture leads to a flame burning more strongly on the outer branch and approaching reattachment at the mixing tube rim, in line with [170, 344]. In particular, the selected operating condition displayed high flashback propensity at a geometric swirl number of 1.1, so that a minimum of 20% axial air injection (AAI) was required to prevent flashback.

The LES simulation of case 100H_{2,nom} does not predict a stable flame, despite applying the same AAI level as in the experiment, and flashback is observed. Figure 10.17 shows the time sequence of a flashback event as predicted by the LES, visualizing midplane contours of instantaneous temperature and mixture fraction. Midplane contours of the difference between the instantaneous axial velocity \tilde{u} and the local value of the theoretical unstretched laminar flame speed (reconstructed from the local mixture fraction \tilde{z}) is also reported as a simple evaluation of favorable conditions for upstream flame propagation. As previously described for case 25H2 of Tab. 10.1, fuel stratification makes the outer flame branch the most reactive region, and this persists in the case with 100% hydrogen fuel as seen in the central row. The green iso-line (top row) identifies the lean flammability limit, showing that the entire boundary layer region at the mixing tube wall consists of flammable mixture, while an air core is visible along the centerline (due to axial air injection). At the mixing tube rim, the flashback event is initiated by flow velocity fluctuations induced by periodic vortex shedding associated with Kelvin–Helmholtz instability [57, 60, 62], visualized by the negative axial velocity values observed at the mixing tube rim (bottom row). Although the flame speed is lower than the average axial flow velocity, instantaneous drops in axial velocity and temporary reversed flow allow

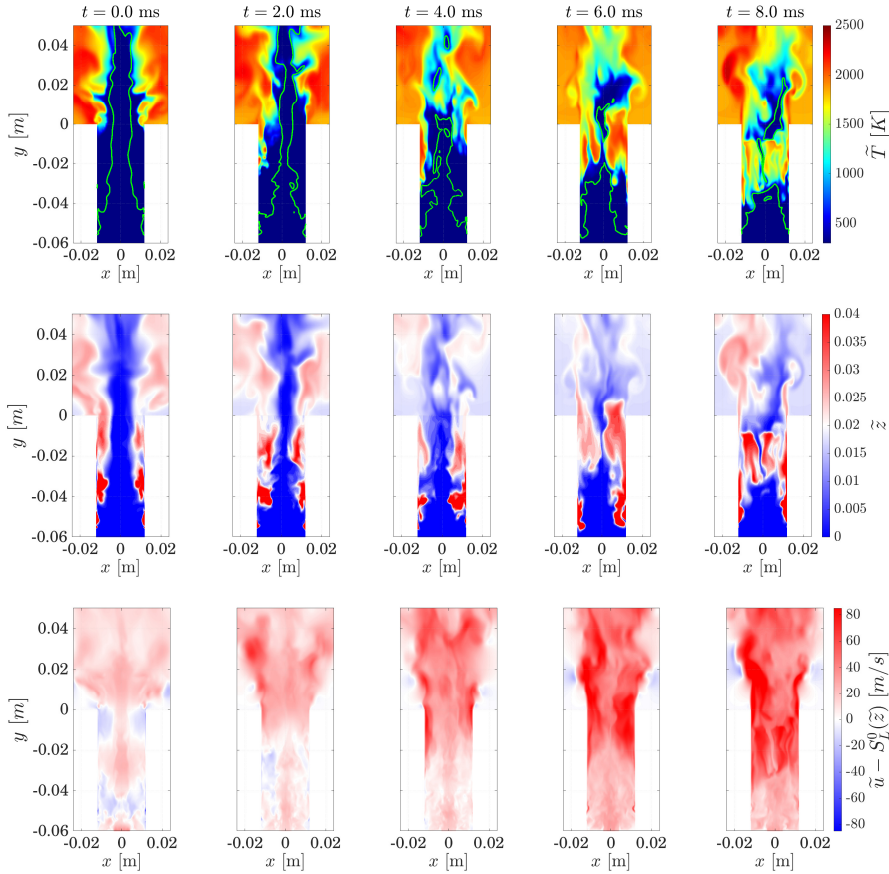


Figure 10.17: Time sequence of a flashback event in case 100H₂_{nom} of Tab. 10.1. Midplane contours of instantaneous temperature (top row) and mixture fraction (central row), where white color corresponds to the nominal mixture fraction value. The bottom row reports midplane contours of the difference between instantaneous axial velocity \bar{u} and the theoretical local laminar flame speed S_L^0 reconstructed *a posteriori* based on local mixture fraction value, reported as a reference for upstream flame propagation potential. The lean flammability limit isoline $z_{\text{lean}} = 0.007$ is reported in green (—).

the flame to propagate upstream along the wall (see $t = 0.0$ ms – 2.0 ms in Fig. 10.17, top and bottom row), similarly to what described in [57, 70]. As it moves upstream, the flame alters the flow field: strong axial acceleration is induced by thermal expansion, exacerbated by the confinement within the mixing tube. This flow acceleration in the boundary layer exceeds the core velocity imposed by axial air injection (AAI), significantly modifying the flow field and mixing features within the mixing tube. The previously stable, not ignitable, lean jet core gets suppressed, the fuel reaches the centerline region and the entire mixture in the mixing tube becomes flammable from $y = -20$ mm downstream (see $t = 6.0$ ms in Fig. 10.17). At this point, the flame front propagates upstream through the entire cross-section. The full flashback event lasts approximately 8 ms.

Due to the discrepancy between LES results and experiments, which did not show flashback events, the effect of heat loss modelling is investigated. As discussed in Chap. 1, heat losses play a crucial role in boundary layer flashback. In the baseline LES model, the reaction rate $\tilde{\omega}$ is set to zero at the wall, but this is insufficient to properly capture the interaction between velocity gradients, chemical reactions, and quenching distance that determines boundary layer flashback [60, 62]. To address this, the correction model described in Sec. 3.2.4 is used to investigate the effects of heat losses at the wall on flame stabilization and flashback. Isothermal walls at a limit case temperature of 300 K are imposed.

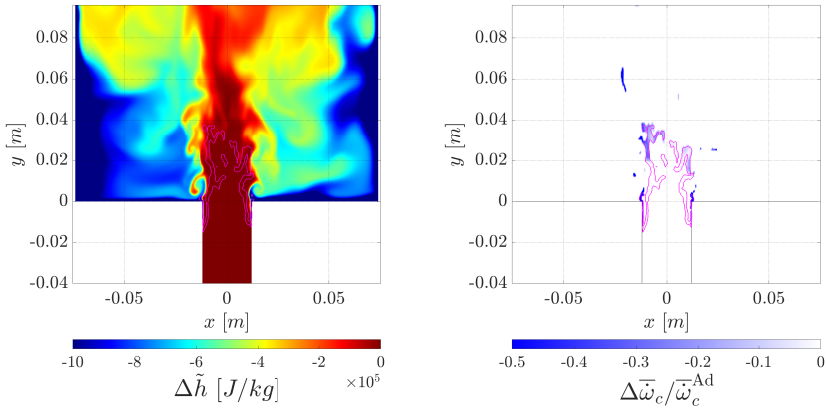


Figure 10.18: **Left:** midplane contour plot of instantaneous enthalpy defect $\Delta\tilde{h}$ with respect to the adiabatic case when isothermal wall at 300 K is imposed. **Right:** midplane contour of relative reaction rate reduction with respect to the adiabatic case $\Delta\bar{\omega}_c/\bar{\omega}_c^{\text{Ad}}$ corresponding to the enthalpy defect conditions reported on the left, resulting from the heat loss model described in Sec. 3.2.4. Iso-lines corresponding to 2% of the maximum reaction rate are reported in magenta (—) to visualize the flame front.

Figure 10.18 (left) shows instantaneous contours of enthalpy defect $\Delta\tilde{h}$, computed as the difference between the local enthalpy value h resulting from the transport equation, and therefore subject to non-adiabatic wall conditions, and the theoretical tabulated adiabatic enthalpy h^{Ad} , only depending on the local mixture composition. The enthalpy flux through the walls cools the combustion products in the outer recirculation zone, which are then recirculated to the flame base. The results are consistent with those presented in similar studies [87], showing a typical maximum enthalpy defect of $-1\text{e}6$ J/kg. A mixing layer is formed between the high-enthalpy mixture from the mixing tube and the lower enthalpy products cooled at the wall. The right panel of Fig. 10.18 shows the reaction rate reduction relative to the adiabatic case $\Delta\bar{\omega}/\bar{\omega}_{\text{Ad}}$, resulting from the local enthalpy defect. Only the outer flame branch attaching to the mixing tube rim is significantly affected by the enthalpy loss, while the rest of the flame remains within the region where the enthalpy defect is zero. When the flame (visualized with the magenta reaction rate isoline as in Fig. 10.8) stabilizes upstream in the exit section of the mixing tube $y \approx -15$ mm, the reaction rate is reduced by up to 50% at the wall. Some milder effects are visible downstream, where cooled products interact with the flame at

locations around $y = 20$ mm.

When the heat loss model is enabled, the flame does not show the flashback events observed for the adiabatic case. However, the flame still exhibits the tendency to propagate upstream into the boundary layer at the mixing tube wall and periodic oscillations are observed in its axial position, within the exit section of the mixing tube, as shown in the time sequence in Fig. 10.19. This phenomenon can be seen as a mild intermittent flashback, as described in literature [71, 72]. Similarly to what observed for the adiabatic case, an instantaneous local decrease in axial velocity, linked to Kelvin-Helmoltz instability, allows the flame to propagate up to 15 mm upstream inside the tube (in about 0.5 ms), see Fig. 10.19 $t = 0.0$ ms – 0.25 ms, bottom row. However, due to the imposed iso-thermal walls, the temperature difference between the reacting mixture and the wall induces a heat flux that reduces the reaction rate (as shown in Fig. 10.18, right). Due to this reduced reactivity, the axial velocity exceeds the flame speed again, and the flame is pushed back out of the mixing tube. It can be seen how in absence of complete flashback, the mixture fraction field remains stable, with lean non-ignitable mixture at the mixing tube core and constant value $\tilde{z} \approx 0.023$ at the mixing tube wall. The evolution in time of the most upstream flame front location, y_f , is plotted in Fig. 10.20. Oscillations with an amplitude of approximately 10 mm and a period of ≈ 1 ms are clearly visible, along with longer-period oscillations (≈ 10 ms) shifting the flame from being entirely outside the mixing tube ($y = 0$) to upstream positions up to $y = -20$ mm. On average, the flame tip stabilizes at a location of $y = -10$ mm. This is further analyzed using Fast Fourier Transform, and the spectrum of the $y_f - \langle y_f \rangle$ signal is shown in Fig. 10.21. The spectrum confirms the presence of a distinct peak at $f = 1090$ Hz (Strouhal number $St = 2.33$, based on mixing tube diameter and bulk velocity), and additional lower-frequency content between 40 and 80 Hz ($St = 0.086$ – 0.17) at comparable amplitudes.

The presented LES analysis confirms that the considered operating condition is highly prone to flashback, consistently with experimental studies, reporting that even a small reduction in AAI or a slight increase in thermal power can trigger sudden flashback. The analysis further shows that heat loss plays a decisive role in flame stabilization near the flashback limit. When heat loss is modelled, the LES no longer predicts flashback, unlike in the adiabatic case. Consistently, wall temperatures remains below 500 K in the experimental setup (adiabatic walls cannot be representative of real conditions), which can explain the absence of flashback in the measurements. Moreover, the periodic oscillations of the flame tip at the mixing tube exit predicted by the LES appear physically plausible. However, it remains unclear whether the flame in the experiment stabilizes fully downstream or fluctuates within the mixing tube, due to limited optical access. More accurate predictions and meaningful comparisons with experimental data would require a more detailed characterization of thermal boundary conditions, or conjugate heat transfer simulations [44].

The results identify the mixing tube rim as the critical point for boundary layer flashback initiation, favored by fuel stratification (investigated in the previous section and in Chap. 9). To mitigate the risk of flashback, strategies aiming at the reduction of the equivalence ratio in the boundary layer can be explored. These are for example air injection into the boundary layer and coaxial fuel–air injection, both proposed for similar swirled combustor configurations [44, 49, 297]. As will be discussed in the next section,

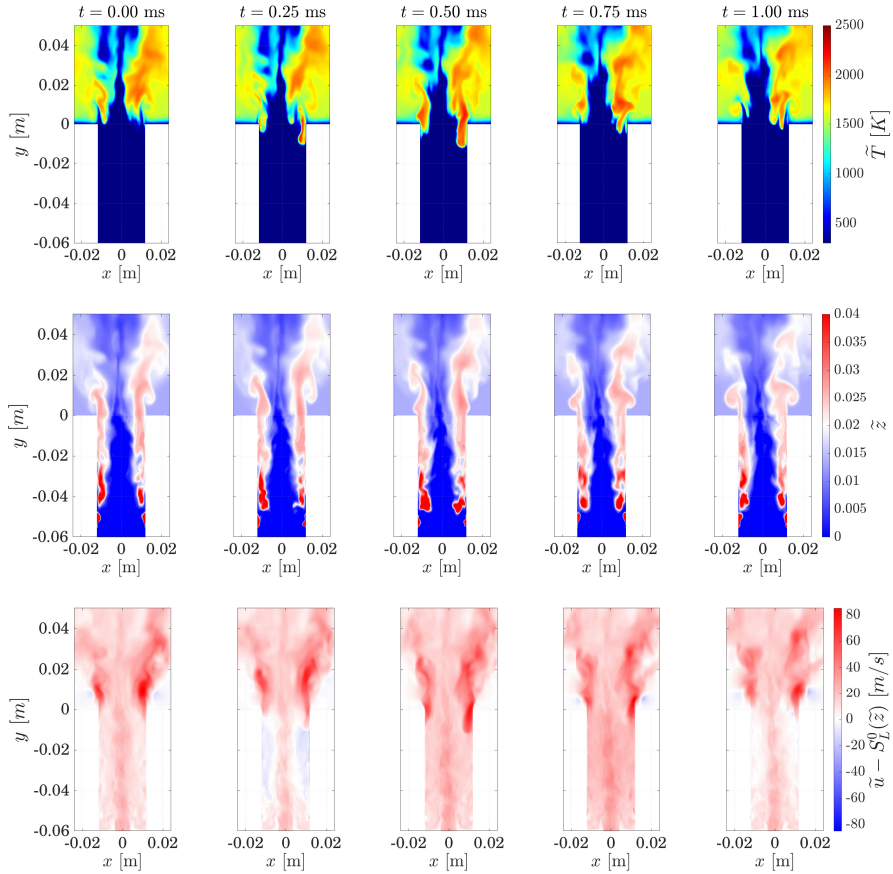


Figure 10.19: Time sequence of the oscillatory flame stabilization dynamics (intermittent flashback) obtained when isothermal walls at 300 K are imposed and the heat loss model is enabled. Midplane contours of instantaneous temperature (top row) and mixture fraction (central row), where white color corresponds to the nominal mixture fraction value. The bottom row reports midplane contours of the difference between instantaneous axial velocity \tilde{u} and the theoretical local laminar flame speed S_L^0 reconstructed *a posteriori* based on local mixture fraction value, reported as a reference for upstream flame propagation potential.

the negative Markstein length of lean hydrogen–air mixtures may further increase local reaction rates in response to the flame tangential strain rate at this location, exacerbating flashback risk.

To summarize, this analysis underlines the need to incorporate wall heat loss in the LES model and to experimentally characterize the thermal boundary conditions in order to accurately predict flame stabilization, position, structure, and consequently emissions. For less reactive mixtures, such as the case with 25% H_2 of Tab. 10.1, neglecting these factors could lead to incorrect predictions of flame anchoring and shape (e.g. an M flame with an attached outer branch), as detailed at the previous section, while for highly reactive mixtures with pure hydrogen, it could discriminate between predicting a

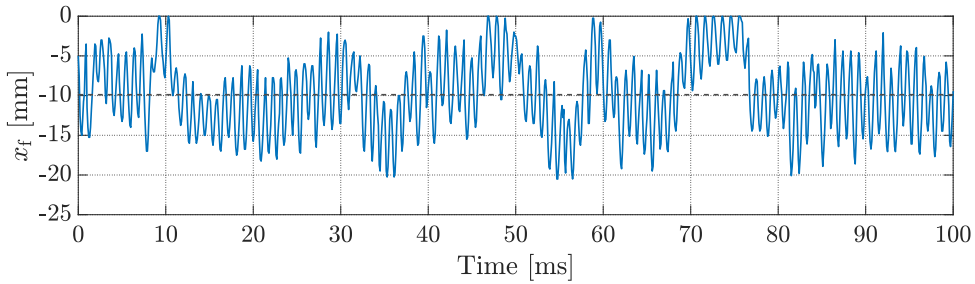


Figure 10.20: Time series of the axial position x_f of the flame tip.

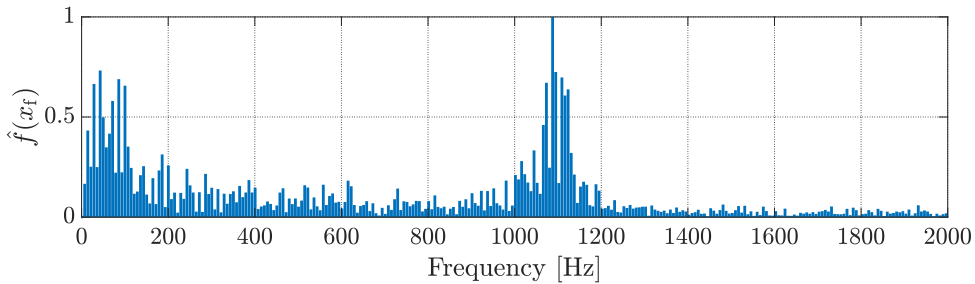


Figure 10.21: Single sided normalized amplitude spectrum of the axial coordinate of flame tip, obtained by fast Fourier transform (FFT).

stable flame or flashback.

10.7. 100% H₂: ULTRA-LEAN CONDITION

Although the inclusion of heat loss modelling in the LES enabled the prediction of a stable flame without flashback for the nominal case 100H_{2,nom} of Tab. 10.1, the flame still exhibited unstable anchoring, with periodic oscillations in its position within the mixing tube. To further explore stable operation with 100% H₂ fuel, the analysis focuses on the operating point 100H₂ of Tab. 10.1, where the total air mass flow rate is increased by 85% with respect to the nominal case. This adjustment leads to a stable flame at the same power output under ultra-lean conditions, with a nominal equivalence ratio of $\phi_{nom} = 0.34$. Such a strategy offers the potential for minimal fuel consumption and reduced NO_x emissions, leveraging the full benefits of lean hydrogen combustion. Since no experiments have been performed under these operating conditions, the LES provides a first assessment of ultra-lean combustion within the TU Delft combustor, with particular emphasis on the effects of axial air injection on mixing, thermal fields, and emissions. Moreover, this stable case offers the possibility to assess the relevance of differential diffusion effects on the flame structure within a technically premixed swirl-stabilized combustor.

10.7.1. FLOW FIELD AND FLAME STRUCTURE: EFFECT OF AAI

When the air massflow rate is increased (case 100H2 of Tab. 10.1), a stable combustion without flashback nor flame tip fluctuations is predicted by the LES. The reduced flame speed, due to the lower equivalence ratio, increased axial velocity, and steeper velocity gradients in the boundary layer prevent the boundary layer flashback observed in the nominal case. As a result, the flame anchoring and overall structure remain qualitatively similar to the 25H2 case, described in Sec. 10.5.2. The contour plots in Fig. 10.22 (left) show a velocity field and flame shape qualitatively similar to those in Figs. 10.5(right). Overall, higher axial velocities are observed due to the increased air mass flow rate, leading to a narrower jet opening angle. The central recirculation zone (CRZ) is reduced both radially and axially. The flame shape, identified by isolines at 2% of the maximum reaction rate, maintains the characteristic M-shape with two branches: an outer branch stabilized along the outer shear layer, and an inner branch stabilized within the CRZ, forming a distributed average turbulent flame brush. Compared to the case with 25% H₂ fuel blend (25H2 case of Tab. 10.1), the flame is approximately 10 mm shorter (about 40 mm long), despite the increased bulk velocity, due to the higher reactivity of the 100% hydrogen fuel.

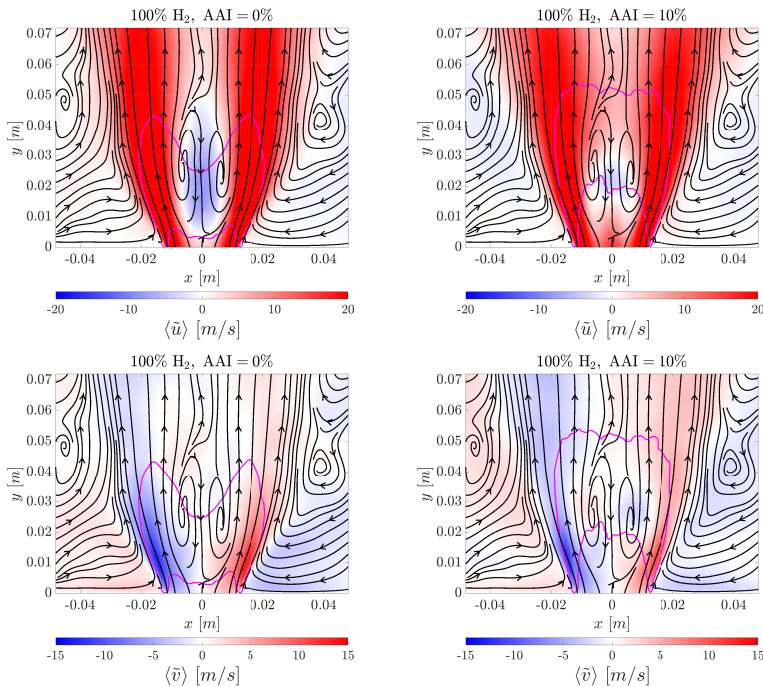


Figure 10.22: Midplane contour plots (with streamlines in black) of mean axial (top) and transversal (bottom) velocity component from LES of the ultra-lean 100% hydrogen case with 0% AAI (left) and 10% AAI (right), corresponding to case 100H2 and 100H2AAI of Tab. 10.1, respectively. The flame brush is identified with isoline at 2% of the maximum progress variable reaction rate $\langle \bar{\omega}_c \rangle$ (—).

The influence of AAI on the 100% H₂ flame under ultra-lean conditions is examined

next using LES results of case 100H2AAI of Tab. 10.1, where 10% of the total air is supplied through AAI. The computed velocity field is compared to the case with 0% AAI in Fig. 10.22. One of the main effects of AAI is a net decrease in swirl number as part of the air enters the centerline without swirling. This affects the vortex breakdown, resulting in a smaller CRZ with lower backflow velocity. The stagnation point at the base of the CRZ shifts downstream compared to the case without AAI (from $y = 4$ mm to $y = 15$ mm) pushed by the increased axial momentum on the centerline. At the same time the peak backflow velocity is halved from -8 m/s to -4 m/s. The centerline velocity recovers positive values right downstream of the CRZ at around $y = 30$ mm, reducing the CRZ length from 46 mm to about 15 mm. Consequently, flame position, shape and anchoring are also affected. As shown by the magenta iso-line, the flame is approximately 15 mm longer than in the case without AAI, and the inner branch stabilizes further downstream, as a result of the increased centerline axial momentum and the downstream-shifted CRZ. The resulting flame shape is qualitatively similar to the one observed experimentally for the nominal 100% H₂ case with 20% AAI (case 100H2_{nom} of Tab. 10.1) reported in [68]. Interestingly, the use of 10% AAI at the considered operating conditions is observed to suppress the formation of PVC and the associated flame fluctuations (not shown).

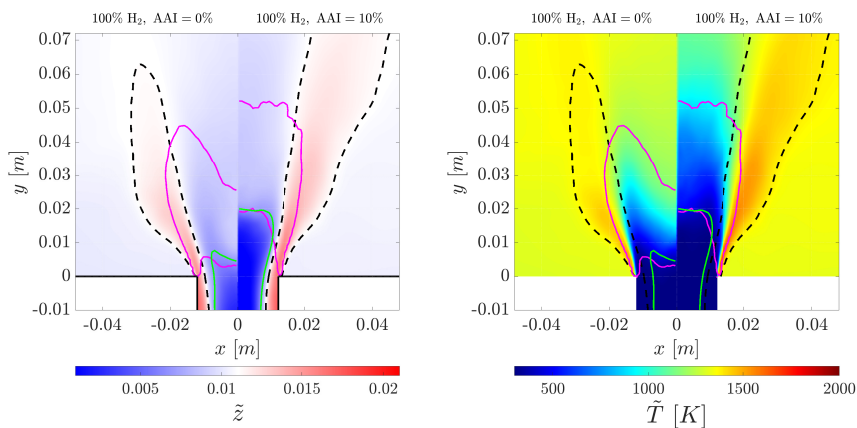


Figure 10.23: Midplane contour plots of mean mixture fraction (left) and temperature (right) from LES of case 100H2 (left half) and 100H2AAI (right half), of Tab. 10.1. Iso-lines legend is as in Fig. 10.8.

The impact of AAI on fuel-air mixing is highlighted in Fig. 10.23, which shows midplane contour plots of time-averaged mixture fraction and temperature. At 0% AAI, the results show similarities with those from case 25H2 of Tab. 10.1 (reported in Fig. 10.8). Indeed, fuel stratification is observed near the mixing tube walls where the mixture fraction reaches $z \approx 0.015$. The mixture fraction isoline at the nominal value $z = 0.01$ identifies the region where the richer mixture (in red) mixes with products at nominal mixture fraction in the outer shear layer and with mixture leaner than nominal conditions across inner shear layer. This stratified region with richer mixture extends up to $y = 60$ mm. Closer to the centerline, the mixture fraction remains below the flammability limit up to $y = 5$ mm in the combustion chamber, as visualized by the green solid line,

and it increases only via recirculation of richer mixture through the CRZ. The central flame branch stabilizes in correspondence of the threshold where the mixture becomes flammable. The thick inner average flame brush appears to burn below the nominal mixture fraction in the CRZ. These mixing patterns are reflected in the thermal field. The nominal adiabatic flame temperature of 1370 K is reached in the outer recirculation zone (ORZ). The outer flame branch, burning under richer conditions exhibits temperatures exceeding the nominal adiabatic flame temperature close to the mixing tube rim while the inner branch shows lower temperatures. Here, the nominal temperature value is reached only around $y = 60$ mm after mixing with richer products. The outer flame branch displays sharp temperature gradients, while the inner flame branch exhibits more diffuse gradients due to lower reaction rate and intense turbulence, which contribute to a thicker average flame brush, similarly to what discussed in Sec. 10.5.2.

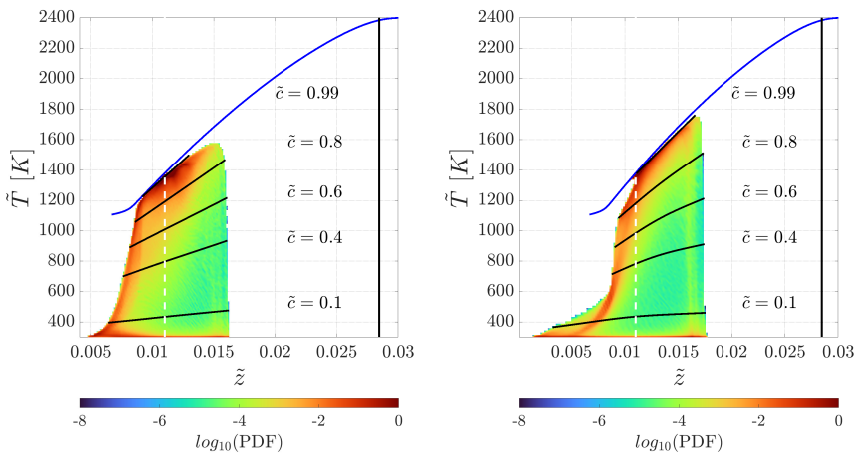


Figure 10.24: Joint probability density function (JPDF) of time averaged temperature (\bar{T}) versus average mixture fraction (\bar{z}) from LES of case 100H2 (left) and 100H2AAI (right) of Tab. 10.1. The adiabatic flame temperature versus reactants mixture fraction computed from unstretched laminar premixed 1D flamelets of hydrogen air mixtures is reported as a blue line (\blackrightarrow). Vertical dashed white line and solid black line mark the nominal mixture fraction value $z_{\text{nom}} = 0.011$ and the stoichiometric condition $z_{\text{stoich}} = 0.028$, respectively. Conditional means of time averaged temperature versus mixture fraction at different progress variable values $\langle \bar{T} | \bar{z} \rangle_{\bar{c}=c^*}$ are also reported as black solid lines.

Axial air injection alters both mixing and thermal fields, notably increasing fuel stratification, as shown in Fig. 10.23 (left). At $y = -10$ mm, a central core of air with low mixture fraction is visible, where fuel penetration is minimal. In contrast, the fuel tends to remain confined within the near-wall region in the mixing tube, which increases the mixture fraction value. As a result, the central core remains below the lean flammability limit up to the CRZ leading point now shifted 20 mm downstream by AAI. Here the mixture enters the flammability range due to mixing with richer pockets of reactants within the CRZ.

The increased fuel stratification leads to a longer flame and thicker turbulent flame brush in the flame region stabilizing within the CRZ. Here, lower temperatures and broader

temperature gradients are observed when AAI is used. Moreover, a longer portion of the outer flame branch burns at conditions richer than nominal. In fact, the mixing layer between the richer outer portion of the jet with the leaner jet core is now elongated, due to the weaker recirculation within the CRZ. When AAI is applied, the rich zone enclosed by the $z = 0.011$ isoline (dashed black line) extends further downstream compared to the case without AAI. This indicates that stratification in product composition and temperature (post-flame region, downstream the magenta line) persists, and that mixing between rich and lean products from the outer and inner flame branch, respectively, occurs over a longer axial distance.

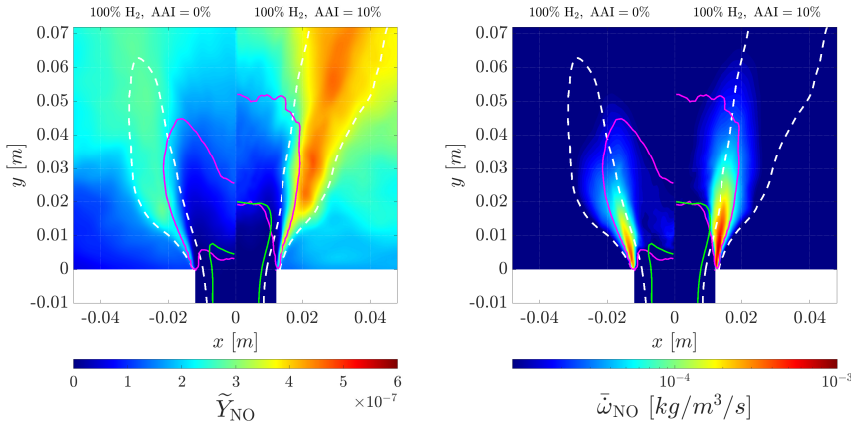


Figure 10.25: Midplane contour plots of time averaged nitric oxide mass fraction (left) and formation rate (right) from LES of case 100H2 (left halves) and 100H2AAI (right halves) of Tab. 10.1. Iso-lines legend is as in Fig. 10.8.

Figure 10.24 shows the joint PDF of time averaged temperature $\langle \tilde{T} \rangle$ and mixture fraction $\langle \tilde{z} \rangle$. In the 0% AAI case (left), fully reacted samples ($\tilde{c} = 1$) are concentrated around the nominal mixture fraction $\tilde{z} \approx 0.011$ at the nominal adiabatic temperature of 1370 K, with scatter in a range of $\tilde{z} \in [0.009, 0.013]$ due to fuel stratification. The highest PDF values are observed at samples leaner than nominal (left of the dashed line) down to $z = 0.005$, corresponding to the points upstream of the CRZ below the flammability limit. Here the lean reactants mix with partially reacted hotter samples, so that progress variable, temperature and mixture fraction increase simultaneously. Equilibrium temperatures near 1200 K are then reached for mixture at $\tilde{z} = 0.009$. Samples between $\tilde{z} \in [0.013, 0.015]$ result in the maximum peak temperature of 1580 K, but they do not reach the corresponding equilibrium temperature, since their mixture fraction decreases to the nominal value as they react, due to mixing with leaner reactants from the jet core and products at the nominal \tilde{z} from the ORZ.

With 10% AAI, the range of fully reacted samples shifts to richer values $z \in [0.01, 0.018]$, which reach equilibrium temperatures up to 1700 K, about 100 K higher than in the case without AAI. This occurs due to the fact that the richer mixture reacting in the outer flame branch mixes with products at the nominal mixture fraction from the ORZ over a longer axial distance, and can therefore reach the equilibrium temperature at higher

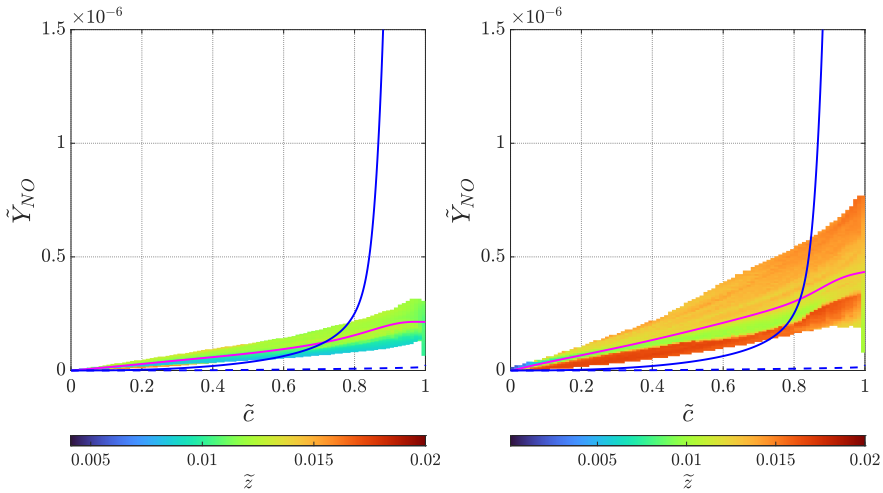


Figure 10.26: Scatter plots of time averaged nitric oxide mass fraction versus progress variable, colored by conditional mixture fraction values from LES of case 100H2 (left) and 100H2AAI (right) of Tab. 10.1. Lines: (—) conditional mean $\langle \tilde{Y}_{NO} | \tilde{c} \rangle$, Y_{NO} values along a reference premixed unstretched 1D flamelets at stoichiometry (—) and nominal equivalence ratio (---).

values of local equivalence ratio. The increased reactants stratification induced by AAI is visible at low progress variable from the wider mixture fraction range extending to as lean as $\tilde{z} = 0.0016$. A linear-like tail appears in the joint PDF plot at the leanest values, indicating mixing between sub-flammability limit samples and partially reacted richer and hotter products at the CRZ base. At $z = 0.008$, as the lean flammability limit is crossed, strong reaction is sustained.

The differences in mixing and peak temperatures influence NO formation. Figure 10.25 shows midplane contours of time-averaged NO mass fraction (left) and formation rates (right), for the 0% AAI case (left column) and the 10% AAI case (right column). With AAI, the NO formation rate increases in the outer flame branch due to increased fuel stratification. Moreover, the flame length is increased by the use of AAI and NO forms over a longer outer flame branch, compared to the case without AAI. This results in higher NO concentrations in the richer products from the outer flame branch (see the region encompassed by the black dashed line) when AAI is employed. Notably the NO consumption observed for the baseline case 25H2 is not present, due to the absence of hydrocarbon fuel.

Plots of time averaged NO mass fraction versus progress variable, colored by the conditional mixture fraction value are shown in Fig. 10.26. Differently from the 25% H₂ case (see Fig. 10.16), an exponential trend of NO with progress variable is not observed, which is instead visible from the 1D flamelet data at $z = 0.02$ reported as a blue line for comparison. This is due to the very lean burning condition, which results in average peak temperature below 1800 K and suppression of NO formation via thermal pathway. This represents a promising outcome for stable ultra-lean hydrogen combustion within the present set up. At such lean conditions the NNH and N₂O formation pathways for NO

become dominant [44] and they still present high sensitivity to the mixture composition. In both cases (0% and 10% AAI) the conditional average of \tilde{Y}_{NO} over \tilde{c} (see magenta line) largely exceeds the NO values for a reference 1D premixed flamelet at the nominal equivalence ratio (dashed blue line), due to the presence of richer mixture. In the 0% AAI case (left), data points cluster around $\tilde{z} = 0.013$ (green color), with scatter in NO values correlated with mixture fraction variations. The case with 10% AAI (right) shows a steeper NO increase with progress variable, especially at $c \approx 0.9$, due to the presence of mixture burning at richer conditions and reaching higher temperatures.

To evaluate global NO emissions in the two cases, a control cross section at $y = 100$ mm is considered, as per the 25H2 case, and results are reported in Tab. 10.3. The NO concentration in ppm and emission index EI_{NO} appear reduced by two and one order of magnitude, respectively, compared to the baseline case with 25% hydrogen in the fuel blend. This can be primarily traced back to the suppression of thermal NO formation by operating at ultra lean conditions and containing the peak temperatures below 1600K. Also, prompt NO formation mechanism is absent as no hydrocarbon is present in the fuel [191]. However, the emission level is 71% above the ultra low theoretical NO equilibrium value (0.07 ppm) calculated for a 1D premixed flamelet at the nominal equivalence ratio, highlighting the detrimental effect of mixture inhomogeneity on NO formation, even at very lean conditions. Employing 10% AAI results in a 60% increase in NO emissions (in volumetric ppm), due to the decreased fuel/air mixing and the increased peak temperatures at the flame base attaching to the mixing tube rim.

Case	X_{NO} [ppm]	NO@15%O ₂ [ppm]	\dot{m}_{NO} [g/s]	EI_{NO} [g _{NO} /kg _f]
100H2	0.216	0.0954	2.79×10^{-6}	2.79×10^{-2}
100H2 AAI	0.346	0.1536	4.00×10^{-6}	4.00×10^{-2}
100H2DD	0.241	0.11	3.17×10^{-6}	3.17×10^{-2}

Table 10.3: NO emissions data as predicted by LES at a control plane $y = 100$ mm for all the 100% hydrogen cases considered in the present study.

The presented analysis highlights the critical contribution of the outer flame branch to NO formation due to its sensitivity to mixture composition even when thermal NO is not the dominant pathway. Differently from the baseline case 25H2, experiments with increasing hydrogen content reported flames burning more and more on the outer branch. Depending on the operating conditions, increasing NO emissions were observed with increasing AAI, which may be now explained with a decrease in mixing quality, in light of the presented results.

10.7.2. EFFECT OF DIFFERENTIAL DIFFUSION

Next, the effects of differential diffusion (DD) are examined in the TU Delft combustor under ultra-lean conditions. Among the main DD effects in premixed flames is the redistribution of enthalpy and mixture fraction under flame stretch (curvature or strain) [154], as reviewed in Chap. 2. To identify regions of high stretch, Fig. 10.27 shows contours of time-averaged and instantaneous flame-tangential strain rate from LES of the ultra-lean 100% hydrogen case with 0% and 10% AAI. Both inner and outer flame branches stabilize against recirculated products (from the CRZ or ORZ), in a manner that shares similarities

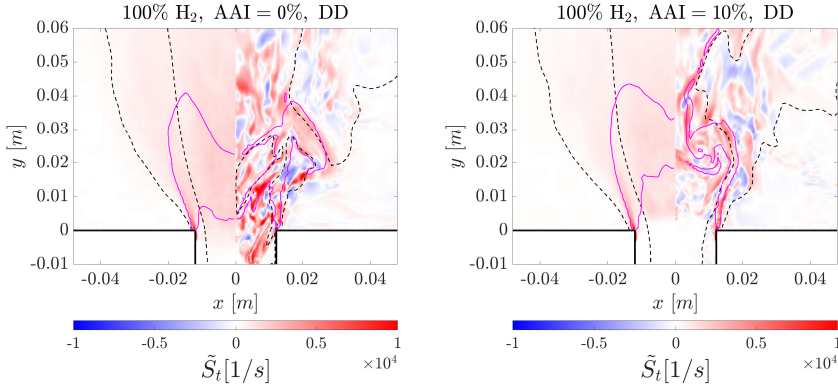


Figure 10.27: Midplane contour plots of time averaged (left halves) and instantaneous (right halves) strain rate tangential to the flame front for the 100% H₂ case without AAI (left) and with 10% AAI (right), corresponding to case 100H2 and 100H2AAI of Tab. 10.1, respectively. Iso-lines legend is as in Fig. 10.22.

with a counterflow configuration. Along the centerline, products are recirculated within the CRZ, which forms a stagnation point for the incoming reactants. The CRZ acts as an aerodynamic obstruction, forcing the fresh mixture to flow around it and generating a region of high positive tangential strain rate near the stagnation point. As a result, the mixture accelerates at the mixing tube exit through the cross-section area left free from the CRZ (see Fig. 10.22), producing elevated tangential strain rates at the mixing tube rim. Similar behavior has been observed in swirled combustors [87, 170, 328], as well as in slot-burner and bluff-body stabilized flames [53, 74, 350], as discussed in Chap. 8. At these conditions, Fig. 10.27 shows moderate mean tangential strain rates, with peaks on the order of 10^4 s^{-1} at the rim and lower values ($\sim 0.4 \text{ s}^{-1}$) inside the CRZ. Instantaneous fields reveal fluctuations in local strain rate produced by turbulent eddies, with peaks exceeding the mean value. The addition of axial air injection (right) reduces both mean and peak strain rates due to the smaller CRZ and weaker backflow, as described in the previous section.

When differential diffusion is modeled, the coupling between strain rate and mixture fraction redistribution is captured, consistently with results for the bluff-body-stabilized burner discussed in Chapter 8. This is visible in Fig. 10.28, where contours of average mixture fraction (left) and temperature (right) are compared for the baseline 0% AAI with (right half) and without (left half) differential diffusion modelling. When differential diffusion is considered, a clear local enrichment is observed near the mixing tube rim, where the flame, already burning at conditions richer than nominal $z \approx 0.015$ ($\phi \approx 0.52$) due to fuel stratification, reaches mixture fraction values of $z \approx 0.02$ ($\phi \approx 0.7$). This enrichment region correlates spatially with the zones of high tangential strain in Fig. 10.27, and leads to higher local product temperatures compared to results without DD modelling. These high-temperature products (up to 2000K), formed at the flame base, subsequently mix with lower z products downstream (outside the magenta flame brush isoline).

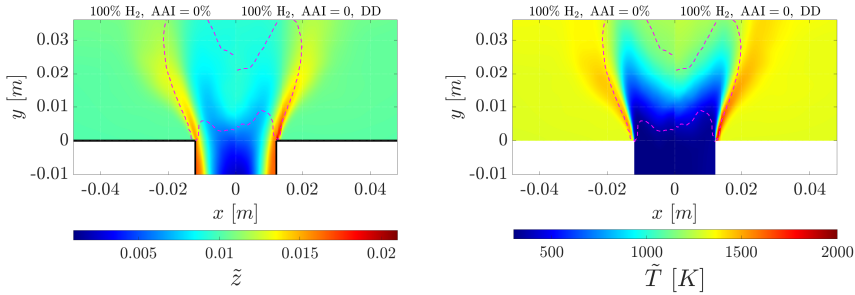


Figure 10.28: Midplane contour plots of mean mixture fraction (left) and temperature (right) from LES of the ultra-lean 100% H₂ case without differential diffusion modelling (left halves) and with differential diffusion modelling (right halves), corresponding to cases 100H2 and 100H2DD of Tab. 10.1, respectively. The mean turbulent flame brush is visualized by magenta isoline (---) of reaction rate at 2% of its maximum value.

The flame appears overall slightly shorter when differential diffusion is modelled, as the reaction rate is enhanced in the outer flame branch in response to the positive tangential strain rate, due to the negative Markstein length of the hydrogen lean mixture. In contrast, minimal differences are observed in the inner flame branch, where the mixture fraction remains unchanged. This is attributed to the strong turbulent mixing of lean reactants near lean blow-off limit with partially reacted products, which dominates over diffusive transport.

The instantaneous joint probability density function (PDF) of temperature versus mixture fraction is shown in Fig. 10.29 and provides quantitative insight into the effects of differential diffusion. Focusing on the bottom of the distribution, at $\tilde{c} \approx 0$, it is observed that the mixedness of the reactants is not significantly influenced by differential diffusion. At this location, corresponding to unreacted conditions ($\tilde{T} = 300$ K), the range of mixture fraction values remains between $\tilde{z} \in [0.005, 0.02]$, centered around the nominal value of $\tilde{z} = 0.011$. This indicates that differential diffusion does not noticeably alter the initial fuel-air mixing upstream of the flame. However, as the reaction progresses toward higher temperature and progress variable values, the inclusion of differential diffusion leads to noticeably richer mixture fractions, in the outer branch region. When differential diffusion is included, the points richer than nominal (corresponding to the outer flame branch) undergo further enriching extending to $\tilde{z} \approx 0.033$, exceeding the stoichiometric value. These richer samples cause increased peak temperatures, reaching up to 2300K (versus a maximum 1900 K equilibrium temperature at $\tilde{z} \approx 0.019$ in the baseline case). In the range $\tilde{z} \in [z_{\text{nom}}, 0.025]$, the conditional average temperature for $c = 0.99$ generally follows the equilibrium flame temperature curve from flamelets computations. However, super-adiabatic temperatures are observed in this region when dif-

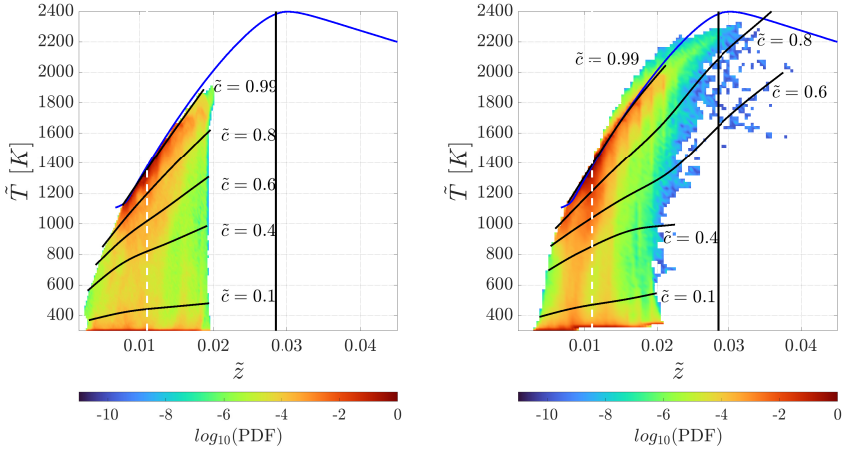


Figure 10.29: Joint probability density function (JPDF) of instantaneous temperature \tilde{T} versus mixture fraction \tilde{z} from LES of the ultra-lean 100% H₂ case without differential diffusion modelling (left) and with differential diffusion modelling (right), corresponding to cases 100H2 and 100H2DD of Tab. 10.1, respectively. Lines: (—) adiabatic flame temperature versus reactants mixture fraction computed from unstretched laminar premixed 1D flamelets of hydrogen air mixtures, dashed white line nominal mixture fraction value $z_{\text{nom}} = 0.011$, (—) stoichiometric condition $z_{\text{stoich}} = 0.028$. Conditional means of temperature versus mixture fraction at different progress variable values $\langle \tilde{T} | \tilde{z} \rangle_{\tilde{c}=c^*}$ are also reported as black lines.

ferential diffusion is modelled, consistently with findings in [338]. These occur due to hotter enriched samples coming from the outer flame branch attaching to the mixing tube rim, where the strain levels are the highest.

Further characterization of the reacting states is provided by Fig. 10.30, which shows the joint PDF of mixture fraction \tilde{z} versus progress variable \tilde{c} at a representative timestep. In the baseline case without DD modelling, the conditional average $\langle \tilde{z} | \tilde{c} \rangle$ (magenta solid line) roughly aligns with the nominal mixture fraction values, with some deviation as reaction progresses. The scatter in mixture fraction around the nominal value is solely caused by the imperfect fuel-air mixing described in the previous section. Differential diffusion induces mixture fraction values exceeding $z = 0.02$ and surpassing the stoichiometric threshold beginning around $c = 0.5$. Despite this increased scatter, the conditional average remains close to the nominal value, indicating that the majority of the sample population (i.e., high JPDF values) is not significantly altered. Most of the mixture fraction variations remain governed by turbulent mixing and initial stratification, while the contribution of differential diffusion and strain-induced redistribution remains secondary in the considered configuration. This differs from the fully premixed cases discussed in Chapters 7 and 8, where mixture fraction variations were entirely driven by differential diffusion, which thus played a dominant role even in the presence of turbulence.

To assess the direct influence of strain on mixture fraction variations, the average mixture fraction conditioned on progress variable is further analyzed at three different instantaneous tangential strain rate levels ($\bar{S}t = 10000, 20000, 30000 \text{ s}^{-1}$), shown as ma-

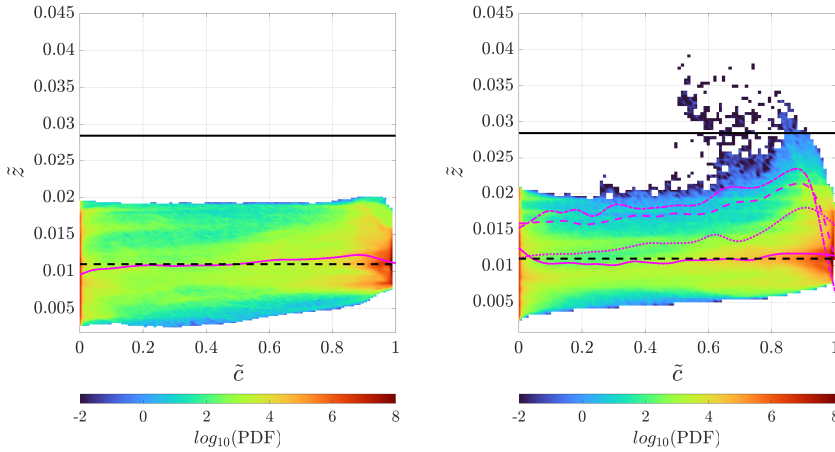


Figure 10.30: Joint probability density function (JPDF) of instantaneous mixture fraction versus progress variable from LES of the ultra-lean 100% H₂ case without differential diffusion modelling (left) and with differential diffusion modelling (right), corresponding to cases 100H2 and 100H2DD of Tab. 10.1, respectively. Lines: (----) nominal mixture fraction value $z = 0.011$, (—) conditional average of mixture fraction versus progress variable $\langle \tilde{z} | \tilde{c} \rangle$. Conditional means of mixture fraction versus progress variable at different tangential strain rate levels $\langle \tilde{z} | \tilde{c} \rangle_{\tilde{S}t = S_t^*}$ are also reported in the right panel: (.....) $\tilde{S}t = 10000 \text{ s}^{-1}$, (-.-.-) $\tilde{S}t = 10000 \text{ s}^{-1}$, (- - -) $\tilde{S}t = 30000 \text{ s}^{-1}$.

genta lines in different dash styles. A clear correlation emerges: higher strain levels result in increased peak mixture fractions, particularly at $c \approx 0.8$. When $c \rightarrow 1$, the conditional mixture fraction rapidly decreases and the trend is inverted: lower strain levels correspond to locally higher conditional mixture fraction values. These observed trends in mixture fraction distribution as a function of strain are consistent with laminar counterflow flamelet calculations at different strain rates, as reported in [39, 53, 351], and with results from turbulent premixed hydrogen flames [225].

The impact of differential diffusion modelling on NO formation is shown in Fig. 10.31, reporting average contour plots of nitric oxide mass fraction Y_{NO} and formation rate $\bar{\omega}_{\text{NO}}$. When differential diffusion is included, the peak NO mass fraction value increases from 2.5×10^{-7} to 6×10^{-7} at the flame base, which is due to the local enrichment produced by the positive flame-tangential strain rate. The higher amount of NO is then convected downstream and its concentration across the post-flame region of the outer flame branch increases with respect to the case without differential diffusion. Fig. 10.31 (right) shows high NO formation rates over a broader area in the outer branch, extending up to $y = 20 \text{ mm}$, when DD modelling is enabled. The inner branch is only mildly affected, with a slightly enhanced NO formation rate.

Instantaneous plots of NO mass fraction versus progress variable colored by the conditional mixture fraction value are reported in Fig. 10.32. In the baseline case (without differential diffusion), stratified regions near $z = 0.02$ produce most of the NO, peaking at 1.3×10^{-6} at $c = 0.95$. These rich products are recirculated in the CRZ (as seen in Fig. 10.31), resulting in NO values around 0.5×10^{-6} at low mixture fraction and progress

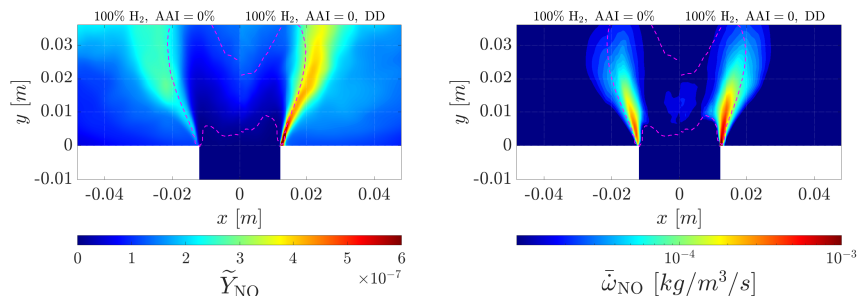


Figure 10.31: Midplane contour plots of mean NO mass fraction (left) and formation rate (right) from LES of the ultra-lean 100% H₂ case without differential diffusion modelling (left halves) and with differential diffusion modelling (right halves), corresponding to cases 100H2 and 100H2DD of Tab. 10.1, respectively. The mean turbulent flame brush is visualized by isoline of reaction rate at 2% of its maximum value (---).

variable. When differential diffusion is included, NO values exponentially increasing with progress variable are observed, due to the richer and hotter mixture at the flame base enabling NO formation via thermal pathway. The peak NO value at $c = 0.95$ rises to 8×10^{-6} , corresponding to near-stoichiometric samples ($z = 0.03$ orange points), matching the NO level for a premixed flamelet at stoichiometry (marked as a blue line). The amount of NO recirculated in the CRZ is also increased, leading to higher NO values at low progress variable and mixture fraction as compared to the baseline. At $c \rightarrow 1$, NO levels decrease, as mixing with leaner products reduces the final emission levels. The average NO mass fraction at $c = 1$ increases by 44 % compared to the baseline, highlighting the importance of including differential diffusion modelling for accurate emissions prediction. On the other hand, even the case without differential diffusion shows NO levels exceeding those predicted for a 1D flamelet at the nominal mixture fraction (dashed blue line), which further highlights the dominant role of stratification.

The \tilde{Y}_{NO} values conditioned over progress variable at different strain rate levels show consistent trends with what shown in Fig. 10.30: higher strain levels lead to higher NO peaks at $\tilde{c} = 0.9$ by inducing local enrichment. As $\tilde{c} \rightarrow 1$, high-strain cases exhibit a sharper drop in NO than low-strain ones, highlighting an effect of NO decreasing with strain at high progress variable, in line with recent studies on strained laminar premixed flamelets [253]. The unstrained conditional average (dashed black line) aligns closely with the global conditional average (solid magenta line), indicating that while differential diffusion and strain affect local NO production, their overall impact on total emissions is moderate.

The secondary role of differential diffusion and strain on global NO emissions is verified by examining the emissions data at the $y = 100$ m control plane, reported in

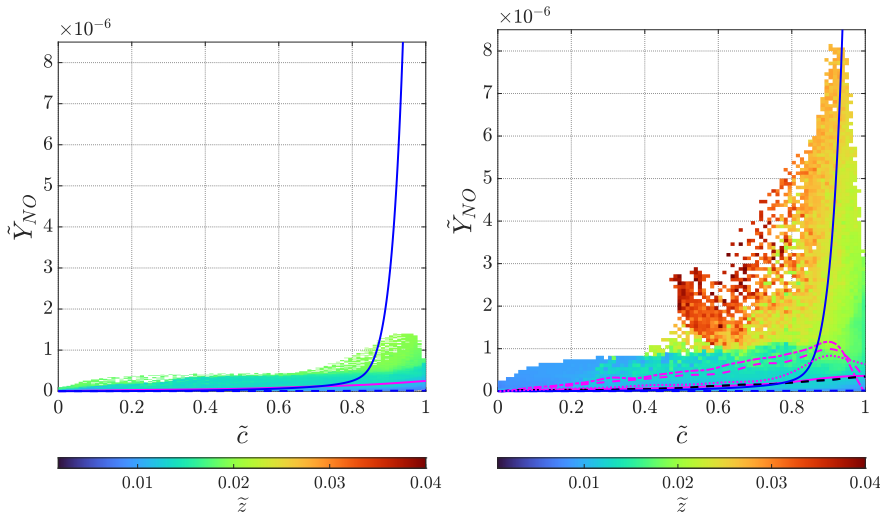


Figure 10.32: Scatter plots of instantaneous NO mass fraction versus progress variable, colored by conditional mixture fraction values from LES of the ultra-lean 100% H₂ case without differential diffusion modelling (left) and with differential diffusion modelling (right), corresponding to cases 100H2 and 100H2DD of Tab. 10.1, respectively. Lines: (—) conditional mean $\langle \tilde{Y}_{NO} | \tilde{z} \rangle$, Y_{NO} values along a reference premixed unstretched 1D flamelets at stoichiometry (—) and nominal equivalence ratio (· · · ·). Conditional means of \tilde{Y}_{NO} over progress variable at different tangential strain rate levels $\langle \tilde{Y}_{NO} | \tilde{z} \rangle_{\tilde{S}t=S_t^*}$ are also reported in the right panel: (· · · ·) $\tilde{S}t = 10000 \text{ s}^{-1}$, (· · · ·) $\tilde{S}t = 10000 \text{ s}^{-1}$, (—) $\tilde{S}t = 30000 \text{ s}^{-1}$.

Tab. 10.3. Enabling differential diffusion modelling results in 12% higher NO emissions (in volumetric ppm). In contrast, the application of 10% AAI, without differential diffusion, showed a 60% increase compared to the baseline ultra-lean 100% H₂ case without differential diffusion and 0% AAI (case 100H2 of Tab. 10.1), which confirms the dominant effect of turbulent mixing and stratification over enrichment caused by differential diffusion and strain. Although the absolute emission levels remain extremely low, and such variations may not significantly impact the overall combustor performance assessment, this analysis provides insight into the relative importance of mixture fraction variations driven by turbulent mixing versus those due to differential diffusion and strain, at the considered set point.

Overall, the results presented in this section highlight that differential diffusion effects are highly localized and primarily associated with regions of elevated strain rate, which require sufficient resolution to be accurately captured. In contrast to fully premixed lean flames, where differential diffusion, strain, and curvature are the main drivers of mixture fraction fluctuations and temperature peaks (see for example Chapters 7-4.3), the technically premixed configuration considered here shows a different behavior. In this case, the influence of differential diffusion on mixture fraction redistribution, flame structure, and emissions is secondary compared to the dominant role of turbulent mixing and fuel stratification in generating mixture fraction and temperature inhomogeneities, as well as NO emissions.

Similarly, thermodynamic instabilities were not observed, due to the mixture inho-

mogeneities controlled by turbulent mixing. Previous studies have reported thermodiffusive instabilities in fully premixed lean hydrogen swirl-stabilized flames [170, 226], which suggests that under conditions of more uniform premixing, differential diffusion effects must be carefully considered, as thermodiffusive instabilities can become a relevant in flame stabilization and structure.

The outer flame branch, which attaches to the rim of the mixing tube, remains the most critical region in terms of thermal loads, flashback risk, and emissions. This arises from the relatively high equivalence ratio caused by stratification, combined with additional local enrichment induced by strain and differential diffusion. Experimental observations for the present setup [68] revealed that increasing the hydrogen content in the fuel leads to reattachment of the outer flame branch, with the flame transitioning from a V-shape to an attached M-shape. In light of the LES results, the increased reaction rate under positive tangential strain at the mixing tube rim, due to the negative Markstein length of very lean hydrogen mixtures, plays a role in this stabilization mechanism, as also noted in [170, 352]. This effect is qualitatively captured by the employed differential diffusion model, through the prediction of induced local enrichment.

10.8. SUMMARY

The TU Delft swirl-stabilized combustor was numerically investigated using the in-house flamelet-based LES model with presumed FDF closure. A power setting of 12 kW and a swirl number of 1.1 were considered. The LES results were validated against available experimental data under both non-reacting and reacting conditions for a fuel mixture of 25% hydrogen and 75% methane, in volume. Very good agreement was observed in the non-reacting case, between the LES results and PIV measurements. However, the central recirculation zone (CRZ) strength and size were underpredicted, possibly due to subtle discrepancies between the simulated and actual swirler geometry. For the reacting case, an acceptable agreement was achieved in the flow field, capturing the flame's overall influence. While the flame shape and volume were qualitatively well predicted, the LES produced a fully attached M-flame burning strongly along the outer shear layer, whereas experiments showed flame quenching near the mixing tube rim and a lifted outer branch. The flamelet model was then used for the first time to investigate full hydrogen operation within the swirled combustor. A near-flashback set point was investigated, followed by a flashback-free operating point under ultra-lean conditions. This second case was used to assess the effects of 10% AAI addition and differential diffusion modelling on flame stability, structure, and emissions.

The main findings can be summarized as follows.

Mixing

In all investigated cases, 25% or 100% hydrogen, non-negligible fuel stratification was present. This resulted in a core of lean mixture (below the flammability limit) along the mixing tube centerline and a richer region at the mixing tube wall. Such stratification introduced significant scatter in composition, temperature, and emissions, with distinct burning characteristics between the inner and outer branches of the flame, which stabilizes in an M-shape. The richer region near the mixing tube wall presents risks for

flashback events, especially in 100% H₂ operations. The outer flame attachment point was also critical in terms of thermal loads and emissions. Mixing is affected by intrinsic PVC dynamics, studied for the 25% case, revealing a core precession at 233 Hz corresponding to a Strouhal number of 0.5. Due to stratification, the PVC induced periodic regions of higher and lower mixture fraction which cause flame oscillations and affect the thermal field. The addition of 10% AAI was observed to suppress PVC dynamics in the ultra lean 100% H₂ case. However, AAI enhanced stratification affecting temperature and emissions peaks.

Heat Losses

The results suggest that heat losses play a non-negligible role in flame stabilization, consistent with literature on swirl-stabilized combustors. Neglecting heat loss in simulations consistently led to the prediction of an attached M-flame, in contrast to the detached flame observed experimentally. This can contribute to the misprediction of the flow field and overestimations of temperature peaks and emissions in LES. Moreover, especially for highly reactive mixtures containing pure hydrogen, the inclusion of heat loss modelling may be discriminant between the prediction of stable flame operation and flashback. In the 100% H₂ fuel case, the LES predicts flashback when using adiabatic thermal boundary conditions at the walls, while a flame stabilizing at the mixing tube rim is obtained when imposing isothermal walls at $T_{\text{wall}} = 300$ K and modelling reaction rate reduction due to heat loss, in better agreement with experimental observations. However, the resulting flame displayed oscillations in its stabilization point upstream of the mixing tube exit and pressure fluctuations at 1000 Hz and 80 Hz. This behavior is physically plausible, but full comparison with experimental data remains limited without validated heat loss models and thermal boundary condition characterization.

Emissions

NO emissions were evaluated across all cases. For the baseline case with 25% hydrogen in the fuel blend (case 25H2 of Tab. 10.1), numerical results showed excellent agreement with experimental measurements. NO emissions were 20% lower than the theoretical equilibrium value from a 1D flamelet at the nominal equivalence ratio, likely due to lean combustion and NO reburning within the CRZ. Compared to experiments, LES slightly overpredicted NO ppm emissions, possibly due to mismatches in flame anchoring; the LES predicted a fully attached outer branch, burning richer than nominal conditions, whereas experiments showed heat loss quenching the attachment point, reducing NO formation. Fuel stratification was identified as a key contributor to NO emission scatter due to its effects on mixture composition and peak temperatures, which favor thermal NO formation.

Under ultra-lean 100% H₂ conditions at nominal equivalence ratio $\phi_{\text{nom}} = 0.34$, NO emissions dropped by two orders of magnitude compared to the baseline while retaining a stable flame, supporting the effectiveness of lean premixed combustion technology. This reduction was mainly due to the absence of prompt NO and, more significantly, the suppression of thermal NO as average maximum temperatures remained below 1600 K. Nevertheless, even in 100% H₂ cases, emissions remained highly sensitive to mixing. Due to stratification, NO emissions were 71% higher than the equilibrium value

at nominal equivalence ratio, computed from 1D premixed flamelets. Employing 10% AAI further increased fuel stratification, raising local temperatures (up to 1800 K) partly reintroducing thermal NO formation, and overall resulting in 60% higher computed NO emissions.

Differential Diffusion

The differential diffusion model accurately captured the interaction between flame tangential strain rate and differential diffusion. An average strain rate of approximately $1 \times 10^4 \text{ s}^{-1}$ was found at the flame base in correspondence to the injector rim, while only $0.4 \times 10^4 \text{ s}^{-1}$ was present in the CRZ. AAI was found to lower the strain levels. The combined effect of differential diffusion and strain produces an enriching effect at the mixing tube rim resulting in 20% higher instantaneous peak temperatures and overall 12% global NO emissions. These results suggest that under current conditions, differential diffusion effects are secondary to turbulent mixing, which dominates mixture fraction scatter, temperature peaks, and emissions. However, accurate modeling of differential diffusion remains essential in view of developments towards better premixed scenarios, where strain and the possible onset of thermodiffusive instabilities can significantly influence flame speed, temperature and flashback propensity [226, 227].

11

CONCLUSIONS AND FUTURE WORK

11.1. SUMMARY AND CONCLUSIONS

Nowadays, most of the power generation worldwide relies on fossil fuel combustion. Developing more sustainable combustion technology is essential for a non-disruptive energy transition to renewable sources, by allowing the continued use of existing infrastructure (such as stationary gas turbine power plants), and decarbonizing hard-to-abate sectors like heavy-duty furnaces and aeronautics. Hydrogen is a promising alternative energy carrier due to its high energy density, carbon-free combustion, and potential for production from renewable energy. Developing robust and cost-effective Large Eddy Simulation (LES) models for hydrogen combustion is a fundamental step towards designing novel efficient, safe and sustainable combustion systems. Among the available LES combustion models, flamelets-based approaches are very robust and cost effective, and have been proven to provide accurate results in the analysis of hydrocarbons flames. However, their extension to hydrogen combustion is still at an early stage, primarily due to the need to properly model differential diffusion effects within the flamelet framework, where the detailed transport of the set of chemical species is reduced to the transport of a low number of controlling variables.

During the course of the present research, the combustion community has made substantial progress in providing new experimental and numerical data for the study of hydrogen combustion. At the beginning of the work, a limited number of reference laboratory turbulent premixed hydrogen flames were available. Since then, major efforts have been directed towards the development of turbulent hydrogen combustors, both for validating numerical tools and for enabling practical applications. This has often involved transitioning from CH_4 -fueled systems to H_2/CH_4 blends, and designing new burners equipped with flashback prevention systems.

On the numerical side, an increasing number of simulations detailed chemistry started to be performed to study of the physics of laminar premixed hydrogen flames, particularly focusing on thermodiffusive instabilities and response to stretch. Moreover, increasing DNS data have become available in literature, with the specific aim of clarifying

the role of differential diffusion in premixed hydrogen flames under turbulent conditions and of supporting the development of predictive LES models for design purposes. In parallel, new model formulations to account for differential diffusion in flamelet-based approaches have been proposed for laminar cases. Their first applications within LES are now being explored and the work within the present thesis represents one of the earliest attempts.

The present research work took place within this rapidly evolving field and contributed along two main directions:

- **Part I:** Development and testing of LES flamelet models for hydrogen combustion. The thesis presents one of the first attempts to incorporate differential diffusion effects into flamelet-based LES models. These models were applied to a range of configurations, including partially premixed, fully premixed, and strained premixed hydrogen flames, demonstrating their potential and limitations.
- **Part II:** Contribution to experimental combustor development. The research also supported the design and characterization of a laboratory-scale, fuel-flexible hydrogen burner. The burner was tested across the full transition from CH₄ to pure H₂, and LES analyses provided new insights into mixing, combustion and emissions features, some of which were not immediately accessible through experiments alone. This setup further enabled the investigation of differential diffusion effects under practically relevant conditions.

A detailed summary and overview of the new findings is presented next for the various chapters of the present thesis.

PART I: DEVELOPMENT OF FLAMELET MODELS FOR TURBULENT HYDROGEN COMBUSTION

At the beginning of the present research one of the few well-documented laboratory scale test cases for hydrogen combustion was the partially premixed lifted hydrogen flame in a hot coflow [77], which provided extensive experimental measurements and was therefore selected as the initial test case for the present study. This test case features a wide range of physical phenomena, including lifted flame aerodynamic stabilization, turbulent mixing of fuel with hot oxidizer and partially premixed combustion mode. The initial analysis, presented in Chap. 5, employs Large Eddy Simulations (LES) using a transported filtered density function closure via Eulerian Stochastic Fields (ESF) with fully detailed chemistry (FC-ESF). This approach minimizes modeling assumptions and allowed for an in-depth investigation of flame stabilization mechanisms. The FC-ESF model shows excellent agreement with experimental measurements in terms of velocity, mixture fraction, major species, and temperature. Both the flame lift-off height and overall flame length are well captured, although a slight underprediction of the lift-off height is noted, highlighting the sensitivity of flame stabilization to inlet turbulence, as further discussed in Appendix B. The analysis provides insight into the stabilization mechanism, controlled by local velocity and turbulent fuel/air mixing. The analysis of the Takeno index reveals that the flame base anchors in a lean premixed mode, while downstream, a richer premixed core is observed, with excess fuel burning in partially premixed mode

with the abundant oxydizer in the coflow. A recently proposed hybrid approach combining flamelet-based thermochemical tabulation (flamelet generated manifold FGM) with ESF-based subgrid closure (FGM-ESF) is tested on the lifted hydrogen flame. Despite relying on premixed flamelet chemistry, the hybrid FGM-ESF approach closely replicates the results obtained with the fully detailed chemistry model, with correct prediction of temperature and major species in agreement with experiments. The model well captures the stabilization mechanism and flame index distribution. However, some discrepancies are observed in the prediction of intermediate species, particularly OH, which is more sensitive than temperature and major species to chemistry modelling and flame stabilization location. Further investigation of the instantaneous burning states reveals that the FGM-ESF model tends to overpredict reaction rates in the rich flame core and near-stoichiometric regions, as compared to fully detailed chemistry. It is shown by *a-posteriori* analysis that a corrective factor for the progress variable reaction rate, accounting for the use of a scaled progress variable and the dependence of the scaling term on mixture fraction in partially premixed combustion, restores the correct burning state. This is therefore adopted in the subsequent applications of flamelets-based LES with scaled progress variables, ensuring consistency in partially premixed conditions even when the thermochemical database is based solely on premixed flamelets.

Chapter. 6 focuses on the development of a flamelet-based model combined with a presumed filtered density function (FDF), which increases modeling assumptions with respect to the FGM-ESF model tested in Chap. 5, but significantly reduces computational cost. This part of the study addresses the closure of the subgrid-scale (SGS) progress variable variance, controlling the shape of the presumed FDF and influencing the filtered reaction rate. The investigation regards the parameter β_c , appearing at the denominator of the subgrid scalar dissipation rate (SDR) of the progress variable, a sink term in its SGS variance transport equation. This parameter needs fine tuning or can be estimated using a dynamic procedure based on the scale similarity assumption. A novel test-filtering method using a Fourier-like differential equation is proposed, and results are compared to those obtained using the standard algebraic filtering approach, explicitly evaluating a Gaussian filter shape. Results on the hydrogen partially premixed flame, previously investigated in Chap. 5, show that when turbulence intensity is sufficiently high and the LES is well-resolved on a block-structured mesh, both the algebraic and differential filters predict similar reacting flow fields. Predictions are in very good agreement with experimental data, confirming the accuracy of the dynamic model. However, on unstructured meshes, the non-orthogonality can introduce numerical noise in the evaluation of filter coefficients with the algebraic approach. In such cases, using the algebraic test-filter leads to an underprediction of the flame lift-off height. This is attributed to an underestimation of the modeling constant β_c , resulting in reduced SGS variance and increased reaction rates. In contrast, the differential filter successfully recovers the correct flame position. To further assess the robustness of the dynamic approach, a methane bluff-body flame at lower turbulence intensity is analyzed under perfectly premixed conditions. The algebraic test filter is observed to produce a bimodal distribution of β_c across its imposed bounds, leading to underpredicted SGS variance and a flame with overly laminar characteristics. Meanwhile, the differential test-filter provides a more meaningful distribution of β_c , resulting in a wrinkled flame structure

that better matches experimental observations. These findings suggest that the proposed differential test-filter is more versatile than its algebraic counterpart, capable of handling a wider range of mesh types and turbulence intensities with only a marginal increase in computational cost. As a result, the dynamic SGS model with the differential filter is adopted for subsequent LES analyses.

In Chapter 7 the flamelets-based LES model with presumed FDF is further developed focusing on the implementation of models for differential diffusion. A turbulent fully premixed hydrogen flame in a slot burner configuration under thermo-diffusively unstable conditions is analyzed first, to isolate the effects of differential diffusion. Two models accounting for differential diffusion at the resolved level are compared: one applies corrections to the mixture fraction equation only, while the other applies corrections to the mixture fraction, progress variable, and enthalpy equations. Results show that both models can capture the coupling between flame curvature and mixture fraction redistribution, leading to flame self-wrinkling and super-adiabatic temperatures. Despite the differences in formulation and implementation, both models predict similar magnitudes of super-adiabatic temperature peaks and broadening of the mixture fraction range. This suggests that, for fully premixed flames at low strain levels and without enthalpy variations beyond the ones caused by differential diffusion, correcting only the mixture fraction field may be sufficient. Effects of differential diffusion are then investigated on the partially premixed lifted hydrogen flame in vitiated coflow, analysed in the previous chapters, as it is characterized by features closer to real combustor applications. Results indicate that first and second order statistics of temperature and mixture fraction are already predicted in very good agreement with experimental measurements even without accounting for differential diffusion, either at the resolved or thermochemical level. This is because turbulent mixing ahead of the stabilization point dominates, causing more significant variations in the mixture fraction field than the ones caused by differential diffusion effects. Moreover, the flame burns in partially premixed mode over the entire flammability range, while differential diffusion effects are typically relevant at lean premixed conditions. Including differential diffusion only at thermochemical level does not affect this mixing, but results in an overall reduction of the reaction rate and a consequent reduction of the temperature gradients. When the correction on the mixture fraction diffusion is included at the resolved level, the jet/coflow inert mixing appears mildly enhanced and an increase in the reaction rate at the flame base and temperature gradients is observed. When corrections are also applied to the progress variable diffusion at the resolved level, the increased flux from products to reactants shifts the flame stabilization point upstream compared to the other tested models.

The differential diffusion model correcting for each controlling variable and enthalpy is selected for further testing and analysis, as described in Chap. 8. It is tested under fully premixed conditions on a bluff body stabilized flame to isolate and investigate the coupling effect between differential diffusion and flame tangential strain. Also in this case, the baseline flamelet LES (without differential diffusion) models shows very accurate results, in the comparison of velocity and reaction rate with PIV and OH^* chemiluminescence experimental data. The differential diffusion model successfully predicts the local redistribution of mixture fraction in regions of high flame tangential strain rate near the bluff body base. This redistribution causes a shift in the reaction source term

peak towards the flame anchoring point, producing a shorter flame, compared to the unity Lewis number case and improving agreement with experiments. Interestingly, the model captured the increase in reaction rate caused by positive strain (as an effect of the negative Markstein length) by the sole use of unstretched flamelets for the thermochemistry database. These findings demonstrate that in the LES context an unstretched flamelet database is effective in mimicking the peculiar physics of lean premixed hydrogen flames that exhibit coupling between strain, curvature and differential diffusion, at least at the investigated conditions, characterized by relatively moderate stretch levels. This requires most of the strain and curvature to be resolved and the use of an appropriate correction for mixture fraction diffusive flux.

In summary, the studies presented in Part I of this thesis demonstrate the robustness and accuracy of LES models based on premixed flamelets for the simulation of hydrogen flames across different turbulence conditions, in both premixed and partially premixed modes.

The key findings can be summarized as follows:

- **Hybrid FGM-ESF approach:** Despite relying on premixed flamelet tabulation, the developed hybrid model accurately reproduces the results of the detailed chemistry approach for a partially premixed hydrogen flame, both in terms of flame stabilization mechanisms and major species concentrations. This confirms the robustness of flamelet-based approaches for turbulent hydrogen combustion and their promising predictive capability in conjunction with FDF closures.
- **Dynamic SGS variance modeling:** A novel strategy based on a differential test filter is developed for the dynamic evaluation of the β_c parameter to model the sub-grid scalar dissipation rate of the progress variable. The approach is shown to be more robust and versatile than the algebraic test filter, particularly on unstructured meshes and across different turbulence regimes.
- **Effects of differential diffusion:**
 - In highly turbulent, partially premixed hydrogen flames burning across the full flammability range, turbulent air-fuel mixing dominates, making explicit modelling of differential diffusion within LES only marginally relevant for predicting the main flame features.
 - In lean premixed hydrogen flames, differential diffusion significantly affects the flame structure even under the investigated turbulence conditions. Dedicated modeling describing the coupling between differential diffusion and stretch (strain and curvature) is therefore essential to capture the relevant flame features.
- **Differential diffusion modelling:**

- The two models correcting for the resolved diffusive flux of the controlling variables, extended to the LES context, effectively capture differential diffusion effects in turbulent premixed hydrogen flames, including thermodiffusive instabilities and superadiabatic temperature peaks.
- The models correctly reproduced the increased reaction rate in response to positive tangential strain (associated with negative Markstein length), by capturing the local mixture enrichment.
- In fully premixed turbulent hydrogen flames, correcting only the mixture fraction diffusive flux yielded results equivalent to correcting for mixture fraction, progress variable, and enthalpy. Nevertheless, further development of a model correcting for all variables enables the inclusion of a wider range of thermochemical states in the database, for example those arising from combined effects of differential diffusion, strain, and heat losses.

PART II: LES STUDY OF A SWIRL-STABILIZED COMBUSTOR

The second part of the present dissertation focuses on the analysis of a laboratory scale swirl-stabilized lean technically premixed combustor, a low technology readiness level (TRL) representation of a fuel-flexible combustion chamber for aeronautical applications.

In Chapter 9, the mixing features of fuel injection as jet in swirling cross-flow configuration in the TU Delft combustor are analyzed in non-reacting conditions. Large Eddy Simulations (LES), solving species transport equations, are employed to study the mixing process numerically. These simulations complemented the experimental work presented in [319], which utilized Mie scattering with a seeded fuel stream to visualize the mixing process and applied particle counting techniques to quantify mixing quality. The study examined how fuel composition, specifically CH_4/H_2 blends, affects fuel-air mixing. In the experiments, helium/air mixtures were used as surrogates for CH_4/H_2 blends to represent different hydrogen concentrations in the fuel stream. LES results validate this experimental methodology, confirming helium as a reliable surrogate for hydrogen in assessing macroscopic mixing behavior in the considered set-up, provided the momentum flux ratio between the fuel and swirling air streams is maintained constant. For CH_4/H_2 blends, the higher diffusivity of H_2 leads to hydrogen enrichment near the mixing tube wall, especially close to the inlet of the combustion chamber. This localized enrichment may be critical for the risk of boundary layer flashback. On the other hand, for a constant momentum flux ratio, fuels with lower density (i.e., higher hydrogen or helium content) result in more effective mixing. Convection tends to promote stratification near the mixing tube exit, close the central recirculation zone, as fuel is pushed towards the mixing tube wall. However, molecular diffusion acts across the windward and leeward shear layers between the fuel jet and the swirling cross flow, redistributing fuel towards the centerline and enhancing radial mixing throughout the streamwise direction. Due to their lower density and higher diffusivity, both hydrogen and helium exhibit reduced downstream stratification compared to methane, contributing to more homogeneous fuel-air mixtures.

The flamelets-based LES model with presumed FDF developed in Part I is applied to analyse the TUDelft swirl-stabilized combustor under reacting conditions, as described

in Chap. 10. Validation against a 25% hydrogen–75% methane case shows good agreement with experimental velocity fields and qualitatively accurate flame structures. While LES predicts a fully attached M-flame burning along the outer shear layer, experiments showed flame quenching near the mixing tube rim and a lifted outer flame branch. The model is then used to study 100% hydrogen operation, exploring both a near-flashback condition and a stable set point without flashback. The latter serves to assess flame stability, structure, and emissions at ultra-lean conditions, focusing on the effects of axial air injection. Moreover, this set point offers the possibility to investigate the effects of differential diffusion modelling within a practical technically premixed hydrogen combustor. The results highlight the significance of imperfect mixing. Both cases with 25% and 100% hydrogen (in volume) in the fuel blend exhibit fuel stratification, as anticipated in the non-reacting studies. This stratification results in a very lean inner branch and richer outer branch, representing a critical point for boundary layer flashback, especially in 100% H₂ operations. Precessing vortex core (PVC) dynamics are found to produce periodic modulations in the mixture fraction field resulting in flame oscillations. In ultra-lean 100% hydrogen operation, 10% AAI suppresses PVC dynamics and stabilizes the flame, but at the cost of increased stratification and NO emissions. Heat losses are observed to substantially affect flame stabilization. Simulations without heat loss modelling consistently predict an attached M-flame, while a detached flame was observed experimentally. This discrepancy can lead to mispredictions in the flow field and overpredicted temperatures. In the pure hydrogen fuel case, heat loss modelling discriminates between the prediction of stable operation or flashback, which also highlights the role of non-adiabatic walls on flame stabilization mechanism within the experimental setup. The LES model captures NO emissions accurately for the 25% hydrogen case, in comparison with experimental measurements, showing peak NO formation at the injector rim due to locally richer conditions. For the ultra-lean 100% hydrogen case ($\phi_{\text{nom}} = 0.34$), NO emissions dropped by two orders of magnitude due to suppressed thermal NO and lack of prompt NO, supporting the effectiveness of ultra-lean hydrogen combustion in the present set-up. However, NO remains sensitive to composition inhomogeneity, and the use of AAI, induces further fuel stratification, which contributes to increased emissions. Differential diffusion effects, although less dominant than turbulent mixing, influence local flame behavior. High tangential strain rates at the injector rim, combined with differential diffusion, enrich the local mixture, increasing peak temperatures and NO by 12% compared to the case where differential diffusion modelling is not included. Compared to the turbulent partially premixed flames explored in part I, however, effects are non-negligible, as overall this combustor operates at globally lean premixed, although stratified conditions. Differential diffusion modelling remains therefore necessary in the development of lean perfectly premixed hydrogen combustion, as strain and possible thermodiffusive instabilities can increase consumption speed and flashback propensity, together with temperature peaks, and emissions as anticipated in other studies in literature [226, 227].

In summary, the LES flamelet model provides detailed insight into the combustion physics of the TUDelft swirl-stabilized burner. Despite some mispredictions, the LES analysis helps to clarify the relevant combustion mechanisms, complement experimental data, and guide technological improvements.

The key findings from Part II can be summarized as follows:

- **Mixing:**

- LES simulations show that imperfect premixing occurs in the analysed setup for both non-reacting and reacting conditions. This was confirmed by parallel experimental work on non-reacting cases [319]. The analysis also validates helium/air mixtures as reliable surrogates for CH_4/H_2 blends in non-reacting experimental studies, provided that the fuel–air momentum flux ratio is maintained constant.
- Fuel stratification is observed at all the investigated hydrogen concentrations in the fuel blend (0%, 40%, 100% in non-reacting cases; 25% and 100% in reacting cases). Due to the fuel injection in swirled crossflow configuration, the fuel tends to remain confined near the premixing tube walls at the studied injection momentum value. Non-reacting studies indicate that higher H_2 content reduces stratification due to its lower density (less outwards radial convection at the mixing tube exit upstream of the CRZ) and higher diffusivity.
- Mixture inhomogeneity directly affects flame structure and leads to scatter in composition, temperature, and emissions. The flame takes an M-shape, with the outer branch burning richer than nominal conditions and the inner flame branch burning leaner. This makes the flame branch attaching to the injector rim particularly critical for flashback risk (especially in the pure H_2 case), for thermal loads, and for NO emissions, particularly under ultra-lean hydrogen conditions.

- **Heat losses:**

- Heat losses significantly influence flame stabilization. Neglecting them leads to fully attached M-flames instead of the detached V-flames observed experimentally. In the nominal case with 100% H_2 , excluding or including heat losses distinguishes between predicting flashback or a more stable flame attaching to the injector rim, in better agreement with experiments. This indicates that, under conditions close to flashback, the relatively low temperature of injector components prevents flashback in the experimental setup.

- **Emissions:**

- For the case with 25% H_2 in the fuel blend, LES predictions match measured NO emissions, confirming the adequacy of the implemented NO model for the analysed globally lean regime. Fuel stratification is identified as the main driver of scatter in NO concentration as it alters mixture fraction distribution and peak temperatures. In each investigated case, most NO is produced at the flame base, in the outer branch attached to the injector rim. In the case using 25% H_2 , mixture inhomogeneities mainly cause local variations in NO

formation, while they do not affect global emission levels which remain close to equilibrium values corresponding to a premixed flamelet at the nominal operating equivalence ratio.

- In the ultra-lean case, using 100% H₂ at $\phi_{nom} = 0.34$ decreases NO emissions by two orders of magnitude compared to the case with 25% H₂ in the fuel blend, due to suppressed thermal NO (temperatures < 1600 K) and absent prompt NO. This demonstrates the potential of the TUDelft combustor of leveraging the wide flammability range of hydrogen to achieve stable lean flames with ultra-low NO emissions.
- At ultra-lean conditions with 100% H₂, the very low NO emission levels remain sensitive to mixture inhomogeneity. Unlike the 25% H₂ case, stratification causes NO to exceed the equilibrium value corresponding to the nominal equivalence ratio by 71%, due to richer zones at the flame base. Adding 10% AAI further increases stratification and local temperatures (~1800 K), reintroducing thermal NO and increasing emissions by 60% compared to the case without AAI. This highlights that improved mixing can further reduce emissions even at already low-NO levels achieved with ultra lean combustion.

- **Differential Diffusion (DD):**

- The DD model, correcting for diffusive fluxes of the controlling variables and enthalpy, captures the interactions between flame-tangential strain rate and differential diffusion. The LES shows maximum positive average and instantaneous strain rates at the injector rim and milder levels close to the stagnation point in the CRZ. Axial air injection is observed to reduce strain levels.
- At the mixing tube rim, the combined effects of strain and DD enriches the local mixture and increase peak temperatures by 20%. Compared to cases without DD modelling, global NO emissions increase by 12%. The flame branch within the CRZ is unaffected, due to local mixture inhomogeneity (close to or below the lean flammability limit) and high turbulence levels.
- Under the present turbulent, stratified conditions, DD effects are secondary to turbulent mixing regarding peak temperatures and emissions. However, accurate DD modelling remains important for more premixed cases, where thermodiffusive instabilities, well documented in literature for lean premixed swirled combustors operating with hydrogen [226, 227], can significantly affect flame speed, temperature, and flashback propensity.

11.2. FINAL CONSIDERATIONS, FUTURE WORK AND RECOMMENDATIONS

Based on the findings of this research, recommendations are provided for future studies in hydrogen combustion physics and LES modeling. In addition, final considerations are drawn regarding the current experimental setup, its potential for technological development, and guidelines for future experimental investigations.

Hydrogen combustion physics and LES modeling:

- The necessity of subgrid-scale models for thermodiffusive (TD) instabilities is to be further investigated, starting from DNS analysis. Currently, flame self-wrinkling and flame surface generation due to TD instabilities can only be captured at the resolved scale. However, thermodiffusive instabilities originating at sub-filter scales may necessitate SGS models to account for unresolved flame surface generation. Similarly, the effect of unresolved flame tangential strain rate should be examined. Small-scale turbulent eddies, despite their short lifespans, can induce high strain rates [56], potentially enriching the mixture and enhancing reaction rates at scales below the LES filter width. A suitable SGS model might be needed to account for this contribution.
- The studies in Chapter 8 showed that resolved strain and differential diffusion effects could be qualitatively captured by correcting the diffusive fluxes of controlling variables and using an unstretched flamelet manifold. Further investigations should evaluate the quantitative accuracy of this approach, and define the strain rate regimes where it remains valid. The potential benefits of incorporating strain rate as a parameter in the manifold and identifying an appropriate controlling variable should also be explored.
- The differential diffusion models used in this work were originally developed for premixed flames with limited mixture fraction variation near the flammability limits. However, the present analysis suggests that in partially premixed regimes, where the mixture fraction spans the entire flammability range, an extended treatment may be necessary. This could involve introducing two mixture fraction parameters: one for fuel-air mixing and another to capture differential diffusion effects (e.g., flame index approach [225]).
- The heat loss modelling presented in Chapter 10 needs further validation. Future work may consider a five-dimensional manifold using an enthalpy-based controlling variable to account for heat loss [135]. This would allow a more accurate representation of thermochemical states under enthalpy defect, particularly under the joint effect of differential diffusion and heat loss. Due to the increased manifold dimensionality, implementation challenges such as memory management and interpolation strategies will need to be addressed.
- The implemented NO modeling strategy would also benefit from refinement and validation. In particular, redefining a progress variable for NO reactions may be necessary to better capture NO formation in stratified flames near stoichiometric conditions. In such regimes, where NO kinetics are significantly slower than the main reaction progress, the progress variable based on major product species may no longer provide an adequate description, as NO keeps forming after the main reaction reaches equilibrium. Approaches employing a different progress variable for NO chemistry or modifying the main one may be explored.
- Recent DNS studies have explored the range of turbulence levels (Karlovitz numbers) at which thermodiffusive instabilities remain relevant in lean hydrogen pre-

mixed flames [61, 168]. Similar DNS studies can be extended to examine the combined effects of strain and turbulence, as well as the interplay between mean and instantaneous strain, thermodiffusive instabilities, and turbulence [353]. Such investigations would contribute to a more comprehensive understanding of turbulent hydrogen combustion physics and support the development of specific LES models.

- The investigation of hydrogen combustion physics has so far focused primarily on atmospheric conditions. Recent literature [158] indicates that high pressure amplifies thermodiffusive instabilities in turbulent lean hydrogen flames, resulting in thinner, faster, and more wrinkled flame fronts. This can have significant implications for LES, particularly concerning grid resolution, subgrid-scale modelling, and the role of differential diffusion under turbulence. A deeper understanding of these mechanisms is essential for developing reliable LES models and supporting hydrogen-based combustor design under gas turbine-relevant conditions
- Recent studies [354] suggest that curvature-induced thermodiffusive instabilities have only localized effects on NO emissions and do not substantially influence global emissions. In contrast, laminar flame simulations [253] show that the combined effects of strain and differential diffusion can suppress NO formation. DNS investigations [353] report similar trends for highly strained turbulent flames, where bulk strain significantly affects NO production, while local curvature and strain fluctuations have a negligible impact. Further investigation and understanding of these phenomena are important for advancing low-NOx hydrogen combustion and for the refinement of LES models.

Considerations for technological development :

- The LES study in Chap. 10 proved the promising application of ultra-lean hydrogen premixed combustion to leverage its wide flammability limit and achieve significantly low NO emissions. It is advised to extend the experimental campaigns towards ultra-lean conditions in order to confirm experimentally the flame stability, the low NO emission levels and the effect of axial air injection. This will also allow further validation of the LES model.
- Further developments to improve mixing are advised in order to lower peak temperatures and NO emissions, especially in the ultra lean case with pure hydrogen, and reducing the risk of boundary layer flashback. In general, the development of strategies to achieve even quicker mixing will allow to reduce the size of premixing section and reduce the volume of flammable mixture in the injection components, less critical for flashback. Strategies such as axial fuel injection or adjustable cross-flow momentum (as discussed in [319]) can be considered. However, careful assessment is advised, more uniform premixing in the case with pure hydrogen may also lead to more relevant differential diffusion effects in the use of pure hydrogen fuel, increasing flashback risk due to coupling with flame strain or promoting thermodiffusive instabilities.

- Accurate experimental characterization of thermal boundary conditions is essential for the correct prediction of flame stabilization and flashback and for validating heat loss modeling approaches. Flashback requires continued attention, especially with the case with 100% H₂. While a stable flame was observed in experimental campaigns [68], further investigation is needed to assess if a temperature increase in the injection components would result in flashback or if the flame stabilizes at the injector rim with periodic upstream propagation (intermittent flashback).
- For the investigated conditions the current geometry results in significantly low flow velocities within the combustion chamber. The resulting high residence times lead to elevated NO levels, as observed both numerically and experimentally: in each investigated case, the equilibrium NO value for the nominal equivalence ratio was reached or exceeded. Moreover, the numerical analysis highlighted the large separation in characteristic timescales between the injector and the various regions in the combustion chamber, which leads to a non-optimal use of computational resources in LES. For the current injector size and airflow rate, reducing the combustion chamber length to reduce the overall flow-through time would simplify LES simulations and improve comparability between experimental and numerical results. Similarly, increasing the confinement ratio (e.g., by reducing the chamber diameter) would shorten residence times in the outer recirculation zone (ORZ), lowering heat losses at the wall and reducing the timescale separation between the jet (and CRZ) and the ORZ. This would allow simulation times long enough for a detailed description of the effects of the ORZ on the jet development. Alternatively, a larger injector operating at higher mass flow rates and power levels could be explored. In the pure hydrogen case, where high flashback propensity was observed, increasing the air mass flow rate within the swirling flow would result in lower flashback risk. This was partly investigated in the LES by increasing the air mass flow rate, which, however, had the dual effect of increasing momentum and decreasing the equivalence ratio.
- The LES study confirmed the presence of intrinsic hydrodynamic instability (i.e., PVC), high flashback propensity and potential intermittent flashback. Given this, an alternative strategy such as micromixing, specifically targeting the combustion properties of hydrogen, could be beneficial, since flashback is intrinsically impeded and thermoacoustic instabilities can be dampened. However, this approach requires dedicated studies on wall effects and heat losses, and its application is limited to gaseous fuels, complicating kerosene integration. Other concepts, such as lean direct injection (LDI) or rich–quick quench–lean burning (RQL), already investigated for kerosene, present significant drawbacks with hydrogen. LDI is intrinsically flashback-free, but the extremely high reactivity of hydrogen can result in attached flames stabilizing at stoichiometric or rich conditions. Similarly, the high reactivity of hydrogen and its resistance to heat loss (cooling) are expected to make quenching in the RQL concept highly challenging, again leading to locally stoichiometric combustion with unacceptable NO levels and thermal loads.

Among these options, it was demonstrated within the TU Delft combustor that

lean premixed combustion with swirl stabilization remains a promising strategy. Fuel flexibility with hydrogen/methane blends has been proven both numerically and experimentally, while numerical studies confirmed stable, ultra-lean operation with very low NO emissions. Hydrodynamic instabilities can be mitigated through axial air injection (AAI), and flashback risks minimized by optimizing mixing, controlling the axial momentum of the reacting mixtures (by controlling air mass flow rate and with AAI), and operating ultra-lean. Unlike LDI or RQL, this strategy allows precise control over the global equivalence ratio (provided fine tuning of fuel injection and AAI), consistently avoiding stoichiometric or rich conditions. Moreover, future integration of kerosene, extending multi-fuel flexibility, appears feasible [27]. The findings of this research, including detailed characterization of velocity fields, residence times, mixing features, and stratification effects in the mixing tube, provide valuable insights for the future design of kerosene injection strategies, enabling optimal mixing and stable operation.

BIBLIOGRAPHY

1. Copernicus Climate Change Service (C3S). *European State of the Climate 2024* <https://climate.copernicus.eu/esotc/2024>. Accessed: 2025-04-23. 2024.
2. NOAA (National Oceanic and Atmospheric Administration). *The NOAA Annual Greenhouse Gas Index (AGGI)* <https://gml.noaa.gov/aggi/aggi.html>. Accessed: 2024-11-01. 2024.
3. IPCC. in *Climate Change 2022: Mitigation of Climate Change. Contribution of Working Group III to the Sixth Assessment Report of the Intergovernmental Panel on Climate Change* (Cambridge University Press, Cambridge, UK and New York, NY, USA, 2022).
4. Noon, M. L. *et al.* Mapping the irrecoverable carbon in Earth's ecosystems. *Nature Sustainability* **5**, 37–46 (2022).
5. United Nations. *Adoption of the Paris Agreement* Conference Document. Conference of Parties, Twenty-first session, Paris, FCCC/CP/2015/L.9/Rev.1, 30 November to 11 December 2015. 2015.
6. European Parliament and Council. *Directive 2014/94/EU of 22 October 2014 on the deployment of alternative fuels infrastructure (Text with EEA relevance)* 2014.
7. Parliament, E. & Council. *Regulation (EU) 2021/1119 of the European Parliament and of the Council of 30 June 2021 establishing the framework for achieving climate neutrality and amending Regulations (EC) No 401/2009 and (EU) 2018/1999 (European Climate Law)* Legal status: In force. 2021.
8. Eurostat. *Energy Statistics – An Overview* https://ec.europa.eu/eurostat/statistics-explained/index.php?title=Energy_statistics_-_an_overview. Accessed: 2025-04-23. 2024.
9. International Energy Agency. *Global Energy Review 2025* <https://www.iea.org/reports/global-energy-review-2025>. Accessed: 2025-04-23. Mar. 2025.
10. Dreizler, A., Pitsch, H., Scherer, V., Schulz, C. & Janicka, J. The role of combustion science and technology in low and zero impact energy transformation processes. *Applications in Energy and Combustion Science* **7**, 100040 (2021).
11. Masri, A. R. Challenges for turbulent combustion. *Proc. Combust. Inst.* **38**, 121–155 (2021).
12. International Energy Agency. *Aviation* <https://www.iea.org/energy-system/transport/aviation>. Accessed: 2025-04-23. 2025.
13. Bergero, C. *et al.* Pathways to net-zero emissions from aviation. *Nature Sustainability* **6**, 404–414 (2023).

14. International Civil Aviation Organization. *ICAO Environmental Report 2022* <https://www.icao.int/environmental-protection/Pages/envrep2022.aspx>. Accessed: 2025-04-23. 2022.
15. International Civil Aviation Organization. *Climate Change Mitigation: CORSIA* <https://www.icao.int/CORSIA>. Accessed: 2025-04-23. 2019.
16. European Union Aviation Safety Agency. *European Aviation Environmental Report 2022* <https://www.easa.europa.eu/en/domains/environment/eaer>. Accessed: 2025-04-23. 2022.
17. Airbus. *Hybrid and Electric Flight* <https://www.airbus.com/en/innovation/energy-transition/hybrid-and-electric-flight>. Accessed: 2025-04-23. 2024.
18. International Air Transport Association. *Aircraft Technology Net Zero Roadmap* <https://www.iata.org/en/programs/sustainability/flynetzero/roadmaps/>. Accessed: 2025-04-23. 2023.
19. International Energy Agency. *ETP Clean Energy Technology Guide* <https://www.iea.org/data-and-statistics/data-tools/etp-clean-energy-technology-guide>. Accessed: 2025-04-23. 2025.
20. European Parliament and Council. *Regulation (EU) 2023/2405 of the European Parliament and of the Council of 18 October 2023 on ensuring a level playing field for sustainable air transport (ReFuelEU Aviation) (Text with EEA relevance)* Regulation (EU) of the European Parliament and of the Council. Accessed: Mar. 11, 2025. 2023. <https://eur-lex.europa.eu/eli/reg/2023/2405/oj>.
21. European Commission. *A Hydrogen Strategy for a Climate-Neutral Europe* Communication from the Commission to the European Parliament, the Council, the European Economic and Social Committee and the Committee of the Regions. Accessed: Mar. 11, 2025. 2020. <https://eur-lex.europa.eu/legal-content/EN/TXT/?uri=CELEX:52020DC0301>.
22. European Commission. *'Fit for 55': delivering the EU's 2030 Climate Target on the way to climate neutrality* <https://eur-lex.europa.eu/legal-content/EN/TXT/?uri=CELEX:52021DC0550>. COM/2021/550 final. Accessed: 2025-04-23. 2021.
23. Airbus. *ZEROe - Hydrogen-Powered Aircraft Concept* Accessed: 2024-03-14. 2024. <https://www.airbus.com/en/innovation/energy-transition/hydrogen/zeroe>.
24. International, C. *Revolutionary Innovation for Sustainable Engines (RISE) Program* Accessed: 2024-03-14. 2024. <https://www.cfmaeroengines.com/rise/>.
25. *Advanced Propulsion & Power Unit (APPU)* Accessed: 2024-03-14. 2024. <https://www.tudelft.nl/lr/appu>.
26. *Hydrogen Optimized multi-fuel Propulsion system for clean and silEnt aircraft* Grant agreement ID: 101096275. 2023. <https://cordis.europa.eu/project/id/101096275>.

27. Dave, K. *et al.* Kerosene-H₂ blending effects on flame properties in a multi-fuel combustor. *Fuel Communications*, 100139 (2025).
28. Lefebvre, A. H. *Lean Premixed/Prevaporized Combustion in Proceedings of the Workshop on Lean Premixed/Prevaporized Combustion* NASA Conference Publication NASA-CP-2016, E-9255. Accessed: 2025-04-23 (NASA, Cleveland, OH, USA, Jan. 1977). <https://ntrs.nasa.gov/citations/19770026353>.
29. Liu, Y. *et al.* Review of modern low emissions combustion technologies for aero gas turbine engines. *Prog. Aerosp. Sci.* **94**, 12–45 (2017).
30. Bothien, M. R., Ciani, A., Wood, J. P. & Fruechtel, G. Toward decarbonized power generation with gas turbines by using sequential combustion for burning hydrogen. *J. Eng. Gas Turbine Power* **141**, 121013 (2019).
31. Pignatelli, F. *et al.* Pilot impact on turbulent premixed methane/air and hydrogen-enriched methane/air flames in a laboratory-scale gas turbine model combustor. *Int. J. Hydrog. Energy* **47**, 25404–25417 (2022).
32. Hassa, C. Partially premixed and premixed aero engine combustors. *Gas Turbine Emissions* **38**, 237 (2013).
33. McKinney, R., Cheung, A., Sowa, W. & Sepulveda, D. *The Pratt & Whitney TALON X low emissions combustor: revolutionary results with evolutionary technology in 45th AIAA aerospace sciences meeting and exhibit* (2007), 386.
34. Herbon, J. *et al.* *Continuous Lower Energy, Emissions and Noise (CLEEN II) Technologies Development – TAPS III Combustor* Final Report DTFAWA-15-A-80013. Public Version (Federal Aviation Administration and GE Aviation, Washington, DC, USA, Sept. 2020). https://www.faa.gov/sites/faa.gov/files/2022-02/ph ase2_ge_taps_combustor_final.pdf.
35. Mongia, H. *TAPS: A fourth generation propulsion combustor technology for low emissions in AIAA International Air and Space Symposium and Exposition: The Next 100 Years* (2003), 2657.
36. Ren, X., Brady, K. B., Xue, X., Sung, C.-J. & Mongia, H. C. Swirl rotation direction effects on lean direct injection pilot mixer performance: Experiments and LES modeling. *Aerospace Science and Technology* **129**, 107808. ISSN: 1270-9638 (2022).
37. Hicks, Y. R. & Tacina, K. M. *Design Guidelines for Swirl-Venturi Fuel-Air Mixers for Lean Direct Injection Combustors* tech. rep. NASA/TM-20210011787 (NASA Glenn Research Center, Dec. 2021). <https://ntrs.nasa.gov/citations/20210011787>.
38. Marek, C. J., Smith, T. D. & Kundu, K. *Low-Emission Hydrogen Combustors for Gas Turbines Using Lean Direct Injection* Technical Memorandum NASA/TM-2005-213556. Presented at the 41st AIAA/ASME/SAE/ASEE Joint Propulsion Conference & Exhibit, Tucson, AZ, July 10–13, 2005. AIAA-2005-3776 (NASA Glenn Research Center, 2005). <https://ntrs.nasa.gov/citations/20080002274>.
39. Pitsch, H. The transition to sustainable combustion: Hydrogen-and carbon-based future fuels and methods for dealing with their challenges. *Proc. Combust. Inst.* **40**, 105638 (2024).

40. International Energy Agency. *Net Zero by 2050: A Roadmap for the Global Energy Sector* <https://www.iea.org/reports/net-zero-by-2050>. Accessed: 2025-04-23. 2021.
41. Nuñez-Jimenez, A. & De Blasio, N. Competitive and secure renewable hydrogen markets: three strategic scenarios for the European Union. *Int. J. Hydrog. Energy* **47**, 35553–35570 (2022).
42. Hydrogen Council, McKinsey & Co. *Hydrogen Insights 2024* :<https://hydrogencouncil.com/en/insights-2024/>. Accessed: 2025-04-23. Sept. 2024.
43. Zeldovich, Y. B. The oxidation of nitrogen in combustion and explosions. *J. Acta Physicochimica* **21**, 577 (1946).
44. Capurso, T., Laera, D., Riber, E. & Cuenot, B. NO_x pathways in lean partially premixed swirling H₂-air turbulent flame. *Combust. Flame* **248**, 112581 (2023).
45. Hendricks, R., Shouse, D. & Roquemore, W. *Water Injected Turbomachinery* tech. rep. NASA/TM-2005-212632. Presented at the 10th International Symposium on Transport Phenomena and Dynamics of Rotating Machinery (ISROMAC-10), Honolulu, HI, March 7–11, 2004 (NASA Glenn Research Center, 2005). <https://ntrs.nasa.gov/citations/20050175876>.
46. Palulli, R. *et al.* Characterisation of non-premixed, swirl-stabilised, wet hydrogen/air flame using large eddy simulation. *Fuel* **350**, 128710 (2023).
47. Giusti, A., Gkantonas, S. & Lalli, N. S. Low-NO_x hydrogen combustion via water-based bubbles: Concept and performance evaluation. *Int. J. Hydrog. Energy* **101**, 1378–1386 (2025).
48. Pousada, P. R. *et al.* Flashback Prevention in a Hydrogen-Fueled Reheat Combustor by Water Injection Optimized With Global Sensitivity Analysis. *J. Eng. Gas Turbine Power* **147** (2025).
49. Reichel, T. G., Terhaar, S. & Paschereit, C. O. *Flow field manipulation by axial air injection to achieve flashback resistance and its impact on mixing quality in 43rd AIAA Fluid Dynamics Conference* (2013), 2603.
50. Law, C. K. *Combustion physics* (Cambridge university press, 2010).
51. Day, M. S. *et al.* Cellular burning in lean premixed turbulent hydrogen-air flames: Coupling experimental and computational analysis at the laboratory scale. *J. Phys. Conf. Ser.* **180**. ISSN: 17426596 (2009).
52. Day, M. *et al.* Turbulence effects on cellular burning structures in lean premixed hydrogen flames. *Combust. Flame* **156**, 1035–1045. ISSN: 0010-2180 (2009).
53. Berger, L., Attili, A. & Pitsch, H. Synergistic interactions of thermodiffusive instabilities and turbulence in lean hydrogen flames. *Combust. Flame* **244**, 112254. ISSN: 0010-2180 (2022).
54. Law, C. *Dynamics of stretched flames in Symp., Int., Combust* **22** (1989), 1381–1402.
55. Law, C. & Sung, C. Structure, aerodynamics, and geometry of premixed flamelets. *Prog. Energy Combust. Sci.* **26**, 459–505 (2000).

56. Poinso, T. J. & Veynante, D. *Theoretical and numerical combustion* (Edwards, 2005).
57. O'Connor, J. Understanding the role of flow dynamics in thermoacoustic combustion instability. *Proc. Combust. Inst.* **39**, 4583–4610. ISSN: 1540-7489 (2023).
58. Kruljevic, B. *et al.* Experimentation and simulation of a swirled burner featuring cross-flow hydrogen injection with a focus on the OH* chemiluminescence. *Combust. Flame* **273**, 113945. ISSN: 0010-2180 (2025).
59. Pers, H., Aniello, A., Morisseau, F. & Schuller, T. Autoignition-induced flashback in hydrogen-enriched laminar premixed burners. *Int. J. Hydrog. Energy* **48**, 10235–10249. ISSN: 0360-3199 (2023).
60. Benim, A. C. & Syed, K. J. in *Flashback Mechanisms in Lean Premixed Gas Turbine Combustion iv* (Academic Press, Boston, 2015). ISBN: 978-0-12-800755-6.
61. Aspden, A., Day, M. & Bell, J. Turbulence–flame interactions in lean premixed hydrogen: transition to the distributed burning regime. *Journal of Fluid mechanics* **680**, 287–320 (2011).
62. Eichler, C. T. *Flame Flashback in Wall Boundary Layers of Premixed Combustion Systems* Fakultät für Maschinenwesen, supervised by Univ.-Prof. Dr.-Ing. Thomas Sattelmayer. Ph.D. thesis (Technische Universität München, Munich, Germany, 2011).
63. Cheng, R. & Oppenheim, A. Autoignition in methane/hydrogen mixtures. *Combust. Flame* **58**, 125–139. ISSN: 0010-2180 (1984).
64. Kiesewetter, F., Konle, M. & Sattelmayer, T. Analysis of Combustion Induced Vortex Breakdown Driven Flame Flashback in a Premix Burner With Cylindrical Mixing Zone. *J. Eng. Gas Turbine Power* **129**, 929–936. ISSN: 0742-4795 (Apr. 2007).
65. Soli, A. & Langella, I. Numerical Investigation of a Coupled Blow-Off/Flashback Process in a High-Pressure Lean-Burn Combustor. *J. Eng. Gas Turbine Power* **145**, 021010. ISSN: 0742-4795 (Nov. 2022).
66. Fritz, J., Kröner, M. & Sattelmayer, T. Flashback in a Swirl Burner With Cylindrical Premixing Zone. *J. Eng. Gas Turbine Power* **126**, 276–283. ISSN: 0742-4795 (June 2004).
67. Marragou, S. *et al.* Modeling of H₂/air flame stabilization regime above coaxial dual swirl injectors. *Combust. Flame* **255**, 112908. ISSN: 0010-2180 (2023).
68. Link, S., Dave, K., de Domenico, F., Rao, A. G. & Eitelberg, G. Experimental analysis of dual-fuel (CH₄/H₂) capability in a partially-premixed swirl stabilized combustor. *Int. J. Hydrog. Energy* **101**, 427–437 (2025).
69. Kröner, M., Sattelmayer, T., Fritz, J., Kiesewetter, F. & Hirsch, C. Flame propagation in swirling flows, effect of local extinction on the combustion induced vortex breakdown. *Combust. Sci. Technol.* **179**, 1385–1416 (2007).
70. Keller, J. *et al.* Mechanism of instabilities in turbulent combustion leading to flashback. *Aiaa Journal* **20**, 254–262 (1982).

71. Tuncer, O., Acharya, S. & Uhm, J. Dynamics, NO_x and flashback characteristics of confined premixed hydrogen-enriched methane flames. *Int. J. Hydrog. Energy* **34**, 496–506. ISSN: 0360-3199 (2009).
72. Lapeyre, C. J. *et al.* Acoustically induced flashback in a staged swirl-stabilized combustor. *Flow Turbul. Combust.* **98**, 265–282 (2017).
73. Kutkan, H., Amato, A., Campa, G., Tay-Wo-Chong, L. & Æsøy, E. *LES of turbulent premixed CH₄/H₂/air flames with stretch and heat loss for flame characteristics and dynamics in Turbo Expo: Power for Land, Sea, and Air* **86007** (2022), V03BT04A021.
74. Yahou, T. *et al.* The role of preferential diffusion on the ignition dynamics of lean premixed hydrogen flames. *Proc. Combust. Inst.* **40**, 105612 (2024).
75. Dawson, J. R. *et al.* Visualization of blow-off events in bluff-body stabilized turbulent premixed flames. *Proc. Combust. Inst.* **33**, 1559–1566 (2011).
76. Esquiva-Dano, I., Nguyen, H. & Escudie, D. Influence of a bluff-body's shape on the stabilization regime of non-premixed flames. *Combust. Flame* **127**, 2167–2180. ISSN: 0010-2180 (2001).
77. Cabra, R. *et al.* Simultaneous laser Raman-Rayleigh-LIF measurements and numerical modeling results of a lifted turbulent H₂/N₂ jet flame in a vitiated coflow. *Proc. Combust. Inst.* **29**, 1881–1888 (2002).
78. Zhou, B., Brackmann, C., Li, Z., Aldén, M. & Bai, X.-S. Simultaneous multi-species and temperature visualization of premixed flames in the distributed reaction zone regime. *Proc. Combust. Inst.* **35**, 1409–1416. ISSN: 1540-7489 (2015).
79. Markides, C. & Mastorakos, E. An experimental study of hydrogen autoignition in a turbulent co-flow of heated air. *Proc. Combust. Inst.* **30**, 883–891. ISSN: 1540-7489 (2005).
80. Oldenhof, E., Tummers, M., van Veen, E. & Roekaerts, D. Role of entrainment in the stabilisation of jet-in-hot-coflow flames. *Combust. Flame* **158**, 1553–1563. ISSN: 0010-2180 (2011).
81. Zhao, D., Gutmark, E. & de Goey, P. A review of cavity-based trapped vortex, ultra-compact, high-g, inter-turbine combustors. *Prog. Energy Combust. Sci.* **66**, 42–82. ISSN: 0360-1285 (2018).
82. Massey, J. C., Langella, I. & Swaminathan, N. A scaling law for the recirculation zone length behind a bluff body in reacting flows. *J. Fluid Mech.* **875**, 699–724 (2019).
83. Funke, H. H.-W., Beckmann, N., Keinz, J. & Horikawa, A. 30 Years of dry-low-NO_x micromix combustor research for hydrogen-rich fuels—an overview of past and present activities. *J. Eng. Gas Turbine Power* **143**, 071002 (2021).
84. Berger, J. Scaling of an aviation hydrogen micromix injector design for industrial GT combustion applications. *Aerotecnica Missili & Spazio* **100**, 239–251 (2021).
85. Syred, N. & Beér, J. M. Combustion in swirling flows: a review. *Combust. Flame* **23**, 143–201 (1974).

86. Huang, Y. & Yang, V. Dynamics and stability of lean-premixed swirl-stabilized combustion. *Prog. Energy Combust. Sci.* **35**, 293–364. ISSN: 0360-1285 (2009).
87. Bénard, P., Lartigue, G., Moureau, V. & Mercier, R. Large-eddy simulation of the lean-premixed preccinsta burner with wall heat loss. *Proc. Combust. Inst.* **37**, 5233–5243 (2019).
88. Chen, Z. X. *et al.* Large Eddy Simulation of a dual swirl gas turbine combustor: Flame/flow structures and stabilisation under thermoacoustically stable and unstable conditions. *Combust. Flame* **203**, 279–300 (2019).
89. I. Langella, Z. X. Chen, N. Swaminathan & S. K. Sadasivuni. Large-Eddy Simulation of Reacting Flows in Industrial Gas Turbine Combustor. *J. Propul. Power* **34**, 1269–1284 (2017).
90. Giusti, A. & Mastorakos, E. Turbulent combustion modelling and experiments: Recent trends and developments. *Flow Turbul. Combust.* **103**, 847–869 (2019).
91. Domingo, P. & Vervisch, L. Recent developments in DNS of turbulent combustion. *Proc. Combust. Inst.* **39**, 2055–2076. ISSN: 1540-7489 (2023).
92. Pitsch, H. A consistent level set formulation for large-eddy simulation of premixed turbulent combustion. *Combust. Flame* **143**, 587–598 (2005).
93. Pope, S. B. *Turbulent Flows* (Cambridge University Press, 2000).
94. Smagorinsky, J. General circulation experiments with the primitive equations: I. The basic experiment. *Monthly weather review* **91**, 99–164 (1963).
95. Yoshizawa, A. Statistical theory for compressible turbulent shear flows, with the application to subgrid modeling. *Phys. Fluids* **29**, 2152–2164 (1986).
96. Germano, M., Piomelli, U., Moin, P. & Cabot, W. H. A dynamic subgrid-scale eddy viscosity model. *Phys. Fluids A* **3**, 1760 (1991).
97. Pope, S. B. Ten questions concerning the large-eddy simulation of turbulent flows. *New J. Phys.* **6**. ISSN: 13672630 (2004).
98. Charlette, F., Meneveau, C. & Veynante, D. A power-law flame wrinkling model for LES of premixed turbulent combustion, part I: Nondynamic formulation and initial tests. *Combust Flame* **131**, 159–180 (2002).
99. Pierce, C. D. & Moin, P. A dynamic model for subgrid-scale variance and dissipation rate of a conserved scalar. *Physics of Fluids* **10**, 3041–3044 (1998).
100. Moin, P., Squires, K., Cabot, W. & Lee, S. A dynamic subgrid-scale model for compressible turbulence and scalar transport. *Physics of Fluids A: Fluid Dynamics* **3**, 2746–2757 (1991).
101. Ferrante, G., Eitelberg, G. & Langella, I. Differential diffusion modelling for LES of premixed and partially premixed flames with presumed FDF. *Combustion Theory and Modelling* **28**, 695–730 (2024).
102. Langella, I., Swaminathan, N., Gao, Y. & Chakraborty, N. Assessment of Dynamic Closure for Premixed Combustion LES. *Combust. Theor. Model.* **19**, 628–656 (2015).

103. Pitsch, H. Large-Eddy Simulation of Turbulent Combustion. *Annu. Rev. Fluid Mech.* **38**, 453–482 (2006).
104. Veynante, D. & Vervisch, L. Turbulent combustion modeling. *Prog. Energy Combust. Sci.* **28**, 193–266 (2002).
105. Van Oijen, J. & de Goey, L. Modelling of premixed laminar flames using flamelet-generated manifold. *Combust. Sci. and Tech.* **161**, 113–137 (2000).
106. M. Ihme, C. M. Cha & H. Pitsch. Prediction of local extinction and re-ignition effects in non-premixed turbulent combustion using a flamelet/progress variable approach. *Proc. Combust. Inst.* **30**, 793–800 (2005).
107. Fiorina, B. *et al.* A filtered tabulated chemistry model for LES of premixed combustion. *Combust. Flame* **157**, 465–475 (2010).
108. Bray, K., Champion, M., Libby, P. & Swaminathan, N. Finite rate chemistry and presumed PDF models for premixed turbulent combustion. *Combust. Flame* **146**, 665–673 (2006).
109. Lipatnikov, A. N., Sabelnikov, V. A., Hernández-Pérez, F. E., Song, W. & Im, H. G. A priori DNS study of applicability of flamelet concept to predicting mean concentrations of species in turbulent premixed flames at various Karlovitz numbers. *Combust. Flame* **222**, 370–382 (2020).
110. Valino, L., Mustata, R. & Letaief, K. B. Consistent behavior of Eulerian Monte Carlo fields at low Reynolds numbers. *Flow Turbul. Combust.* **96**, 503–512 (2016).
111. Breda, P., Yu, C., Maas, U. & Pfitzner, M. Validation of an Eulerian stochastic fields solver coupled with reaction–diffusion manifolds on LES of methane/air non-premixed flames. *Flow Turbul. Combust.* **107**, 441–477 (2021).
112. Driscoll, J. F. *et al.* Premixed flames subjected to extreme turbulence: Some questions and recent answers. *Prog. Energy Combust. Sci.* **76**, 100802 (2020).
113. Van den Bergh, A. A. *Design and test of a swirl-stabilized methane combustor with axial air injection* Accessed: 2025-04-15. Master thesis (Delft University of Technology, 2022). <https://repository.tudelft.nl/record/uuid:5262b98f-bf7d-481d-b2ff-e2816d3c9e12>.
114. Popa, V. A. *Cold Flow Analysis of a Dual Swirl Stabilized Combustion Chamber* Accessed: 2025-04-15. Master thesis (Delft University of Technology, 2022). <https://repository.tudelft.nl/record/973ae549-f6c5-4f7d-89ce-4c490ca874cf>.
115. Vermeijlen, S. *Swirl-Stabilised Hydrogen Combustor with Axial Air Injection: Numerical Simulations and Cold Flow Experiments* Accessed: 2025-04-15. Master thesis (Delft University of Technology, 2021). <https://repository.tudelft.nl/record/bb2c1c3d-f4bc-47e4-b694-34d493f628b2>.
116. Risch, T. K. Curve Fits of the NIST-JANNAF Thermochemical Tables Fourth Edition. *Armstrong Flight Research Center, Edwards Irvinem, CA, USA* (2021).
117. Sutherland, W. LII. The viscosity of gases and molecular force. *The London, Edinburgh, and Dublin Philosophical Magazine and Journal of Science* **36**, 507–531 (1893).

118. Wilke, C. R. A viscosity equation for gas mixtures. *Journal of Chemical physics* **18**, 517–519 (1950).
119. Herning, F. & Zipperer, L. Calculation of the viscosity of technical gas mixtures from the viscosity of the individual gases. *Gas u. Wasserfach* **79**, 69 (1936).
120. Davidson, T. A. *A simple and accurate method for calculating viscosity of gaseous mixtures* (US Department of the Interior, Bureau of Mines, 1993).
121. Langella, I. Large Eddy Simulation of premixed Combustion Using Flamelets. *PhD Thesis* (Oct. 2016).
122. Hirschfelder, J. O., Curtiss, C. F. & Bird, R. B. Molecular theory of gases and liquids. *Molecular theory of gases and liquids* (1964).
123. Schlup, J. & Blanquart, G. Reproducing curvature effects due to differential diffusion in tabulated chemistry for premixed flames. *Proc. Combust. Inst.* **37**, 2511–2518. ISSN: 1540-7489 (2019).
124. Regele, J. D., Knudsen, E., Pitsch, H. & Blanquart, G. A two-equation model for non-unity Lewis number differential diffusion in lean premixed laminar flames. *Combust. Flame* **160**, 240–250 (2013).
125. Mukundakumar, N., Efimov, D., Beishuizen, N. & van Oijen, J. A new preferential diffusion model applied to FGM simulations of hydrogen flames. *Combust. Theory Model.* **25**, 1245–1267. ISSN: 17413559 (2021).
126. Rahman, M. & Saghir, M. Thermodiffusion or Soret effect: Historical review. *International Journal of Heat and Mass Transfer* **73**, 693–705 (2014).
127. Howarth, T., Day, M. S., Pitsch, H. & Aspden, A. Thermal diffusion, exhaust gas recirculation and blending effects on lean premixed hydrogen flames. *Proc. Combust. Inst.* **40**, 105429 (2024).
128. Fruzza, F. *et al.* The importance of Soret effect, preferential diffusion, and conjugate heat transfer for flashback limits of hydrogen-fueled perforated burners. *Proc. Combust. Inst.* **40**, 105581. ISSN: 1540-7489 (2024).
129. Mathur, S., Tondon, P. & Saxena, S. Thermal conductivity of binary, ternary and quaternary mixtures of rare gases. *Molecular physics* **12**, 569–579 (1967).
130. Mizobuchi, Y., Shinjo, J., Ogawa, S. & Takeno, T. A numerical study on the formation of diffusion flame islands in a turbulent hydrogen jet lifted flame. *Proc. Combust. Inst.* **30**, 611–619. ISSN: 0082-0784 (2005).
131. Wu, Z., Masri, A. R. & Bilger, R. W. An Experimental Investigation of the Turbulence Structure of a Lifted H₂/N₂ Jet Flame in a Vitiated Co-Flow. *Flow, Turbul. Combust.* **76**, 61–81. ISSN: 13866184 (2006).
132. Matalon, M. Flame dynamics. *Proc. Combust. Inst.* **32**, 57–82 (2009).
133. Nicolai, H., Dressler, L., Janicka, J. & Hasse, C. Assessing the importance of differential diffusion in stratified hydrogen–methane flames using extended flamelet tabulation approaches. *Phys. Fluids* **34** (2022).

134. Donini, A., Bastiaans, R. J., Van Oijen, J. A. & De Goey, L. P. Differential diffusion effects inclusion with flamelet generated manifold for the modeling of stratified premixed cooled flames. *Proc. Combust. Inst.* **35**, 831–837. ISSN: 15407489 (2015).
135. van Oijen, J. A., Donini, A., Bastiaans, R. J. M., Boonkamp, J. H. M. t. & de Goey, L. P. H. State-of-the-art in premixed combustion modeling using flamelet generated manifolds. *Prog. Energy Combust. Sci.* **57**, 30–74 (2016).
136. Z. X. Chen, I. Langella, R. S. Barlow & N. Swaminathan. Prediction of local extinctions in piloted jet flames with inhomogeneous inlets using unstrained flamelets. *Combust. Flame* **212**, 415–432 (2020).
137. Bray, K., Domingo, P. & Vervisch, L. Role of the progress variable in models for partially premixed turbulent combustion. *Combust. Flame* **141**, 431–437 (2005).
138. Peters, N. *Turbulent Combustion* (Cambridge University Press, 2000).
139. Bilger, R. W., Stårner, S. H. & Kee, R. J. On Reduced Mechanism for Methane-Air Combustion in Nonpremixed Flames. *Combust. Flame* **80**, 135–149 (1990).
140. Masri, A. & Barlow, R. On conserved scalars that preserve stoichiometric mixture fraction. *Combust. Flame* **260**, 113224. ISSN: 0010-2180 (2024).
141. Eindhoven University of Technology. *CHEM1D. A one dimensional laminar flame code* 2021.
142. Smith, G. P. *et al.* *GRI-Mech 3.0: A Mechanism for Natural Gas Combustion* http://www.me.berkeley.edu/gri_mech/. Accessed: 2025-04-04. 2000.
143. *Chemical-Kinetic Mechanisms for Combustion Applications* San Diego Mechanism web page, Mechanical and Aerospace Engineering (Combustion Research), University of California at San Diego. <http://combustion.ucsd.edu>.
144. Matalon, M., Cui, C. & Bechtold, J. Hydrodynamic theory of premixed flames: effects of stoichiometry, variable transport coefficients and arbitrary reaction orders. *Journal of fluid mechanics* **487**, 179–210 (2003).
145. Howarth, T. L., Lehmann, T., Gauding, M. & Pitsch, H. Role of enthalpy transport in laminar premixed hydrogen flames at atmospheric and elevated pressures. *arXiv preprint arXiv:2503.19865* (2025).
146. Bechtold, J. & Matalon, M. Effects of stoichiometry on stretched premixed flames. *Combust. Flame* **119**, 217–232 (1999).
147. Matalon, M. & Matkowsky, B. J. Flames as gasdynamic discontinuities. *Journal of Fluid Mechanics* **124**, 239–259 (1982).
148. Schepers, S. N. & van Oijen, J. A. FGM Modeling of Thermo-Diffusive Unstable Lean Premixed Hydrogen-Air Flames. *arXiv preprint arXiv:2503.02620* (2025).
149. Williams, F. A. *Combustion Theory* (CRC Press, 2018).
150. Groot, G., Van Oijen, J., De Goey, L., Seshadri, K. & Peters, N. The effects of strain and curvature on the mass burning rate of premixed laminar flames. *Combust. Theory Model.* **6**, 675 (2002).
151. Clavin, P. & Joulin, G. in *Turbulent reactive flows* 213–240 (Springer, 1989).

152. Acquaviva, M. R., Porcarelli, A. & Langella, I. Influence of Soret effect on flame structure and NO_x emissions in highly strained lean premixed counterflow hydrogen flames. *Fuel* (2025).
153. Porcarelli, A. & Langella, I. Mitigation of preferential diffusion effects by intensive strain in lean premixed hydrogen flamelets. *Proc. Combust. Inst.* **40**, 105728 (2024).
154. Lapenna, P. E., Berger, L., Creta, F. & Pitsch, H. in *Hydrogen for Future Thermal Engines* 93–139 (Springer, 2023).
155. Wen, X., Berger, L., Vom Lehn, E., Parente, A. & Pitsch, H. Numerical analysis and flamelet modeling of NO_x formation in a thermodiffusively unstable hydrogen flame. *Combust. Flame* **253**, 112817 (2023).
156. Berger, L., Attili, A. & Pitsch, H. Intrinsic instabilities in premixed hydrogen flames: parametric variation of pressure, equivalence ratio, and temperature. Part 2–Non-linear regime and flame speed enhancement. *Combust. Flame* **240**, 111936 (2022).
157. Berger, L., Attili, A. & Pitsch, H. Intrinsic instabilities in premixed hydrogen flames: Parametric variation of pressure, equivalence ratio, and temperature. part 1-dispersion relations in the linear regime. *Combust. Flame* **240**, 111935 (2022).
158. Rieth, M., Gruber, A. & Chen, J. H. The effect of pressure on lean premixed hydrogen-air flames. *Combust. Flame* **250**, 112514. ISSN: 0010-2180 (2023).
159. Damköhler, G. The effect of turbulence on the flame velocity in gas mixtures. *Zeitschrift fuer Elektrochemie und Angewandte Physikalische Chemiw* **46** (1947).
160. Driscoll, J. F. *et al.* Premixed flames subjected to extreme turbulence: Some questions and recent answers. *Prog. Energy Combust. Sci.* **76**, 100802. ISSN: 0360-1285 (2020).
161. Aspden, A., Day, M. & Bell, J. Towards the distributed burning regime in turbulent premixed flames. *Journal of fluid mechanics* **871**, 1–21 (2019).
162. Wu, M., Kwon, S., Driscoll, J. & Faeth, G. Turbulent premixed hydrogen/air flames at high Reynolds numbers. *Combustion science and technology* **73**, 327–350 (1990).
163. Lapointe, S., Savard, B. & Blanquart, G. Differential diffusion effects, distributed burning, and local extinctions in high Karlovitz premixed flames. *Combust. Flame* **162**, 3341–3355. ISSN: 0010-2180 (2015).
164. Lipatnikov, A. & Chomiak, J. Molecular transport effects on turbulent flame propagation and structure. *Prog. Energy Combust. Sci.* **31**, 1–73 (2005).
165. Rieth, M., Gruber, A., Williams, F. A. & Chen, J. H. Enhanced burning rates in hydrogen-enriched turbulent premixed flames by diffusion of molecular and atomic hydrogen. *Combust. Flame* **239**, 111740 (2022).
166. Chu, H., Berger, L., Gauding, M., Attili, A. & Pitsch, H. Effects of dilatation and turbulence on tangential strain rates in premixed hydrogen and iso-octane flames. *Journal of Fluid Mechanics* **981**, A5 (2024).
167. Aspden, A., Day, M. & Bell, J. Characterization of low Lewis number flames. *Proc. Combust. Inst.* **33**, 1463–1471 (2011).

168. Berger, L., Attili, A., Gauding, M. & Pitsch, H. Effects of Karlovitz number variations on thermodiffusive instabilities in lean turbulent hydrogen jet flames. *Proc. Combust. Inst.* **40**, 105219 (2024).
169. Howarth, T., Picciani, M., Richardson, E., Day, M. & Aspden, A. Direct numerical simulation of a high-pressure hydrogen micromix combustor: Flame structure and stabilisation mechanism. *Combust. Flame* **265**, 113504. ISSN: 0010-2180 (2024).
170. Aoki, K., Shimura, M., Park, J., Minamoto, Y. & Tanahashi, M. Response of heat release rate to flame straining in swirling hydrogen-air premixed flames. *Flow Turbul. Combust.* **104**, 451–478 (2020).
171. Janicka, J. & Sadiki, A. Large eddy simulation of turbulent combustion systems. *Proc. Combust. Inst.* **30**, 537–547. ISSN: 1540-7489 (2005).
172. Ferziger, J. & Peric, M. *Computational Methods for Fluid Dynamics* (Springer, 1999).
173. Lilly, D. A proposed modification of the germano sugrid-scale closure method. *Phys Fluids A* **4**, 633–635 (1992).
174. Ghosal, S. & Moin, P. The basic equations for the large eddy simulation of turbulent flows in complex geometry. *J. Comput. Phys.* **118**, 24–37 (1995).
175. Favre, A. Problems of hydrodynamics and continuum mechanics. *Soc. Indust.*, 231–266 (1969).
176. Chai, X. & Mahesh, K. Dynamic k-Equation Model for Large Eddy Simulation of Compressible Flow. *J. Fluid Mech.* **699**, 385–413 (2012).
177. Langella, I., Swaminathan, N., Gao, Y. & Chakraborty, N. LES of premixed combustion: Sensitivity to SGS velocity modelling. *Combust. Sci. Technol.* **189**, 43–78 (2015).
178. Mira, D. *et al.* Numerical Characterization of a Premixed Hydrogen Flame Under Conditions Close to Flashback. *Flow Turbul. Combust.* **104**, 479–507. ISSN: 15731987 (2020).
179. Pitsch, H. & Steiner, H. Large-eddy simulation of a turbulent piloted methane/air diffusion flame (Sandia flame D). *Physics of fluids* **12**, 2541–2554 (2000).
180. Peters, N. & Rogg, B. *Reduced kinetic mechanisms for applications in combustion systems* (Springer Science & Business Media, 2008).
181. Cazères, Q., Pepiot, P., Riber, E. & Cuenot, B. A fully automatic procedure for the analytical reduction of chemical kinetics mechanisms for computational fluid dynamics applications. *Fuel* **303**, 121247 (2021).
182. Maas, U. & Pope, S. B. Simplifying chemical kinetics: intrinsic low-dimensional manifolds in composition space. *Combust. Flame* **88**, 239–264 (1992).
183. Gicquel, O., Darabiha, N. & Thévenin, D. Liminar premixed hydrogen/air counterflow flame simulations using flame prolongation of ILDM with differential diffusion. *Proc. Combust. Inst.* **28**, 1901–1908 (2000).
184. Fiorina, B. *et al.* Modelling non-adiabatic partially premixed flames using flame-prolongation of ILDM. *Combust. Theory Model.* **7**, 449–470 (2003).

185. Blasco, J., Fueyo, N., Dopazo, C. & Ballester, J. Modelling the Temporal Evolution of a Reduced Combustion Chemical System With an Artificial Neural Network. *Combust. Flame* **113**, 38–52. ISSN: 0010-2180 (1998).
186. Chen, J.-Y., Blasco, J., Fueyo, N. & Dopazo, C. An economical strategy for storage of chemical kinetics: Fitting in situ adaptive tabulation with artificial neural networks. *Proc. Combust. Inst.* **28**, 115–121 (2000).
187. Hansinger, M., Ge, Y. & Pfitzner, M. Deep residual networks for flamelet/progress variable tabulation with application to a piloted flame with inhomogeneous inlet. *Combust. Sci. Technol.* **194**, 1587–1613 (2022).
188. Nejaamtheen, M. N. & Choi, J.-Y. A Comprehensive Review of Flamelet Methods: Future Directions and Emerging Challenges. *Energies* **18**, 45 (2024).
189. Liew, S., Bray, K. & Moss, J. A stretched laminar flamelet model of turbulent non-premixed combustion. *Combust. Flame* **56**, 199–213 (1984).
190. Pitsch, H., Chen, M. & Peters, N. *Unsteady flamelet modeling of turbulent hydrogen-air diffusion flames* in *Symposium (international) on combustion* **27** (1998), 1057–1064.
191. Ihme, M. & Pitsch, H. Modeling of radiation and nitric oxide formation in turbulent nonpremixed flames using a flamelet/progress variable formulation. *Physics of Fluids* **20** (2008).
192. Hu, Y. & Kurose, R. Large-eddy simulation of turbulent autoigniting hydrogen lifted jet flame with a multi-regime flamelet approach. *Int. J. Hydrog. Energy* **44**, 6313–6324. ISSN: 03603199 (2019).
193. Knudsen, E. & Pitsch, H. Capabilities and limitations of multi-regime flamelet combustion models. *Combust. Flame* **159**, 242–264. ISSN: 0010-2180 (2012).
194. Pope, S. Computationally efficient implementation of combustion chemistry using in situ adaptive tabulation. *Combust. Theory Model.* **1**, 41–63 (1997).
195. Gicquel, L., Staffelbach, G. & Poinso, T. Large Eddy Simulations of gaseous flames in gas turbine combustion chambers. *Prog. Energy Combust. Sci.* **38**, 782–817. ISSN: 0360-1285 (2012).
196. Spalding, D. B. *Mixing and Chemical Reaction in Steady Confined Turbulent Flames* in *Proceedings of the 13th Symposium (International) on Combustion* (The Combustion Institute, Pittsburgh, 1971), 649–657.
197. Said, R. & Borghi, R. *A Simulation with a Cellular Automaton for Turbulent Combustion Modelling* in *Proceedings of the Twenty-Second Symposium (International) on Combustion* (The Combustion Institute, Pittsburgh, 1988), 569–577.
198. Im, H. G., Lund, T. S. & Ferziger, J. H. Large eddy simulation of turbulent front propagation with dynamic subgrid models. *Physics of Fluids* **9**, 3826–3833 (1997).
199. Kerstein, A. R., Ashurst, W. T. & Williams, F. A. Field equation for interface propagation in an unsteady homogeneous flow field. *Physical Review A* **37**, 2728 (1988).

200. Pitsch, H. A G-equation formulation for large-eddy simulation of premixed turbulent combustion. *Center for turbulence research annual research briefs* **4**, 3–14 (2002).
201. Moureau, V., Fiorina, B. & Pitsch, H. A level set formulation for premixed combustion LES considering the turbulent flame structure. *Combust. Flame* **156**, 801–812 (2008).
202. Boger, M., Veynante, D., Boughanem, H. & Trouvé, A. *Direct numerical simulation analysis of flame surface density concept for large eddy simulation of turbulent premixed combustion* in *Symposium (International) on combustion* **27** (1998), 917–925.
203. Gubba, S. R., Ibrahim, S. S. & Malalasekera, W. Dynamic flame surface density modelling of flame deflagration in vented explosion. *Combust. Expl. Shock Waves* **48**, 393–405 (2012).
204. Wang, G., Boileau, M., Veynante, D. & Truffin, K. Large eddy simulation of a growing turbulent premixed flame kernel using a dynamic flame surface density model. *Combust. Flame* **159**, 2742–2754 (2012).
205. Knikker, R., Veynante, D. & Meneveau, C. A dynamic flame surface density model for large eddy simulations of turbulent premixed combustion. *Phys. Fluids* **16**, 91 (2004).
206. Colin, O., Ducros, F., Veynante, D. & Poinso, T. A thickened flame model for large eddy simulations of turbulent premixed combustion. *Physics of fluids* **12**, 1843–1863 (2000).
207. Gaucherand, J., Schulze-Netzer, C., Laera, D. & Poinso, T. A subgrid-scale model to account for thermo-diffusive effects in artificially thickened LES models for lean turbulent premixed ammonia/hydrogen flames. *Proc. Combust. Inst.* **40**, 105198. ISSN: 1540-7489 (2024).
208. Wang, G., Boileau, M. & Veynante, D. Implementation of a dynamic thickened flame model for large eddy simulations of turbulent premixed combustion. *Combust. Flame* **158**, 2199–2213 (2011).
209. Volpiani, P., Schmitt, T. & Veynante, D. A posteriori tests of a dynamic thickened flame model for large eddy simulations of turbulent premixed combustion. *Combust. Flame* **174**, 166–178 (2016).
210. Legier, J.-P., Poinso, T. & Veynante, D. *Dynamically thickened flame LES model for premixed and non-premixed turbulent combustion* in *Proceedings of the summer program* **12** (2000), 157–168.
211. Z. X. Chen, N. A. K. D. Doan, S. Ruan, I. Langella & N. Swaminathan. A priori investigation of subgrid correlation of mixture fraction and progress variable in partially premixed flames. *Combust. Theory Model.* **22**, 862–882 (2018).
212. Bray, K. N. C., Libby, P. A. & Moss, J. Unified modeling approach for premixed turbulent combustion—Part I: General formulation. *Combust. Flame* **61**, 87–102 (1985).

213. Libby, P. A., Bray, K. & Moss, J. B. Effects of finite reaction rate and molecular transport in premixed turbulent combustion. *Combust. Flame* **34**, 285–301 (1979).
214. Jones, W. & Prasad, V. Large Eddy Simulation of the Sandia Flame Series (D–F) using the Eulerian stochastic field method. *Combust. Flame* **157**, 1621–1636 (2010).
215. Bilger, R. Conditional moment closure for turbulent reacting flow. *Physics of Fluids A: Fluid Dynamics* **5**, 436–444 (1993).
216. Navarro-Martinez, S., Kronenburg, A. & Mare, F. D. Conditional moment closure for large eddy simulations. *Flow Turbul. Combust.* **75**, 245–274 (2005).
217. Dunn, M. J., Masri, A. R. & Bilger, R. W. A new piloted premixed jet burner to study strong finite-rate chemistry effects. *Combust. Flame* **151**, 46–60. ISSN: 0010-2180 (2007).
218. Zhou, B. *et al.* Thin reaction zone and distributed reaction zone regimes in turbulent premixed methane/air flames: Scalar distributions and correlations. *Combust. Flame* **175**. Special Issue in Honor of Norbert Peters, 220–236. ISSN: 0010-2180 (2017).
219. Roberts, W. L., Driscoll, J. F., Drake, M. C. & Goss, L. P. Images of the quenching of a flame by a vortex—To quantify regimes of turbulent combustion. *Combust. Flame* **94**, 58–69. ISSN: 0010-2180 (1993).
220. Lipatnikov, A. N., Sabelnikov, V. A., Hernández-Pérez, F. E., Song, W. & Im, H. G. *A priori* DNS study of applicability of flamelet concept to predicting mean concentrations of species in turbulent premixed flames at various Karlovitz numbers. *Combust. Flame* **222**, 370–382 (2020).
221. Wang, H., Hawkes, E. R., Savard, B. & Chen, J. H. Direct numerical simulation of a high Ka CH₄/air stratified premixed jet flame. *Combust. Flame* **193**, 229–245. ISSN: 0010-2180 (2018).
222. Srinivasan, S. & Menon, S. Linear eddy mixing model studies of high Karlovitz number turbulent premixed flames. *Flow Turbul. Combust.* **93**, 189–219 (2014).
223. Aspden, A. A numerical study of diffusive effects in turbulent lean premixed hydrogen flames. *Proc. Combust. Inst.* **36**, 1997–2004. ISSN: 1540-7489 (2017).
224. Böttler, H. *et al.* Can flamelet manifolds capture the interactions of thermo-diffusive instabilities and turbulence in lean hydrogen flames?—An a-priori analysis. *Int. J. Hydrog. Energy* **56**, 1397–1407 (2024).
225. Berger, L., Attili, A., Gauding, M. & Pitsch, H. LES combustion model for premixed turbulent hydrogen flames with thermodiffusive instabilities: a priori and a posteriori analysis. *Journal of Fluid Mechanics* **1003**, A33 (2025).
226. Kai, R., Tokuoka, T., Nagao, J., Pillai, A. L. & Kurose, R. LES flamelet modeling of hydrogen combustion considering preferential diffusion effect. *Int. J. Hydrog. Energy* **48**, 11086–11101 (2023).
227. Yao, M. X. & Blanquart, G. Capturing differential diffusion effects in large eddy simulation of turbulent premixed flames. *Proc. Combust. Inst.* **40**, 105500. ISSN: 1540-7489 (2024).

228. Lapenna, P. E. *et al.* Data-driven subfilter modelling of thermo-diffusively unstable hydrogen–air premixed flames. *Combust. Theory Model.* **25**, 1064–1085 (2021).
229. Han, W., Raman, V. & Chen, Z. LES/PDF modeling of autoignition in a lifted turbulent flame: Analysis of flame sensitivity to differential diffusion and scalar mixing time-scale. *Combust. Flame* **171**, 69–86. ISSN: 15562921 (2016).
230. Dodoulas, I. A. & Navarro Martinez, S. Large eddy simulation of premixed turbulent flames using the probability density function approach. *Flow Turbul. Combust.* **90**, 645–678 (2013).
231. Mehl, C., Poncet, S., Truffin, K. & Colin, O. Large Eddy Simulation of large-scale hydrogen deflagrations using the Thickened Flame Model with stretch sensitivity adaptation and thermo-diffusive instability modeling. *Int. J. Hydrog. Energy* **93**, 457–468. ISSN: 0360-3199 (2024).
232. Avdić, A., Kuenne, G., di Mare, F. & Janicka, J. LES combustion modeling using the Eulerian stochastic field method coupled with tabulated chemistry. *Combust. Flame* **175**, 201–219 (2017).
233. Pope, S. PDF methods for turbulent reactive flows. *Prog. Energy Combust. Sci.* **11**, 119–192. ISSN: 0360-1285 (1985).
234. Jones, W. & Navarro-Martinez, S. Large eddy simulation of autoignition with a sub-grid probability density function method. *Combust. Flame* **150**, 170–187 (2007).
235. Haworth, D. C. Progress in probability density function methods for turbulent reacting flows. *Prog. Energy Combust. Sci.* **36**, 168–259 (2010).
236. Valiño, L. A field Monte Carlo formulation for calculating the probability density function of a single scalar in a turbulent flow. *Flow Turbul. Combust.* **60**, 157–172 (1998).
237. McDermott, R. & Pope, S. A particle formulation for treating differential diffusion in filtered density function methods. *J. Comput. Phys.* **226**, 947–993. ISSN: 0021-9991 (2007).
238. Hansinger, M., Pfitzner, M. & Sabelnikov, V. A. LES of oxy-fuel jet flames using the Eulerian Stochastic Fields method with differential diffusion. *Proc. Combust. Inst.* **38**, 2665–2672. ISSN: 1540-7489 (2021).
239. I. Langella & N. Swaminathan. Unstrained and strained flamelets for LES of premixed combustion. *Combust. Theory Model.* **20**, 410–440 (2016).
240. A. Soli, I. Langella & Z. X. Chen. Analysis of Flame Front Breaks Appearing in LES of Inhomogeneous Jet Flames Using Flamelets. *Prog. Energy Combust. Sci.* **49**, 189–208 (2021).
241. Chen, Z. X., Langella, I., Barlow, R. S. & Swaminathan, N. Prediction of local extinctions in piloted jet flames with inhomogeneous inlets using unstrained flamelets. *Combust. Flame* **212**, 415–432. ISSN: 15562921 (2020).
242. I. Langella, N. Swaminathan & R. W. Pitz. Application of Unstrained Flamelet SGS Closure for Multi-Regime Premixed Combustion. *Combust. Flame* **173**, 161–178 (2016).

243. I. Langella, N. A. K. Doan, N. Swaminathan & S. B. Pope. Study of subgrid-scale velocity models for reacting and nonreacting flows. *Phys. Rev. Fluids* **3** (2018).
244. Dunstan, T., Minamoto, Y., Chakraborty, N. & Swaminathan, N. Scalar dissipation rate modelling for large eddy simulation of turbulent premixed flames. *Proc. Combust. Inst.* **34**, 1193–1201 (2013).
245. Gao, Y., Chakraborty, N. & Swaminathan, N. Dynamic closure of scalar dissipation rate for Large Eddy Simulations of turbulent premixed combustion: A Direct Numerical Simulations analysis. *Flow Turbul. Combust.* **95**, 775–802 (2015).
246. Massey, J. C., Langella, I. & Swaminathan, N. Large eddy simulation of a bluff body stabilised premixed flame using flamelets. *Flow Turbul. Combust.* **101**, 973–992 (2018).
247. Knudsen, E. & Pitsch, H. A dynamic model for the turbulent burning velocity for large eddy simulation of premixed combustion. *Combust. Flame* **154**, 740–760 (2008).
248. Moureau, V., Domingo, P. & Vervisch, L. From large-eddy simulation to direct numerical simulation of a lean premixed swirl flame: Filtered laminar flame-pdf modeling. *Combust. Flame* **158**, 1340–1357 (2011).
249. Nambully, S., Domingo, P., Moureau, V. & Vervisch, L. A filtered-laminar-flame PDF sub-grid scale closure for LES of premixed turbulent flames. Part I: Formalism and application to a bluff-body burner with differential diffusion. *Combust. Flame* **161**, 1756–1774 (2014).
250. De Swart, J. A., Bastiaans, R. J., van Oijen, J. A., de Goey, L. P. H. & Cant, R. S. Inclusion of preferential diffusion in simulations of premixed combustion of hydrogen/methane mixtures with flamelet generated manifolds. *Flow Turbul. Combust.* **85**, 473–511 (2010).
251. Wang, L., Pitsch, H., Yamamoto, K. & Orij, A. An efficient approach of unsteady flamelet modeling of a cross-flow-jet combustion system using LES. *Combust. Theory Model.* **15**, 849–862 (2011).
252. Sanders, J., Chen, J.-Y. & Gökalp, I. Flamelet-based modeling of NO formation in turbulent hydrogen jet diffusion flames. *Combust. Flame* **111**, 1–15 (1997).
253. Porcarelli, A., Kruljević, B. & Langella, I. Suppression of NO_x emissions by intensive strain in lean premixed hydrogen flamelets. *Int. J. Hydrog. Energy* (2023).
254. Æsøy, E., Aguilar, J. G., Bothien, M. R., Worth, N. A. & Dawson, J. R. Acoustic-Convective Interference in Transfer Functions of Methane/Hydrogen and Pure Hydrogen Flames. *J. Eng. Gas Turbine Power* **143**, 121017/1–121017/10 (2021).
255. Æsøy, E. & Dawson, J. R. *TNF workshop* <https://tnfworkshop.org/bluff-body-hydrogen-flame-ntnu-trondheim/> (2024).
256. Beér, J. & Chigier, N. *Combustion Aerodynamics [by] J.M. Beér and N.A. Chigier* (Applied Science Publishers Limited, 1972).
257. Bressloff, N. W. A parallel pressure implicit splitting of operators algorithm applied to flows at all speeds. *Int. J. Numer. Methods Fluids* **36**, 497–518 (2011).

258. Nicoud, F. & Ducros, F. Subgrid-scale stress modelling based on the square of the velocity gradient tensor. *Flow Turbul. Combust.* **62**, 183–200 (1999).
259. Kornev, N. & Hassel, E. Method of random spots for generation of synthetic inhomogeneous turbulent fields with prescribed autocorrelation functions. *Commun. Numer. Meth. Eng.* **23**, 35–43 (2007).
260. Cao, R. R., Pope, S. B. & Masri, A. R. Turbulent lifted flames in a vitiated coflow investigated using joint PDF calculations. *Combust. Flame* **142**, 438–453. ISSN: 00102180 (2005).
261. Ferrante, G., Chen, Z. X. & Langella, I. Dynamic modelling of subgrid scalar dissipation rate in premixed and partially premixed flames with differential filter. *Appl. Therm. Eng.* **248**, 123233 (2024).
262. Yamashita, H., Shimada, M. & Takeno, T. *A numerical study on flame stability at the transition point of jet diffusion flames* in *Symp. (Int.) on Combust.* **26** (1996), 27–34.
263. Peters, N. Laminar diffusion flamelet models in non-premixed turbulent combustion. *Prog. Energy Combust. Sci.* **10**, 319–339 (1984).
264. Domingo, P., Vervisch, L. & Veynante, D. Large-eddy simulation of a lifted methane jet flame in a vitiated coflow. *Combust. Flame* **152**, 415–432 (2008).
265. Lipatnikov, A. N. & Sabelnikov, V. A. An extended flamelet-based presumed probability density function for predicting mean concentrations of various species in premixed turbulent flames. *Int. J. Hydrogen Energy* **45**, 31162–31178 (2020).
266. Knikker, R., Veynante, D. & Meneveau, C. *A priori* testing of a similarity model for large eddy simulations of turbulent premixed combustion. *Proc. Combust. Inst.* **29**, 2105–2111 (2002).
267. Park, G. I., Bassenne, M., Urzay, J. & Moin, P. A simple dynamic subgrid-scale model for LES of particle-laden turbulence. *Phys. Rev. Fluids* **2**, 044301 (2017).
268. Gordon, R., Starner, S., Masri, A. & Bilger, R. *Further Characterisation of Lifted Hydrogen and Methane Flames Issuing into a Vitiated Coflow* in *Proceedings of the 5th Asia-Pacific conference on combustion* (2005), 333–336.
269. Spalding, D. B. A single formula for the law of the wall. *J. Appl. Mech.* **28**, 455–458 (1961).
270. UCSD. *Chemical-Kinetic Mechanisms for Combustion Applications* San Diego Mechanism web page, Mechanical and Aerospace Engineering (Combustion Research), University of California at San Diego. Last Accessed: 2023-10-06. <http://combustion.ucsd.edu>.
271. Cabra, R., Chen, J. Y., Dibble, R. W., Karpetis, A. N. & Barlow, R. S. Lifted methane-air jet flames in a vitiated coflow. *Combust. Flame* **143**, 491–506. ISSN: 00102180 (2005).
272. Selle, L. *et al.* Compressible large eddy simulation of turbulent combustion in complex geometry on unstructured meshes. *Combust. Flame* **137**, 489–505 (2004).

273. Langella, I., Swaminathan, N., Williams, F. A. & Furukawa, J. Large-Eddy Simulation of Premixed Combustion in the Corrugated-Flamelet Regime. *Combust. Sci. Technol.* **188**, 1565–1591 (2016).
274. Berger, L., Kleinheinz, K., Attili, A. & Pitsch, H. Characteristic patterns of thermodynamically unstable premixed lean hydrogen flames. *Proc. Combust. Inst.* **37**, 1879–1886. ISSN: 1540-7489 (2019).
275. Benim, A. C., Pfeiffelmann, B., Ocloń, P. & Taler, J. Computational investigation of a lifted hydrogen flame with LES and FGM. *Energy* **173**, 1172–1181. ISSN: 03605442 (2019).
276. Xia, Y. *et al.* Numerical simulations of a lifted hydrogen jet flame using flamelet generated manifold approach. *J. Eng. Gas Turbine. Power* **144**, 091009 (2022).
277. Kazakov, A. & Frenklach, M. *DRM 19, Mechanism of elementary chemical reaction developed by the Gas Research Institute (GRI)* 1995. <http://combustion.berkeley.edu/drm/>.
278. Li, J., Zhao, Z., Kazakov, A. & Dryer, F. L. An updated comprehensive kinetic model of hydrogen combustion. *Int. J. Chem. Kinet.* **36**, 566–575 (2004).
279. Ó Conaire, M., Curran, H. J., Simmie, J. M., Pitz, W. J. & Westbrook, C. K. A comprehensive modeling study of hydrogen oxidation. *Int. J. Chem. Kinet.* **36**, 603–622 (2004).
280. Burke, M. P., Chaos, M., Ju, Y., Dryer, F. L. & Klippenstein, S. J. Comprehensive H₂/O₂ kinetic model for high-pressure combustion. *Int. J. Chem. Kinet.* **44**, 444–474 (2012).
281. Issa, R. I. Solution of the implicitly discretised fluid flow equations by operator-splitting. *J. Comput. Phys.* **62**, 40–65 (1986).
282. Lapenna, P. E., Lamioni, R. & Creta, F. Subgrid modeling of intrinsic instabilities in premixed flame propagation. *Proc. Combust. Inst.* **38**, 2001–2011. ISSN: 1540-7489 (2021).
283. Lapenna, P. E., Remiddi, A., Molinaro, D., Indelicato, G. & Creta, F. A-posteriori analysis of a data-driven filtered wrinkled flamelet model for thermodynamically unstable premixed flames. *Combustion and Flame* **259**, 113126. ISSN: 0010-2180 (2024).
284. Masucci, A., Ferrante, G., Ghisu, T., Giusti, A. & Langella, I. Investigation of Differential Diffusion and Strain Coupling in Large Eddy Simulations of Hydrogen-Air Flames. *Combust. Sci. Technol.* **0**, 1–17 (2026).
285. Chen, Z. X., Langella, I., Barlow, R. S. & Swaminathan, N. Prediction of local extinctions in piloted jet flames with inhomogeneous inlets using unstrained flamelets. *Combust. Flame* **212**, 415–432 (2020).
286. Bilger, R., Stárner, S. & Kee, R. On reduced mechanisms for methane- air combustion in nonpremixed flames. *Combust. Flame* **80**, 135–149 (1990).
287. Celik, I., Cehreli, Z. & Yavuz, I. Index of resolution quality for large eddy simulations. *J. Fluids Eng.* (2005).

288. Porcarelli, A., Lapenna, P. E., Creta, F. & Langella, I. Stability analysis of thermodynamically unstable counterflow lean premixed hydrogen flames. *Proc. Combust. Inst.* **41**, 105906. ISSN: 1540-7489 (2025).
289. Sommerer, Y. *et al.* Large eddy simulation and experimental study of flashback and blow-off in a lean partially premixed swirled burner. *Journal of Turbulence* **5**, 037 (2004).
290. Ferrante, G., Doodeman, L., Rao, A. G. R. & Langella, I. *LES of Hydrogen-Enriched Methane Flames in a Lean-Burn Combustor With Axial Air Injection in Turbo Expo: Power for Land, Sea, and Air* **86960** (2023), V03BT04A015.
291. Doodeman, L. W. *Numerical Simulation of a Premixed Hydrogen Gas Turbine Combustor* Mentor: Ivan Langella; Committee member: A. Rao. Master's thesis (Delft University of Technology, Faculty of Aerospace Engineering, Delft, The Netherlands, Nov. 2022). <https://resolver.tudelft.nl/uuid:df146801-51cf-4555-ae97-e1348560a6ca>.
292. Abbasciano, G. *Large Eddy Simulations of a Lean Premixed Swirl-Stabilized Combustor* Supervisor: Giacomo Bruno Azzurro Persico; Co-supervisor: Ivan Langella. Master's thesis (Politecnico di Milano, School of Industrial and Information Engineering, Milan, Italy, Dec. 2023). <https://www.politesi.polimi.it/handle/10589/214450>.
293. Tao, C. & Zhou, H. Effect of hydrogen blending on thermoacoustic instability and flashback dynamics in partially premixed methane-air flames. *Fuel* **393**, 135007 (2025).
294. Allison, P. M., Driscoll, J. F. & Ihme, M. Acoustic characterization of a partially-premixed gas turbine model combustor: Syngas and hydrocarbon fuel comparisons. *Proc. Combust. Inst.* **34**, 3145–3153 (2013).
295. Marragou, S., Magnes, H., Poinot, T., Selle, L. & Schuller, T. Stabilization regimes and pollutant emissions from a dual fuel CH₄/H₂ and dual swirl low NO_x burner. *Int. J. Hydrog. Energy* **47**, 19275–19288 (2022).
296. Marragou, S. *et al.* Experimental analysis and theoretical lift-off criterion for H₂/air flames stabilized on a dual swirl injector. *Proc. Combust. Inst.* **39**, 4345–4354 (2023).
297. Reichel, T. G., Goeckeler, K. & Paschereit, O. Investigation of lean premixed swirl-stabilized hydrogen burner with axial air injection using OH-PLIF imaging. *J. Eng. Gas Turbine Power* **137**, 111513 (2015).
298. Karagozian, A. R. The jet in crossflow. *Physics of Fluids* **26** (2014).
299. Margason, R. J. Fifty years of jet in cross flow research. In *AGARD, Computational and Experimental Assessment of Jets in Cross Flow* (1993).
300. Meier, W., Weigand, P., Duan, X. R. & Giezendanner-Thoben, R. Detailed characterization of the dynamics of thermoacoustic pulsations in a lean premixed swirl flame. *Combust. Flame* **150**, 2–26 (2007).
301. Karyeyen, S., Feser, J. S. & Gupta, A. K. Hydrogen concentration effects on swirl-stabilized oxy-colorless distributed combustion. *Fuel* **253**, 772–780. ISSN: 0016-2361 (2019).

302. Fric, T. & Roshko, A. Vortical structure in the wake of a transverse jet. *J. Fluid Mech.* **279**, 1–47 (1994).
303. Majander, P. & Siikonen, T. Large-eddy simulation of a round jet in a cross-flow. *International Journal of Heat and Fluid Flow* **27**, 402–415. ISSN: 0142-727X (2006).
304. Cortelezzi, L. & Karagozian, A. R. On the formation of the counter-rotating vortex pair in transverse jets. *Journal of Fluid Mechanics* **446**, 347–373 (2001).
305. Salewski, M., Stankovic, D. & Fuchs, L. Mixing in Circular and Non-circular Jets in Crossflow. *Flow Turbulence and Combustion* **80**, 255–283 (Apr. 2008).
306. Liscinsky, D., True, B. & Holdeman, J. Crossflow mixing of noncircular jets. *Journal of Propulsion and Power* **12** (Mar. 1995).
307. Wegner, B., Huai, Y. & Sadiki, A. Comparative study of turbulent mixing in jet in cross-flow configurations using LES. *International Journal of Heat and Fluid Flow* **25**. Selected papers from the 4th International Symposium on Turbulence Heat and Mass Transfer, 767–775. ISSN: 0142-727X (2004).
308. Schetz, J. A. & Harsha, P. T. Injection and Mixing in Turbulent Flow (Progress in Aeronautics and Astronautics, Vol. 68). *Journal of Fluids Engineering* **102**, 525–525. ISSN: 0098-2202 (Dec. 1980).
309. Crabb, D., Durão, D. F. G. & Whitelaw, J. H. A Round Jet Normal to a Crossflow. *Journal of Fluids Engineering-transactions of The Asme* **103**, 142–153 (1981).
310. Holdeman, J. D. Mixing of multiple jets with a confined subsonic crossflow. *Prog. Energy Combust. Sci.* **19**, 31–70. ISSN: 0360-1285 (1993).
311. Kandakure, M. T., Patkar, V. C., Patwardhan, A. W. & Patwardhan, J. A. Mixing with Jets in Cross-Flow. *Industrial & Engineering Chemistry Research* **48**, 6820–6829 (2009).
312. Li, Z., Murugappan, S., Gutmark, E. & Vallet, L. *Numerical Simulation and Experiments of Jets in Cross Flow* in *Collection of Technical Papers - 44th AIAA Aerospace Sciences Meeting* **6** (Jan. 2006). ISBN: 978-1-62410-039-0.
313. Bons, J. P., Sondergaard, R. & Rivir, R. B. The Fluid Dynamics of LPT Blade Separation Control Using Pulsed Jets. *Journal of Turbomachinery* **124**, 77–85. ISSN: 0889-504X (Feb. 2001).
314. Bilger, W. & Dibble, R. W. Differential Molecular Diffusion Effects in Turbulent Mixing. *Combust. Sci. Technol.* **28**, 161–172 (1982).
315. Syred, N., Chigier, N. & Beér, J. Flame stabilization in recirculation zones of jets with swirl. *Symposium (International) on Combustion* **13**. Thirteenth symposium (International) on Combustion, 617–624. ISSN: 0082-0784 (1971).
316. Ahmed, S. & So, R. Characteristics of air jets discharging normally into a swirling crossflow. *AIAA Journal* **25**, 429–435 (Feb. 1987).
317. So, R. & Ahmed, S. Helium jets discharging normally into a swirling air flow. *Experiments in fluids* **5**, 255–262 (1987).

318. Tan, T., Fan, W. & Zhang, R. A numerical and experimental investigation into the mixing mechanism of hydrogen transverse jets into an air swirl flow. *Physics of Fluids* **36**, 037147 (Mar. 2024).
319. Link, S. *et al.* Experimental and numerical investigation of mixing in a partially premixed CH₄/H₂ combustor. *Int. J. Hydrog. Energy* **141**, 176–192 (2025).
320. Oamjee, A. & Sadanandan, R. Suitability of helium gas as surrogate fuel for hydrogen in H₂-Air non-reactive supersonic mixing studies. *Int. J. Hydrog. Energy* **47**, 9408–9421. ISSN: 0360-3199 (2022).
321. Demayo, T., Leong, M., Samuelsen, G. & Holdeman, J. Assessing jet-induced spatial mixing in a rich, reacting crossflow. *Journal of propulsion and power* **19**, 14–21 (2003).
322. OpenFOAM. *WaveTransmissiveFvPatchField Class Reference* Accessed: 2025-02-25. 2021. https://cpp.openfoam.org/v13/classFoam_1_1%20waveTransmissiveFvPatchField.html#details.
323. Merk, M. *et al.* Measurement and simulation of combustion noise and dynamics of a confined swirl flame. *AIAA Journal* **56**, 1930–1942 (2018).
324. Poinso, T. J. & Lelef, S. K. Boundary conditions for direct simulations of compressible viscous flows. *J. Comput. Phys.* **101**, 104–129 (1992).
325. Fang, Z. *et al.* Thermal mixing and structure of the jet in swirling crossflow. *Physics of Fluids* **36** (2024).
326. Dimotakis, P. E. Turbulent mixing. *Annu. Rev. Fluid Mech.* **37**, 329–356 (2005).
327. Bevilaqua, P. M. & Lykoudis, P. S. Turbulence memory in self-preserving wakes. *J. Fluid Mech.* **89**, 589–606 (1978).
328. Jaravel, T., Riber, E., Cuenot, B. & Bulat, G. Large eddy simulation of an industrial gas turbine combustor using reduced chemistry with accurate pollutant prediction. *Proc. Combust. Inst.* **36**, 3817–3825 (2017).
329. Franzelli, B., Riber, E., Gicquel, L. Y. & Poinso, T. Large eddy simulation of combustion instabilities in a lean partially premixed swirled flame. *Combust. Flame* **159**, 621–637 (2012).
330. Franzelli, B., Riber, E. & Cuenot, B. Impact of the chemical description on a Large Eddy Simulation of a lean partially premixed swirled flame. *Comptes Rendus Mécanique* **341**, 247–256 (2013).
331. Gövert, S., Mira, D., Kok, J. B., Vázquez, M. & Houzeaux, G. The effect of partial premixing and heat loss on the reacting flow field prediction of a swirl stabilized gas turbine model combustor. *Flow Turbul. Combust.* **100**, 503–534 (2018).
332. Perrin-Terrin, J.-B. *et al.* Plasma-assisted combustion of hydrogen swirling flames: Extension of lean blowout limit and NO_x emissions. *Proc. Combust. Inst.* **40**, 105546 (2024).
333. Gong, Y., Fredrich, D., Marquis, A. J. & Jones, W. P. Numerical investigation of combustion instabilities in swirling flames with hydrogen enrichment. *Flow Turbul. Combust.* **111**, 953–993 (2023).

334. Pachano, L. *et al.* Numerical assessment of the effect of hydrogen enrichment of a technically premixed swirl-stabilized natural gas flame in Turbo Expo: Power for Land, Sea, and Air **86953** (2023), V03AT04A076.
335. Meloni, R., Nassini, P. & Andreini, A. Model development for the simulation of the hydrogen addition effect onto the NO_x emission of an industrial combustor. *Fuel* **328**, 125278. ISSN: 0016-2361 (2022).
336. Nagao, J. *et al.* Large-eddy simulation of a lean-premixed hydrogen flame in a low-swirl combustor under combustion instability. *Physics of Fluids* **35** (2023).
337. Kumar, A. D., Massey, J. C., Boxx, I. & Swaminathan, N. Effects of hydrogen enrichment on thermoacoustic and helical instabilities in swirl stabilised partially premixed flames. *Flow Turbul. Combust.* **112**, 689–727 (2024).
338. Amerighi, M., Andreini, A., Reichel, T., Tanneberger, T. & Paschereit, C. LES investigation of a swirl stabilized technically premixed hydrogen flame with FGM and TFM models. *Applied Thermal Engineering* **247**, 122944 (2024).
339. De Lauso, V. *Hydrogen-Enriched Methane Flames in a Swirl Stabilized Combustor with Axial Air Injection* Mentor: I. Langella, Flight Performance and Propulsion. Master's thesis (Delft University of Technology, Faculty of Aerospace Engineering, 2024). <http://resolver.tudelft.nl/uuid:5d233be1-d8bb-4369-bd2e-6ed5278fb8eb>.
340. Saxena, P. & Williams, F. A. Testing a small detailed chemical-kinetic mechanism for the combustion of hydrogen and carbon monoxide. *Combust. Flame* **145**, 316–323. ISSN: 0010-2180 (2006).
341. Liu, W. & Jones, W. LES of dual-swirl non-premixed H₂ turbulent flame using Eulerian stochastic fields. *Combust. Flame* **275**, 114094. ISSN: 0010-2180 (2025).
342. Cadence Design Systems. *Fidelity Pointwise for CFD Meshing* Accessed: 2025-07-17. 2024. https://www.cadence.com/en_US/home/tools/system-analysis/computational-fluid-dynamics/fidelity.html#fidelity-pointwise.
343. Richardson, E., Aditya, K., Shin, D. & Chen, J. *Fluid age -based modelling for premixed combustion in shear flows* in Eleventh International Symposium on Turbulence and Shear Flow Phenomena (TSFP11) (2019).
344. Guiberti, T. F., Durox, D., Scouflaire, P. & Schuller, T. Impact of heat loss and hydrogen enrichment on the shape of confined swirling flames. *Proc. Combust. Inst.* **35**, 1385–1392 (2015).
345. Syred, N. A review of oscillation mechanisms and the role of the precessing vortex core (PVC) in swirl combustion systems. *Prog. Energy Combust. Sci.* **32**, 93–161 (2006).
346. Galley, D., Ducruix, S., Lacas, F. & Veynante, D. Mixing and stabilization study of a partially premixed swirling flame using laser induced fluorescence. *Combust. Flame* **158**, 155–171 (2011).

347. Oberleithner, K., Stöhr, M., Im, S. H., Arndt, C. M. & Steinberg, A. M. Formation and flame-induced suppression of the precessing vortex core in a swirl combustor: Experiments and linear stability analysis. *Combust. Flame* **162**, 3100–3114. ISSN: 0010-2180 (2015).
348. Link, S., Dave, K., Eitelberg, G., Gangoli Rao, A. & de Domenico, F. *The influence of the confinement ratio on the precessing vortex core dynamics in a counter-rotating dual swirler* in *Turbo Expo: Power for Land, Sea, and Air* **86960** (2023), V03BT04A001.
349. Biagioli, F. & Güthe, F. Effect of pressure and fuel–air unmixedness on NO_x emissions from industrial gas turbine burners. *Combust. Flame* **151**, 274–288. ISSN: 0010-2180 (2007).
350. Kutkan, H. *et al.* Modeling of turbulent premixed CH₄/H₂/air flames including the influence of stretch and heat losses. *J. Eng. Gas Turbine Power* **144**, 011020 (2022).
351. Porcarelli, A. & Langella, I. Mitigation of preferential diffusion effects by intensive strain in lean premixed hydrogen flamelets. *Proc. Combust. Inst.* **40**, 105728 (2024).
352. Kutkan, H. *Modelling Turbulent Premixed CH₄/H₂/air Flames with Effects of Stretch, Heat Loss and Non-unity Lewis Number for Flame Stabilization and Dynamics* PhD thesis (Università degli studi di Genova, 2023).
353. Fathi, M., Hickel, S., Doan, N. A. K. & Langella, I. Effects of intense strain on flame structure and NO_x generation in turbulent counterflow lean-premixed hydrogen flames. *Combust. Flame* **282**, 114459 (2025).
354. Lehmann, T., Dimidziev, N., Howarth, T. L., Gauding, M. & Pitsch, H. Effects of Intrinsic Flame Instabilities on Nitrogen Oxide Formation in Laminar Premixed Ammonia/Hydrogen/Air Flames. *arXiv preprint arXiv:2503.13370* (2025).

A

APPENDIX A

A.1. MESH SENSITIVITY FOR THE LIFTED FLAME IN HOT COFLOW

Turbulence resolution is among the most sensitive aspects for the Cabra flame (test case A), as it affects the jet/coflow mixing and the intensity of the shear layer, ultimately determining the correct prediction of the jet flow features and flame stabilization. Moreover, the Cabra flame exhibits a strong sensitivity to the imposed turbulent boundary conditions. A mesh sensitivity is carried out in this section to provide some evidence on the above points. Note that by meaning of Pope's criterion (Fig. 6.1 in the main text) the 3M cells unstructured mesh has a degree of refinement which is comparable to the 1M cells block-structured grid in the region of the flame, as 80% of the turbulent kinetic energy is resolved in both cases.

In Figs. A.1-A.2 the sensitivity of the computed statistics to the mesh refinement is reported for both the block-structured (BS) and unstructured (US) meshes. Note that, due to time limitation and limited resources, we have performed the additional simulations for the non-reactive case, implying comparisons with experiments are meaningful only upstream of the flame front (about $x = 11D$). The following observations are made:

- For the BS mesh, for which the 1M cells case yields already a good match with experiments, the predicted turbulent flow field appears to be almost insensitive to the mesh refinement.
- Refining the unstructured mesh from 3M to 8M cells does not lead to substantial differences in the turbulent velocity and temperature fields prediction, while some improvement is observed from the mixture fraction radial profiles. This suggests that numerical diffusion plays a stronger role on the US mesh as one would expect.
- The rms level at $1D$ obtained using the US meshes is under-predicted as compared to experiment, which leads to incorrect mixing further downstream. Given the strong sensitivity of the studied flame to the turbulence level upstream, the value of l_0 imposed at the inlet was changed in the simulations presented in Section 6.3

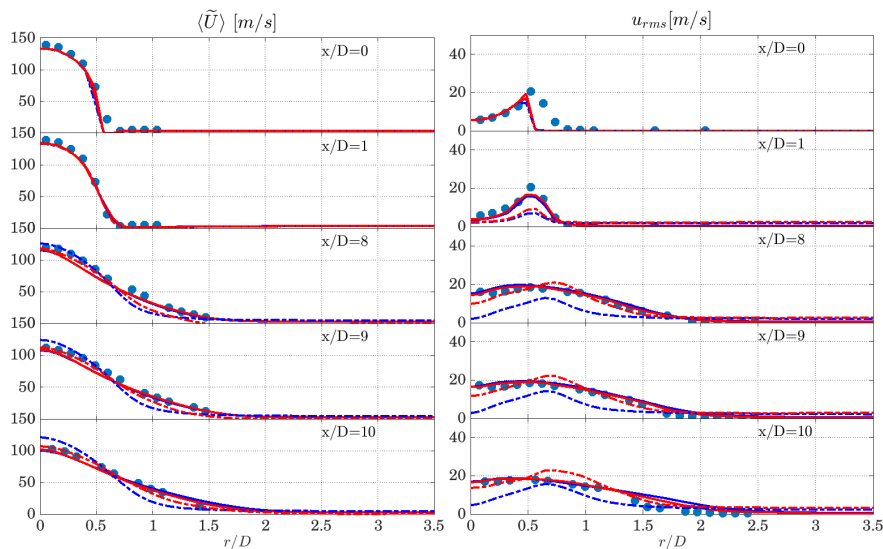


Figure A.1: Radial profiles of time averaged (left) and rms (right) axial velocity at different axial locations from experimental measurements (symbols) and LES: 1M cells BS mesh (—), 3M cells US mesh (- -), 8M cells BS mesh (—), and 8M cells US mesh (- -). All simulations refer to an integral length scale reported at the inlet of $l_0 = 0.07D$.

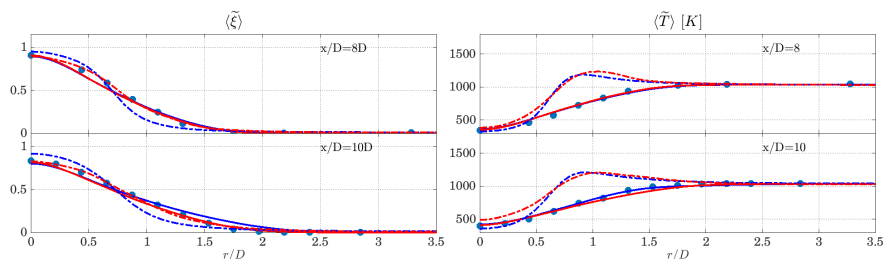


Figure A.2: Radial profiles of time averaged mixture fraction (left) and temperature (right) at different axial locations from experimental measurements (symbols) and LES. Legend is as for Fig. A.1.

in order to ensure that the lift-off height would remain about the same as for the BS mesh in the reacting flow case.

Further indication of the effect of numerical diffusion is illustrated in Fig. A.3, showing instantaneous contours of velocity field at two transversal locations, $x = 0D$ (nozzle exit), and $x = 1D$. Results show that at $x = 0D$, where the synthetic turbulence conditions are imposed, similar turbulent characteristics are obtained on block-structured and unstructured meshes. Nevertheless, differences are clearly observable one diameter downstream, which is a result of stronger numerical diffusion in the unstructured mesh case and imposed integral length scale. This results suggest that to obtain the same level of turbulence resolution of the block-structured mesh one has to further refine the mesh in the unstructured case. This additional refinement is however not performed in

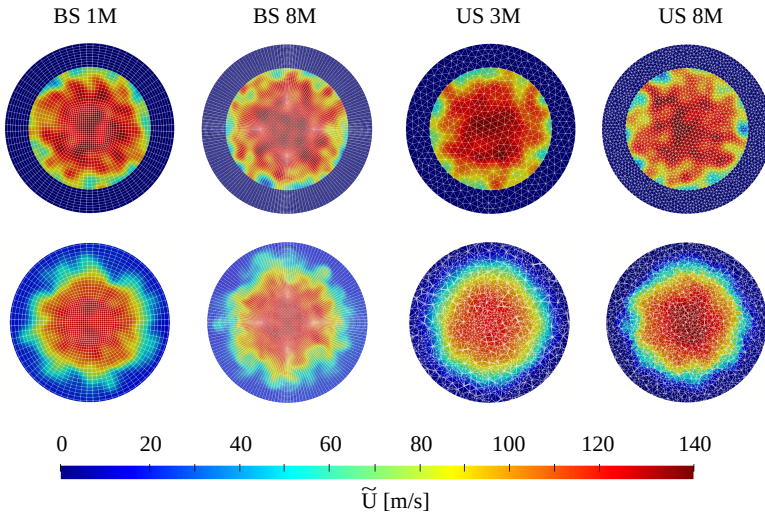


Figure A.3: Instantaneous velocity field at $x = 0D$ (top) and $x = 1D$ (bottom) for different meshes.

this study since the objective is to compare algebraic and differential test-filters, which is performed at a fixed LES filter size. Nevertheless, the analysis above indicates that one has to be mindful when interpreting results obtained from block-structured and unstructured meshes.

B

APPENDIX B

B.1. CABRA FLAME: SENSITIVITY TO INLET TURBULENCE

The Cabra flame, in particular its lift-off height, was observed to be very sensitive to the turbulent inlet conditions [260]. For this reason a preliminary analysis is carried out to ensure an accurate prediction of the jet spreading rate and its mixing with the coflow. Measured axial and radial rms velocity profiles, u' and v' , reported in [260], are used as input parameters for the synthetic turbulence model [259] at the inlet. A sensitivity analysis on the imposed integral length scale ℓ_0 is carried out, together with an investigation of the effects caused by the velocity rms intensity on jet spreading and turbulent mixing. The imposed integral length scale is varied between 7% and 50% of the nozzle diameter D , and the rms intensity is varied from the measured value (characterized by a peak of 20% of jet bulk velocity) to 5% of this value. Mean temperature and mixture fraction centreline profiles are compared to experimental measurements [77] in Fig. B.1. The region upstream of the flame stabilisation location, $x \leq 10D$, is dominated by the mixing of the fuel stream with the coflow, which affects the distribution of mixture fraction and rms velocity and in turn the flame lift-off height. Results show that reducing velocity rms and integral length scale at the inlet causes a weaker jet spreading rate and a slower jet/coflow mixing. This results in a longer potential core, which is indicated by the less steep decay of mixture fraction along the centreline. A similar effect of the rms intensity was observed in [260]. Nevertheless, the effect of inlet rms is observed to be mild as compared to that of the integral length scale at the inlet ℓ_0 . For $\ell_0 = 0.5D$ in particular an overprediction of the mixing intensity is observed, resulting in the mixture fraction quickly falling within the flammability range and a consequent stabilisation of the flame significantly more upstream as compared to the experiments. A good match with the measurements is observed instead for $\ell_0 = 0.07D$. This condition is thus used for the simulations in the present study.

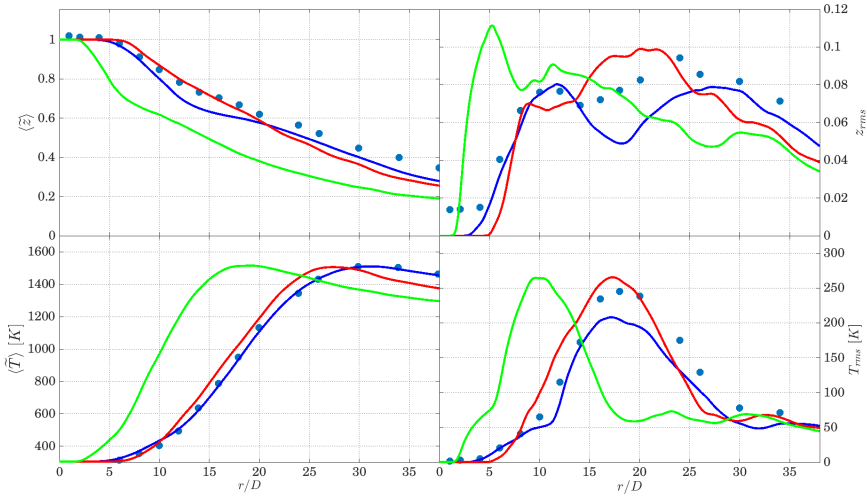


Figure B.1: Centreline profiles of mean and rms temperature and mixture fraction. Symbols: experimental measurements from [77]. Lines: LES results obtained using the following conditions at the nozzle inlet: $\max(u_{rms}) = 20$ m/s, $\ell_0 = 0.07D$ (—); $\max(u_{rms}) = 20$ m/s, $\ell_0 = 0.5D$ (—); $\max(u_{rms}) = 1$ m/s, $\ell_0 = 0.15D$ (—).

B.2. CABRA FLAME: SENSITIVITY TO KINETIC MECHANISM

A parametric analysis is performed here to investigate on the effects of the chosen kinetic mechanism in the flamelet database on the flame lift-off height and the predicted statistics in the LES. Fig. B.2 shows the contour plots of the water-based scaled progress variable reaction rate in the progress variable and mixture fraction space resulting from 1D flamelets computation, as described in Sec. 7.1.1. The following kinetic mechanisms are compared: DRM19 [277], Li *et al.* [278], Ó Conaire [279], and San Diego [270]. The peak reaction rate value for each flamelet and from each mechanism is also plotted against mixture fraction in Fig. B.2. When the assumption of species equidiffusivity is used, Li *et al.* and Ó Conaire mechanisms result in lower reaction rate peak values with respect to DRM19 and San Diego, and the peak location is found at slightly richer conditions than in the other two mechanisms. The San Diego mechanism gives the highest reaction rate values for the lean flamelets, followed by DRM19 that gives the highest values on the rich side. As compared to San Diego mechanism, Li *et al.* and Ó Conaire give similar values on the rich side and lower values for lean flamelets. When differential diffusion is included, the reaction rate values are observed to increase on the rich side and decrease on the lean side as compared to the equidiffusivity case, with the peak shifting towards richer conditions. Also, the range in progress variable space with non-zero reaction rate is narrower for the lean flamelets and wider for the rich ones. Differences are further observed in the reaction rates predicted by the various mechanisms when differential diffusion is taken into account. In particular, the DRM19 mechanism yields a higher increase of maximum reaction rate on the rich flamelets when differential diffusion is included as compared to the other mechanisms. On the lean side, Li *et al.* and Ó Conaire mechanisms exhibit the weakest reaction rate.

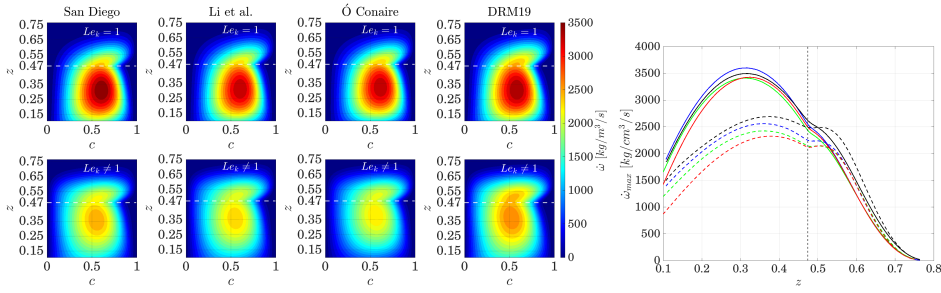


Figure B.2: Left: contour plots of water-based scaled progress variable reaction rate in the $c - z$ space for a jet/coflow flamelet database with the reactants conditions reported in Tab. 4.1. Calculations obtained with unity Lewis number (top) and mixture averaged diffusion model (bottom), using different kinetic mechanisms. The stoichiometric condition $z_{st} = 0.474$ is marked as a horizontal white dashed line. Right: maximum reaction rate value versus mixture fraction from flamelet computations obtained using San Diego [270] (—), Ó Conaire [279] (—), Li *et al.* [278] (—) and DRM19 [277] (—) mechanisms. Solid and dashed lines refer respectively to the cases without and with differential diffusion. The stoichiometric condition $z_{st} = 0.474$ is marked as a vertical black dashed line.

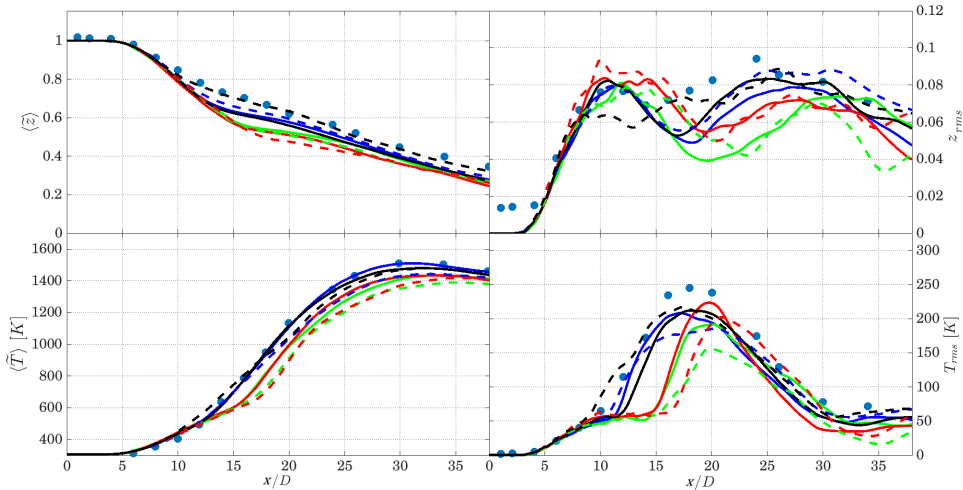


Figure B.3: Centreline profiles of mean and rms temperature and mixture fraction $\bar{\phi}$. Symbols: experimental measurements from [77]. Lines: LES results obtained using San Diego [270] (—), Ó Conaire [279] (—), Li *et al.* [278] (—) and DRM19 [277] (—) mechanisms. Solid and dashed lines refer respectively to the cases without and with differential diffusion modelling.

The aforementioned differences in the flamelets database affect the flame characteristics in the LES. This can be appreciated by looking at the average and rms centerline temperature profiles in Fig. B.3. The lower reaction rates observed for Li *et al.* and Ó Conaire mechanisms in the unity-Lewis case result in an overestimation of lift-off height (identified in the figure by the steep increase of centreline temperature) and consequently lower temperatures at downstream locations. San Diego and DRM19 yield instead similar predictions, with the former predicting the flame anchoring point slightly

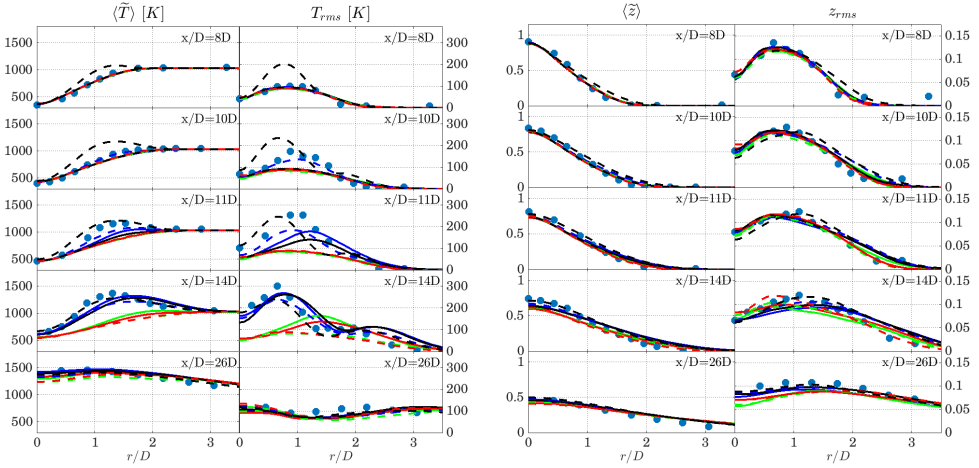


Figure B.4: Radial profiles of time averaged and rms values of temperature and mixture fraction. Legend as for Fig. B.3.

more upstream (see also radial average and rms temperature profiles in Fig. B.4). When differential diffusion is included in the database, different trends are observed for the various mechanism. San Diego and DRM19 mechanisms yield a more upstream prediction of the flame anchoring point (see Figs. B.3 and B.4), which is due to the higher reaction rate at rich conditions observed for these mechanisms in Fig. B.2. An overprediction of the flame lift-off height with respect to the unity Lewis number case is observed instead when Li *et al.* and Ó Conaire mechanisms are used. This is due to the fact that these mechanisms yield the lowest reaction rate values for the lean flamelets. Overall, the San Diego mechanism is observed to yield the best match with experimental results and is therefore used in the present work for the analysis presented in the main text.

B.3. SENSITIVITY TO THE DIFFERENTIAL DIFFUSION MODEL VARIABLES

The strategies to model differential diffusion at the resolved scales presented in the main text were originally developed for DNS of laminar flames. When applied to the LES framework, the filtering operation and the use of the presumed FDF can result in an attenuation of the correcting terms responsible for the controlling variables redistribution. These are the mixture fraction source term in models M1_{RES} and M1_{TAB}, and the gradients of the parameters β_j in model M2. For this reason, a sensitivity analysis of model M2 is carried out by increasing the magnitude of parameter β_z in Eq. (3.29) by a factor of four. This sensitivity analysis may also provide an overview of the expected trend associated with the use of a subgrid model for the differential diffusion/flame curvature interaction, imposing increased resolved diffusive fluxes. The case with increased β_z (renamed here as M2a to avoid confusion) is compared to the baseline case M2 of Table 7.1 discussed in the main text.

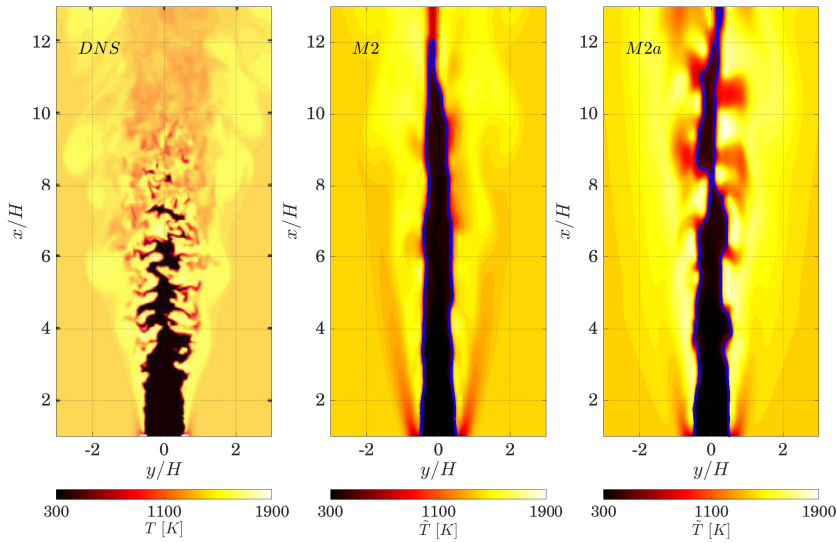


Figure B.5: Midplane temperature contours from DNS [53] (left), LES M2 model of Table 7.1 (centre) and LES M2a case with increased β_z value in Eq. (3.29) (right).

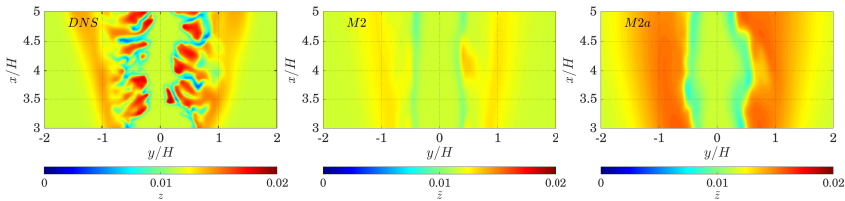


Figure B.6: Midplane mixture fraction contours from DNS [53] (left), LES M2 model of Table 7.1 (centre) and LES M2a case with increased β_z value in Eq. (3.29) (right).

For the premixed flame, the increase in the mixture fraction diffusive flux correction leads to a significantly stronger development of thermodiffusive instabilities. As can be observed from the temperature contour plots in Fig. B.5, the flame front appears more wrinkled in case M2a as compared to case M2, with formation of more pronounced cusps and occurrence of higher superadiabatic temperature peaks. Consistently, contour plots in Fig. B.6 show lower mixture fraction values upstream of the flame front for case M2a (increased value of β_z), and in the presence of cusps, as well as higher values of mixture fraction downstream of the flame front, in correspondence of convex flame front curvature towards the reactants. This leads to a broader range of mixture fraction values in closer agreement to the one observed in the DNS [53]. The comparison of the scatter plots in Fig. B.7 (bottom) confirms that the reciprocal interaction between the higher mixture fraction diffusive flux (caused by higher values of β_z) and increased flame wrinkling leads to a broader mixture fraction range in the burning states, as compared

B

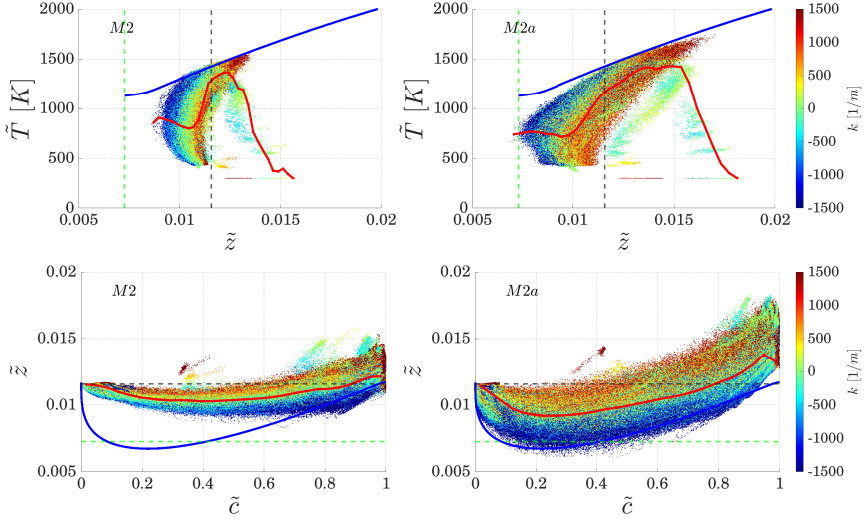


Figure B.7: Scatter plots of filtered temperature versus filtered mixture fraction (top) and mixture fraction versus filtered progress variable (bottom) obtained from the LES of the premixed slot burner using LES model M2 of Table 7.1 (centre) and LES model M2a with increased β_z value in Eq. (3.29) (right). Only values within the flame, identified using $0.1 < \tilde{c} < 0.9$, are considered. Lines as in Fig. 7.5.

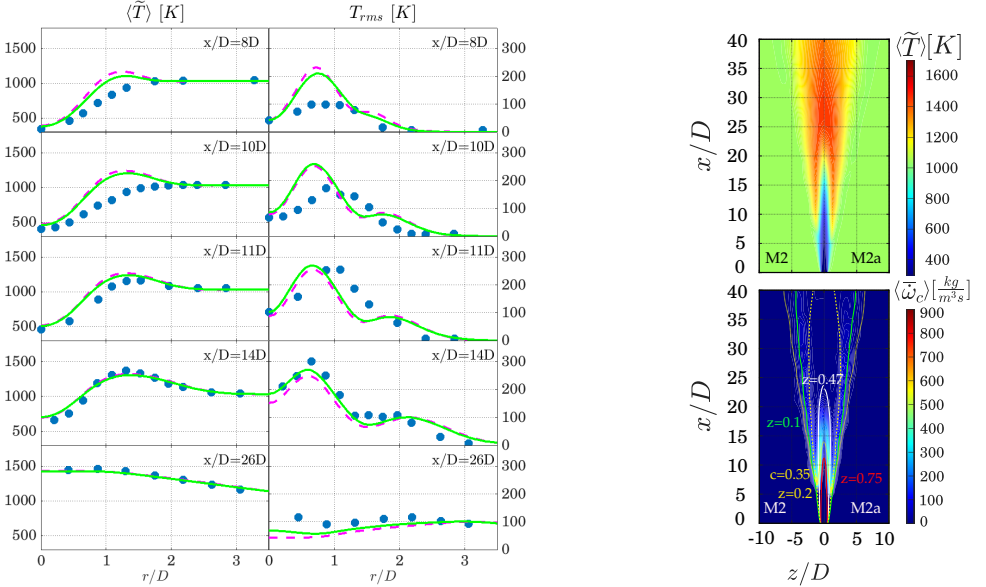


Figure B.8: Left: Radial profiles of time-averaged and rms values of temperature. Symbols: measurements [77]. Lines: LES results with models M2 of Table 7.2 (—) and M2a case with increased β_z value in Eq. (3.29) (—). Right: Mid-plane contours of time-averaged (top) temperature, and averaged filtered reaction rate (bottom) obtained from LES using the models M2 and M2a. Lines as in Fig. 7.6.

to the baseline case. In particular, model M2a shows overall leaner zero curvature burning states and all the mixture fraction values of the unstretched laminar flamelet (blue line) are reached, in correspondence of highly negative flame front curvatures. Moreover, model M2a predicts richer states associated with positive curvature throughout the progress variable range and in particular more towards the products $\tilde{c} > 0.5$. The scatter plots of temperature (top row) show that richer reacting states predicted in case M2a are responsible for the higher aforementioned temperature peaks. The stronger mixture fraction diffusive flux couples with flame front curvature, enhancing the mechanism of flame wrinkling, as observable from the higher values of curvature magnitude.

The same analysis is repeated for the partially premixed lifted flame, although the sensitivity to the parameter β_z is milder than in the premixed case. The temperature and averaged reaction rate contour plots in Fig. B.8 show that a 4 times increment in β_z results in an upstream shift of the flame base of about $2D$. The same behaviour can be observed from the radial profiles in Fig. right. This sensitivity highlights the relevance of the mixture fraction diffusive flux. In facts, even if turbulent mixing remains predominant for the studied lifted flame, an increased mixture fraction diffusive flux enhances the inert jet/coflow mixing upstream of the flame and can cause a significant redistribution of mixture fraction on the flame front, which in turns leads to an upstream prediction of the flame stabilization point.

ACKNOWLEDGEMENTS

It will be hard to enclose in a few pages all the gratitude I have for the many people who made this achievement possible, but I will try. Aside from all the objectives, knowledge and results, this PhD journey made me know incredible new people and helped me realize how important those already in my life are. For this reason, I want to spend some words to acknowledge them.

First of all, I want to thank my copromotor and daily supervisor Ivan for believing in me from day one and mentoring me throughout these years. Thank you for the constant support in the difficult initial moments, when everything still seemed uncertain. Thank you for introducing me to the fascinatingly complex field of numerical combustion, guiding me through the intricate logic of OpenFOAM, and helping me develop the challenging skill of scientific writing. Thank you for being demanding when necessary, pushing me to improve and grow, but at the same time always extremely supportive, especially when meeting deadlines meant revising until 3 AM. And I want to thank my promoters Arvind and Georg for guiding me in learning how to be a scientist, giving me the chance to question and at the same time defend every choice made and every result obtained. Your trust and guidance helped me develop both independence and critical thinking. Thank you Arvind for your aphorisms, the stimulating conversations, and the fun times shared at conferences and work trips. Thank you Georg for the engaging lunchtime conversations about fluid dynamics annotated on table napkins, your challenging questions, and the beautiful flow visualization pictures. Thank you for the guidance you gave me by sharing your professional and personal experiences. These exchanges always left me with something valuable to reflect on.

Moving on, I want to give an enormous thank you to my colleagues and friends who supported me during these years. Meeting them and/or strengthening our friendship was among the best outcomes of pursuing this PhD journey.

Thank you to Matteo, for our friendship that in just two months escalated from being the only two office mates in pandemic times to inseparable fellow adventurers. Thank you for all the road trips, nautical expeditions, and the kilometers of coastline explored that lead us to meet the most incredible mythological characters. In these years, you taught me a lot, you have been a reference point for me and a true example of perseverance, commitment, altruism and integrity. And thank you to Katariina, thank you both guys for your kindness and hospitality, always ready to give me some thoughtful advice and to go for a soothing walk together.

Thanks to Davide (Duracell) for the countless hours spent on the roads across Europe importing Italian goods to the Netherlands, turning transportation missions into epic adventures. And thank you to the sweet Federica, for your support and for bearing all my worries and complaints while I was preparing every single progress meeting. Thank you both guys for the picnics by the Dutch canals where we canoed and fished creatures of the abyss, the gourmet dinners, ski trips, and sailing (mis)adventures. Thanks

for contributing to the formulation and experimental testing of proposition number ten accompanying this dissertation.

Thank you to Fabio for all our sea and mountain adventures, late nights in the office, the many hours spent jamming in cubicles, and endless discussions about how to balance everything in a happy life. And to Lorenzo G., for the lunches in Pescara, for his contagious laughter that crosses walls, and even for failing the belaying exam together. Thank you for the RANS of the APPU combustor that you ran “for fun”, showing that the swirling jet would actually open at steady state.

To Francesco (Falce) for being my coach and guide in research, life, and sailing. I am deeply grateful for your wise advice and for all the times your experience got us out of trouble. And of course also to his wife Giulia, thank you both for your hospitality, our piracy sailing adventures, the cosy dinners together, and for adopting me along the way (I was clearly pre-testing your parental skills).

My office mates Evert and André, thank you for your everyday company and the enlightening conversations on hydrogen flames. Thank you Evert for the incredible dinners you cooked for us and for leading the decoration of the office with a nice plantation. Thank André for all the climbing sessions and your free Portuguese classes. Thanks to all my colleagues and friends I met at FPT: Andrea, Alessandro C., Francesco N., Dabo, Francesco T., Francesco V., Josh, Murillo, Wessel, Ankit, Debduitta, Floyd, Nikki, Nitish C., Nitish A., Alessio, Kilian, Antonio S., Reynard, Blanca, Ruben, Kostas, Ardy, Carmine, Emanuele, Anastasia, Cristina. Thank you for the many shared moments: the debates at the coffee machine, barbecues, conquering clubs, sailing trips, skiing inside fridges, climbing, beach volleyball lunch breaks, and countless more that made these years special and the time at work so enjoyable.

To the group of pyromaniacs and visiting pyromaniacs with whom we shared collaborations, ideas, and a lot of enthusiasm for combustion, working together with you has been really inspiring and fun. My colleagues and friends Kaushal and Sarah, my experimental allies in the APPU journey. Thank you for all the time spent together trying to figure out what was going on within that quartz tube and for all the fun work trips that it allowed us to share. The numerics masters Alessandro P. and Marisa, you have been amazing colleagues and friends. Thank you both for all your help, support, knowledge, and encouragement throughout these years. Many thanks as well to Antonio M. for the fruitful collaboration and the many interesting conversations. Thanks to Boris, for helping me moving my first steps in numerical combustion and OpenFOAM coding. And many thanks to Francesco F., my other OpenFOAM guru. Thanks to Francesca for her commitment and hard work to develop a top-notch combustion lab. Rishikesh, thank you for the pyrotechnic show during my first visit to the TU Delft lab and for the fascinating conversations about combustion and society, sorry for introducing you to the addiction to surfing. Turhan, thank you for your amazing positive and supportive attitude, and for gifting humanity your unmatched funk guitar lines. And thanks to the next-gen combustion researchers Alam, Emre, Pablo, Vaibhav, and Minhea, combustion research at TU Delft relies on you! I also want to thank the master students I had the honour to supervise. Vittorio, who later became a PhD candidate and colleague, I truly admire your passion and dedication (dedicage) to combustion science. And of course Lennard, Victor, and Giacomo A., thank you for your valuable collaboration on the stud-

ies that contributed to this research. It was enriching to discuss the fundamentals of combustion with you and to watch you grow into experts.

To Andres, I would call this chapter three of our adventures together in collecting degrees from each European country, I think we are doing quite well so far! And to Barbora, thank you both for your support when I moved to this new country, for all the dinners and engaging game nights together. Even if we do not see each other as often lately, it is comforting to know that I have friends like you living just 300 meters away.

Thanks to Alessandro M. for going on reconnaissance in the Netherlands. What an incredible twist of destiny to start as desk mates in high school and end up moving to the same country. And thank you to Dominika, thank you both for the many wonderful moments full of music, dinners and inspiring conversations shared during these years.

To Luca, for teaching me how to climb and ski and always being ready for the next expedition through the mountains, either upwards, downwards (or upside down).

Thanks to Gabriele for the countless adventures together: finless rides, hot springs, Volveiro expeditions. Thank you for the guided tours to "La Cueva" and the lab, and for trusting me as your arquebus safety expert. And thanks to Katerina, thank you both for your friendship and for always offering me such a happy, fun, and welcoming retreat by the ocean.

I want to thank my forever friends: Michele, Marco P, Raphael and Elena, Eugenio, Federico, Aurora, Celeste, Lucrezia, Valentina, Teresa, Alessandro B., Anthony and Alessandra, Giacomo V, Ilaria, Arianna, Filippo, Lorenzo B., David and Caterina, Diego, and Giulia. The more years pass, the more I realize how lucky I am to have you all, to have grown up together and to share a friendship that remains so strong despite the many kilometers between us. Even if we do not see each other as often as I would like, the time spent with you will always feel like home.

A huge thank you to my family: Zia Cri, Zia Fra, Marco A., Vale, Bob, and the sweetest Leo and Noa. And above all, thank you to Margherita, Luigi, and Giacomo, to my dear grandparents Laura and my dearly missed Enrico, Irma, and Salvatore. This achievement would never have been possible without you. You are my roots and my northern star and I would not be the person I am without your unconditional love. Thank you for always being there for me, for believing in me, and for all your words of comfort in the darkest moments.

And of course to my beloved Rosie, thank you for supporting me in the hardest moments, when everything seemed endless. Thank you for helping me bring order to the chaos and reminding me to focus on taking care of myself, not only on my sometimes overwhelming objectives. I know it was quite hard to be close to me in my negative moments, and for this I am even more deeply grateful to have you by my side.

CURRICULUM VITÆ

Gioele FERRANTE

17-05-1995 Born in Ancona, Italy.

WORK EXPERIENCE

- 2021–2026 PhD Candidate in CFD for turbulent hydrogen combustion
Delft University of Technology, Delft (The Netherlands)
Thesis: Large eddy simulation of hydrogen combustion: Development of models and applications for sustainable power generation
Promotors: Prof. Dr.-Ing. G. Eitelberg
Prof.dr. A. Gangoli Rao
Dr. I. Langella
- 2020 Intern in CFD, R&D Department
Dallara Automobili, Varano de' Melegari (PR) (Italy)
- 2019 Intern and Master Thesis Student in Fluid Dynamics
KTH Fluid Mechanics department, Stockholm (Sweden)
- 2016–2018 Aerodynamicist and Computational Fluid Dynamics (CFD) Engineer
UniBo Motorsport Formula SAE Team, Bologna (Italy)

EDUCATION

- 2017–2019 Master of Science in Aerospace Engineering, Dual Degree
University of Bologna, Bologna (Italy)
Kungliga Tekniska högskolan, Stockholm (Sweden)
Thesis: Interscale transport of Reynolds stresses in wall-bounded flows.
Supervisors: Prof.dr. P. H. Alfredsson, Prof.dr. A. Talamelli,
Prof.dr. R. Örlü
- 2014–2017 Bachelor of Science in Aerospace Engineering
University of Bologna, Bologna (Italy)

LIST OF PUBLICATIONS

1. A. Masucci, **G. Ferrante**, T. Ghisu, A. Giusti, I. Langella, *Investigation of Differential Diffusion and Strain Coupling in Large Eddy Simulations of Hydrogen-Air Flames*, [Combustion Science and Technology](#), 1–17 (2026)..
2. S. Link, **G. Ferrante**, K. Dave, G. Monti, G. Eitelberg, F. de Domenico, *Experimental and numerical investigation of mixing in a partially premixed CH₄/H₂ combustor*, [International Journal of Hydrogen Energy](#) **141**, 176-192 (2025).
3. **G. Ferrante**, G. Eitelberg, I. Langella, *Differential diffusion modelling for LES of premixed and partially premixed flames with presumed FDF*, [Combustion Theory and Modelling](#), **28**(6), 695–730 (2024).
4. **G. Ferrante**, Z. X. Chen, I. Langella, *Dynamic modelling of subgrid scalar dissipation rate in premixed and partially premixed flames with differential filter*, [Applied Thermal Engineering](#) **248**, 123233 (2024).
5. **G. Ferrante**, L. Doodeman, A. Gangoli Rao, I. Langella, *LES of hydrogen-enriched methane flames in a lean-burn combustor with axial air injection*, [Proceedings of the ASME Turbo Expo 2023](#) **3B**, V03BT04A015 (2023).

